

The SINFONI Black Hole Survey: The Black Hole Fundamental Plane revisited and the paths of (co-) evolution of supermassive black holes and bulges.

R.P. Saglia^{1,2}, M. Opitsch^{1,2,3}, P. Erwin^{1,2}, J. Thomas^{1,2}, A. Beifiori^{1,2}, M. Fabricius^{1,2}, X. Mazzalay^{1,2}, N. Nowak⁴, S.P. Rusli^{1,2}, R. Bender^{1,2}

ABSTRACT

We investigate the correlations between the black hole mass M_{BH} , the velocity dispersion σ , the bulge mass M_{Bu} , the bulge average spherical density ρ_h and its spherical half mass radius r_h , constructing a database of 97 galaxies (31 core ellipticals, 17 power-law ellipticals, 30 classical bulges, 19 pseudo bulges) by joining 72 galaxies from the literature to 25 galaxies observed during our recent SINFONI black hole survey. For the first time we discuss the full error covariance matrix. We analyse the well known M_{BH} - σ and M_{BH} - M_{Bu} relations and establish the existence of statistically significant correlations between M_{Bu} and r_h and anti-correlations between M_{Bu} and ρ_h . We establish five significant bivariate correlations (M_{BH} - σ - ρ_h , M_{BH} - σ - r_h , M_{BH} - M_{Bu} - σ , M_{BH} - M_{Bu} - ρ_h , M_{BH} - M_{Bu} - r_h) that predict M_{BH} of 77 core and power-law ellipticals and classical bulges with measured and intrinsic scatter as small as ≈ 0.36 dex and ≈ 0.33 dex respectively, or 0.26 dex when the subsample of 45 galaxies defined by Kormendy & Ho (2013) is considered. In contrast, pseudo bulges have systematically lower M_{BH} , but approach the predictions of all the above relations at spherical densities $\rho_h \geq 10^{10} M_\odot/kpc^3$ or scale lengths $r_h \leq 1$ kpc. These findings fit in a scenario of co-evolution of BH and classical-bulge masses, where core ellipticals are the product of dry mergers of power-law bulges and power-law Es and bulges the result of (early) gas-rich mergers and of disk galaxies. In contrast, the (secular) growth of BHs is decoupled from the growth of their pseudo bulge hosts, except when (gas) densities are high enough to trigger the feedback mechanism responsible for the existence of the correlations between M_{BH} and galaxy structural parameters.

Subject headings: galaxies:bulges;galaxies:fundamental parameters;galaxies:supermassive black holes;galaxies:elliptical and lenticular, cD; galaxies: spiral

1. Introduction

The last two decades have made clear that supermassive black holes are ubiquitous at the centres of galaxies with bulges. The galaxy velocity dispersion σ (Ferrarese & Merritt 2000; Gebhardt et al. 2000; Gültekin et al. 2009b; McConnell et al. 2011; Mc-

Connell & Ma 2013), luminosity (Dressler 1989; Kormendy 1993; Kormendy & Richstone 1995; Kormendy & Gebhardt 2001; Marconi & Hunt 2003), bulge mass M_{Bu} (Magorrian et al. 1998; Häring & Rix 2004) and the mass of the black hole M_{BH} are proportional with a scatter of a factor of 2, which implies that galaxy bulges and black holes somehow grew in lock step. Important clues concerning this interconnection are encoded in the steepness and intrinsic scatter of scaling laws like the M_{BH} - σ and the M_{BH} - M_{Bu} relations. Kormendy & Ho (2013, and references therein) re-derive the global correlations with black hole mass and review the interpretation framework of these findings. When black holes accrete mass, they shine as quasars or AGN, and this activity interferes with the star for-

¹Max-Planck-Institut für extraterrestrische Physik, Giessenbachstrasse, D-85748 Garching, Germany

²Universitäts-Sternwarte München, Scheinerstrasse 1, D-81679 München, Germany

³Exzellenzcluster Universe, Boltzmannstr. 2, D-85748 Garching, Germany

⁴Stockholm University, Department of Astronomy, Oskar Klein Centre, AlbaNova, SE-10691 Stockholm, Sweden

mation which contributes to bulge growth. Gas can make it to the central region of a galaxy, where a black hole (hereafter BH) might sit, when non-axisymmetric distortions and/or temporal variations of the gravitational potential are strong enough. This can happen through secular evolution of a disk, possibly related to the formation and dissolution of bars, which also leads to the build-up of a pseudo bulge. These pseudo bulges structurally resemble disks, e.g. in their flattening and rotational support. Mergers are another channel to funnel material towards the central region of a galaxy. Mergers produce classical bulges and elliptical galaxies. Different regimes of the M_{BH} - σ and M_{BH} - M_{Bu} scaling relations isolate different stages and modes of BH and/or bulge growth (Kormendy et al. 2011; Mathur et al. 2012; Kormendy & Ho 2013). At the low-mass end galaxies are disk dominated (possibly with pseudo bulges), mergers are unimportant and those few scaling relations that do exist mostly probe secular evolution processes in disks. At the high-mass end, gas-poor mergers dominate and drive the formation of core ellipticals, where the most massive BHs live. Here, the averaging effect of a succession of major mergers is expected to reduce the fractional dispersion of the M_{BH} - M_{Bu} relation (Peng 2007). Core ellipticals have stellar densities mildly increasing towards the center (Faber et al. 1997; Kormendy et al. 2009), a result of binary black hole scouring (Ebisuzaki et al. 1991; Milosavljević & Merritt 2001) that also leaves a dynamical imprint on the stellar orbits (Thomas et al. 2014) and generates a tight correlation between core radius and BH mass (Kormendy et al. 2009; Kormendy & Bender 2009; Rusli et al. 2013a). Core ellipticals are also slow rotators and mildly triaxial (Nieto & Bender 1989; Kormendy & Bender 1996; Faber et al. 1997; Emsellem et al. 2007; Lauer 2012), a further clue to their dry merger origin. In between the two extremes, early gas-rich, dissipational mergers of disk galaxies are responsible for the formation of classical bulges and power-law ellipticals and the lock step accretion on the central BHs mirrored in the M_{BH} - σ and M_{BH} - M_{Bu} relations (King 2003; Hopkins et al. 2007b,a). Power-law ellipticals have stellar densities steeply increasing towards the center, a result of star formation in the high density central gas concentration originating during a gas rich merger (Faber et al. 1997; Kormendy et al. 2009). They are axisymmetric and fast rotators (Nieto et al. 1991; Faber et al. 1997; Emsellem et al. 2007), reminiscent of the structure and dynamics of disk galaxies (Bender 1988;

Kormendy & Bender 1996).

Here we reconsider this scenario by discussing the relationship between the residuals from the M_{BH} - σ and M_{BH} - M_{Bu} relations and the average spherical stellar-mass density (or scale length) of the classical or pseudo bulges and pay particular attention to the families of galaxies discussed above, core and power-law ellipticals, classical and pseudo bulges and the possible presence of bars. Attempts to detect a 'second parameter' or "BH Fundamental Plane" (BH FP) ¹ are numerous and contradictory. Feoli & Mele (2005) ask the question whether the black hole masses correlate with the kinetic energy of elliptical galaxies. Aller & Richstone (2007) claim based on a sample of ~ 20 galaxies that the black hole masses best correlate with $E_g^{0.6}$, where $E_g \sim M_{Bu}^2/r_h$ is the bulge gravitational binding energy. With $M_{Bu} \sim r_h \sigma^2$ and $\rho \sim M_{Bu}/r_h^3$ this implies $M_{BH} \sim \rho^{0.2} M_{Bu} \sim r_h^{-0.6} M_{Bu}^{1.2} \sim M_{Bu}^{0.6} \sigma^{1.2} \sim \rho^{-0.3} \sigma^3 \sim r_h^{0.6} \sigma^{2.4}$, where ρ is the mean density of the bulge and r_h its scale-length. A further empirical study of the BH FP is given by Barway & Kembhavi (2007).

Hopkins et al. (2007b,a) investigate the BH FP with the help of hydrodynamical simulations, finding that the empirical relations $M_{BH} \sim \sigma^{3.0 \pm 0.3} R_e^{0.43 \pm 0.19}$ and $M_{BH} \sim M_{Bu}^{0.54 \pm 0.17} \sigma^{2.2 \pm 0.5}$ can be explained theoretically by noting that the black hole mass should scale as $M_{Bu}^{0.5} \sigma^2$. Graham (2008) reports that the BH FP is possibly driven by the barred galaxies in the sample. Nevertheless, Graham et al. (2001) and more recently Savorgnan et al. (2013) argue for a strong correlation between BH mass and galaxy concentration. Feoli & Mancini (2009) and Mancini & Feoli (2012) investigate the relation between BH mass and kinetic energy of the bulge $M_{BH} \sim M_{Bu} \sigma^2$, discussing the existence of a main-sequence like diagram. Soker & Meiron (2011) propose that the black hole masses should correlate with $M_{Bu} \sigma$. In contrast, Sani et al. (2011) fail to detect bivariate correlations. Beifiori et al. (2012) find only weak evidence for bivariate correlations by analysing 49 galaxies from Gültekin et al. (2009b) and a large sample of galaxies with upper limits to BH masses from Beifiori et al. (2009). Finally, Graham & Scott (2013) claim that "Sersic galaxies" follow a quadratic more than a linear M_{BH} - M_{Bu} relation. We will see that to settle the issue it is important to consider a large database with dynamically mea-

¹This is different from the Fundamental Plane of black hole activity discovered by Merloni et al. (2003).

sured BH masses and accurate bulge plus disk decompositions, and to distinguish between the different families of objects (core and power-law ellipticals, classical bulges and pseudo bulges, barred objects), which to some extent obey different residual correlations.

The structure of the paper is the following. In Sect. 2 we describe the data sample and the methods used to measure the bulge average densities. In Sect. 3 we discuss the error matrix, exploring the covariances between the parameters. In Sect. 4 we discuss the method adopted to investigate multivariate correlations between our parameters. In Sect. 5 we present the results of our correlation analysis. In Sect. 6 we investigate which of the quantities $M_{Bu}^{0.5}\sigma^2$, $M_{Bu}\sigma^2$ and $M_{Bu}\sigma$ best correlate with black hole masses and discuss the implications for the coevolution of bulges and black holes. In Sect. 7 we draw our conclusions. Four appendices discuss how we measure effective velocity dispersions (App. A), how we determine the luminosity profiles and the mass-to-light ratios (hereafter M/L) of bulges (App. B) and how we compute simple Jeans M/L for some of our galaxies (App. C). App. D lists correlation results for a restricted sample of galaxies.

2. The data sample

2.1. Distances, BH masses and velocity dispersions

Our sample includes galaxies from Gültekin et al. (2009b), Sani et al. (2011), McConnell et al. (2011), McConnell & Ma (2013), and Kormendy & Ho (2013). We tested various combinations of these datasets, obtaining compatible results. Here, we start with the database (morphological type, distances, black hole masses, velocity dispersions and their errors) of Kormendy & Ho (2013), without those galaxies belonging to our SINFONI black hole survey (see below). We supplement this list with 8 galaxies (NGC 2974, NGC 3079, NGC 3414, NGC 4151, NGC 4552, NGC 4621, NGC 5813, NGC 5846) which are quoted by Sani et al. (2011). References to the original sources can be found in these two papers. We estimate the errors on distances from NED; they amount typically to 9%. We compute symmetrized logarithmic errors for black hole masses and velocity dispersions.

We do not consider three galaxies with upper limits on their black hole masses (namely NGC 2778, NGC 4382, IC2560). Furthermore, we exclude the following objects. Cygnus A has an uncertain BH mass and

velocity dispersion (Kormendy & Ho 2013); moreover the strong internal dust absorption prevents the derivation of a reliable photometric profile. IC 1481 is undergoing a merger, which makes the derivation of a reliable photometric profile difficult. The determination of the extremely large BH mass of NGC 1277 (van den Bosch et al. 2012) has been questioned by Emsellem (2013). For NGC 4945 the 'binding mass of $\sim 10^6 M_\odot$ within 0.3 pc' quoted in the abstract and the conclusions of Greenhill et al. (1997) comes from maser measurements that point to a non-Keplerian rotation.

We complement these measurements with the 25 determinations from our SINFONI black hole survey; 9 of these values are currently unpublished. They are all based on the stellar dynamical analysis of our SINFONI kinematics, coupled with extended long-slit or integral field stellar kinematics of the outer regions of the galaxies. A detailed description of the SINFONI dataset, the methods and of some specific cases can be found in Nowak et al. (2007), Nowak et al. (2008), Nowak et al. (2010), Rusli et al. (2011), Rusli et al. (2013b), Mazzalay et al. (2016), Erwin et al. (2016), Thomas et al. (2016), Bender et al. (2016). In summary, our SINFONI black hole sample consists of 30 galaxies that we observed with the Spectrograph for INtegral Field Observations in the Near Infrared (Eisenhauer et al. 2003; Bonnet et al. 2003, SINFONI,) at the UT4 of the Very Large Telescope under nearly diffraction limited conditions. The sample was selected to explore poorly populated regions of the $M_{BH}-\sigma$ and $M_{BH}-M_{Bu}$ correlations, with particular attention to high velocity dispersion early-type galaxies, low velocity dispersion and pseudo bulge galaxies, mergers and galaxies with low luminosity AGNs. Through our Schwarzschild axisymmetric code (Thomas et al. 2004, 2005) we determine the best fitting black hole mass M_{BH} (and the mass-to-light ratio M/L of the stellar component(s)), taking into account the bulge and disk components of the galaxies separately when necessary. The appropriate dark matter potential is also considered when necessary (Rusli et al. 2013b). We summarize in Fig. 36 the resulting M/L and M_{BH} for the 9 galaxies that will be discussed in the papers in preparation quoted above; see also Appendix B.

Distances for the SINFONI sample are directly measured (from Cepheids or surface brightness fluctuations) or computed from the redshifts using the standard cosmology ($\Omega = 0.3$, $\Lambda = 0.7$, $H_0 = 70$). We

determine the σ for our SINFONI galaxies using the long-slit and integral field stellar kinematics used in the modeling (see Appendix A).

2.2. Bulge masses, sizes and densities

For all galaxies except the Milky Way, we compute bulge masses, half-light radii and densities from the photometry of the galaxies, decomposed into a bulge and further components (a disk, a bar, a ring) when necessary. For some galaxies we find evidence for composite (classical plus pseudo) bulges (Erwin et al. 2015): in these cases we consider the classical component of the two. We note that some other disk galaxies identified as having pseudo bulges may prove to have composite bulges as well, but the necessary data for a proper assessment is currently lacking for many. We use the dynamically determined mass-to-light ratios M/L taken from the literature or our own modeling to convert light into mass. For the Milky Way we use the axisymmetric bulge density profile of McMillan (2011), which we integrate spherically to get $M_{MW}(< r)$. A detailed description of the methods and procedures is given in the Appendices B and C; here we give a short summary only.

We measure surface brightness profiles from images taken from the Spitzer archive or SDSS (York et al. 2000) and the ESO Key Program described in Scorza et al. (1998), or take them from the literature. Bulge-disk decompositions, when necessary, are taken from Fisher & Drory (2008), Gadotti (2008), Sani et al. (2011), Beifiori et al. (2012), Vika et al. (2012) or are performed by us (in 16 cases), using the program of Erwin (2015) or the procedures of Fisher & Drory (2008). Mass-to-light ratios come from different types of dynamical modeling, that can be based on spherical distribution functions (Kronawitter et al. 2000), or Schwarzschild modeling (Schulze & Gebhardt 2011), Jeans equations (Haring & Rix 2004), or gas dynamics (Dalla Bonta et al. 2009). If none of this is available, they are computed by matching the stellar kinetic energy profiles $\sqrt{v^2(R) + \sigma^2(R)}$ or the central velocity dispersion through spherical Jeans equations (see Appendix B). When not already done by the authors, we correct the M/L for galactic extinction following Schlegel et al. (1998) and we transform them to the band of the available surface brightness profiles using the galaxy colors from the Hyperleda database (Paturel et al. 2003). We adopt this approach to test whether dynamically determined M/L can deliver bulge masses and densities that better correlate (i.e. with smaller

scatter) with BH masses. Kormendy & Ho (2013) consider M/L determinations from colors, deriving a M_{BH} - M_{Bu} relation with impressive small scatter (0.29 dex). In principle, stellar-population M/L determinations could be uncertain, because they depend on the proper choice of the stellar initial mass function (Thomas et al. 2011; Cappellari et al. 2013) and internal dust corrections, see discussion in Rusli et al. (2013a). We investigate this issue using the bulge masses quoted by Kormendy & Ho (2013) for the 45 galaxies used in their fits (see below).

We circularize the bulge photometry and deproject it assuming spherical symmetry to derive the spherical luminosity density $l_S(r)$. We then compute the spherical luminosity:

$$L_S(< r) = \int_0^r 4\pi r^2 l_S(r) dr. \quad (1)$$

For the SINFONI sample of galaxies we have also performed an axisymmetric deprojection of the (decomposed bulge and disk) surface brightness profiles and derived the axisymmetric luminosity density $l_A(r, \theta, i)$, where r and θ are spherical coordinates and i the assumed inclination angle. We spherically integrate l_A to get a second estimate of the spherical luminosity L_A :

$$L_A(< r) = \int_{Sphere(r)} l_A dV. \quad (2)$$

Fig. 1 compares the spherical luminosity profiles derived using Eqs. 1 and 2. L_S and L_A are similar within 0.05 dex, with typical deviations less than 0.02 dex. The most deviant profiles are for flattened galaxies seen nearly edge-on.

The spherical mass profile of the bulge is $M(< r) = L(< r) \times M/L$, where the mass-to-light ratio M/L is determined dynamically. We discuss in the Appendix B on a case by case basis the applied transformations necessary to homogenize the used photometry and M/L .

We extend $M(< r)$ to large radii using a spline extrapolation of the surface brightness, adding a further point to the measured profile at very large radii (typically several tens to hundreds of arcsec depending on the size of the bulges) and with a surface brightness of 70 mag/arcsec². This generates a deprojected density decreasing as r^{-3} at large radii, see Fig. 4. Then we get the bulge mass as:

$$M_{Bu} = M(< \infty) = M(< r_{max}) + M_{extrap}, \quad (3)$$

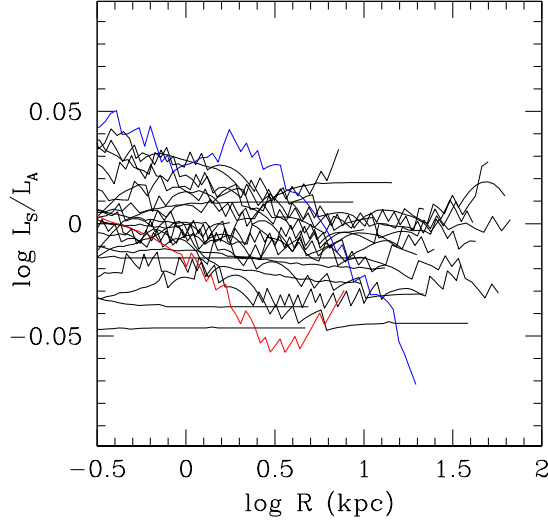


Fig. 1.— The comparison between the spherical luminosity profiles derived using Eqs. 1 and 2 for the SINFONI galaxies. The red (NGC 4486a) and blue (NGC 4751) lines show the most deviant profiles.

where r_{max} is the distance of the last measured surface brightness point and M_{extrap} is the light contribution due to the extrapolation to the last computed deprojected density point. We define the half-light radius r_h of the bulge component as the radius where $M(< r_h) = M_{Bu}/2$. The bulge's averaged density within r_h is

$$\rho_h = \frac{M_{Bu}/2}{4\pi r_h^3/3}. \quad (4)$$

Fig. 4 shows that the bulge masses (to the precision given in Table 1) are reached at approximately $20 r_h$, where we effectively cut the density profiles, not to have to worry about the logarithmic divergence of the mass profile implied by the r^{-3} behaviour of our extrapolation.

In addition, for all galaxies except the Milky Way we compute the projected circularized half-luminosity radius R_e of the bulge from the curve of growth of the projection along the line of sight of the luminosity density profile. Examples of the procedure are given in Fig. 2 discussed below. We get $R_e/r_h = 0.74$ on average, with $rms = 0.01$.

Fig. 2 shows four examples of our surface bright-

ness profiles, to clarify the role of extrapolation in the determination of R_e and r_h . For these galaxies our derived R_e differ by more than 0.3 dex from the r_e values quoted by Rusli et al. (2013a), Table 2, from a Core-Sersic fit (see comments in Appendix B). By construction, our procedure reproduces the observed profile perfectly. This is not always true, when for example Sersic or Core-Sersic fits are used to derive scale radii, as done in Rusli et al. (2013a). We quantify the amount of extrapolation involved in our analysis in Sect. 2.3.

We compute spherically averaged densities for all classes of objects in our sample in order to have a homogeneous data set. But is it physically meaningful to consider spherical half-mass radii and spherically averaged densities also for pseudo bulges? Our current understanding (Erwin et al. 2015, and references therein) is that these structures are more similar to disks than spheroids. Therefore, for these objects (except the Milky Way) we also estimate cylindrical average densities:

$$\rho_{h,c} = \frac{M_{Bu}/2}{\pi a_e^2 h_z}, \quad (5)$$

where $a_e = R_e(a/b)^{1/2}$ is the projected half-luminosity radius along the major axis (the proper scale length of an inclined disk), a/b the major to minor axis ratio of the bulge (taken from the decompositions described in Appendix B), and h_z an estimate of the thickness. We consider the case of (a) a fixed thickness of $h_z = 0.2$ kpc or (b) a thickness $h_z = 0.2a_e/1.67$, which is 20% of the exponential scale-length of the disk $h = a_e/1.67$. Fig. 3 shows the results. On average, the scale lengths do not change much ($\langle \log a_e/r_h \rangle = -0.016$), because the a/b dependency compensates the R_e/r_h ratio. However, the cylindrical densities are one order of magnitude larger ($\langle \log \rho_{h,c}/\rho_h \rangle = 1.31$ for $h_z = 0.2a_e/1.67$).

Table 1 lists the galaxy names (Column 1), the galaxy type (Column 2), a series of flags (Column 3 to 8, see description in the footnote of the table), the distance used (Column 9) and the logarithms of the measured values of the parameters M_{BH} (in M_\odot), σ (in km/s), M_{Bu} (in M_\odot), ρ_h (in M_\odot/kpc^3), r_h (in kpc) with their errors in Columns 10 to 14 (see also Sect. 3), plus the values of R_e (in arcsec) in Column 15. Table 2 lists the cylindrical average quantities for pseudo bulges, with galaxy names (Column 1), the logarithms of a_e (in kpc) and $\rho_{c,h}$ (in M_\odot/kpc^3 , computed with $h_z = 0.2a_e/1.67$). As discussed above, we

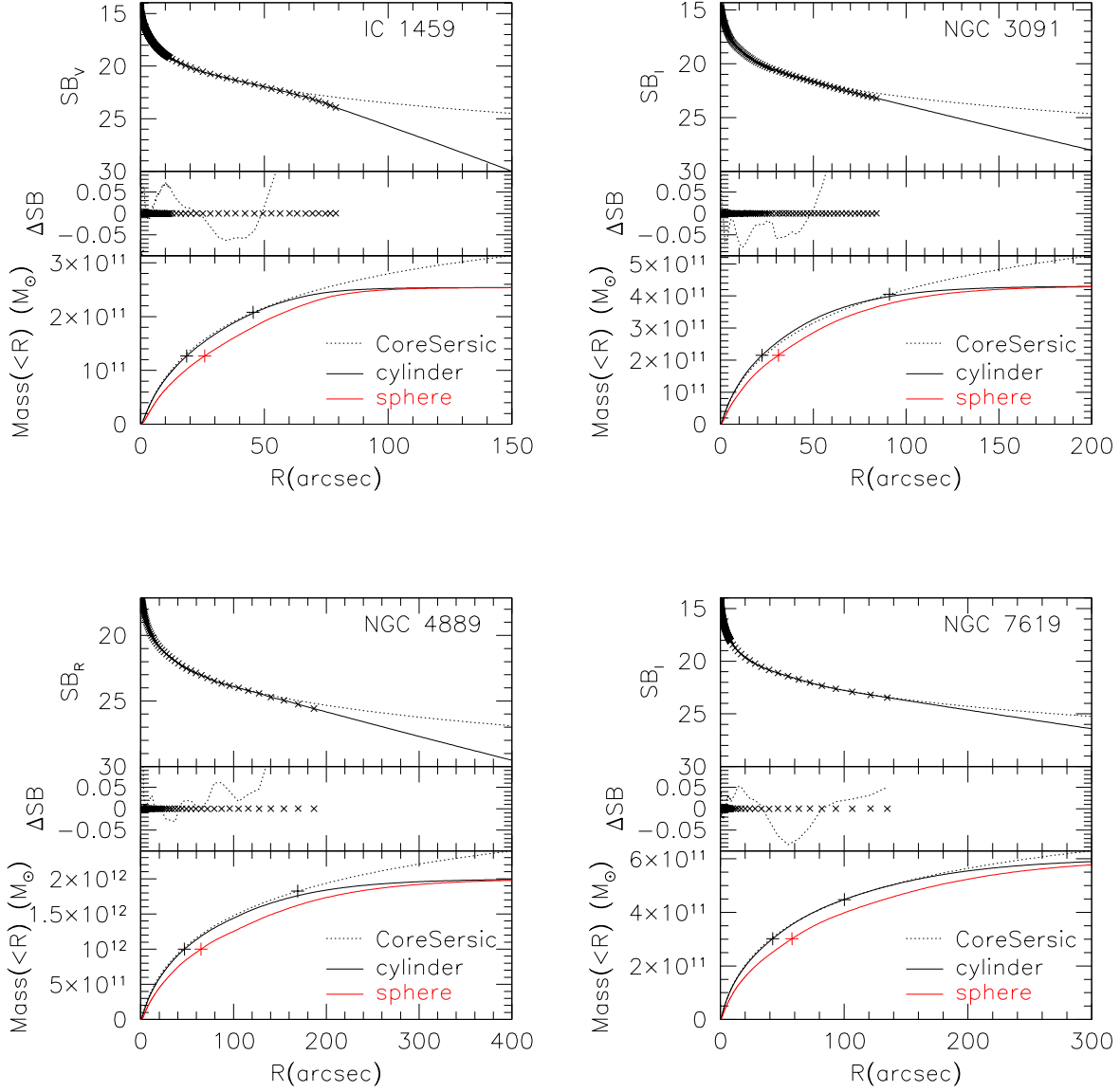


Fig. 2.— For each of the core ellipticals IC1459, NGC 3091, NGC 4889, and NGC 7619 we present three plots. The plots at the top show the observed circularized surface brightness profiles (crosses), together with the projection along the line of sight of the luminosity density we derived (full line). The dotted lines show the best-fitting Core-Sersic profile of Rusli et al. (2013a). The plots in the middle show the differences in surface brightness between the data and the projected luminosity density profiles (crosses) and the Core-Sersic fits (dotted lines) of Rusli et al. (2013a). The plots at the bottom show three lines: our spherical (full red lines) and cylindrical (full black lines) mass profiles and the (cylindrical) mass profile implied by the Core-Sersic fits of Rusli et al. (2013a). The three crosses show the positions of r_h and R_e listed in Table 1 and r_e from Table 2 of Rusli et al. (2013a).

also consider the bulge masses quoted by Kormendy & Ho (2013) for the 45 galaxies used in their fits, here after KH45. They are given in Table 3, coupled to our sizes r_h to derive colour-based density estimates. This procedure is uncertain, since we do not know how the bulge plus disk decompositions of Kormendy & Ho (2013) were performed. In detail, Table 3 gives the names of the galaxies of the KH45 sample (Column 1), the bulge masses (Column 2, computed from luminosities using mass-to-light ratios M/L_C derived from colors), and the spherical bulge densities (Column 4) computed using the r_h of Table 1. The logarithmic errors (Column 3 and 5) are computed as described in Sect. 3.

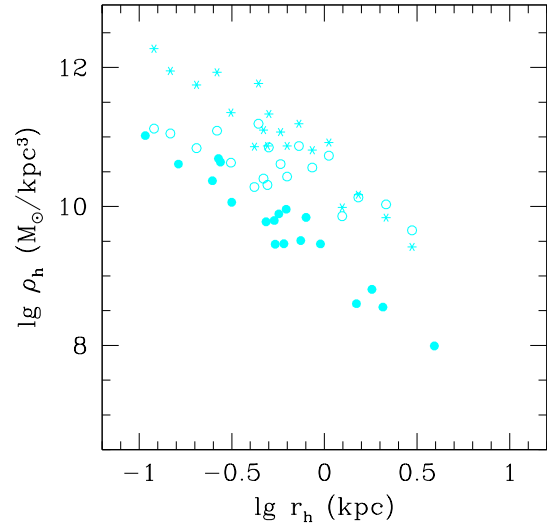


Fig. 3.— Cylindrical averaged scalelengths and densities of pseudo bulges, assuming vertical scale height $h_z = 0.2$ kpc (open circles) or $h_z/h = 0.2$ (stars); see Eq. 5, case (a) and (b) respectively. The filled points show the spherical average quantities.

TABLE 1
THE GALAXY SAMPLE WITH THE VALUES OF THE MEASURED PARAMETERS.

Galaxy	Type	S	T	m	b	B	M	$D (Mpc)$	$\log M_{BH} (M_{\odot})$	$\log \sigma (km.s^{-1})$	$\log M_{BH} (M_{\odot})$	$\log \rho_h (M_{\odot} kpc^{-3})$	$\log \tau_{rh} (kpc)$	$R_e ('')$
MW	She	0	3	0	1	1	0	0.008 ± 0.001	6.633 ± 0.048	2.021 ± 0.084	10.375 ± 0.069	9.283 ± 0.111	0.056 ± 0.032	-
Circinus	SABc	0	3	0	1	1	2	2.820 ± 0.470	6.057 ± 0.105	1.898 ± 0.017	9.170 ± 0.089	10.011 ± 0.153	0.788 ± 0.072	8.9
A1836	BCGE	0	0	0	0	0	4	152.400 ± 8.426	9.573 ± 0.061	2.459 ± 0.021	11.028 ± 0.135	7.292 ± 0.187	1.237 ± 0.060	17.2
IC1459	E4	0	0	0	0	0	2	28.920 ± 3.739	9.394 ± 0.079	2.520 ± 0.007	11.401 ± 0.076	8.800 ± 0.153	0.359 ± 0.069	8.6
IC2599	BCGE	0	0	0	0	0	1	49.200 ± 3.628	9.114 ± 0.073	2.908 ± 0.022	12.028 ± 0.110	6.993 ± 0.355	1.893 ± 0.146	68.1
NGC0221	E2	0	1	0	0	1	2	0.805 ± 0.030	6.889 ± 0.193	2.886 ± 0.017	8.627 ± 0.022	10.346 ± 0.042	-0.947 ± 0.019	21.2
NGC0224	S0	0	2	0	0	1	2	0.774 ± 0.032	8.135 ± 0.161	2.228 ± 0.021	10.448 ± 0.021	9.258 ± 0.038	-0.012 ± 0.018	92.9
NGC0234	S0	0	0	0	0	0	1	24.220 ± 2.224	8.938 ± 0.053	2.253 ± 0.031	11.630 ± 0.075	8.108 ± 0.136	0.807 ± 0.066	47.1
NGC0821	S0	0	2	0	0	1	1	1.810 ± 0.197	7.217 ± 0.137	2.370 ± 0.021	11.344 ± 0.082	0.734 ± 0.158	-0.730 ± 0.158	34.8
NGC1023	S0	0	2	0	1	1	2	15.800 ± 0.901	6.016 ± 0.065	2.132 ± 0.021	11.321 ± 0.102	10.339 ± 0.064	-0.301 ± 0.132	7.5
NGC1088	S0	0	3	0	0	1	2	15.900 ± 0.901	6.634 ± 0.245	2.179 ± 0.030	9.242 ± 0.305	12.388 ± 0.519	1.339 ± 0.344	0.5
NGC1104	S0	0	3	0	0	1	4	57.980 ± 6.399	7.850 ± 0.051	2.170 ± 0.015	10.292 ± 0.205	8.353 ± 0.042	0.538 ± 0.048	9.5
NGC1184	S0bc	0	3	0	0	1	3	21.800 ± 3.384	8.478 ± 0.343	2.044 ± 0.015	9.732 ± 0.141	7.353 ± 0.089	-0.219 ± 0.104	4
NGC1309	S0	0	3	0	0	0	1	20.850 ± 0.672	8.945 ± 0.356	2.498 ± 0.094	11.789 ± 0.021	10.155 ± 0.043	1.115 ± 0.051	103.7
NGC2273	S0	0	3	0	0	1	3	29.800 ± 1.063	6.935 ± 0.067	2.161 ± 0.021	10.250 ± 0.087	10.755 ± 0.153	-0.561 ± 0.028	1.5
NGC2349	S0	0	3	0	0.5	1	1	12.700 ± 1.642	7.167 ± 0.367	2.097 ± 0.031	9.875 ± 0.145	9.242 ± 0.237	-0.140 ± 0.101	8.6
NGC2748	S0	0	3	0	1	1	2	23.400 ± 3.244	7.647 ± 0.240	2.276 ± 0.021	10.733 ± 0.156	9.745 ± 0.303	-0.246 ± 0.150	3.6
NGC2787	S0/a	0	3	1	0	1	3	67.100 ± 2.381	7.600 ± 0.088	2.276 ± 0.042	10.470 ± 0.126	11.131 ± 0.154	-0.774 ± 0.076	3.5
NGC2960	E2	0	3	1	0	1	3	21.800 ± 2.381	7.033 ± 0.069	2.356 ± 0.021	11.440 ± 0.058	8.845 ± 0.144	-0.099 ± 0.046	1.8
NGC2974	E4	0	2	0	0	0	1	3.604 ± 0.133	8.230 ± 0.129	2.155 ± 0.021	10.424 ± 0.065	8.732 ± 0.133	0.403 ± 0.060	21.6
NGC3031	S0	0	2	0	1	1	2	15.900 ± 1.246	6.308 ± 0.049	2.165 ± 0.021	9.898 ± 0.057	10.690 ± 0.082	-0.011 ± 0.066	41.4
NGC3079	S0cd	0	2	0	0.5	1	2	9.540 ± 0.306	8.953 ± 0.095	2.362 ± 0.021	11.072 ± 0.110	8.865 ± 0.389	-0.572 ± 0.034	25.2
NGC3115	S0	0	3	0	1	1	2	23.750 ± 2.630	7.322 ± 0.232	2.124 ± 0.021	9.754 ± 0.067	9.770 ± 0.129	-0.438 ± 0.163	42.2
NGC3227	S0	0	3	0	1	1	2	21.380 ± 1.972	8.378 ± 0.114	2.312 ± 0.021	10.288 ± 0.061	10.350 ± 0.094	-0.315 ± 0.057	3.1
NGC3245	S0	0	1	0	0	0	1	10.700 ± 0.456	8.250 ± 0.253	2.161 ± 0.021	10.460 ± 0.083	8.172 ± 0.332	-0.455 ± 0.132	3.5
NGC3377	E5	0	0	0	0	0	1	10.900 ± 0.542	8.619 ± 0.113	2.314 ± 0.021	10.940 ± 0.045	8.572 ± 0.113	0.488 ± 0.047	48.2
NGC3379	E1	0	0	0	0	0	1	11.400 ± 0.741	7.033 ± 0.214	2.164 ± 0.021	10.980 ± 0.039	9.895 ± 0.076	-0.246 ± 0.035	7.6
NGC3384	S0	0	3	0	1	1	3	49.200 ± 8.194	7.196 ± 0.330	2.170 ± 0.039	10.263 ± 0.111	9.859 ± 0.167	-0.206 ± 0.072	2
NGC3393	SABa	0	3	0	1	1	3	25.200 ± 2.738	8.400 ± 0.071	2.312 ± 0.021	11.008 ± 0.081	8.409 ± 0.239	0.589 ± 0.088	23.3
NGC3414	S0pec	0	2	0	1	1	1	20.510 ± 1.702	8.517 ± 0.127	2.328 ± 0.022	10.948 ± 0.176	8.307 ± 0.491	0.573 ± 0.219	27.4
NGC3485	S0	0	2	0	1	1	1	22.650 ± 1.775	8.137 ± 0.157	2.360 ± 0.021	11.521 ± 0.074	8.829 ± 0.092	0.829 ± 0.092	4.5
NGC3607	E1	0	0	0	0	0	1	22.750 ± 1.688	8.667 ± 0.098	2.260 ± 0.021	10.909 ± 0.092	7.889 ± 0.158	0.799 ± 0.158	42.7
NGC3608	E1	0	0	0	0	0	1	92.200 ± 10.638	9.959 ± 0.139	2.431 ± 0.044	12.022 ± 0.152	1.338 ± 0.342	1.338 ± 0.342	35.3
NGC3942	E1	0	0	0	0	1	4	14.300 ± 1.253	8.927 ± 0.082	2.439 ± 0.011	10.580 ± 0.277	10.595 ± 0.287	-0.313 ± 0.042	5.2
NGC3998	S0	0	2	0	1	1	1	13.350 ± 1.726	8.255 ± 0.173	2.255 ± 0.022	10.588 ± 0.080	9.840 ± 0.142	-0.135 ± 0.064	8.4
NGC4026	S0	0	2	0	0.5	1	1	20.000 ± 2.772	7.813 ± 0.076	2.193 ± 0.022	9.988 ± 0.075	9.729 ± 0.128	-0.221 ± 0.060	4.6
NGC4151	S0	0	2	0	1	1	1	7.270 ± 0.503	7.577 ± 0.030	2.061 ± 0.038	9.790 ± 0.034	9.471 ± 0.062	-0.201 ± 0.030	13.3
NGC4158	SABbc	0	2	0	1	1	1	32.360 ± 2.835	8.723 ± 0.097	2.498 ± 0.021	11.887 ± 0.131	7.775 ± 0.802	1.063 ± 0.205	54.2
NGC4261	E2	0	0	0	0	0	2	26.580 ± 3.931	8.990 ± 0.155	2.384 ± 0.022	10.950 ± 0.105	8.993 ± 0.241	0.345 ± 0.102	12.5
NGC4291	E1	0	2	0	0.5	1	1	22.910 ± 1.372	8.656 ± 0.188	2.352 ± 0.021	10.588 ± 0.072	9.818 ± 0.231	-0.128 ± 0.090	4.9
NGC4342	S0	0	0	0	0	0	1	18.510 ± 0.597	8.966 ± 0.046	2.471 ± 0.024	11.740 ± 0.052	7.759 ± 0.209	1.022 ± 0.084	84
NGC4388	S0	0	3	0	1	1	3	16.550 ± 1.601	6.864 ± 0.043	1.996 ± 0.044	10.422 ± 0.102	8.552 ± 0.171	0.316 ± 0.067	19.2
NGC4388	S0bc	0	3	0	1	1	3	16.010 ± 0.516	7.843 ± 0.086	2.223 ± 0.021	10.880 ± 0.041	8.254 ± 0.115	0.568 ± 0.048	35.7
NGC4459	E2	0	1	0	0	0	1	15.250 ± 0.492	7.954 ± 0.239	2.279 ± 0.021	11.131 ± 0.071	8.538 ± 0.283	0.557 ± 0.111	35.2
NGC4473	E5	0	1	0	0	0	1	16.680 ± 0.615	9.789 ± 0.031	2.511 ± 0.022	11.869 ± 0.071	7.222 ± 0.249	1.241 ± 0.095	158.4
NGC4486	E1	0	0	0	0	0	1	16.440 ± 1.786	8.654 ± 0.124	2.346 ± 0.022	11.420 ± 0.058	9.660 ± 0.100	-0.154 ± 0.047	6.5
NGC4526	S0	0	2	0	1	1	4	15.300 ± 0.987	8.699 ± 0.051	2.401 ± 0.021	11.420 ± 0.107	7.714 ± 0.604	0.928 ± 0.232	82.6
NGC4564	S0	0	2	0	0	0	1	15.940 ± 0.514	7.945 ± 0.124	2.210 ± 0.022	11.704 ± 0.069	9.126 ± 0.177	0.207 ± 0.074	15.3
NGC4596	S0	0	2	0	0.5	1	2	9.870 ± 0.819	8.823 ± 0.045	2.134 ± 0.022	10.671 ± 0.037	9.795 ± 0.080	0.936 ± 0.059	133.6
NGC4596	S0	0	2	0	1	1	2	16.550 ± 6.229	7.885 ± 0.260	2.380 ± 0.022	10.423 ± 0.166	9.170 ± 0.333	0.110 ± 0.164	11.9
NGC4649	E2	0	1	0	0	0	1	18.300 ± 2.962	8.602 ± 0.085	2.352 ± 0.021	11.120 ± 0.119	8.272 ± 0.401	0.643 ± 0.167	36.7
NGC4649	E2	0	0	0	0	0	1	16.460 ± 0.607	9.674 ± 0.099	2.580 ± 0.022	11.849 ± 0.093	7.837 ± 0.373	1.033 ± 0.150	99.5
NGC4697	E5	0	1	0	0	0	1	12.540 ± 0.404	8.305 ± 0.112	2.248 ± 0.020	11.021 ± 0.056	7.889 ± 0.179	0.736 ± 0.072	65.8
NGC4736	Sub	0	3	0	1	1	2	5.000 ± 0.786	6.831 ± 0.123	2.079 ± 0.022	9.482 ± 0.081	10.373 ± 0.143	-0.605 ± 0.068	7.7
NGC4826	Sub	0	3	0	0	1	2	7.270 ± 1.177	6.193 ± 0.131	2.017 ± 0.013	10.038 ± 0.087	8.597 ± 0.153	0.173 ± 0.072	31.3
NGC4839	E4	0	0	0	0	0	1	102.000 ± 5.169	8.932 ± 0.268	2.540 ± 0.006	12.305 ± 0.102	6.861 ± 0.307	1.507 ± 0.123	47.1
NGC5077	E3	0	0	0	0	0	4	38.700 ± 8.442	7.755 ± 0.084	2.346 ± 0.022	11.055 ± 0.114	8.453 ± 0.212	0.560 ± 0.099	14
NGC5128	E3	0	0	1	0	0	1	3.620 ± 0.200	8.436 ± 0.167	2.176 ± 0.022	10.636 ± 0.107	8.930 ± 0.129	0.261 ± 0.040	76.9
NGC5576	E3	0	1	0	0	0	1	25.680 ± 1.657	8.436 ± 0.126	2.262 ± 0.021	11.060 ± 0.073	8.178 ± 0.171	0.653 ± 0.065	26.1
NGC5813	E1-2	0	0	0	0	0	1	32.200 ± 2.672	8.851 ± 0.058	2.362 ± 0.021	11.770 ± 0.089	7.981 ± 0.220	0.954 ± 0.096	42.4
NGC5845	E3	0	1	0	0	0	1	25.870 ± 4.067	$8.688 \pm 0.$					

TABLE 1—Continued

Galaxy	Type	S	T	m	b	B	M	D (Mpc)	$\log M_{BH}$ (M_{\odot})	$\log \sigma$ (km s $^{-1}$)	$\log M_{Bu}$ (M_{\odot})	$\log \rho_h$ ($M_{\odot} kpc^{-3}$)	$\log r_h$ (kpc)	R_e (")
NGC6364	SBb	0	3	0	1	1	3	147.60 \pm 16.035	7.489 \pm 0.047	2.199 \pm 0.041	10.497 \pm 0.099	8.805 \pm 0.128	0.256 \pm 0.047	1.9
NGC6323	SBab	0	3	0	0	1	3	113.400 \pm 12.320	7.004 \pm 0.048	2.199 \pm 0.072	10.691 \pm 0.147	7.990 \pm 0.176	0.593 \pm 0.053	5.3
NGC7052	E3	0	3	0	0	0	2	70.400 \pm 8.449	8.598 \pm 0.230	2.425 \pm 0.021	11.357 \pm 0.110	7.700 \pm 0.270	0.911 \pm 0.118	17.4
NGC7357	S0	0	2	0	0	1	2	12.530 \pm 1.214	6.954 \pm 0.302	1.826 \pm 0.019	9.518 \pm 0.062	9.037 \pm 0.097	-0.148 \pm 0.043	8.7
NGC7382	SBab	0	3	0	1	1	3	22.300 \pm 9.845	7.741 \pm 0.205	2.193 \pm 0.053	9.480 \pm 0.217	10.058 \pm 0.388	-0.300 \pm 0.186	2.2
NGC7768	E4	0	0	0	0	0	1	116.000 \pm 27.495	9.127 \pm 0.181	2.410 \pm 0.044	11.982 \pm 0.190	6.970 \pm 0.615	1.363 \pm 0.235	30
UGC3789	SABab	0	3	0	0	1	3	49.900 \pm 5.421	6.985 \pm 0.085	2.029 \pm 0.049	10.053 \pm 0.105	9.513 \pm 0.133	-0.128 \pm 0.047	2.3
NGC3307	S0	1	2	0	0	1	1	52.800 \pm 5.736	8.602 \pm 0.060	2.310 \pm 0.007	10.510 \pm 0.050	10.120 \pm 0.096	-0.178 \pm 0.047	1.9
NGC1316	SAB0	1	2	1	0	0	1	18.600 \pm 0.600	8.176 \pm 0.254	2.363 \pm 0.004	11.150 \pm 0.262	8.883 \pm 0.684	0.447 \pm 0.314	65.2
NGC1332	S0	1	2	0	0	1	1	22.300 \pm 1.851	9.161 \pm 0.076	2.467 \pm 0.010	11.000 \pm 0.048	10.000 \pm 0.079	0.025 \pm 0.036	7.3
NGC1374	E3	1	2	0	0	1	1	19.230 \pm 0.655	8.763 \pm 0.062	2.225 \pm 0.009	10.700 \pm 0.073	8.377 \pm 0.199	-0.322 \pm 0.072	3
NGC1398	SBab	1	2	0	0	1	1	24.770 \pm 4.125	8.033 \pm 0.083	2.369 \pm 0.007	10.160 \pm 0.074	10.200 \pm 0.145	1.134 \pm 0.204	71.8
NGC1407	E0	1	0	0	0	0	1	28.050 \pm 3.367	9.653 \pm 0.079	2.443 \pm 0.003	11.740 \pm 0.157	7.418 \pm 0.469	0.954 \pm 0.137	26.2
NGC3091	E3	1	0	0	0	0	1	51.570 \pm 5.603	9.568 \pm 0.067	2.436 \pm 0.016	11.700 \pm 0.108	7.918 \pm 0.337	0.889 \pm 0.130	22.4
NGC3368	SAB0	1	3	0	0	0	1	51.250 \pm 8.296	9.556 \pm 0.072	2.477 \pm 0.017	11.630 \pm 0.106	8.044 \pm 0.300	-1.264 \pm 0.040	0.8
NGC3489	SAB	1	3	0	1	2	1	10.400 \pm 0.959	6.875 \pm 0.076	2.122 \pm 0.003	8.483 \pm 0.068	11.350 \pm 0.097	-1.009 \pm 0.030	1.2
NGC3627	SAB(s)b	1	3	0	1	2	1	12.100 \pm 0.837	6.778 \pm 0.051	1.949 \pm 0.002	8.725 \pm 0.036	10.830 \pm 0.063	-0.367 \pm 0.047	1.7
NGC3923	E4	1	3	0	1	1	1	10.050 \pm 1.092	6.929 \pm 0.048	2.088 \pm 0.002	9.050 \pm 0.048	11.020 \pm 0.095	1.069 \pm 0.103	85.3
NGC4371	SB0+(r)	1	3	0	0	0	1	20.880 \pm 2.700	9.449 \pm 0.115	2.347 \pm 0.020	11.360 \pm 0.093	7.435 \pm 0.245	-0.122 \pm 0.038	6.9
NGC4371	E2	1	3	0	0	1	2	16.900 \pm 1.481	6.845 \pm 0.074	2.134 \pm 0.005	9.901 \pm 0.040	9.344 \pm 0.078	1.282 \pm 0.106	168.3
NGC4472	E2	1	0	0	0	0	1	17.140 \pm 0.592	9.398 \pm 0.037	2.482 \pm 0.011	11.910 \pm 0.069	7.137 \pm 0.263	-0.131 \pm 0.119	7.2
NGC4486a	dE0	1	1	0	0	0	1	16.000 \pm 0.516	7.100 \pm 0.147	2.160 \pm 0.006	10.280 \pm 0.082	9.750 \pm 0.281	-0.393 \pm 0.018	2.3
NGC4751	SABb	1	3	0	0	0	1	16.550 \pm 0.610	8.602 \pm 0.024	2.172 \pm 0.026	9.847 \pm 0.027	10.700 \pm 0.043	-0.271 \pm 0.030	5
NGC4699	E	1	3	0	0	1	1	16.500 \pm 1.141	7.301 \pm 0.080	2.197 \pm 0.008	9.909 \pm 0.038	9.798 \pm 0.064	0.627 \pm 0.047	1.9
NGC4751	SABb	1	3	0	0	1	2	18.900 \pm 2.053	8.246 \pm 0.052	2.238 \pm 0.010	9.816 \pm 0.057	10.770 \pm 0.099	0.526 \pm 0.109	18.9
NGC3018	E3	1	1	0	0.5	0	1	26.920 \pm 2.925	9.146 \pm 0.056	2.538 \pm 0.016	11.070 \pm 0.087	8.366 \pm 0.256	0.659 \pm 0.077	17
NGC3238	E	1	0	0	0	0	1	40.550 \pm 4.867	8.021 \pm 0.078	2.321 \pm 0.007	11.120 \pm 0.063	8.222 \pm 0.175	1.101 \pm 0.093	29.4
NGC3419	E	1	0	0	0	0	1	64.100 \pm 6.964	9.672 \pm 0.158	2.523 \pm 0.002	11.750 \pm 0.195	7.319 \pm 0.997	1.306 \pm 0.103	53.8
NGC3516	E	1	0	0	0	0	1	36.200 \pm 6.106	9.860 \pm 0.144	2.365 \pm 0.011	12.010 \pm 0.151	7.170 \pm 0.275	1.107 \pm 0.093	32.6
NGC6861	E	1	1	0	0	0	1	38.440 \pm 6.349	9.519 \pm 0.058	2.522 \pm 0.015	11.790 \pm 0.069	7.846 \pm 0.214	1.107 \pm 0.093	20.5
NGC7619	E	1	0	0	0	0	1	27.300 \pm 4.547	9.301 \pm 0.084	2.390 \pm 0.003	11.340 \pm 0.116	8.918 \pm 0.354	0.563 \pm 0.220	42.1
NGC7619	E	1	0	0	0	0	1	51.520 \pm 7.380	9.398 \pm 0.108	2.469 \pm 0.007	11.780 \pm 0.156	7.379 \pm 0.493	1.159 \pm 0.204	42.1

Column 1: galaxy name; Column 2: galaxy type; Column 3: Flag S; $S = 0$ flag identifies galaxies from the literature, $S = 1$ identifies galaxies belonging to the SINFONI sample. Column 4: Flag T; T=0 for core ellipticals, 1 for power-law ellipticals, 2 for classical bulges, 3 for pseudo bulges. Column 5: Flag m; m=1 identifies merger remnants. Column 6: The b flag; b=1 identifies barred galaxies, b=0.5 if a bar cannot be excluded because the galaxy is edge-on. Here we follow the strategy of classifying a galaxy as barred even when discrepant opinions are present, see comments in Appendix B. Column 7: Flag B; B=0 identifies galaxies where M_{Bu} comes from the measured photometric profile, B=1 identifies galaxies where M_{Bu} is computed after a bulge plus disk decomposition, B=2 identifies composite galaxies, where both a classical and a pseudo bulge are present. In these cases M_{Bu} is the mass of the classical bulge component. Column 8: Flag M; M=0 indicates the special case of the Milky Way, see text, M=1 indicates that the M/L was computed from distribution function or Schwarzschild modeling, M=2 from Jeans modeling of central kinematics profiles, M=3 from Jeans modeling of central stellar velocity dispersions, M=4 from gas dynamics. See Appendix B for comments on single galaxies. Column 9: distance and its error. Column 10: black hole mass and its error. Column 11: velocity dispersion and its error. Column 12: bulge mass and its error. Column 13: bulge spherical average density and its error. Column 14: bulge spherical half-mass radius and its error. Column 15: bulge cylindrical half-mass radius.

TABLE 2
THE CYLINDRICAL PARAMETERS OF THE PSEUDO BULGES.

Galaxy	$\log a_e(kpc)$	$\log \rho_{h,c}(M_{\odot}kpc^{-3})$
Circinus	-0.8313	11.95
IC2560	-0.06558	10.81
NGC1300	-0.3074	10.87
NGC2273	-0.5796	11.93
NGC2748	-0.3778	10.86
NGC2960	-0.1376	11.19
NGC3079	-0.3559	11.77
NGC3227	-0.3287	11.1
NGC3384	0.02405	10.92
NGC3393	-0.3002	11.33
NGC4388	0.3326	9.84
NGC4736	-0.6902	11.75
NGC4826	0.09586	9.985
NGC6264	0.183	10.17
NGC6323	0.4727	9.418
NGC7582	-0.5045	11.35
UGC3789	-0.2014	10.87
NGC3627	-0.9195	12.27
NGC4501	-0.2367	11.07

Column 1: galaxy name. Column 2: bulge cylindrical major axis half-mass radius. Column 3: bulge cylindrical average density.

TABLE 3
THE BULGE MASSES AND DENSITIES OF KORMENDY & HO (2013).

Galaxy	$\log M_{Bu,C}(M_{\odot})$	$\delta \log M_{Bu,C}(M_{\odot})$	$\log \rho_{h,C}(M_{\odot} kpc^{-3})$	$\log \rho_{h,C}(M_{\odot} kpc^{-3})$
IC1459	11.6	0.1459	8.999	0.142
NGC0221	9.05	0.1053	10.97	0.1041
NGC0224	10.35	0.09694	9.462	0.09182
NGC0524	11.26	0.1247	7.737	0.1585
NGC0821	10.98	0.144	7.864	0.3854
NGC1023	10.53	0.1105	10.45	0.09558
NGC1194	10.64	0.1305	8.044	0.1046
NGC1399	11.5	0.09493	7.064	0.1045
NGC2549	9.71	0.1518	9.207	0.2301
NGC3115	10.92	0.1394	8.713	0.3955
NGC3245	10.69	0.1209	10.75	0.1012
NGC3377	10.5	0.1177	8.212	0.3394
NGC3379	10.91	0.1032	8.492	0.1362
NGC3585	11.26	0.2011	8.619	0.4923
NGC3608	11.01	0.1313	7.69	0.4016
NGC3998	10.67	0.1187	10.68	0.1064
NGC4026	10.33	0.1453	9.812	0.127
NGC4258	9.86	0.1082	9.54	0.09493
NGC4291	10.85	0.1627	8.893	0.2214
NGC4374	11.62	0.1033	7.63	0.2246
NGC4473	10.85	0.1078	8.256	0.2925
NGC4486	11.72	0.104	7.072	0.2571
NGC4526	11.02	0.1303	10.56	0.1017
NGC4564	10.38	0.1059	8.835	0.1915
NGC4594	11.47	0.1156	7.74	0.1031
NGC4649	11.64	0.1235	7.618	0.3796
NGC4697	10.97	0.1018	7.838	0.1947
NGC5077	11.28	0.2094	8.677	0.1506
NGC5576	11	0.1096	8.119	0.1767
NGC5845	10.57	0.1733	10.32	0.1849
NGC6086	11.69	0.1155	8.86	0.1013
NGC7457	9.56	0.1232	9.08	0.1009
NGC7768	11.75	0.2579	6.737	0.5879
NGC1332	11.26	0.1152	10.26	0.09697
NGC1374	10.63	0.1078	8.313	0.2112
NGC1407	11.71	0.194	7.386	0.4655
NGC1550	11.31	0.1476	7.528	0.3321
NGC3031	10.42	0.1065	9.531	0.1725
NGC3091	11.58	0.1789	7.99	0.2851
NGC4486a	9.92	0.1207	9.39	0.2922
NGC4472	11.86	0.1107	7.092	0.2741

2.3. Errors on r_h , ρ_h and M_{Bu}

We now turn to the errors affecting the quantities r_h , ρ_h , and M_{Bu} . Errors on the distance affect all of them, as well as the errors coming from the extrapolation to compute total luminosities. Errors on M_{Bu} and ρ_h have a further component due to the M/L factor (see Sect. 3). We estimate the fractional error on the bulge mass due to extrapolation as $\delta M_{Bu}/M_{Bu} = M_{extrap}/M_{Bu}$. It is on average 9%. We then determine the logarithmic derivatives $a_{rM} = d \log r / d \log M$, $a_{\rho M} = d \log \rho / d \log M$, and $a_{\rho r} = d \log \rho / d \log r$ at $r = r_h$ by a least-squares fit in a region $\pm 0.1 \text{ dex}$ around the mass point $\log M_{Bu}/2$. The logarithmic errors on M_{Bu} , r_h , ρ_h due to extrapolation are then $d \log M_{Bu} = \delta M_{Bu}/M_{Bu} \times \log e$, $d \log r_h = a_{rM} d \log M_{Bu}$, $d \log \rho_h = a_{\rho M} d \log M_{Bu}$. Fig. 4 shows the bulge density and mass profiles of our galaxy sample. Fig. 5 shows the histograms of the values of the parameters a_{rM} , $a_{\rho M}$ and $a_{\rho r}$. Their values can be derived from Table 1 using the equations given in Table 4 (see Sect. 3 for a full description of this Table). On average, we have $\rho \sim r^{-2.3}$ near $r \sim r_h$, which implies $M \sim r^{3-2.3} = r^{0.7}$, or $r \sim M^{1.5}$ and $\rho \sim M^{-2.3 \times 1.5} = M^{-3.5}$. Therefore, the logarithmic errors on r_h due to the extrapolation are on average 1.5 times larger than the ones on M_{Bu} , while the logarithmic errors on ρ_h are 3.5 times larger.

2.4. External comparisons

In Fig. 6 we compare our bulge masses to the ones reported by McConnell & Ma (2013), Kormendy & Ho (2013) (where we exclude pseudo bulges with classical components), Rusli et al. (2013b) (where we show only galaxies fitted by one component) and Erwin et al. (2015). They compare reasonably well, with an rms scatter of $\approx 0.2 \text{ dex}$ and estimated error bars of 0.1 dex. The most deviant point in the comparison with McConnell & Ma (2013) is NGC 3245. The difference stems from their large assumed B/T ratio (0.76). The Kormendy & Ho (2013) points deviating more strongly are pseudo bulges, in particular NGC 4388 and NGC 6323, and the classical bulge of NGC 4526, see discussion in Appendix B. The fits discussed in Sect. 5 and presented in the Tables 13 and 14 show that using the bulge masses of Kormendy & Ho (2013), which are derived using M/L from colors, does not change our conclusions. The differences with the masses of Rusli et al. (2013a) are within the

estimated errors due to the extrapolation. The four most deviant galaxies are discussed in detail in Fig. 2. Some of the masses of Erwin et al. (2015) come from the sample of Laurikainen et al. (2011), who did not publish distances; the latter were provided to us by Laurikainen (private comm.). For five galaxies Erwin et al. (2015) quote (bulge) masses a factor 10 smaller than what we get. The differences originate mainly from the amount of extrapolation (see below). In addition, Erwin et al. (2015) derive stellar masses based on M/L from colors.

Fig. 7, upper left, shows the comparison between our bulge masses and the ones reported by Scott et al. (2013). The latter are not based on proper bulge plus disk decompositions, but are instead derived from total K_S -band magnitudes by applying a statistical bulge-to-disk correction that depends on morphological type. In addition, their conversion of light into mass involves (dust-corrected) M/L values derived from $(B - K)$ colors. The overall scatter in Fig. 7 (0.36 dex) matches the total uncertainty quoted by Scott et al. (2013). For galaxies where we measure $\log M_{Bu} < 10.8$ the agreement is fair (the average difference is 0.05 dex). However, at larger masses Scott et al. (2013) derive values 0.34 dex smaller. This and the missing distinction between classical and pseudo bulges drive the steepening of the M_{BH} - M_{Bu} relation at small bulge masses of ‘‘Sersic galaxies’’ noticed by Graham & Scott (2013).

Fig. 7, upper right, shows the comparison between our bulge masses and the ones reported by the ATLAS3D collaboration (Cappellari et al. 2013) for the galaxies where we do not apply a decomposition. Cappellari et al. (2013) do not attempt any extrapolation, this probably explains most of the measured average shift of -0.11 dex. The measured scatter matches our error estimates. Similar conclusions are reached when we compare the half-mass radii (Fig. 7, bottom left). Finally and for completeness, Fig. 7, bottom right, shows the comparison between the velocity dispersions used here and the σ_e values reported by Cappellari et al. (2013). The ATLAS3D are systematically smaller by $\approx 10\%$; the scatter is a bit larger than the errors.

Fig. 8 compares our bulge circularized half-luminosity radii R_e to literature values from Laurikainen et al. (2010); Sani et al. (2011); Beifiori et al. (2012); Vika et al. (2012); Rusli et al. (2013b); Läscher et al. (2014). We use the fitted bulge axis ratios (b/a) tabulated by Sani et al. (2011) to trans-

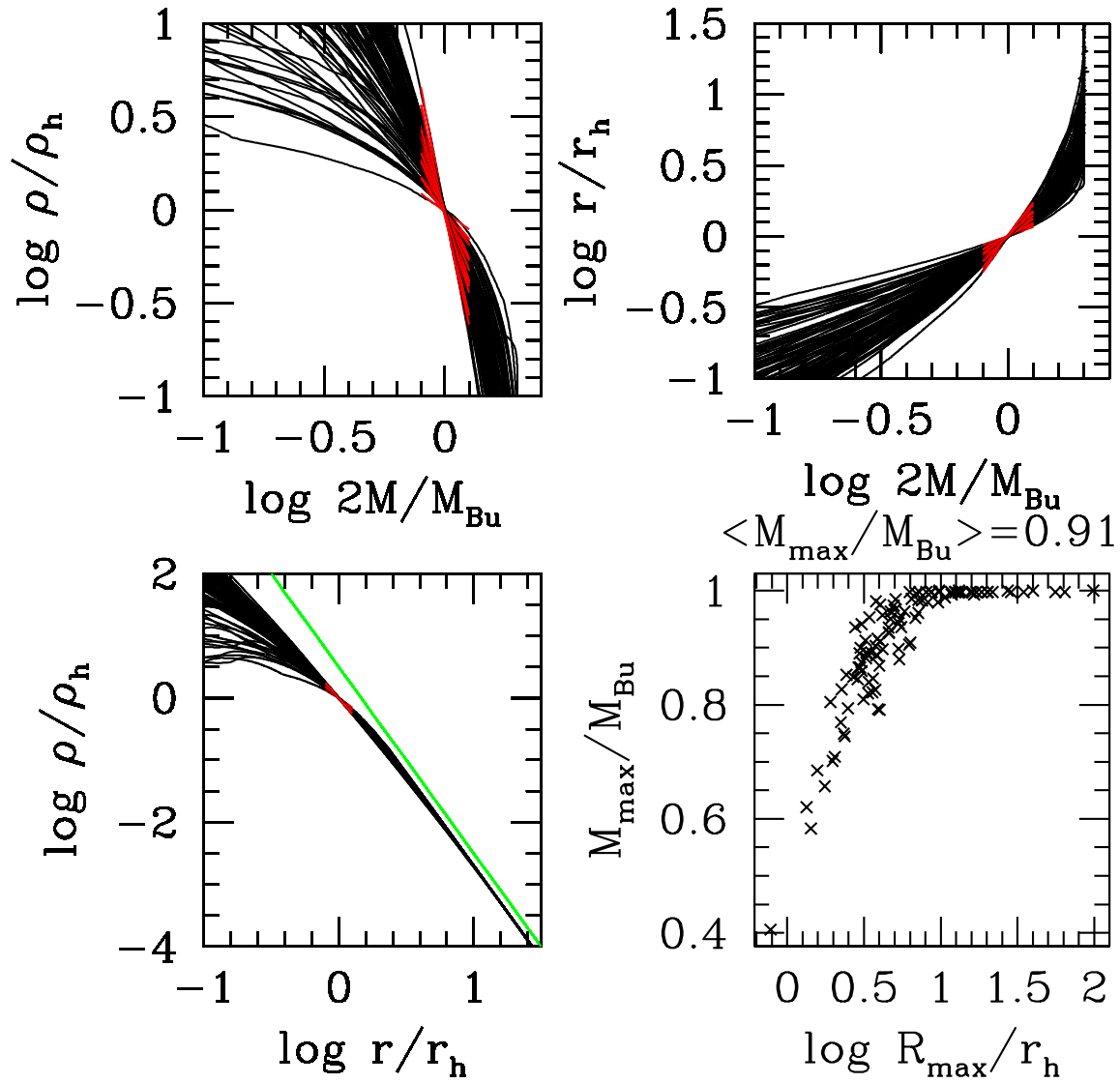


Fig. 4.— The bulge density and mass profiles of our galaxy sample. The red lines show the region where the logarithmic derivatives $a_{\rho M}$ (top left), a_{rM} (top right) and $a_{\rho r}$ (bottom left) are fitted. The green line shows $\rho \propto r^{-3}$. Bottom right: the correlation between the radial extent of the profile in units of r_h and the fractional bulge mass sampled. On average, our profiles probe $\approx 91\%$ of the bulge mass.

TABLE 3—*Continued*

Galaxy	$\log M_{Bu,C}(M_\odot)$	$\delta \log M_{Bu,C}(M_\odot)$	$\log \rho_{h,C}(M_\odot kpc^{-3})$	$\log \rho_{h,C}(M_\odot kpc^{-3})$
NGC4751	10.99	0.1439	8.486	0.256
NGC5516	11.65	0.1387	7.404	0.2169
NGC6861	11.21	0.1925	8.587	0.5468
NGC7619	11.61	0.1879	7.211	0.487

Column 1: galaxy name; Column 2 and 3: bulge masses from Kormendy & Ho (2013) derived from colors with our error estimates; Column 4 and 5: bulge densities derived from colors using the r_h of Table 1 and errors.

form their major-axis bulge half-luminosity radii a_e into $R_e = a_e \times (b/a)^{0.5}$. Laurikainen et al. (2010); Vika et al. (2012); Läsker et al. (2014) did not publish their fitted b/a values, therefore we adopt the axis ratios $(b/a)_{25}$ given by Hyperleda and compute $R_e = a_e \times (b/a)_{25}^{0.5}$. The observed spread is larger than our estimated errors, with several galaxies where our bulge R_e differs by more than 0.3 dex from the literature values. We discuss these objects in Appendix B, where we justify our choices. Some discrepancies stem from differences in the photometric band and the assumed ellipticity. Often the differences in R_e correlate with the fitted value of n_{Ser} : they are small when $n_{Ser} \approx 3 - 5$, which matches approximately our assumed extrapolation. Our R_e are larger than the literature values when $n_{Ser} \leq 3$ and smaller when $n_{Ser} \geq 5$. However, the major contributors are the fitting procedures adopted.

If we perform the same check for the 16 galaxies discussed in the Appendix B, Tables 20 to 33, where we perform multi-component fits, we find that the R_e we give in Table 1 (that are derived from the curve of growth of the spherical densities projected along the line of sight) agree with the ones from the fits to within 9%.

3. The error matrix

In Sect. 2 we described the data sample. For each galaxy we collected the distance D , the central black hole mass M_{BH} , the average velocity dispersion σ , the bulge mass M_{Bu} and mass-to-light ratio M/L , the bulge half-light radius r_h and the bulge average density ρ_h within r_h . We also computed errors on each quantity. We now discuss how we estimated the total error covariances on the decimal logarithms of the

parameters σ , M_{BH} , M_{Bu} , r_h , and ρ_h . All black hole correlation analyses performed in the past have ignored covariances, although some are obvious (e.g. black hole and bulge masses scale with the distance). Here we attempt to quantify them systematically to assess their importance (or lack thereof). This is not always possible in a rigorous way: some error correlations are hidden in the modeling procedure (e.g. the anti-correlation between mass-to-light ratio and black hole mass) and cannot be reconstructed from the published material; what follows is sometimes simply our best guess. The Tables 4 and 5 summarise our results for the two cases where the bulge masses are computed from mass-to-light ratios derived dynamically or from colors. In the first case we have:

1. Since dynamically determined M/L ratios scale as the square of velocities, we consider an additional error term on $(\delta \log M/L)^2$ of $4f(\delta \log \sigma)^2$, when we see that the quoted error on M/L given in Table 34 is too small given the kinematics available. Here f is a fudge factor that can be either 0 or 1 and is listed in Table 4. Therefore we use an effective error $(\delta M/L)_{eff}$, where we add in quadrature the two error contributions.
2. The total error on the black hole mass $\log M_{BH}$ comes from the fitting procedure and the error on the distance discussed in Sect. 2. We add both terms in quadrature. Depending on the type of data and their spatial resolution, the errors on M_{BH} and on the mass-to-light ratio M/L can be anticorrelated (Rusli et al. 2013b): $\delta \log M_{BH}^{fit} = a_{BH} \delta \log M/L$ with $a_{BH} \leq 0$. This dependency is important when computing the covariances $\delta \log M_{BH} \delta \log \sigma$ and

$\delta \log M_{BH} \delta \log \rho_h$. We list the adopted values of a_{BH} (which can be 0, -1, or -2) in Table 4: black hole masses not coming from stellar dynamical data (e.g., maser or gas dynamics measurements) must have $a_{BH} = 0$. The values $a_{BH} = -1$ or -2 come from typical χ^2 contour plots as a function of $\log M_{BH}$ and $\log M/L$ (see Nowak et al. 2010; Rusli et al. 2011, 2013b). In Fig. 9 we show the case of NGC 3923, for which we assign $a_{BH} = -1$.

3. The total error on the bulge mass $\log M_{Bu}$ comes from the residual extrapolation of Eq. 3, the error on the distance discussed above, and the error on the mass-to-light ratio. We add the three terms in quadrature. The external comparisons performed in the previous section show that this error estimate is probably too small. Therefore we also consider solutions where we add 0.15 dex in quadrature to $\delta \log M_{Bu}$.
4. The total error on the half-luminosity radius r_h comes from the extrapolation in Eq. 3 and the error on the distance. We add both terms in quadrature, weighting the mass extrapolation term with the correlation coefficient a_{rM}^2 .
5. The total error on the average density ρ_h within the half-luminosity radius comes from the extrapolation in Eq. 3, the error(s) on M/L (see above) and the error on the distance. We add the four terms in quadrature, weighting the mass extrapolation term with the correlation coefficient $a_{\rho M}^2$ and the distance error by a factor 2^2 (since $\rho \sim M/r^3 \sim D^{-2}$). Following the reasoning applied to $\delta \log M_{Bu}$, we also consider solutions where we add 0.15 dex in quadrature to $\delta \log \rho_h$.
6. The errors on M_{BH} and σ can be correlated through the M/L term, which scales as the square of velocity (see above).
7. The errors on M_{BH} and M_{Bu} are correlated through the distance and possibly anticorrelated through the M/L term (since a_{BH} is negative).
8. The errors on M_{BH} and r_h are correlated through the distance.
9. The errors on M_{BH} and ρ_h are anti-correlated through the distance and possibly through the M/L term.

10. The errors on M_{Bu} and σ are correlated through the M/L term, see above.
11. The errors on M_{Bu} and r_h are correlated through the mass extrapolation term and the distance.
12. Errors on M_{Bu} and ρ_h are correlated through the mass extrapolation and the M/L terms, and anticorrelated through the distance. Moreover, when we consider solutions where we add 0.15 dex in quadrature to $\delta \log M_{Bu}$ and $\delta \log \rho$, we augment the covariance element $\delta \log M_{Bu} \delta \log \rho_h$ by the same amount in quadrature.
13. Errors on $\log r_h$ and $\log \rho_h$ are correlated through the mass extrapolation term and anti-correlated through the distance.
14. Errors on $\log \rho_h$ and $\log \sigma$ are correlated through the M/L term.

For some galaxies the black hole mass is determined independently from the bulge M/L , for example from maser or gas rotation curves. In this case $a_{BH} = 0$. For some galaxies setting $a_{BH} = -2$ and $f = 1$ produces covariance matrices with negative determinants. In these cases we increase a_{BH} to -1 or 0 , and/or we set $f = 0$. Table 4 reports the values of the terms averaged over the sample. The most poorly determined parameter is ρ_h , followed by M_{BH} . On average, the off-diagonal terms of the covariance matrix are smaller than the diagonal terms; therefore ignoring them, as done in the past, is not a bad approximation.

The Tables 1 and 6 list the values of each term for each galaxy of the sample.

In the case of mass-to-light ratios derived from colors, we get:

1. We assume that the error on the $\log M/L_C$ from colors is equal to the error on bulge masses quoted by Kormendy & Ho (2013).
2. The total error on the black hole mass $\log M_{BH}$ is unchanged, and is as described above.
3. The total error squared on the bulge mass $\log M_{Bu,C}$ has an increased dependence on the distance error, that now goes as $4(\delta \log D)^2$. This is because the mass-to-light ratio derived

Table 4: The error correlations between the parameters for mass-to-light ratios derived dynamically.

N	Quantity	Mean value
0	$(\delta \log \sigma)^2$	0.0006
1	$(\delta \log M/L)_{eff}^2 = (\delta \log M/L)^2 + 4f(\delta \log \sigma)^2$	0.0038
2	$(\delta \log M_{BH})^2 = (\delta \log M_{BH}^{fit})^2 + (\delta \log D)^2$	0.023
3	$(\delta \log M_{Bu})^2 = (\delta \log M_{Bu}^{ext})^2 + (\delta \log D)^2 + (\delta \log M/L)_{eff}^2$	0.012
4	$(\delta \log r_h)^2 = a_{rM}^2 (\delta \log M_{Bu}^{ext})^2 + (\delta \log D)^2$	0.015
5	$(\delta \log \rho_h)^2 = a_{\rho M}^2 (\delta \log M_{Bu}^{ext})^2 + (\delta \log M/L)_{eff}^2 + 4(\delta \log D)^2$	0.087
6	$\delta \log M_{BH} \delta \log \sigma = 2fa_{BH}(\delta \log \sigma)^2$	-0.0003
7	$\delta \log M_{BH} \delta \log M_{Bu} = (\delta \log D)^2 + a_{BH}(\delta \log M/L)_{eff}^2$	0.0023
8	$\delta \log M_{BH} \delta \log r_h = (\delta \log D)^2$	0.0037
9	$\delta \log M_{BH} \delta \log \rho_h = -2(\delta \log D)^2 + a_{BH}(\delta \log M/L)_{eff}^2$	-0.009
10	$\delta \log M_{Bu} \delta \log \sigma = 2f(\delta \log \sigma)^2$	0.0005
11	$\delta \log M_{Bu} \delta \log r_h = a_{rM}(\delta \log M_{Bu}^{ext})^2 + (\delta \log D)^2$	0.01
12	$\delta \log M_{Bu} \delta \log \rho_h = a_{\rho M}(\delta \log M_{Bu}^{ext})^2 + (\delta \log M/L)_{eff}^2 - 2(\delta \log D)^2$	-0.0185
13	$\delta \log r_h \delta \log \rho_h = a_{\rho M}a_{rM}(\delta \log M_{Bu}^{ext})^2 - 2(\log D)^2$	-0.035
14	$\delta \log \rho_h \delta \log \sigma = 2f(\delta \log \sigma)^2$	0.0005

from colors is distance-independent, and therefore bulge masses scale as luminosities with the square of the distance.

4. The total error on $\log r_h$ is unchanged, and is as described above.
5. The total error squared on $\log \rho_{h,C}$ has a reduced dependence on the distance error, that now goes as $(\delta \log D)^2$. This stems from the increased dependence on distance of the bulge mass (see point 3).
6. Errors on $\log M_{BH}$ and $\log \sigma$ can be correlated through the M/L as above and are unchanged.
7. The correlation between the errors on $\log M_{BH}$ and $\log M_{Bu,C}$ is only due to the distance and amounts to $2(\delta \log D)^2$ because of the dependence of bulge masses on distance (see above).
8. Errors on $\log M_{BH}$ and $\log r_h$ are correlated through the distance as before.
9. The anti-correlation between the errors on $\log M_{BH}$ and $\log \rho_{h,C}$ is only due to the distance and amounts to $-(\delta \log D)^2$ because of the dependence of bulge masses on distance (see above).
10. There is no correlation between the errors on $\log M_{Bu,C}$ and on $\log \sigma$.

11. The errors on $\log M_{Bu,C}$ and $\log r_h$ are correlated through the mass extrapolation term and with a stronger dependence on the distance error squared (as $2(\delta \log D)^2$) from the D^2 scaling of bulges masses.
12. The errors on $\log M_{Bu,C}$ and $\log \rho_{h,C}$ are correlated through the mass extrapolation term and the M/L_C dependency and anticorrelated through the distance, as in the previous case.
13. The errors on $\log r_h$ and $\log \rho_{h,C}$ are correlated through the mass extrapolation term and anticorrelated (with the reduced dependency $-(\delta \log D)^2$) through the distance.
14. The errors on $\log \rho_{h,C}$ and $\log \sigma$ are not correlated.

The average values of the covariance matrix elements listed in Tables 4 and 5 are similar, with $\delta \log M_{Bu,C}$ larger than $\delta \log M_{Bu}$.

The Tables 3 and 7 list the values of each term for each galaxy of the sample of Kormendy & Ho (2013) considered here.

Table 5: The error correlations between the parameters for mass-to-light ratios derived from colors.

N	Quantity	Mean value
0	$(\delta \log \sigma)^2$	0.0005
1	$(\delta \log M/L_C)^2 = (\delta M_{Bu,C})^2$	0.008
2	$(\delta \log M_{BH})^2 = (\delta \log M_{BH}^{fit})^2 + (\delta \log D)^2$	0.022
3	$(\delta \log M_{Bu,C})^2 = (\delta \log M_{Bu}^{ext})^2 + 4(\delta \log D)^2 + (\delta \log M/L_C)^2$	0.019
4	$(\delta \log r_h)^2 = a_{rM}^2 (\delta \log M_{Bu}^{ext})^2 + (\delta \log D)^2$	0.013
5	$(\delta \log \rho_{h,C})^2 = a_{\rho M}^2 (\delta \log M_{Bu}^{ext})^2 + (\delta \log M/L_C)^2 + (\delta \log D)^2$	0.073
6	$\delta \log M_{BH} \delta \log \sigma = 2f a_{BH} (\delta \log \sigma)^2$	-3×10^{-6}
7	$\delta \log M_{BH} \delta \log M_{Bu,C} = 2(\delta \log D)^2$	0.004
8	$\delta \log M_{BH} \delta \log r_h = (\delta \log D)^2$	0.002
9	$\delta \log M_{BH} \delta \log \rho_h = -2(\delta \log D)^2$	-0.002
10	$\delta \log M_{Bu,C} \delta \log \sigma = 0$	0
11	$\delta \log M_{Bu,C} \delta \log r_h = a_{rM} (\delta \log M_{Bu}^{ext})^2 + 2(\delta \log D)^2$	0.01
12	$\delta \log M_{Bu,C} \delta \log \rho_{h,C} = a_{\rho M} (\delta \log M_{Bu}^{ext})^2 + (\delta M/L_C)^2 - 2(\delta \log D)^2$	-0.01
13	$\delta \log r_h \delta \log \rho_{h,C} = a_{\rho M} a_{rM} (\delta \log M_{Bu}^{ext})^2 - 2(\log D)^2$	-0.03
14	$\delta \log \rho_{h,C} \delta \log \sigma = 0$	0

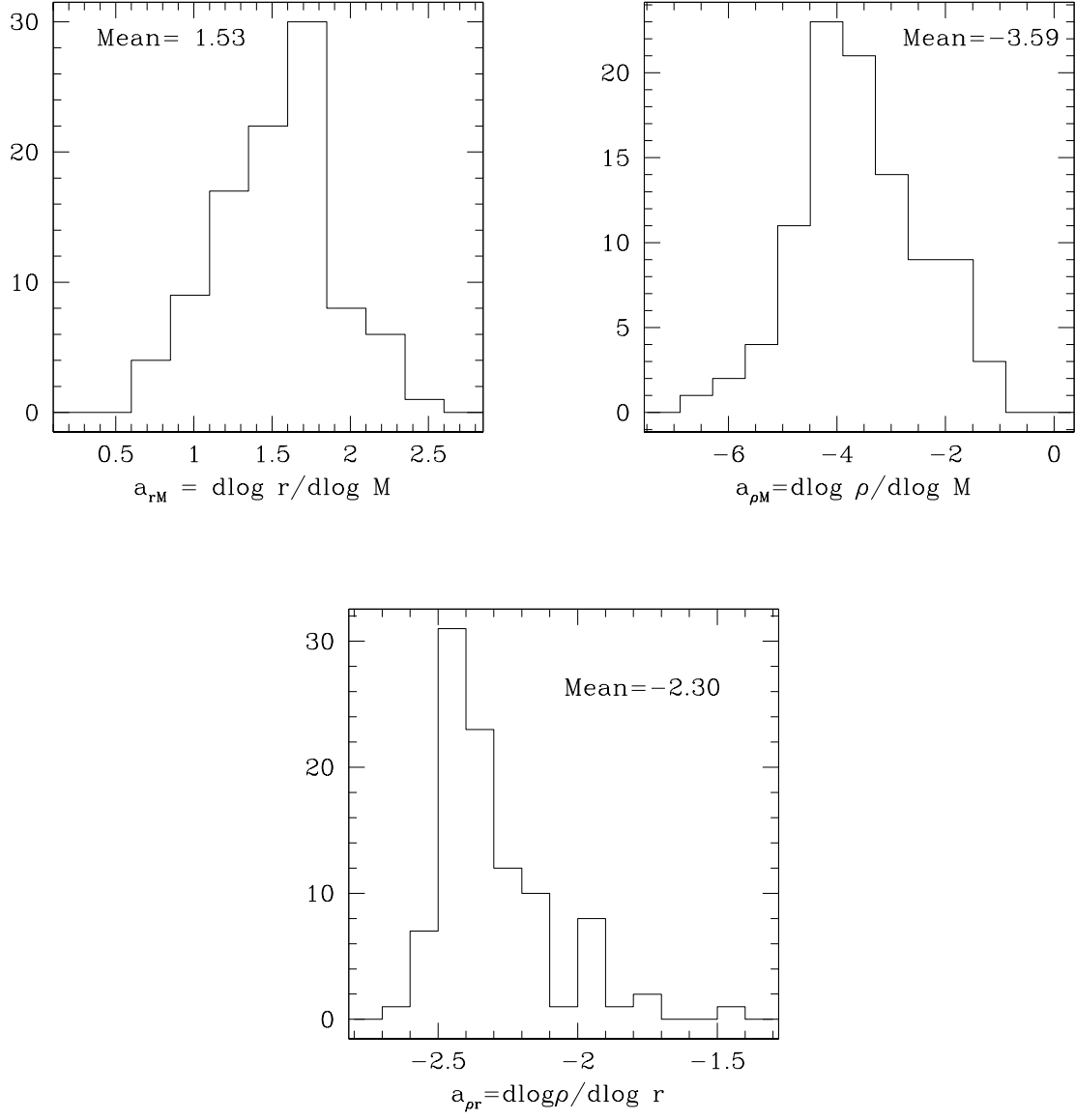


Fig. 5.— The histograms of the values of the logarithmic derivatives a_{rM} (top left), $a_{\rho M}$ (top right) and $a_{\rho r}$ (bottom).

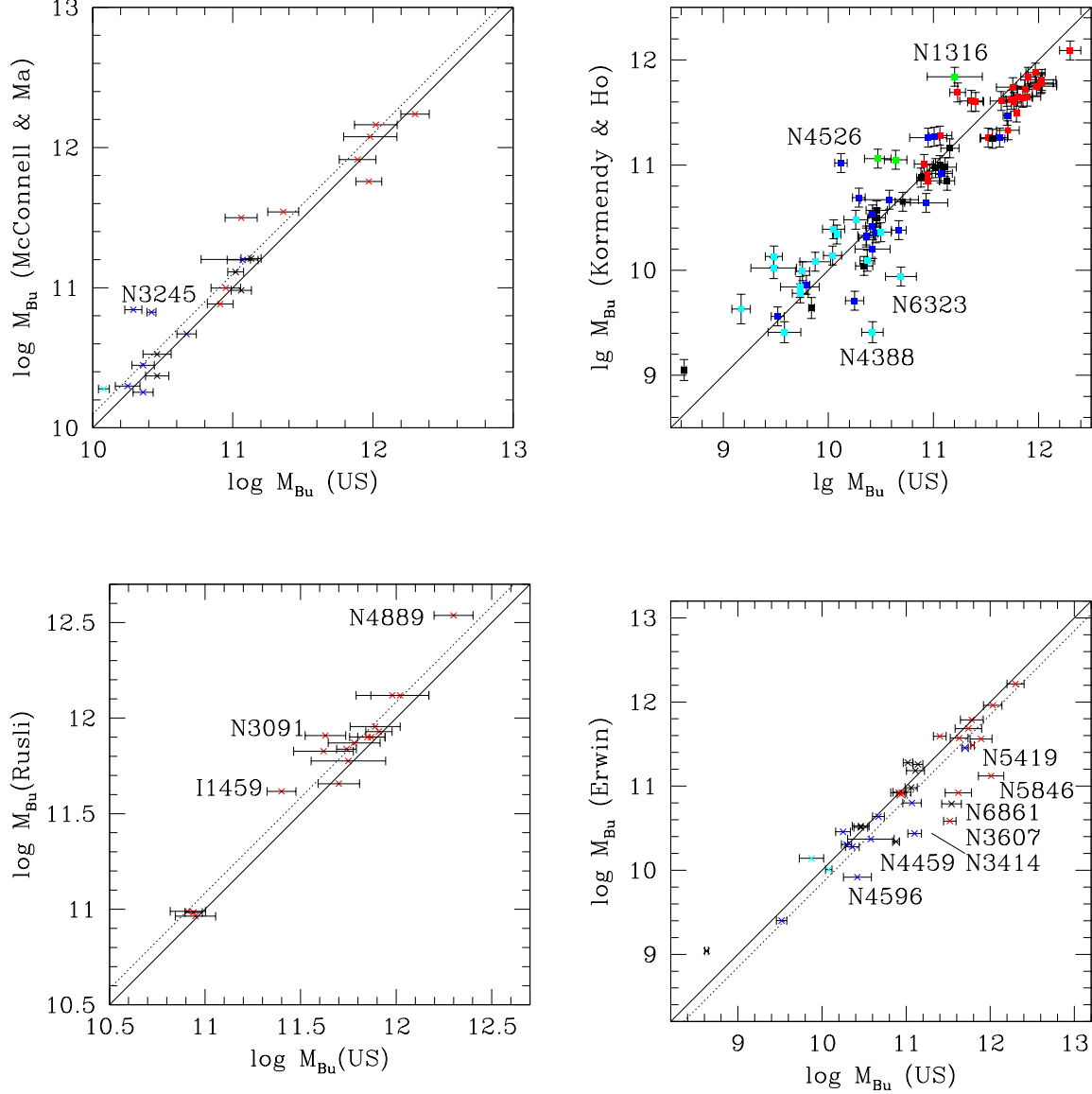


Fig. 6.— The bulge masses compared to the values of McConnell & Ma (2013, top left), Kormendy & Ho (2013, top right), Rusli et al. (2013a, bottom left) and Erwin et al. (2015, bottom right). Red points are core ellipticals, black points are power-law ellipticals, blue points are classical bulges, cyan points are pseudo bulges, green points are mergers. In the upper left plot we exclude the galaxies where we consider the classical component of a composite (pseudo plus classical) bulge. In the bottom right plot we show only galaxies fitted by one component. The full line shows the one-to-one relation, the dotted line is shifted to fit the datapoints on average (indistinguishable from the full line for the sample of Kormendy & Ho 2013).

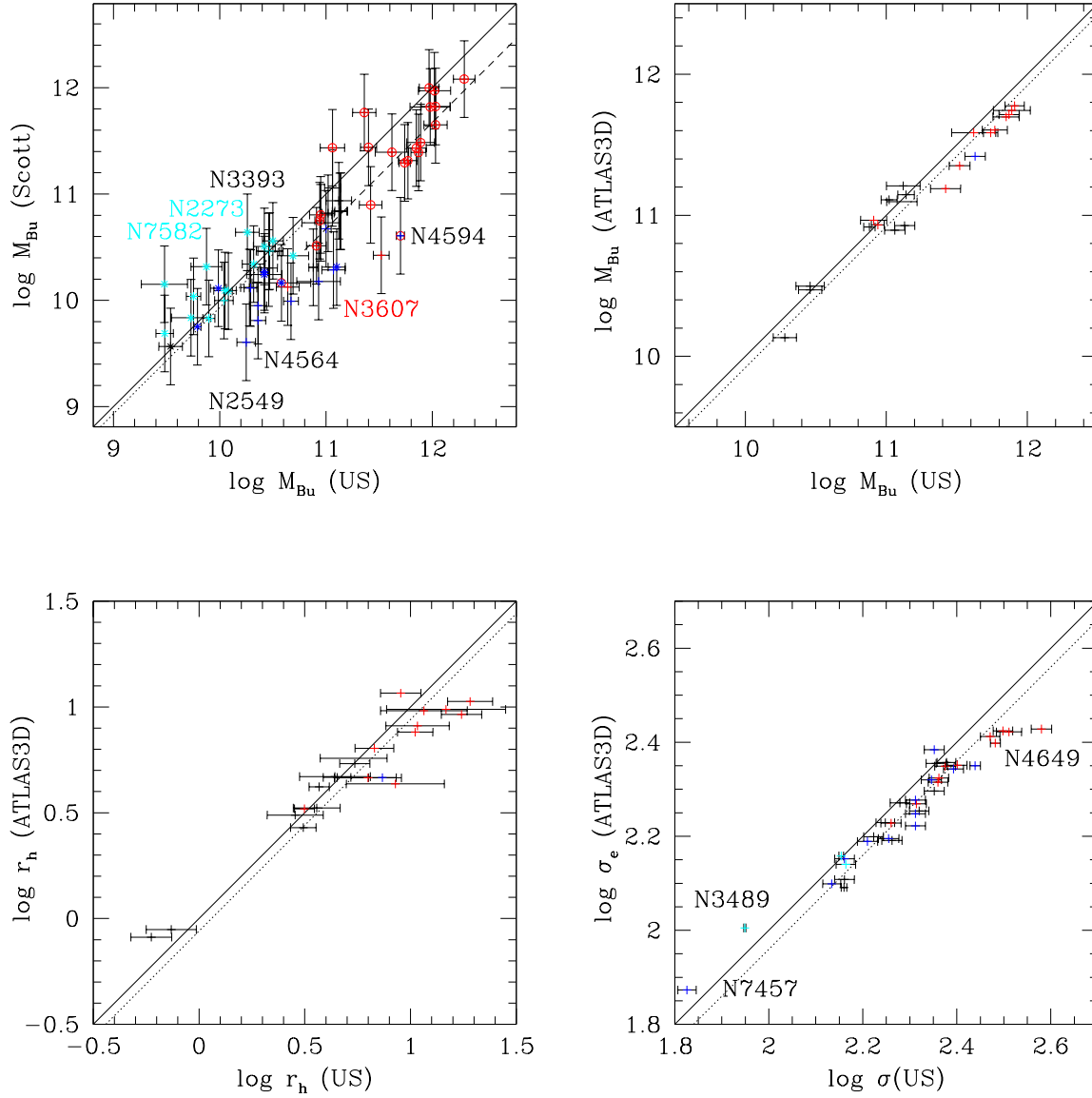


Fig. 7.— Top left: our bulge masses compared to the values of Scott et al. (2013). We exclude NGC 1399 and NGC 6086, where we subtract the outer halo from the profile. Colors and continuous line as in Fig. 6; the dotted and dashed lines are shifted to fit the datapoints at $\log M_{\text{Bu}} < 10.8$ and $\log M_{\text{Bu}} \geq 10.8$ respectively; circles indicate Core-Sersic galaxies according to the classification of Scott et al. (2013), asterisks indicate galaxies that we classified as barred. Top right: the bulge masses compared to the values of Cappellari et al. (2013) for the galaxies where we do not apply a decomposition. Bottom left: the half-mass radii compared to the values of Cappellari et al. (2013) for the galaxies where we do not apply a decomposition. Bottom right: the velocity dispersions compared to the σ_e values of Cappellari et al. (2013). The three most deviant galaxies are labelled. Colors and continuous lines as above. The dotted lines are shifted to the average difference.

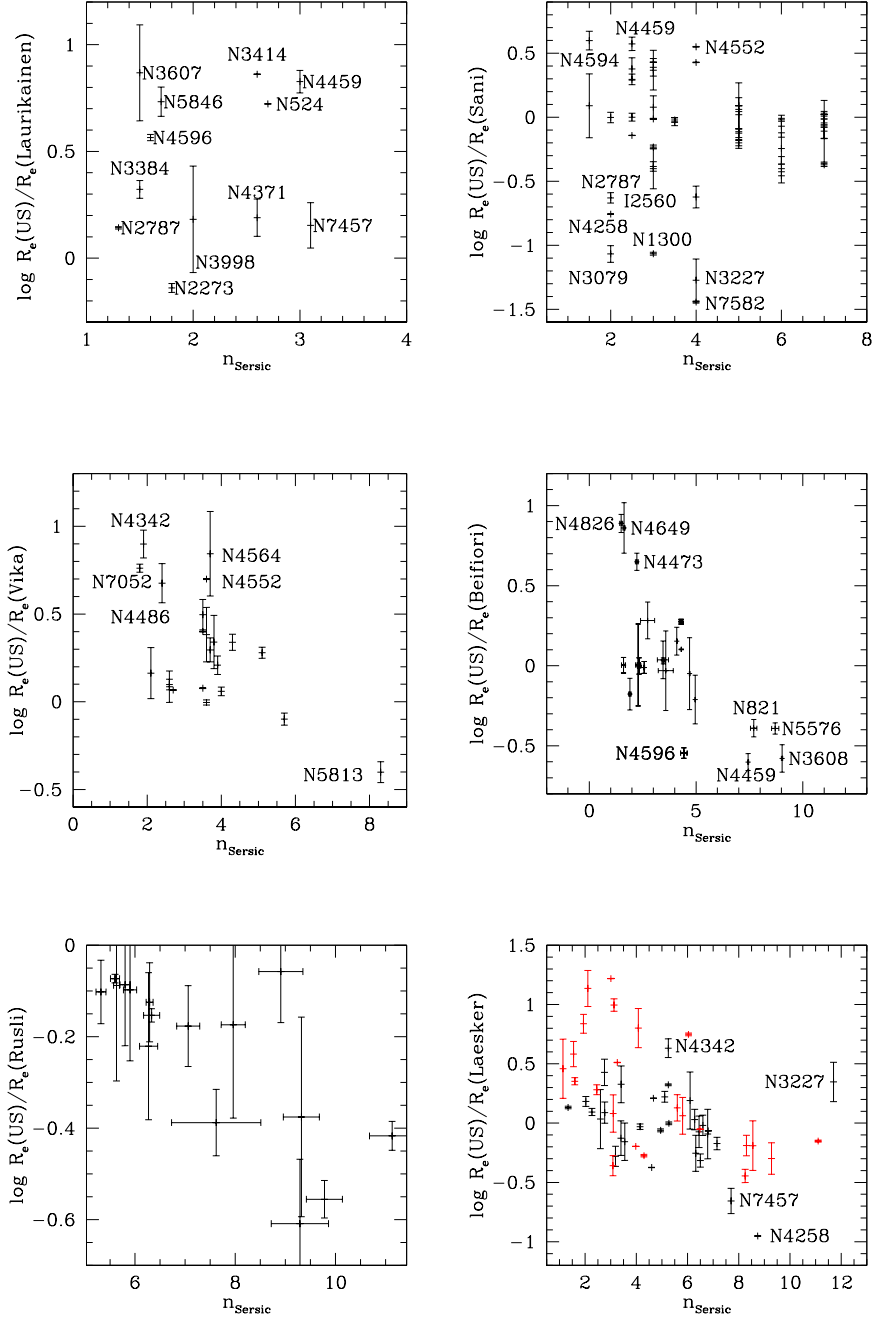


Fig. 8.— The bulge circularized half-luminosity radius R_e compared to the values of Laurikainen et al. (2010, top left), Sani et al. (2011, top right), Vika et al. (2012, middle left), Beifiori et al. (2012, middle right), Rusli et al. (2013b, bottom left) and Läsker et al. (2014, bottom right) as a function of the fitted Sersic index n_{Sersic} . The red points in the comparison to Läsker et al. (2014) indicate their 'best' solution.

TABLE 6
THE VALUES OF THE ERROR COVARIANCE MATRICES: OFF-DIAGONAL TERMS.

Galaxy	α_{BH}	f	$\delta \log M_{BH}$ $\delta \log \sigma$	$\delta \log M_{BH}$ $\delta \log M_{Bu}$	$\delta \log M_{BH}$ $\delta \log r_h$	$\delta \log M_{BH}$ $\delta \log \rho_h$	$\delta \log M_{Bu}$ $\delta \log \sigma$	$\delta \log M_{Bu}$ $\delta \log r_h$	$\delta \log M_{Bu}$ $\delta \log \rho_h$	$\delta \log r_h$ $\delta \log \rho_h$	$\delta \log \rho_h$ $\delta \log \sigma$
MW	0	0	0.00000000	0.00102400	0.00102400	-0.00204800	0.00000000	0.00279996	-0.00360376	-0.00528875	0.00000000
Circinus	0	0	0.00000000	0.00518400	0.00518400	-0.01036800	0.00000000	0.00518913	-0.00772816	-0.01038157	0.00000000
A1836	0	1	0.00000000	0.00057600	0.00057600	-0.00115200	0.00000000	0.00267647	0.01019260	-0.00828498	0.00089280
IC1459	-1	0	-0.00000000	0.00117500	0.00113600	-0.00823300	0.00000000	0.00415655	-0.00672214	-0.01005465	0.00000000
IC4296	0	1	0.00000000	0.00102400	0.00102400	-0.00204800	0.00093300	0.01312244	-0.00722144	-0.05108090	0.00093300
NGC0221	-2	0	-0.00000000	-0.00005040	0.00025600	-0.00081840	0.00000000	0.00034204	-0.00055272	-0.00771187	0.00000000
NGC0224	-2	0	-0.00000000	0.00011180	0.00032400	-0.00086020	0.00000000	0.00032516	-0.00054437	-0.00655085	0.00000000
NGC0524	0	1	0.00000000	0.00160000	0.00160000	-0.00320000	0.00089180	0.00328546	-0.00458597	-0.00968235	0.00089180
NGC0821	-2	1	-0.00173000	-0.00369240	0.00115600	-0.00716040	0.00000000	0.01497032	-0.03331196	-0.05986855	0.00086500
NGC1023	0	0	0.00000000	0.00102400	0.00102400	-0.00204800	0.00000000	0.0102543	-0.00204867	-0.02052571	0.00000000
NGC1068	0	1	0.00000000	0.05954000	0.05954000	-0.11907999	0.00081180	0.05954083	-0.08837061	-0.11908121	0.00081180
NGC1194	0	1	0.00000000	0.00221800	0.00221800	-0.00443600	0.01009800	0.00229553	0.03497470	-0.00470692	0.01009800
NGC1300	0	0	0.00000000	0.03386000	0.03386000	-0.06772000	0.00000000	0.03391462	-0.06782499	-0.06786712	0.00000000
NGC1399	0	0	0.00000000	0.00019600	0.00019600	-0.00039200	0.00000000	0.00043114	-0.00085702	-0.00146191	0.00000000
NGC2273	0	1	0.00000000	0.00078400	0.00078400	-0.00156800	0.00196240	0.00078465	-0.01877527	-0.00156863	0.00196240
NGC2549	-1	1	-0.00088060	0.00103220	0.00136000	-0.00837580	0.00088060	0.00728061	-0.01419533	-0.02351997	0.00088060
NGC2748	0	1	0.00000000	0.02250000	0.02250000	-0.04500000	0.00071400	0.02250098	-0.04327431	-0.04500188	0.00071400
NGC2787	0	0	0.00000000	0.00518400	0.00518400	-0.01036800	0.00000000	0.00563447	-0.01115634	-0.01166805	0.00000000
NGC2960	0	1	0.00000000	0.00211600	0.00211600	-0.00423200	0.00352600	0.00212848	0.00944793	-0.00427684	0.00352600
NGC2974	0	0	0.00000000	0.00230400	0.00230400	-0.00460800	0.00309165	-0.00592979	-0.00787469	-0.00000000	0.00000000
NGC3031	0	1	0.00000000	0.00025600	0.00025600	-0.00051200	0.00090540	0.00328737	-0.00558498	-0.00994234	0.00090540
NGC3079	0	1	0.00000000	0.00115600	0.00115600	-0.00231200	0.00086694	0.00115721	-0.00027405	-0.00231520	0.00086694
NGC3115	-2	1	-0.00172840	-0.00320566	0.00032400	-0.00417766	0.00086420	0.01652079	-0.03743427	-0.06282222	0.00086420
NGC3227	-2	0	-0.00000000	-0.00161800	0.00230400	-0.00853000	0.00000000	0.00281822	-0.00389962	-0.00682885	0.00000000
NGC3245	-2	0	-0.00000000	-0.00232200	0.00160000	-0.00712200	0.00000000	0.00171867	-0.00184446	-0.00346348	0.00000000
NGC3377	-2	1	-0.00176120	-0.00385340	0.00032400	-0.00482540	0.00088060	0.00908298	-0.02037912	-0.04350170	0.00088060
NGC3379	-2	0	-0.00000000	-0.00144900	0.00048400	-0.00290100	0.00000000	0.00150424	-0.00245705	-0.00510774	0.00000000
NGC3384	0	0	0.00000000	0.00078400	0.00078400	-0.00156800	0.00000000	0.00111568	-0.00184045	-0.00253374	0.00000000
NGC3393	0	1	0.00000000	0.00518400	0.00518400	-0.01036800	0.00172740	0.00518493	-0.00322946	-0.01036968	0.00172740
NGC3414	0	1	0.00000000	0.00221800	0.00221800	-0.00443600	0.00089803	0.00602675	-0.01155801	-0.02290207	0.00089803
NGC3585	-2	1	-0.00201560	-0.00465320	0.00129600	-0.00854120	0.00100780	0.03685222	-0.07949613	-0.10677002	0.00100780
NGC3607	-2	1	-0.00174360	-0.00302320	0.00115600	-0.00649120	0.00087180	0.00517189	-0.01005872	-0.02014504	0.00087180
NGC3608	-2	0	-0.00000000	-0.00272200	0.00078400	-0.00507400	0.00000000	0.01286058	-0.03004822	-0.06245575	0.00000000
NGC3842	-2	0	-0.00000000	-0.00676400	0.00250000	-0.01426400	0.00000000	0.03250545	-0.07438256	-0.14378713	0.00000000
NGC3998	0	0	0.00000000	0.00144400	0.00144400	-0.00288800	0.00000000	0.00171955	0.07136787	-0.00368429	0.00000000
NGC4026	-1	1	-0.00094460	0.00028330	0.00136000	-0.00912470	0.00094460	0.00380532	-0.00495370	-0.00841749	0.00094460
NGC4151	0	0	0.00000000	0.00360000	0.00360000	-0.00720000	0.00000000	0.00360226	-0.00524429	-0.00720798	0.00000000
NGC4258	0	0	0.00000000	0.00090000	0.00090000	-0.00180000	0.00000000	0.00090150	-0.00156229	-0.00180523	0.00000000
NGC4261	0	0	0.00000000	0.00144400	0.00144400	-0.00288800	0.00000000	0.02379194	-0.05434294	-0.10225459	0.00000000
NGC4291	-2	1	-0.00185800	-0.00596200	0.00409600	-0.01825000	0.00092900	0.00760714	-0.01171311	-0.02330892	0.00092900
NGC4342	-2	1	-0.00180600	-0.00525600	0.00067600	-0.00728400	0.00090300	0.00406954	-0.00701535	-0.02018439	0.00090300
NGC4374	-1	0	-0.00000000	-0.00049100	0.00019600	-0.00107900	0.00000000	0.00367986	-0.00837319	-0.01732530	0.00000000
NGC4388	0	0	0.00000000	0.00176400	0.00176400	-0.00352800	0.00000000	0.00368642	-0.00062733	-0.00990079	0.00000000
NGC4459	-1	0	-0.00000000	-0.00049070	0.00019600	-0.00107870	0.00000000	0.00147212	-0.00274696	-0.00532598	0.00000000
NGC4473	-2	1	-0.00169520	-0.00407760	0.00019600	-0.00466560	0.00084760	0.00595497	-0.01279830	-0.03099224	0.00084760
NGC4486	0	0	0.00000000	0.00025600	0.00025600	-0.00051200	0.00000000	0.00411383	-0.00725172	-0.02304576	0.00000000
NGC4526	0	0	0.00000000	0.00221800	0.00221800	-0.00443600	0.00000000	0.00222178	-0.00325176	-0.00444890	0.00000000
NGC4552	0	1	0.00000000	0.00078400	0.00078400	-0.00156800	0.00085532	0.02151213	-0.05315189	-0.13933082	0.00085532
NGC4564	0	1	0.00000000	0.00019600	0.00019600	-0.00039200	0.00092140	0.00369338	-0.00625168	-0.01257196	0.00092140
NGC4594	0	0	0.00000000	0.00129600	0.00129600	-0.00259200	0.00000000	0.00142279	-0.00286399	-0.00310202	0.00000000
NGC4596	0	1	0.00000000	0.02560000	0.02560000	-0.05120000	0.00073520	0.02631555	-0.05135706	-0.05405618	0.00073520
NGC4621	0	1	0.00000000	0.00490000	0.00490000	-0.00980000	0.00090143	0.01746883	-0.03815935	-0.06640238	0.00090143
NGC4649	-2	0	-0.00000000	-0.00427600	0.00025600	-0.00504400	0.00000000	0.01190487	-0.02707213	-0.05537556	0.00000000
NGC4697	0	0	0.00000000	0.00019600	0.00019600	-0.00039200	0.00000000	0.00290751	-0.00556928	-0.01248113	0.00000000
NGC4736	0	0	0.00000000	0.00462400	0.00462400	-0.00924800	0.00000000	0.00462492	-0.00728876	-0.00924963	0.00000000
NGC4826	-1	1	-0.00031400	0.00374480	0.00490000	-0.01095520	0.00031400	0.00503434	-0.00755235	-0.01037050	0.00031400
NGC4889	-2	1	-0.00015668	-0.00676536	0.00048400	-0.00821736	0.00007834	0.00862240	-0.01555452	-0.03650644	0.00007834
NGC5077	-2	1	-0.00185520	0.00120360	0.00883600	-0.02253040	0.00092760	0.00949040	-0.01540556	-0.02010439	0.00092760
NGC5128	0	0	0.00000000	0.00057600	0.00057600	-0.00115200	0.00000000	0.00145456	0.00703146	-0.00324545	0.00000000
NGC5576	-1	1	-0.00091380	-0.00293260	0.00078400	-0.00528460	0.00091380	0.00242247	-0.00200007	-0.01039793	0.00091380
NGC5813	0	1	0.00000000	0.00129600	0.00129600	-0.00259200	0.00086279	0.00697637	-0.01302767	-0.02044558	0.00086279
NGC5845	-2	1	-0.00160040	0.00060800	0.00462400	-0.01326400	0.00080020	0.00861897	-0.01573795	-0.01925507	0.00080020
NGC5846	0	0	0.00000000	0.00160000	0.00160000	-0.00320000	0.00000000	0.04308930	-0.10483564	-0.19428015	0.00000000
NGC6086	-1	1	-0.00001492	-0.00109684	0.00129600	-0.00498484	0.00001492	0.00138738	0.00146205	-0.00295196	0.00001492
NGC6251	-2	1	-0.00176120	-0.00614840	0.00129600	-0.01003640	0.00088060	0.00735691	-0.01364734	-0.02887339	0.00088060
NGC6264	0	0	0.00000000	0.00221800	0.00221800	-0.00443600	0.00000000	0.00221883	0.00310852	-0.00443722	0.00000000
NGC6323	0	0	0.00000000	0.00221800	0.00221800	-0.00443600	0.00000000	0.00258465	0.01379189	-0.00569656	0.00000000
NGC7052	-2	1	-0.00180480	-0.00482760	0.00270400	-0.01293960	0.00090240	0.01062736	-0.01976312	-0.03080237	0.00090240
NGC7457	0	1	0.00000000	0.00176400	0.00176400	-0.00352800	0.00075740	0.00180232	-0.00160043	-0.00366793	0.00075740
NGC7582	0	0	0.00000000	0.03460000	0.03460000	-0.06919999	0.00000000	0.03460121	-0.05675261	-0.06920315	0.00000000
NGC7768	0	1	0.00000000	0.01040000	0.01040000	-0.02080000	0.00388800	0.04072450	-0.08605497	-0.15456009	0.00388800
UGC3789	0	0	0.00000000	0.00221800	0.00221800	-0.00443600	0.00000000	0.00221885	0.00444446	-0.00443731	0.00000000
NGC0307	0	1	0.00000000	0.00221800	0.00221800	-0.00443600	0.00008884	0.00221933	-0.00419436	-0.00443999	0.00008884
NGC1316	0	1	0.00000000	0.00019600	0.00019600	-0.00039200	0.00003881	0.08107346	-0.17447022		

4. Exploring multivariate correlations

In the following we investigate the correlations between all measured parameters. We assume that the n measured values of the dependent variable η_i (with i running from 1 to n), can be expressed as:

$$\eta_i = \vec{\alpha}^T \cdot \vec{\xi}_i + ZP + N(0, \epsilon), \quad (6)$$

where $\vec{\xi}_i$ are the measured values of the independent vector of variables, $N(0, \epsilon)$ is a normal random variable with zero mean and variance ϵ^2 , with ϵ representing the intrinsic scatter in η_i , and ZP and $\vec{\alpha}$ are the zero-point and the multi-linear coefficients. We compute ZP , $\vec{\alpha}$ and ϵ following Kelly (2007) and making use of his IDL routines. To this purpose we compute the covariance error matrices:

$$C_i = \begin{pmatrix} \delta^2 \eta_i & \delta \eta_i \delta \vec{\xi}_i \\ \delta \eta_i \delta \vec{\xi}_i & \delta \vec{\xi}_i \delta \vec{\xi}_i \end{pmatrix}. \quad (7)$$

The square roots of their diagonal terms are given in the Tables 1 and 3, the off-diagonal terms can be found in the Tables 6 and 7.

Kelly's routines provide the posterior probabilities $P(\vec{\alpha}, ZP, \epsilon)$ of the fitted parameters $\vec{\alpha}, ZP, \epsilon$. We quote as best-fit parameters the averages of these distributions with errors given by the rms. We show two examples of this procedure in Fig. 10 and 11. Fig. 10 shows the one-dimensional case of the $\log M_{BH} = a \log \sigma + ZP$ relation for the subsample CorePowerE-ClassPC (see below and Table 8). As expected, the

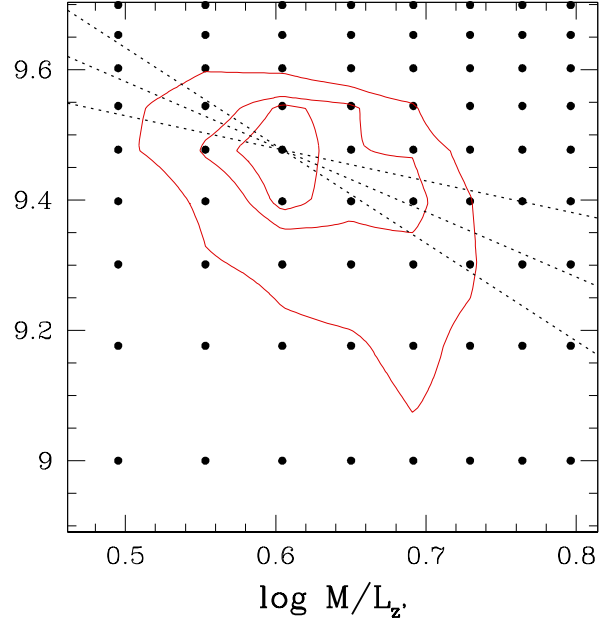


Fig. 9.— The χ^2 contours as a function of $\log M/L$ and $\log M_{BH}$ for NGC 3923. The filled points show the grid of computed models. The dotted lines show the lines of correlated errors $\Delta \log M_{BH} = a_{BH} \Delta \log M/L_z$, for $a_{BH} = -0.5, -1, -1.5$.

TABLE 6—Continued

NGC4371	0	1	0.00000000	0.00144400	0.00144400	-0.00288800	0.00004773	0.00145530	-0.00276670	-0.00292754	0.00004773
NGC4472	0	0	0.00000000	0.00022500	0.00022500	-0.00045000	0.00000000	0.00623316	-0.01395564	-0.02764212	0.00000000
NGC4486a	0	1	0.00000000	0.00019600	0.00019600	-0.00039200	0.00007537	0.00908209	-0.02046265	-0.03306464	0.00007537
NGC4486b	0	0	0.00000000	0.00025600	0.00025600	-0.00051200	0.00000000	0.00030891	-0.00018686	-0.00067849	0.00000000
NGC4501	-2	1	-0.00026617	-0.00013134	0.00090000	-0.00283134	0.00013309	0.00090122	-0.00128698	-0.00180322	0.00013309
NGC4699	0	1	0.00000000	0.00221800	0.00221800	-0.00443600	0.00019092	0.00221892	-0.00345774	-0.00443764	0.00019092
NGC4751	0	1	0.00000000	0.00221800	0.00221800	-0.00443600	0.00053312	0.00825643	-0.01720868	-0.02762641	0.00053312
NGC5018	-2	1	-0.00021631	0.00205479	0.00270400	-0.00605721	0.00010815	0.00451187	-0.00950904	-0.01342547	0.00010815
NGC5328	-2	1	-0.00002499	-0.00348797	0.00221800	-0.01014197	0.00001249	0.07293955	-0.18097316	-0.39152691	0.00001249
NGC5419	0	0	0.00000000	0.00221800	0.00221800	-0.00443600	0.00000000	0.00721928	0.00110698	-0.02481270	0.00000000
NGC5516	0	0	0.00000000	0.00221800	0.00221800	-0.00443600	0.00000000	0.00601705	-0.01328545	-0.01972207	0.00000000
NGC6861	-2	1	-0.00003291	0.00489019	0.00518400	-0.01066181	0.00001645	0.02407962	-0.05868636	-0.12175512	0.00001645
NGC7619	-1	1	-0.00010842	0.00106015	0.00384400	-0.01047185	0.00010842	0.02500535	-0.05654635	-0.09997252	0.00010842

Column 1: galaxy name; Column 2 and 3: α_{BH} and f factors, see 3; Column 4: error covariances between M_{BH} and σ ; Column 5: error covariances between M_{BH} and M_{Bu} ; Column 6: error covariances between M_{BH} and r_h ; Column 7: error covariances between M_{BH} and ρ_h ; Column 8: error covariances between M_{Bu} and σ ; Column 9: error covariances between M_{Bu} and r_h ; Column 10: error covariances between M_{Bu} and ρ_h ; Column 11: error covariances between r_h and ρ_h ; Column 12: error covariances between ρ_h and σ .

TABLE 7

THE VALUES OF THE ERROR COVARIANCE MATRICES: OFF-DIAGONAL TERMS FOR THE KORMENDY & HO (2013) SAMPLE.

Galaxy	$\delta \log M_{BH}$ $\delta \log M_{Bu,C}$	$\delta \log M_{BH}$ $\delta \log \rho_{h,C}$	$\delta \log M_{Bu,C}$ $\delta \log r_h$	$\delta \log M_{Bu,C}$ $\delta \log \rho_{h,C}$	$\delta \log r_h$ $\delta \rho_{h,C}$
IC1459	0.006272	-0.003136	0.007293	-0.0005831	-0.006919
NGC0221	0.000512	-0.000256	0.000598	0.009294	-0.0005159
NGC0224	0.000648	-0.000324	0.0006492	0.00745	-0.0003268
NGC0524	0.0032	-0.0016	0.004885	0.000887	-0.008082
NGC0821	0.002312	-0.001156	0.01613	-0.02763	-0.05871
NGC1023	0.002048	-0.001024	0.002049	0.006049	-0.001029
NGC1194	0.004436	-0.002218	0.004514	0.003483	-0.002489
NGC1399	0.000392	-0.000196	0.0006271	0.00713	-0.001266
NGC2549	0.006272	-0.003136	0.01042	-0.008197	-0.02038
NGC3115	0.000648	-0.000324	0.01684	-0.0311	-0.0625
NGC3245	0.0032	-0.0016	0.003319	0.004655	-0.001863
NGC3377	0.000648	-0.000324	0.009407	-0.01437	-0.04318
NGC3379	0.000968	-0.000484	0.001988	0.004676	-0.004624
NGC3585	0.002592	-0.001296	0.03815	-0.07402	-0.1055
NGC3608	0.001568	-0.000784	0.01364	-0.0237	-0.06167
NGC3998	0.002888	-0.001444	0.003164	0.004598	-0.00224
NGC4026	0.006272	-0.003136	0.006941	0.0002975	-0.005281
NGC4258	0.0018	-0.0009	0.001801	0.006297	-0.0009052
NGC4291	0.008192	-0.004096	0.0117	-0.00864	-0.01921
NGC4374	0.000392	-0.000196	0.003876	-0.0009602	-0.01713
NGC4473	0.000392	-0.000196	0.006151	-0.006832	-0.0308
NGC4486	0.000512	-0.000256	0.00437	-0.002294	-0.02279
NGC4526	0.004436	-0.002218	0.00444	0.003655	-0.002231
NGC4564	0.000392	-0.000196	0.003889	-0.0004435	-0.01238
NGC4594	0.002592	-0.001296	0.002719	0.005203	-0.001806
NGC4649	0.000512	-0.000256	0.01216	-0.02124	-0.05512
NGC4697	0.000392	-0.000196	0.003104	0.001064	-0.01229
NGC5077	0.01767	-0.008836	0.01833	-0.01112	-0.01127
NGC5576	0.001568	-0.000784	0.003206	0.002386	-0.009614
NGC5845	0.009248	-0.004624	0.01324	-0.009713	-0.01463
NGC6086	0.002592	-0.001296	0.002683	0.005289	-0.001656
NGC7457	0.003528	-0.001764	0.003566	0.004482	-0.001904
NGC7768	0.0208	-0.0104	0.05112	-0.08686	-0.1442
NGC1332	0.002592	-0.001296	0.002593	0.005505	-0.001299
NGC1374	0.000438	-0.000219	0.004583	-0.002129	-0.01557
NGC1407	0.005408	-0.002704	0.03235	-0.0594	-0.09202
NGC1550	0.004436	-0.002218	0.01337	-0.01832	-0.04287
NGC3031	0.000512	-0.000256	0.003543	0.0007061	-0.009686
NGC3091	0.0098	-0.0049	0.01696	-0.01886	-0.03338
NGC4472	0.00045	-0.000225	0.006458	-0.007113	-0.02742
NGC4486a	0.000392	-0.000196	0.009278	-0.01325	-0.03287
NGC4751	0.004436	-0.002218	0.01047	-0.01071	-0.02541
NGC5516	0.004436	-0.002218	0.008235	-0.005464	-0.0175
NGC6861	0.01037	-0.005184	0.02926	-0.05073	-0.1166
NGC7619	0.007688	-0.003844	0.02885	-0.05123	-0.09613

Column 1: galaxy name; Column 2: error covariances between M_{BH} and $M_{Bu,C}$; Column 3: error covariances between M_{BH} and $\rho_{h,C}$; Column 4: error covariances between $M_{Bu,C}$ and r_h ; Column 5: error covariances between $M_{Bu,C}$ and $\rho_{h,C}$; Column 6: error covariances between r_h and $\rho_{h,C}$.

errors in the slope and the zero-point are highly correlated.

Fig. 11 shows the two-dimensional case of the $\log M_{BH} = a \log \sigma + b \log \rho_h + ZP$ relation discussed below, again for the subsample CorePowerE-ClassPC. Strong error correlations are present between the two fitted slopes and the zero-point. By integrating the posterior probability for positive values of b ($P(b > 0) = 0.9999$) we show that we have detected this bivariate correlation robustly. Furthermore, to assess whether we are overfitting the data by considering bivariate correlations involving black hole masses, we also compute the corrected Akaike information criterion (Akaike 1973; Hurvich & Tsai 1989, cAIC). It is defined as:

$$cAIC(k) = AIC(k) + \frac{2k(k+1)}{n-k-1}, \quad (8)$$

where n is the number of data points, k is the number of free parameters ($k = 3$ for monovariate correlations and $k = 4$ for bivariate correlations) and AIC is the Akaike information criterion:

$$AIC(k) = 2k - 2\ln P_{best}(k), \quad (9)$$

where P_{best} is the likelihood of the best-fitting solution with k parameters. There is evidence for bivariate correlations if

$$\Delta cAIC = cAIC(k=4) - cAIC(k=3) < 0. \quad (10)$$

The relative probability of the two solutions is $RP = \exp(\Delta cAIC/2)$, so the bivariate correlation is strongly preferred when $\Delta cAIC < -2$. Equivalent conclusions are obtained by considering the Bayesian information criterion $BIC = -2 \ln P_{best} + k \ln n$ (Schwarz 1978) and $\Delta BIC = BIC(k=4) - BIC(k=3)$.

We implement this schema as follows. We marginalize the posterior probability of the bivariate fits $P(a, b, ZP, \epsilon)$ over (b, ZP, ϵ) or (a, ZP, ϵ) to get the posterior distribution of a , $P_{k=4}(a)$ or b , $P_{k=4}(b)$, respectively. This is well approximated by a Gaussian, $P_{k=4}(a) = \frac{1}{\sqrt{2\pi\delta a_{best}}} \exp[-\frac{(a-a_{best})^2}{2\delta a_{best}^2}]$ or $P_{k=4}(b) = \frac{1}{\sqrt{2\pi\delta b_{best}}} \exp[-\frac{(b-b_{best})^2}{2\delta b_{best}^2}]$, see Fig. 11, where a_{best} and δa_{best} , b_{best} and δb_{best} are given in the Tables 12, 14 and 37, where we omit the label *best* for simplicity. Therefore the probability of our best fitting bivariate solutions is $P_{best,k=4} = \frac{1}{\sqrt{2\pi\delta a_{best}}}$ or $P_{best,k=4} = \frac{1}{\sqrt{2\pi\delta b_{best}}}$. We compare this to the probability of one of the two possible best fitting monovariate (i.e., $k = 3$) solutions for each combination

of parameters we considered, having either $a = 0$ or $b = 0$. We choose the one with the smallest intrinsic and measured scatter. In this way we are sure to get the most stringent test for the evidence of bivariate correlations. For instance, in the case of the $M_{BH}-M_{Bu}-\sigma$ correlation, this is $M_{BH}-\sigma$, which corresponds to the bivariate solution with $a = 0$. In all other cases we consider the bivariate solution with $b = 0$.

In practice, we compute the marginalized posterior distribution $P_{k=4}(a, b)$, verify that the maximum of $P_{k=4}(a = 0, b)$ is reached for $b = b_{best,k=3}$ for the $M_{BH}-M_{Bu}-\sigma$ correlation and that the maximum of $P_{k=4}(a, b = 0)$ is reached for $a = a_{best,k=3}$ for all the other correlations, where $a_{best,k=3}$ or $b_{best,k=3}$ are given in the Tables 11, 13 and 36, listing our monovariate (i.e., $k = 3$) solutions (where again we dropped the label *best*, $k = 3$ for simplicity). Then we set $P_{best,k=3} = P_{best,k=4}(a = 0) = \frac{1}{\sqrt{2\pi\delta a_{best}}} \exp[-(a_{best}/\delta a_{best})^2/2]$ for the $M_{BH}-M_{Bu}-\sigma$ correlation or $P_{best,k=3} = P_{best,k=4}(b = 0) = \frac{1}{\sqrt{2\pi\delta b_{best}}} \exp[-(b_{best}/\delta b_{best})^2/2]$ for all the other correlations.

Finally we get:

$$2\ln[P_{best}(k=4)/P_{best}(k=3)] = (b_{best}/\delta b_{best})^2 \quad (11)$$

or

$$2\ln[P_{best}(k=4)/P_{best}(k=3)] = (a_{best}/\delta a_{best})^2 \quad (12)$$

for the the $M_{BH}-M_{Bu}-\sigma$ correlation or all the others, respectively.

Following the discussion given in the introduction, we consider 12 (sub-)samples. The first one (All) is made of the galaxies of Table 1, with the exception of NGC 4486b. This galaxy deviates strongly from every correlation involving its black hole mass, despite the fact that our SINFONI BH mass (see Appendix B) is 30% smaller than the value adopted by Kormendy & Ho (2013). As done by Kormendy & Ho (2013), we discard it from all the subsamples and fits discussed below. The other subsamples are core ellipticals (CoreE); core and power-law ellipticals (CorePowerE); core and power-law ellipticals, plus classical bulges (CorePowerEClass); core and power-law ellipticals, classical bulges and classical bulge components of (composite) pseudo bulges (CorePowerEClassPC); the same for just SINFONI measurements (CorePowerEClassPCSINFONI); the same for just measurements from the literature (CorePowerE-

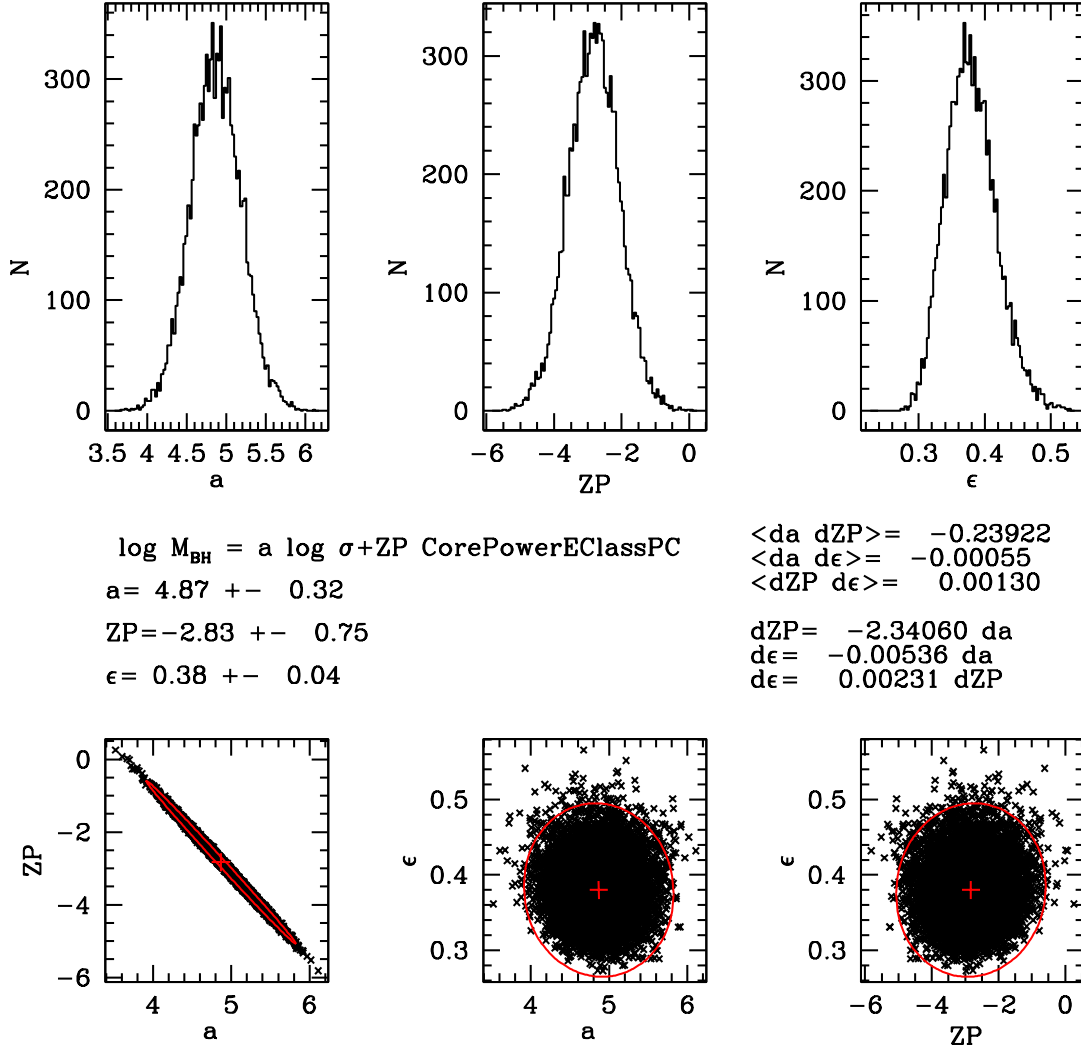


Fig. 10.— Top row: the posterior probability distributions of the fitted parameters of the correlation between $\log M_{\text{BH}}$ and $\log \sigma$ for the subsample CorePowerEClassPC. Middle row: mean values of the parameters and errors, off-diagonal terms of the parameter variance matrix and resulting correlations between parameter errors. Bottom row: the correlations between all possible pairs of parameters. The red ellipse shows the 3σ contours.

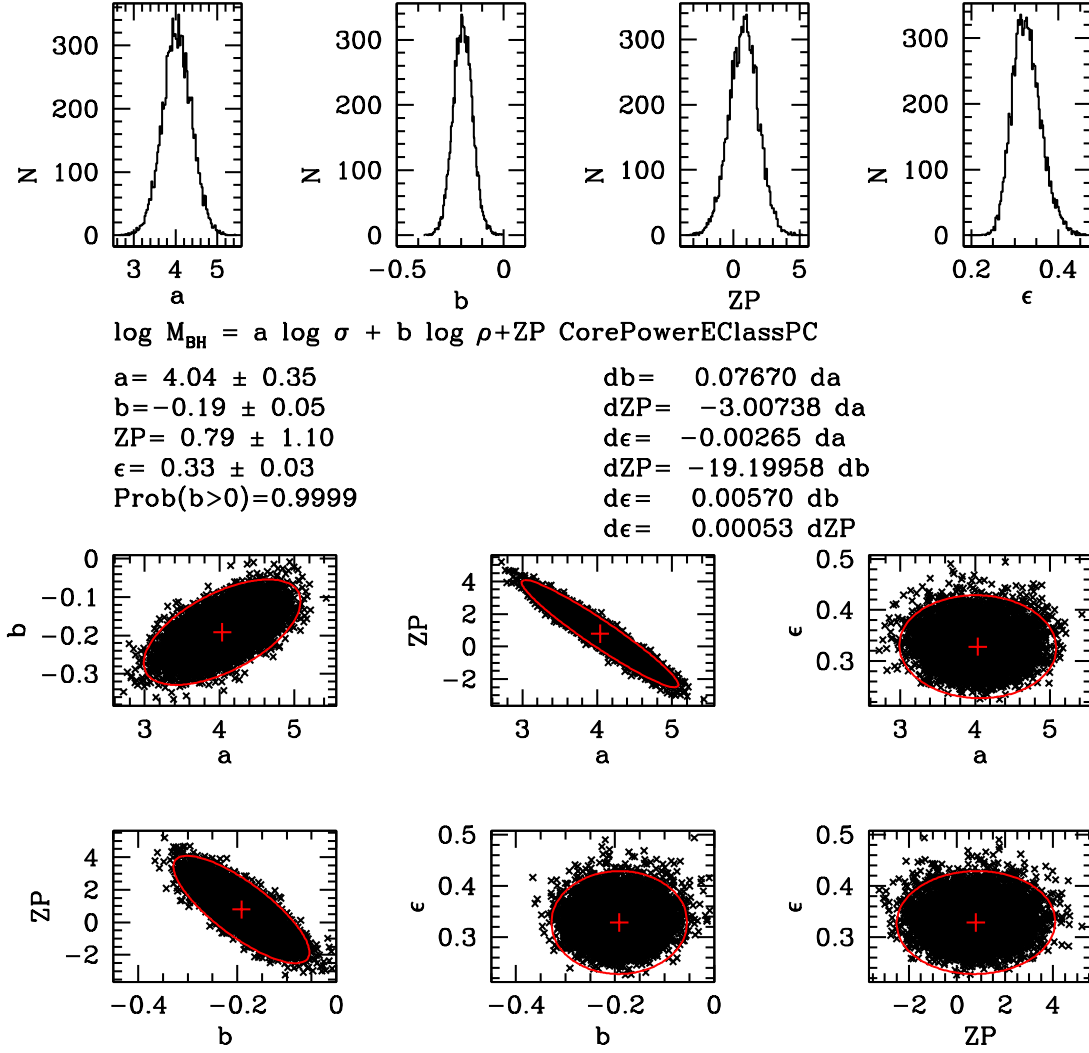


Fig. 11.— Top row: the posterior probability distributions of the fit to the relation $\log M_{\text{BH}} = \alpha \sigma + \beta \rho + ZP$ for the subsample CorePowerEClassPC. Middle row: mean values of the parameters and errors, and correlations between parameter errors. The plots at the bottom show the correlations between all possible pairs of parameters. The red ellipses show the 3σ contours.

ClassPCLit); the same without barred galaxies (CorePowerEClassnoBars); power-law ellipticals (PowerE); power-law ellipticals and classical bulges (PowerE-Class); power-law ellipticals classical bulges and classical bulge components of pseudo (composite) bulges (PowerEClassPC); pseudo bulges (Pseudo). Furthermore, we consider more or less stringent selection criteria to include or exclude measurements of different quality. Table 8 describes how the subsamples are constructed from Table 1 using the flags listed there.

With this set of subsamples we aim at assessing two questions. On the one hand, we want to understand the influence of our SINFONI data set, which provides almost 1/4 of the full database. On the other hand, we want to explore the degree to which we can unify the different types of galaxies in one common picture. The Tables 9 to 12 report the results of the fits obtained for the different families of objects.

Fig. 12 shows the correlations between the parameters M_{Bu} , r_h and ρ_h for the galaxies of Table 1 without NGC 4486b, see above. The fourth plot presents the virial relation between M_{Bu} , r_h and velocity dispersions σ for the same sample. There are no obvious outliers; the galaxies NGC 1332, NGC 3998 and NGC 6861 have denser bulges than expected given their bulge masses, and NGC 7457 and NGC 221 have less dense bulges.

Bulge masses (see Table 9, sample All) scale as $M_{Bu} \sim r_h^{1.3 \pm 0.04}$ with estimated intrinsic scatter $\epsilon = 0.24 \pm 0.02$ dex, or as $M_{Bu} \sim \rho_h^{-0.7 \pm 0.04}$ with $\epsilon = 0.42 \pm 0.03$. Consistently, bulge average densities scale as $\rho_h \sim r_h^{-1.72 \pm 0.04}$. These correlations hold within the errors for all subsamples considered, with no appreciable differences between the literature and the SINFONI sample. The correlations for core ellipticals are tighter. Only pseudo bulges follow relations which are different at the $2 - 3\sigma$ level ($M_{Bu} \sim r_h^{1.02 \pm 0.16}$, $M_{Bu} \sim \rho_h^{-0.4 \pm 0.1}$, $\rho_h \sim r_h^{-1.96 \pm 0.16}$).

For pressure-supported, self-gravitating systems in virial equilibrium dynamical masses are expected to scale as:

$$M = 10^{6.064} (R_e/kpc) (\sigma/kms^{-1})^2 M_\odot \quad (13)$$

(Cappellari et al. 2006). Using spherical half-luminosity radii we find

$$M_{Bu} = 10^{6.67 \pm 0.38} r_h^{0.98 \pm 0.04} \sigma^{1.65 \pm 0.17}, \quad (14)$$

with 40% scatter (see Table 10, sample CorePowerE-ClassPC). The coefficients are similar within $1 - 2\sigma$

for all the subsamples which exclude pseudo bulges. In particular, there is no significant difference if we use just the SINFONI or just the literature sample. For pseudo bulges the dynamical masses are roughly factor 3 smaller for given r_h and σ with larger scatter. Core ellipticals follow a tighter relation with just 30% intrinsic scatter and a shallower dependence on velocity dispersion ($M_{Bu} = 10^{7.96 \pm 0.99} r_h^{1.03 \pm 0.13} \sigma^{1.09 \pm 0.44}$). The slope difference is significant only at the 2σ level and could point to the systematic uncertainties in the role of dark matter, as discussed in Thomas et al. (2011). Discussing in detail the origin of the differences between Eqs. 13 and 14 goes beyond the scope of the paper.

When we augment the errors on the bulge mass and density by 0.15 dex (see Sect. 3), the fitted parameters remain essentially the same with somewhat larger errors, except for the estimated intrinsic scatter, which is approximately reduced by 0.15 dex in quadrature and therefore statistically compatible with zero.

5. BH Correlation analysis

We now proceed to examine correlations involving the BH mass. We start by investigating four one-dimensional correlations of the type $y = ax + ZP + N(0, \epsilon)$:

$$M_{BH} - \sigma : \log M_{BH} = a \log \sigma + ZP, \quad (15)$$

$$M_{BH} - M_{Bu} : \log M_{BH} = a \log M_{Bu} + ZP, \quad (16)$$

$$M_{BH} - r_h : \log M_{BH} = a \log r_h + ZP, \quad (17)$$

$$M_{BH} - \rho_h : \log M_{BH} = a \log \rho_h + ZP. \quad (18)$$

Table 11 summarizes the results, giving the number of galaxies in each subsample, the best-fit values of a and ZP with errors, the estimated intrinsic scatter ϵ , and the measured scatter rms . In addition, we list the Spearman coefficient r_s and the probability P_{r_s} of its value being greater caused by chance. Fig. 13 presents the correlation plots.

In agreement with the literature, we find that the strongest correlations with the lowest measured and intrinsic scatter are with σ . The correlations with M_{Bu} are strong, except for the pseudo bulge subsample. Correlations with sizes or anti-correlations with densities are generally weaker (and non-existent for pseudo bulges), but still robust for several subclasses. The measured slopes of the correlations of the Eqs. 15 to

TABLE 8
THE (SUB-)SAMPLES CONSIDERED IN THE CORRELATION ANALYSIS.

Sample	Selection flags	Explanation
All	$T \leq 3$ and $b \leq 1$ and $B \leq 2$	All galaxies without NGC 4486b
CoreE	$T = 0$	Core ellipticals
CorePowerE	$T \leq 1$	Core and power-law ellipticals without NGC 4486b
CorePowerEClass	$T \leq 2$	Core and power-law ellipticals plus classical bulges without NGC 4486b
CorePowerEClassPC	$T \leq 2$ plus ($T = 3$ and $B = 2$)	Core and power-law ellipticals, classical bulges and classical component of composite bulges without NGC 4486b
CorePowerEClassPCSINFONI	$T \leq 2$ and $S = 1$ plus ($T = 3$ and $B = 2$ and $S = 1$)	Core and power-law ellipticals, classical bulges and classical component of composite bulges, only SINFONI measurements without NGC 4486b
CorePowerEClassPCLit	$T \leq 2$ and $S = 0$ plus ($T = 3$ and $B = 2$ and $S = 0$)	Core and power-law ellipticals, classical bulges and classical component of composite bulges, only literature measurements
CorePowerEClassnoBars	$T \leq 2$ and $b \leq 0.5$	Core and power-law ellipticals, classical bulges and classical component of composite bulges but without barred objects and without NGC 4486b
PowerE	$T = 1$	Power-law ellipticals without NGC 4486b
PowerEClass	$1 \leq T \leq 2$	Power-law ellipticals and classical bulges without NGC 4486b
PowerEClassPC	$1 \leq T \leq 2$ plus ($T = 3$ and $B = 2$)	Power-law ellipticals classical bulges and classical component of composite bulges without NGC 4486b
Pseudo	$T = 3$ and $B \neq 2$	Pseudo bulges

Flags (see also Table 1): T (type, 0 for core ellipticals, 1 for power-law ellipticals, 2 for classical bulges, 3 for pseudo bulges), b (0: no bar, 1: barred), B (0 for one-component galaxy, 1 for bulge plus disk galaxy, 2 for galaxy with composite (classical plus pseudo) bulge plus disk).

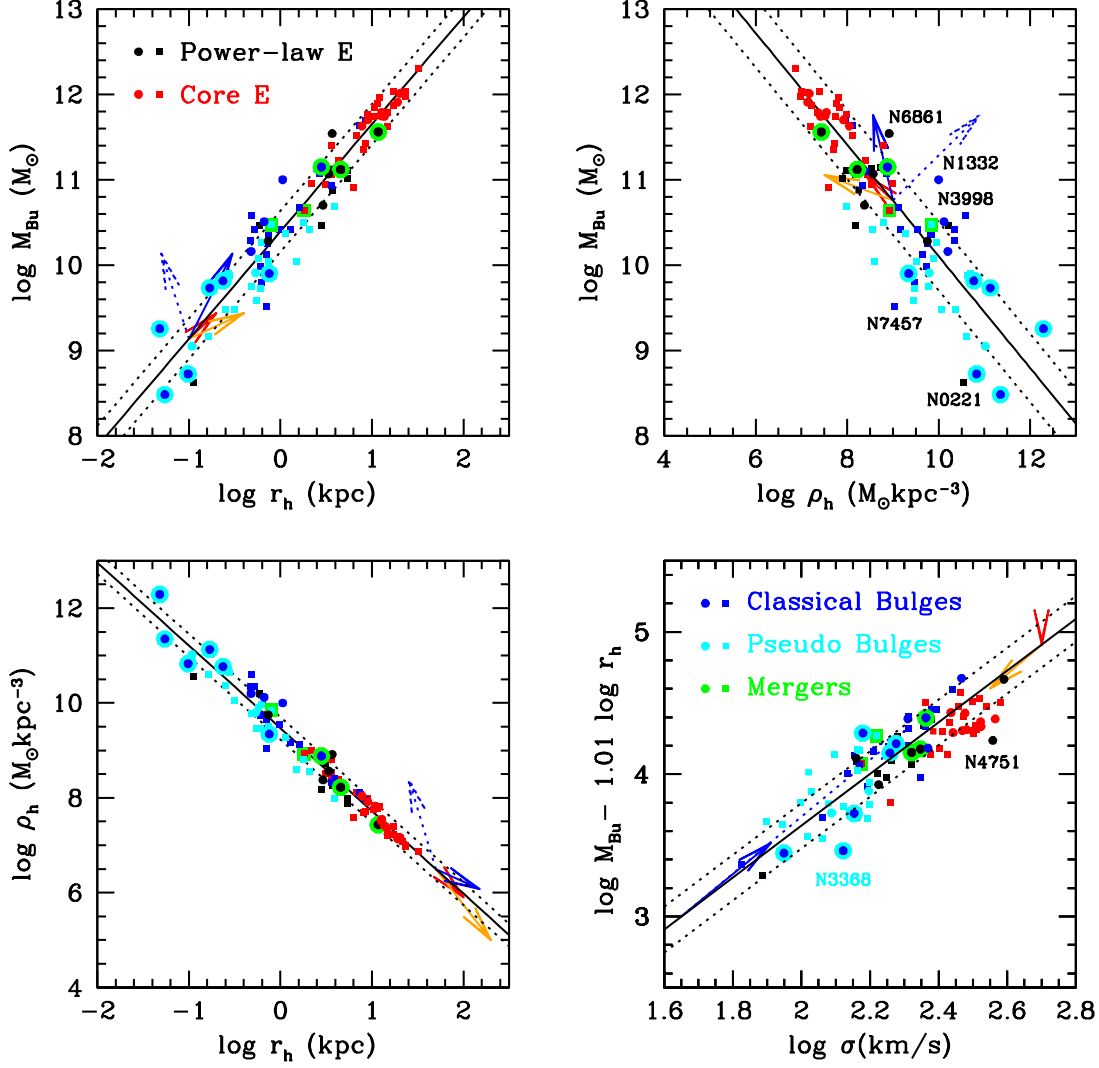


Fig. 12.— The correlations between the bulge parameters M_{Bu} , r_h , ρ_h and σ . Squares are data from the literature, circles are galaxies from our SINFONI survey. We plot core galaxies in red, power-law ellipticals in black, classical bulges in blue, pseudo bulges in cyan. Mergers have a green annulus. Blue dots with a cyan annulus are the classical bulge components of composite bulges. The labels name particularly deviant galaxies. The full lines indicate the best fit relations given in the Tables 9 and 10 for the CorePowerEClassPC sample. The dotted lines indicate the estimated intrinsic scatter. Arrows describe the effect of an equal mass dry merger (red), of a sequence of minor mergers doubling the bulge mass (orange), an equal-mass, gas-rich merger of two spiral galaxies with 20% bulge mass and bulge-scales ratio r_h^f/r_h^i of 3 (blue) or 0.5 (dotted blue), see also Sect. 6 and Table 16. As expected, the red arrow in the bottom right plot has zero length.

TABLE 9
ONE-DIMENSIONAL CORRELATIONS WITHIN BULGE PARAMETERS.

Fit	Sample	N	a	da	ZP	dZP	ϵ	$d\epsilon$	rms
$M_{Bu}-r_h$	All	96	1.285	0.041	10.35	0.029	0.241	0.02	0.251
	CoreE	31	1.246	0.104	10.41	0.101	0.131	0.028	0.151
	CorePowerE	47	1.37	0.072	10.27	0.062	0.186	0.026	0.2
	CorePowerEClass	71	1.245	0.055	10.4	0.041	0.228	0.022	0.232
	CorePowerEClassPC	77	1.256	0.046	10.39	0.034	0.238	0.022	0.245
	CorePowerEClassnoBars	61	1.261	0.065	10.39	0.052	0.231	0.025	0.228
	CorePowerEClassPCSINFONI	22	1.24	0.094	10.43	0.078	0.268	0.05	0.232
	CorePowerEClassPCLit	57	1.261	0.056	10.38	0.04	0.236	0.026	0.245
	PowerE	16	1.348	0.174	10.25	0.108	0.302	0.073	0.26
	PowerEClass	40	1.204	0.108	10.4	0.053	0.287	0.037	0.278
	PowerEClassPC	46	1.234	0.081	10.39	0.045	0.294	0.035	0.291
	Pseudo	19	1.018	0.156	10.16	0.069	0.234	0.05	0.209
$M_{Bu}-\rho_h$	All	96	-0.678	0.04	16.78	0.363	0.414	0.033	0.423
	CoreE	31	-0.63	0.101	16.53	0.79	0.219	0.044	0.245
	CorePowerE	47	-0.743	0.078	17.35	0.637	0.332	0.043	0.347
	CorePowerEClass	71	-0.626	0.051	16.42	0.442	0.379	0.036	0.379
	CorePowerEClassPC	77	-0.654	0.044	16.64	0.389	0.401	0.036	0.405
	CorePowerEClassnoBars	61	-0.624	0.061	16.41	0.511	0.386	0.04	0.375
	CorePowerEClassPCSINFONI	22	-0.643	0.087	16.6	0.751	0.443	0.082	0.386
	CorePowerEClassPCLit	57	-0.655	0.053	16.63	0.466	0.401	0.043	0.404
	PowerE	16	-0.666	0.171	16.57	1.48	0.499	0.12	0.442
	PowerEClass	40	-0.514	0.089	15.34	0.812	0.45	0.057	0.434
	PowerEClassPC	46	-0.582	0.074	15.91	0.696	0.479	0.055	0.468
	Pseudo	19	-0.42	0.113	14	1.098	0.345	0.075	0.307
ρ_h-r_h	All	96	-1.716	0.041	9.428	0.029	0.242	0.02	0.251
	CoreE	31	-1.756	0.105	9.49	0.104	0.133	0.027	0.151
	CorePowerE	47	-1.634	0.072	9.352	0.063	0.187	0.027	0.199
	CorePowerEClass	71	-1.758	0.056	9.48	0.041	0.229	0.022	0.231
	CorePowerEClassPC	77	-1.745	0.047	9.468	0.035	0.238	0.022	0.244
	CorePowerEClassnoBars	61	-1.743	0.065	9.466	0.052	0.231	0.024	0.227
	CorePowerEClassPCSINFONI	22	-1.758	0.093	9.503	0.077	0.264	0.049	0.231
	CorePowerEClassPCLit	57	-1.737	0.055	9.457	0.04	0.236	0.026	0.245
	PowerE	16	-1.662	0.177	9.336	0.111	0.306	0.074	0.259
	PowerEClass	40	-1.795	0.106	9.482	0.052	0.286	0.037	0.277
	PowerEClassPC	46	-1.764	0.082	9.468	0.045	0.294	0.035	0.29
	Pseudo	19	-1.959	0.156	9.249	0.069	0.233	0.051	0.21

Column 1: Fit type; Column 2: Sample type, see Table 8; Column 3: number of data points; Column 4 and 5: slope of the correlation and its error; Column 6 and 7: zero-point of the correlation and its errors; Column 8 and 9: intrinsic scatter and its errors; Column 10: measured scatter.

TABLE 10
THE TWO-DIMENSIONAL CORRELATION $\log M_{Bu} = a \log r_h + b \log \sigma + ZP$ FOR DIFFERENT SAMPLES.

Fit	Sample	a	da	b	db	ZP	dZP	ϵ	$d\epsilon$	rms	$P(b \neq 0)$
$M_{Bu}-r_h-\sigma$	All	0.974	0.039	1.638	0.148	6.699	0.33	0.146	0.013	0.157	0.9999
	CoreE	1.033	0.133	1.091	0.443	7.957	0.993	0.117	0.022	0.119	0.9923
	CorePowerE	1.024	0.078	1.487	0.245	6.991	0.54	0.126	0.017	0.128	0.9999
	CorePowerEClass	0.94	0.047	1.633	0.167	6.735	0.375	0.136	0.014	0.136	0.9999
	CorePowerEClassPC	0.978	0.042	1.65	0.17	6.666	0.383	0.146	0.014	0.15	0.9999
	CorePowerEClassnoBars	0.911	0.054	1.721	0.177	6.546	0.395	0.133	0.015	0.131	0.9999
	CorePowerEClassPCSINFONI	0.93	0.084	1.814	0.35	6.271	0.803	0.161	0.032	0.138	0.9999
	CorePowerEClassPCLit	0.993	0.051	1.645	0.202	6.687	0.454	0.147	0.017	0.152	0.9999
	PowerE	0.996	0.13	1.671	0.382	6.575	0.841	0.17	0.043	0.136	0.9995
	PowerEClass	0.966	0.067	1.76	0.195	6.454	0.439	0.15	0.02	0.143	0.9999
	PowerEClassPC	1.012	0.055	1.818	0.2	6.301	0.45	0.161	0.02	0.16	0.9999
	Pseudo	0.975	0.132	1.472	0.604	7.066	1.274	0.185	0.045	0.18	0.988

Column 1: Fit type; Column 2: Sample type, see Table 8; Column 3 and 4: first variable slope of the correlation and its error; Column 5 and 6: second variable slope of the correlation and its error; Column 7 and 8: zero-point of the correlation and its errors; Column 9 and 10: intrinsic scatter and its errors; Column 11: measured scatter; Column 12: probability of the bivariate correlation (see text).

18 are steeper for the subsamples including core ellipticals. In contrast, all correlations for the subsamples excluding core ellipticals and pseudo bulges are similar within the errors. BH masses in pseudo bulges correlate (weakly) only with σ , and this with a flatter slope than for the other samples.

As noticed before, when we augment the errors on the bulge mass and density by 0.15 dex (see Sect. 3), the fitted parameters of the $M_{BH}-M_{Bu}$ and $M_{BH}-\rho_h$ correlations remain essentially the same with somewhat larger errors; but the estimated intrinsic scatter is approximately reduced by 0.15 dex in quadrature.

This confirms the results reported in the literature. In particular:

- a) the slopes of the $M_{BH}-\sigma$ and $M_{BH}-M_{Bu}$ relations agree with published results within the quoted errors;
- b) core ellipticals have more massive BHs than other classical bulges, at a given σ or bulge mass, when correlations derived using samples including non-core galaxies are adopted; moreover, the smallest intrinsic and measured scatter of the $M_{BH}-\sigma$ and $M_{BH}-M_{Bu}$ relations are measured for the sample of core ellipticals;
- c) power-law early type galaxies and classical bulges follow similar $M_{BH}-\sigma$ and $M_{BH}-M_{Bu}$ relations;
- d) pseudo bulges have smaller BH masses than the rest of the sample at a given σ or M_{Bu} .

Our sample indicates that the $M_{BH}-\sigma$ relation is possibly a better predictor (i.e. with lower intrinsic scatter) of M_{BH} than the $M_{BH}-M_{Bu}$ relation; this remains true even when we augment the errors on the bulge mass by 0.15 dex in quadrature. However, the difference is not statistically significant. Kormendy & Ho (2013) argue on the basis of their KH45 sample that both relations are equivalent (see Table 13 and discussion below).

Graham & Scott (2013) claim that “Sersic galaxies” follow a quadratic $M_{BH}-M_{Bu}$ relation. We disagree with this interpretation: *classical* bulges (all with a Sersic profile) and Core-Sersic galaxies follow the same linear $M_{BH}-M_{Bu}$ relations within the errors. The steepening of the relation at low bulge masses for “Sersic galaxies” seen by Graham & Scott (2013) stems from their possibly uncertain bulge masses (see

Fig. 7) and the fact that they do not distinguish between pseudo and classical bulges. We also disagree with their interpretation of the role of barred galaxies: considering barred galaxies with classical bulges delivers the same $M_{BH}-\sigma$ and $M_{BH}-M_{Bu}$ relations within the errors that we derive for non-barred classical bulges and early-type galaxies. Again, it is the pseudo bulges, not the barred classical bulges, that deviate from the $M_{BH}-\sigma$ and $M_{BH}-M_{Bu}$ relations.

The intrinsic and measured scatter of our $M_{BH}-\sigma$ and $M_{BH}-M_{Bu}$ relations are generally larger than the values quoted in previous studies, although the coefficients of the relations are compatible within the errors. This stems from the sample of objects that comes from our SINFONI survey, where we deliberately observed objects with extreme properties (i.e., objects with small or large velocity dispersions, particularly compact objects, or merger remnants).

Finally, we explicitly show that galaxy sizes and densities correlate with BH masses too, although with larger scatter. This and the discrepant results about the existence of the “BH Fundamental Plane” quoted in Sect. 1 motivate our next step, which is to investigate five two-parameter correlations of the type $z = ax + by + ZP + N(0, \epsilon)$:

$$M_{BH} - \sigma - \rho_h : \log M_{BH} = a \log \sigma + b \log \rho_h + ZP, \quad (19)$$

$$M_{BH} - M_{Bu} - \rho_h : \log M_{BH} = a \log M_{Bu} + b \log \rho_h + ZP, \quad (20)$$

$$M_{BH} - \sigma - r_h : \log M_{BH} = a \log \sigma + b \log r_h + ZP, \quad (21)$$

$$M_{BH} - M_{Bu} - r_h : \log M_{BH} = a \log M_{Bu} + b \log r_h + ZP. \quad (22)$$

$$M_{BH} - M_{Bu} - \sigma : \log M_{BH} = a \log M_{Bu} + b \log \sigma + ZP, \quad (23)$$

Table 12 gives the results for the 12 (sub-)samples considered above: the values of the best-fit parameters a , b , and ZP with their errors of the correlations of the type $z = ax + by + ZP$, the intrinsic and measured scatter ϵ and rms , the probability of the bivariate correlation $P(b \neq 0)$ of $b \leq 0$ (if $b_{fit} > 0$), or of $b \geq 0$ (if $b_{fit} < 0$), the value of $\Delta cAIC$ and of $RP = \exp(\Delta cAIC/2)$ (the relative probability of the mono- and bivariate solutions), the Spearman correlation coefficient of the residuals $z - ax$ with y , and the probability of the latter’s value being greater due to chance.

TABLE 11
ONE-DIMENSIONAL CORRELATIONS WITH BLACK HOLE MASSES.

Fit	Sample	N	a	da	ZP	dZP	ϵ	d ϵ	rms	r_S	$P(r_S)$
$M_{BH} \cdot \sigma$	All	96	5.246	0.274	-3.77	0.631	0.417	0.037	0.459	0.9109	6.59e-38
	CoreE	31	4.772	0.794	-2.476	1.942	0.332	0.06	0.366	0.6936	1.52e-05
	CorePowerE	47	4.713	0.458	-2.393	1.099	0.38	0.05	0.399	0.8005	1.45e-11
	CorePowerEClass	71	4.546	0.33	-2.03	0.78	0.348	0.037	0.38	0.8677	1.24e-22
	CorePowerEClassPC	77	4.868	0.32	-2.827	0.75	0.38	0.038	0.409	0.883	2.42e-26
	CorePowerEClassPCSINFONI	22	4.976	0.72	-3.025	1.72	0.502	0.093	0.446	0.7134	0.000194
	CorePowerEClassPCLit	57	4.829	0.372	-2.756	0.867	0.335	0.044	0.388	0.9015	1.18e-21
	CorePowerEClassnoBars	61	4.566	0.36	-2.05	0.858	0.343	0.04	0.379	0.8501	4.48e-18
	PowerE	16	3.992	0.874	-0.856	2.01	0.496	0.122	0.416	0.6676	0.00471
	PowerEClass	40	3.806	0.442	-0.421	1.016	0.347	0.05	0.35	0.8006	5.58e-10
	PowerEClassPC	46	4.227	0.446	-1.452	1.015	0.397	0.051	0.401	0.8211	2.77e-12
	Pseudo	19	2.129	1.349	2.526	2.832	0.455	0.108	0.45	0.4159	0.0766
	All	96	0.962	0.066	-2.099	0.716	0.535	0.044	0.54	0.8505	5.64e-20
	CoreE	31	0.906	0.23	-1.35	2.672	0.431	0.07	0.423	0.5728	0.000759
$M_{BH} \cdot M_{Bu}$	CorePowerE	47	0.986	0.114	-2.309	1.293	0.436	0.055	0.442	0.7308	5.49e-09
	CorePowerEClass	71	0.885	0.08	-1.155	0.887	0.424	0.043	0.444	0.7776	1.51e-15
	CorePowerEClassPC	77	0.846	0.064	-0.713	0.697	0.431	0.041	0.447	0.8147	2e-19
	CorePowerEClassPCSINFONI	22	0.945	0.12	-1.643	1.335	0.447	0.086	0.403	0.8557	3.84e-07
	CorePowerEClassPCLit	57	0.794	0.074	-0.231	0.805	0.417	0.049	0.438	0.8081	3.01e-14
	CorePowerEClassnoBars	61	0.925	0.094	-1.618	1.059	0.435	0.048	0.448	0.7512	3.07e-12
	PowerE	16	0.912	0.226	-1.579	2.454	0.55	0.134	0.461	0.43	0.0964
	PowerEClass	40	0.783	0.132	-0.094	1.411	0.448	0.061	0.451	0.5717	0.000116
	PowerEClassPC	46	0.758	0.095	0.166	1.002	0.453	0.056	0.452	0.6782	2.24e-07
	Pseudo	19	0.094	0.298	6.058	2.968	0.519	0.115	0.477	0.0158	0.949
	All	96	1.149	0.104	7.894	0.074	0.644	0.05	0.628	0.7704	4.49e-20
	CoreE	31	1.05	0.318	8.162	0.319	0.456	0.075	0.444	0.5862	0.000529
	CorePowerE	47	1.3	0.178	7.864	0.158	0.488	0.062	0.489	0.6739	2.08e-07
	CorePowerEClass	71	0.999	0.122	8.122	0.093	0.52	0.05	0.524	0.7057	6.33e-12
$M_{BH} \cdot r_h$	CorePowerEClassPC	77	0.991	0.098	8.119	0.076	0.528	0.048	0.529	0.7482	5.26e-15
	CorePowerEClassPCSINFONI	22	1.096	0.203	8.257	0.171	0.6	0.113	0.514	0.8229	2.57e-06
	CorePowerEClassPCLit	57	0.929	0.109	8.059	0.083	0.501	0.055	0.508	0.7333	8.74e-11
	CorePowerEClassnoBars	61	1.071	0.15	8.064	0.122	0.53	0.056	0.529	0.6853	1.11e-09
	PowerE	16	1.166	0.374	7.804	0.235	0.636	0.151	0.536	0.2647	0.322
	PowerEClass	40	0.726	0.212	8.105	0.105	0.571	0.074	0.555	0.3646	0.0207
	PowerEClassPC	46	0.798	0.155	8.063	0.089	0.575	0.068	0.559	0.4988	0.000419
	Pseudo	19	0.098	0.326	7.022	0.15	0.524	0.111	0.474	0.1299	0.596
	All	96	-0.589	0.07	13.49	0.633	0.734	0.058	0.721	-0.7016	1.71e-15
	CoreE	31	-0.517	0.195	13.21	1.529	0.483	0.08	0.475	-0.4815	0.00609
	CorePowerE	47	-0.7	0.124	14.53	1.008	0.55	0.071	0.564	-0.5899	1.28e-05
	CorePowerEClass	71	-0.472	0.078	12.7	0.674	0.597	0.057	0.599	-0.6346	2.81e-09
	CorePowerEClassPC	77	-0.493	0.064	12.85	0.567	0.612	0.055	0.61	-0.6879	4.77e-12
	CorePowerEClassPCSINFONI	22	-0.539	0.134	13.46	1.16	0.72	0.132	0.614	-0.7811	1.78e-05
$M_{BH} \cdot M_{Bu}^{0.5} \cdot \sigma^2$	CorePowerEClassPCLit	57	-0.466	0.073	12.53	0.641	0.575	0.063	0.58	-0.6732	9.59e-09
	CorePowerEClassnoBars	61	-0.493	0.094	12.87	0.79	0.614	0.064	0.609	-0.6064	2.23e-07
	PowerE	16	-0.553	0.249	13.07	2.146	0.73	0.178	0.628	-0.2029	0.451
	PowerEClass	40	-0.234	0.125	10.39	1.137	0.631	0.082	0.616	-0.2232	0.166
	PowerEClassPC	46	-0.323	0.097	11.15	0.913	0.657	0.076	0.637	-0.3878	0.00776
	Pseudo	19	-0.065	0.162	7.628	1.58	0.52	0.113	0.472	-0.1869	0.444
	All	96	1.198	0.061	-3.673	0.613	0.417	0.036	0.439	0.9122	3.37e-38
	CoreE	31	1.185	0.212	-3.492	2.274	0.356	0.062	0.371	0.6802	2.56e-05
	CorePowerE	47	1.168	0.107	-3.336	1.121	0.363	0.048	0.382	0.8032	1.09e-11
	CorePowerEClass	71	1.096	0.075	-2.57	0.769	0.333	0.036	0.363	0.8588	1.01e-21
	CorePowerEClassPC	77	1.093	0.063	-2.538	0.64	0.342	0.034	0.367	0.881	4.36e-26
	CorePowerEClassPCSINFONI	22	1.157	0.125	-3.089	1.295	0.396	0.075	0.359	0.8472	6.55e-07
	CorePowerEClassPCLit	57	1.05	0.072	-2.156	0.723	0.316	0.041	0.356	0.8854	6.01e-20
	CorePowerEClassnoBars	61	1.12	0.085	-2.821	0.885	0.341	0.04	0.372	0.8353	5.75e-17
$M_{BH} \cdot M_{Bu} \cdot \sigma^2$	PowerE	16	1.059	0.21	-2.292	2.103	0.463	0.115	0.392	0.5971	0.0146
	PowerEClass	40	1.007	0.114	-1.698	1.137	0.343	0.049	0.351	0.745	3.52e-08
	PowerEClassPC	46	1.023	0.093	-1.874	0.913	0.354	0.045	0.359	0.8023	2.04e-11
	Pseudo	19	0.358	0.389	3.719	3.564	0.504	0.114	0.466	0.1975	0.418
	All	96	0.747	0.042	-3.205	0.648	0.456	0.038	0.468	0.8948	1.08e-34
	CoreE	31	0.743	0.148	-3.083	2.448	0.379	0.065	0.386	0.6505	7.43e-05
	CorePowerE	47	0.746	0.072	-3.161	1.165	0.38	0.05	0.397	0.7847	6.72e-11
	CorePowerEClass	71	0.69	0.05	-2.23	0.789	0.358	0.038	0.385	0.8384	7.39e-20
	CorePowerEClassPC	77	0.673	0.042	-1.963	0.651	0.367	0.036	0.389	0.8644	4.25e-24
	CorePowerEClassPCSINFONI	22	0.726	0.081	-2.662	1.279	0.404	0.077	0.365	0.876	9.19e-08
	CorePowerEClassPCLit	57	0.64	0.049	-1.512	0.756	0.347	0.042	0.38	0.8591	1.25e-17
	CorePowerEClassnoBars	61	0.711	0.059	-2.588	0.935	0.366	0.043	0.392	0.8132	1.71e-15
	PowerE	16	0.687	0.14	-2.3	2.17	0.479	0.119	0.408	0.5765	0.0194
	PowerEClass	40	0.636	0.08	-1.432	1.217	0.373	0.052	0.379	0.7181	1.83e-07
	PowerEClassPC	46	0.629	0.062	-1.321	0.931	0.381	0.048	0.385	0.7827	1.31e-10
	Pseudo	19	0.155	0.244	4.822	3.444	0.522	0.115	0.471	0.06231	0.8

Column 1: Fit type; Column 2: Sample type, see Table 8; Column 3: number of data points; Column 4 and 5: slope of the correlation and its error; Column 6 and 7: zero-point of the correlation and its errors; Column 8 and 9: intrinsic scatter and its errors; Column 10: measured scatter; Column 11 and 12: Spearman coefficient and its probability.

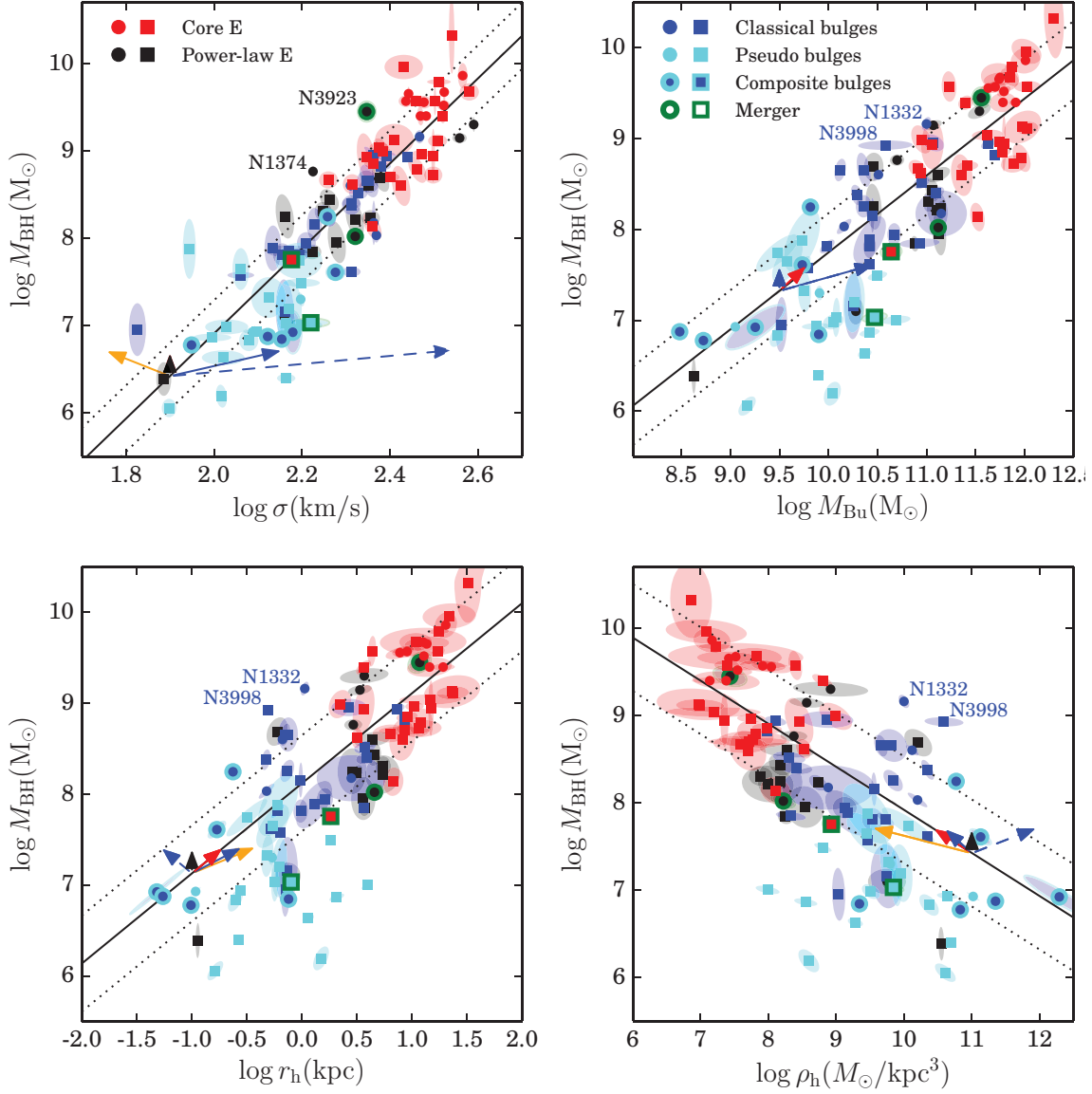


Fig. 13.— Top: the $M_{BH}-\sigma$ (left) and $M_{BH}-M_{Bu}$ (right) relations. Bottom: the $M_{BH}-r_h$ (left) and $M_{BH}-\rho_h$ (right) relations. Symbols as in Fig. 12. The ellipses show the 1σ errors. The labels name particularly deviant galaxies. The full lines indicate the relations given in Tab. 11 for the CorePowerEClassPC sample. The dotted lines indicate the estimated intrinsic scatter. Arrows describe the effect of an equal mass dry merger (red), of a sequence of minor mergers doubling the bulge mass (orange), an equal-mass, gas-rich merger of two spiral galaxies with 20% bulge mass with bulge-scales ratio r_h^f/r_h^i 3 (blue) or 0.5 (dotted blue), and doubling the BH mass through accretion or BH merging (black), see Sect. 6 and Table 16.

The correlations involving σ ($M_{BH}-\sigma-\rho_h, M_{BH}-\sigma-r_h, M_{BH}-M_{Bu}-\sigma$) are established with high confidence for all subsamples except core ellipticals, power-law ellipticals, and pseudo bulges (each of these classes have ≈ 30 or less objects). In particular, for the sample CorePowerEClassPC (the 77 galaxies that are not pseudo bulges) the relations:

$$\log M_{BH} = (4.04 \pm 0.35) \log \sigma - (0.19 \pm 0.05) \log \rho_h + (0.79 \pm 1.11), \quad (24)$$

$$\log M_{BH} = (3.74 \pm 0.40) \log \sigma + (0.38 \pm 0.09) \log r_h - (0.35 \pm 0.90) \quad (25)$$

and

$$\log M_{BH} = (0.37 \pm 0.09) M_{Bu} + (3.19 \pm 0.52) \log \sigma - (2.93 \pm 0.66) \quad (26)$$

have a measured/intrinsic scatter of just 0.36/0.33 dex, 0.05 dex less than the respective one-dimensional solution $M_{BH}-\sigma$, a probability $P(b \neq 0) > 0.99$, very negative $\Delta cAIC$ values (< -13 , or relative probabilities of the mono- and bivariate solutions less than 0.001) and a strong Spearman coefficient value ($|r_S| > 0.5$ with $P(r_S) < 10^{-6}$) of the residuals $z - ax$ with the y variable. We illustrate the three correlations in the top and bottom left panels of Fig. 14.

As in the single variable correlations presented in Fig. 13, the subsample of pseudo bulges (see Fig. 14, bottom right, and Fig. 15, top and bottom left) has smaller black hole masses for a given velocity dispersion. The smallest offsets are observed at the largest densities and smallest scale-lengths, and pseudo bulges smaller than 1 kpc, or denser than $10^{10} M_\odot / \text{kpc}^3$ roughly follow the correlations defined by the other subsamples. As a consequence, it is not possible to derive a tight bivariate correlation that simultaneously describes the behavior of core, power-law ellipticals, classical and pseudo bulges. If we fit the sample All, we get a steeper σ coefficient and a measured and intrinsic scatter larger by 0.06-0.07 dex than for the subsample without pseudo bulges. Nevertheless, the bivariate correlation remains highly significant ($P(b \neq 0) > 0.99$) and the Spearman coefficient value of the correlation of the residuals $z - ax$ with the y variable is strong ($|r_S| > 0.49$, $P(r_S) < 4 \times 10^{-7}$).

The right-hand plots of Fig. 5 illustrate what happens if we use the cylindrical densities and radii for pseudo bulges that we calculate from Eq. 15 and $h_z = 0.2a_e/1.67$. Since densities are increased and

scalelengths do not change much, only the density threshold above which pseudo bulges follow the scaling relations of the other subsamples changes, to about $10^{11} M_\odot / \text{kpc}^3$.

The evidence for the correlations $M_{BH}-M_{Bu}-\rho_h$ and $M_{BH}-M_{Bu}-r_h$ is weaker but still convincing. Here the bivariate correlations derived for the CorePowerEClassPC sample are significant at the 98% level, the $\Delta cAIC$ values are negative (< -2.3) with relative probability of the mono- and bivariate solutions less than 0.32, with large Spearman correlation coefficients ($|r_S| > 0.45$) and low $P(r_S)$ probabilities ($P(r_S) < 4 \times 10^{-5}$ for the residuals $z - ay$, but only a marginal reduction (by 0.01 dex) of the measured scatter compared to the monovariate correlations is achieved. We derive the following relations:

$$\log M_{BH} = (1.11 \pm 0.14) \log M_{Bu} + (0.23 \pm 0.11) \log \rho_h - (5.52 \pm 2.42), \quad (27)$$

$$\log M_{BH} = (1.33 \pm 0.24) \log M_{Bu} - (0.68 \pm 0.32) \log r_h - (5.74 \pm 2.53). \quad (28)$$

Stronger bivariate correlations are obtained when excluding Core ellipticals (the subsample PowerEClassPC), see discussion below.

This lets us present the correlations $M_{BH}-M_{Bu}-\rho_h$ and $M_{BH}-M_{Bu}-r_h$ in a slightly different fashion in Fig. 16. There we plot the two relations separately for the subsamples CoreE, PowerEClassPC and Pseudo. First, we note that the subsample of Core Es is offset to the left of the PowerEClassPC sequence at lower densities and to the right at larger scale lengths. Indeed, fitting the $M_{BH}-M_{Bu}-\rho_h$ and $M_{BH}-M_{Bu}-r_h$ relations to the PowerEClassPC sample delivers steeper slopes for both the ρ_h and r_h dependence.

Second, as found above, the pseudo bulges tend to have lower black hole masses at any bulge mass. Fig. 17 shows that pseudo bulges with large densities or small scalelengths tend to be closer to the $M_{BH}-M_{Bu}-\rho_h$ and $M_{BH}-M_{Bu}-r_h$ relations defined by the other subsamples.

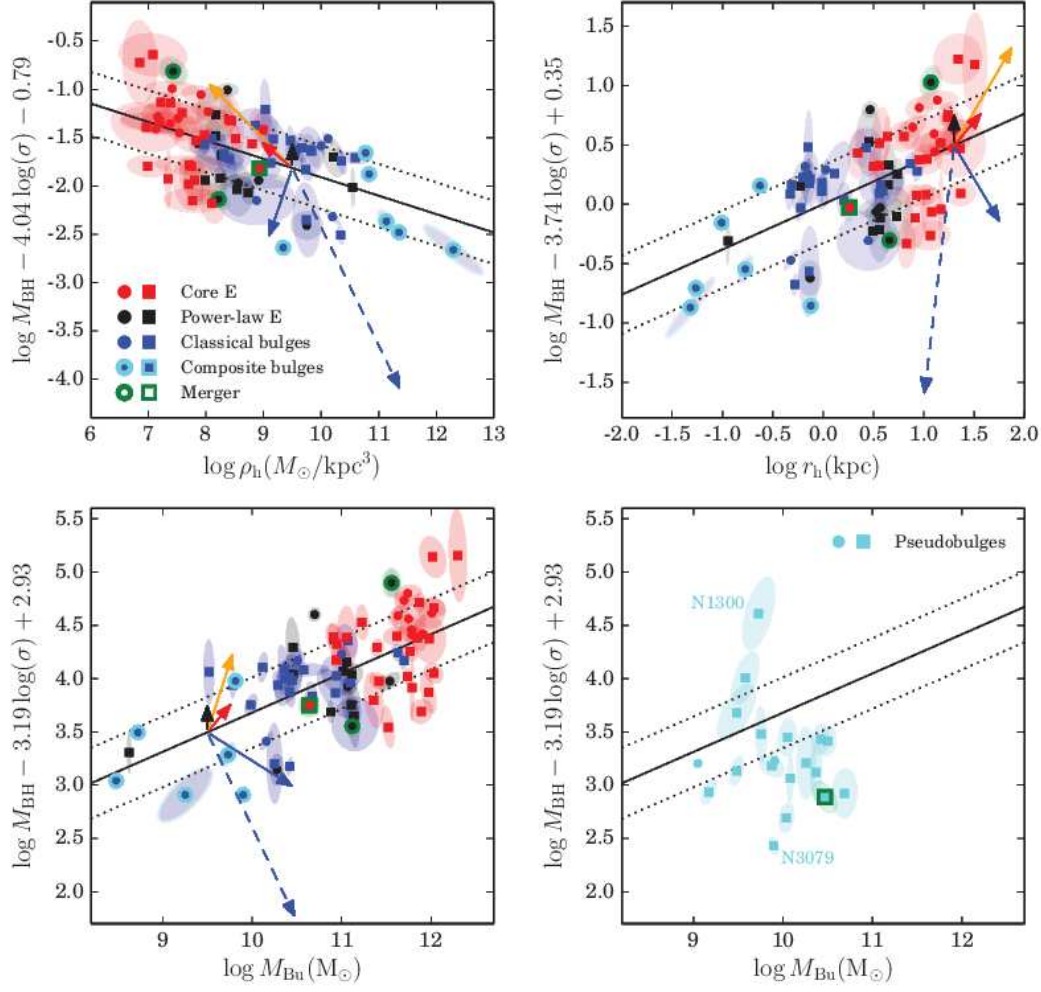


Fig. 14.— Illustration of the bivariate correlations $M_{BH}-\sigma-\rho_h$ (top left), $M_{BH}-\sigma-r_h$ (top right) and $M_{BH}-M_{Bu}-\sigma$ (bottom left and right). In each panel we plot the corresponding best-fit relations for the CorePowerEClassPC subsample using full lines, with dotted lines showing the estimated intrinsic scatter. Galaxy data points from the various subsamples are plotted with different colors: core galaxies in red, power-law ellipticals in black, classical bulges in blue, pseudo bulges in cyan. Mergers have a green annulus. Blue dots with a cyan annulus are the classical bulge components of (composite) pseudo bulges. Squares indicate data from the literature and circles data from our SINFONI survey. The ellipses show the 1σ errors. Arrows describe the effect of an equal mass dry merger (red), of a sequence of minor mergers which double the bulge mass (orange), an equal-mass, gas-rich merger of two spiral galaxies with 20% bulge mass and bulge-scales ratio r_h^f/r_h^i of 3 (blue) or 0.5 (dotted blue), and doubling the BH mass through accretion or BH merging (black), see also Sect. 6 and Table 16.

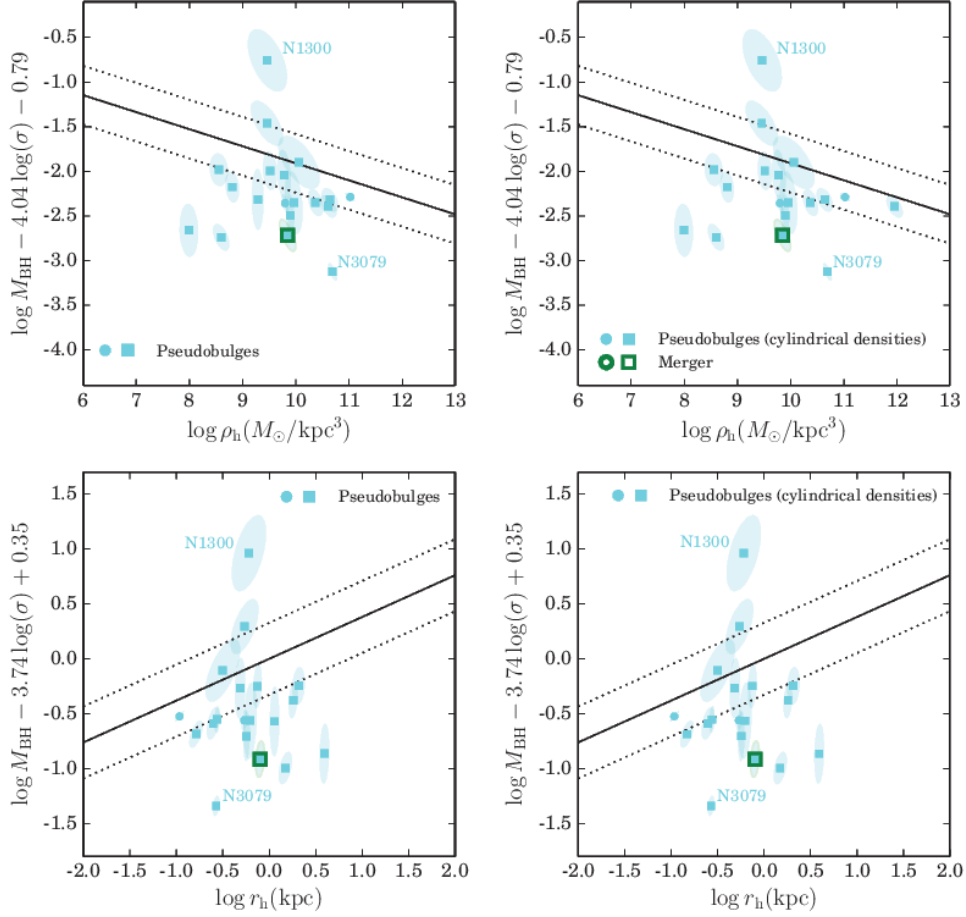


Fig. 15.— Illustration of the bivariate correlations M_{BH} - σ - ρ_h (top) and M_{BH} - σ - r_h (bottom) for pseudo bulges (cyan points). Squares indicate data from the literature and circles data from our SINFONI survey. The ellipses show the 1σ errors. Lines and arrows as in Fig. 14. The left plot is for spherical densities and radii (see Eq. 4), the plot to the right for cylindrical densities and radii with $h_z = 0.2a_e/1.67$ (see Eq. 5).

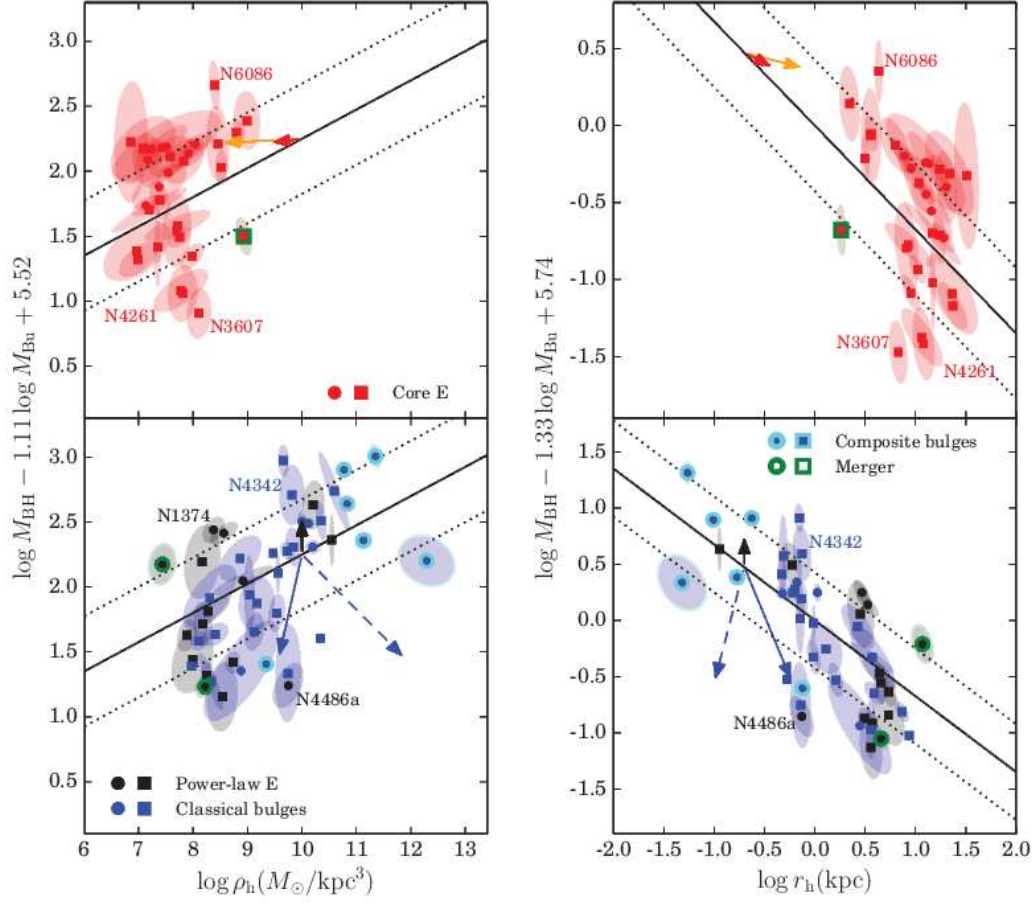


Fig. 16.— As for Fig. 14, but showing how different subsamples relate to the M_{BH} - M_{Bu} - ρ_h (left panels) and the M_{BH} - M_{Bu} - r_h (right panels) bivariate correlations. In each set of panels we plot the corresponding best-fit relations for the CorePowerEClassPC sample using full lines, with the dotted lines showing estimated intrinsic scatter. Individual panels show different subsamples: core galaxies (top panels), and PowerEClassPC (bottom panels). The labels name particularly deviant galaxies. The ellipses show the 1σ errors. Colors, arrows and point types as in Fig. 14.

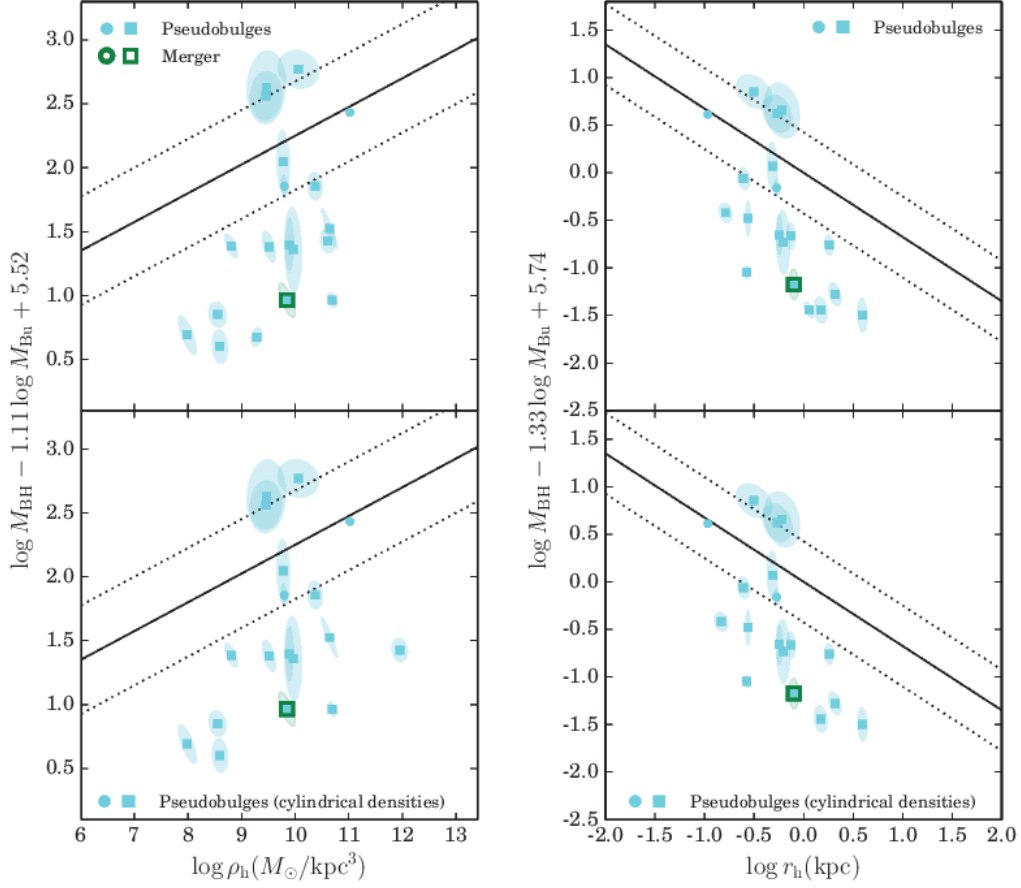


Fig. 17.— As for Fig. 16, but showing pseudo bulges only. The plots at the top are for spherical densities and radii (see Eq. 4), the plots at the bottom for cylindrical densities and radii with $h_z = 0.2a_e/1.67$ (see Eq. 5).

TABLE 12
TWO-DIMENSIONAL CORRELATIONS WITH BLACK HOLE MASSES.

Fit	Sample	a	dt	b	db	ZP	zFP	ϵ	$d\epsilon$	rms	$P(b \neq 0)$	$\Delta cAIC$	RP	r_S	$P(r_S)$
$M_B H \cdot \sigma \cdot \eta_h$	All	4.511	0.32	-0.183	0.046	-0.049	1.038	0.379	0.035	0.409	0.9999	-13.41	0.001	-0.4934	3.27e-07
	CoreE	4.472	1.035	-0.103	0.181	-0.94	3.593	0.334	0.061	0.354	0.7242	2.328	3.203	-0.2972	0.104
	CorePowerE	3.887	0.533	-0.258	0.101	1.669	1.887	0.345	0.047	0.356	0.9929	-4.153	0.125	-0.4976	0.000422
	CorePowerEClass	3.958	0.348	-0.176	0.052	0.859	1.116	0.314	0.035	0.339	0.9903	-9.336	0.009	-0.4546	6.83e-05
	CorePowerEClassPC	4.037	0.35	-0.191	0.046	0.788	1.101	0.328	0.034	0.349	0.9909	-15.28	0	-0.5152	1.63e-06
	CorePowerEClassPCSFONFI	3.988	0.821	-0.218	0.11	1.201	2.638	0.453	0.087	0.384	0.9749	-0.929	0.629	-0.6477	0.00112
	CorePowerEClassPCLit	4.015	0.37	-0.188	0.047	1.208	1.14	0.275	0.038	0.325	0.9909	-13.66	0.001	-0.4144	0.00135
	CorePowerEClassPCSBars	4.085	0.863	-0.278	0.165	2.694	2.845	0.448	0.117	0.354	0.9897	-3.664	0.16	-0.4232	0.00679
	PowerE	3.489	0.863	-0.278	0.165	2.694	2.845	0.448	0.117	0.354	0.9897	-3.664	0.16	-0.4232	0.00679
	PowerEClass	3.705	0.421	-0.149	0.068	1.174	1.208	0.324	0.047	0.324	0.9836	-2.344	0.31	-0.3131	0.0491
	PowerEClassPC	3.873	0.414	-0.182	0.058	1.057	1.213	0.348	0.045	0.345	0.9836	-7.559	0.023	-0.4194	0.00371
	Pseudo	2.119	1.419	-0.063	0.154	3.166	3.33	0.48	0.17	0.446	0.6709	3.087	4.682	-0.207	0.395
	Pseudo	1.231	1.048	0.246	0.114	-7.183	2.539	0.535	0.044	0.532	0.9834	-2.51	0.285	-0.4218	1.87e-05
$M_B H \cdot M_B u \cdot \eta_h$	All	1.036	0.52	0.129	0.401	-3.854	8.955	0.436	0.075	0.425	0.9999	2.546	3.572	0.1093	0.558
	CoreE	1.082	0.247	0.097	0.214	-4.178	4.414	0.442	0.056	0.442	0.6748	2.19	2.989	0.1333	0.372
	CorePowerE	1.128	0.16	0.218	0.116	-5.693	2.674	0.426	0.043	0.435	0.9689	-1.296	0.523	0.3818	0.00102
	CorePowerEClass	1.107	0.142	0.225	0.106	-5.922	2.419	0.425	0.042	0.439	0.9823	-2.284	0.319	0.4507	3.9e-05
	CorePowerEClassPC	1.307	0.252	0.299	0.185	-8.228	4.269	0.422	0.085	0.382	0.9487	0.386	1.213	0.5257	0.012
	CorePowerEClassPCSFONFI	0.993	0.17	0.236	0.131	-6.583	2.965	0.425	0.05	0.435	0.9261	0.262	1.14	0.3278	0.0128
	CorePowerEClassPCLit	1.193	0.176	0.236	0.131	-6.583	2.965	0.425	0.05	0.435	0.9261	0.262	1.14	0.3278	0.0128
	CorePowerEClassPCSBars	1.002	0.379	0.105	0.321	-3.464	6.513	0.571	0.146	0.459	0.6349	3.529	5.838	0.07647	0.778
	PowerE	1.056	0.18	0.296	0.128	-5.704	2.874	0.431	0.061	0.42	0.9887	-2.89	0.236	0.5073	0.000834
	PowerEClass	1.056	0.151	0.291	0.113	-5.664	2.511	0.424	0.055	0.426	0.9931	-4.236	0.12	0.5725	3.22e-05
	PowerEClassPC	1.056	0.151	0.291	0.113	-5.664	2.511	0.424	0.055	0.426	0.9931	-4.236	0.12	0.5725	3.22e-05
	Pseudo	-0.138	0.476	-0.13	0.273	9.63	6.998	0.544	0.123	0.47	0.6933	3.03	4.55	-0.2789	0.247
	Pseudo	4.258	0.373	0.538	0.096	-1.616	0.834	0.383	0.035	0.413	0.9999	-11.66	0.003	0.5049	1.55e-07
	Pseudo	4.396	1.178	0.181	0.369	-1.734	2.63	0.337	0.062	0.356	0.9999	-2.408	3.333	0.275	0.134
$M_B H \cdot \sigma \cdot \eta_h$	All	1.001	0.867	-0.303	1.161	-3.319	9.003	0.436	0.072	0.424	0.9999	-2.782	0.249	-0.6331	4.97e-12
	CoreE	1.101	0.851	-0.279	0.644	-4.161	4.634	0.443	0.057	0.442	0.9999	2.581	3.635	-0.1863	0.316
	CorePowerE	1.168	0.451	-0.279	0.644	-4.161	4.634	0.443	0.057	0.442	0.9999	2.581	3.635	-0.1863	0.316
	CorePowerEClass	1.353	0.266	-0.661	0.347	-5.971	2.772	0.426	0.044	0.435	0.9705	-2.207	3.015	-0.2394	0.105
	CorePowerEClassPC	1.332	0.243	-0.675	0.317	-5.738	2.578	0.426	0.044	0.439	0.9848	-2.294	0.318	-0.5733	1.74e-07
	CorePowerEClassPCSFONFI	1.612	0.247	-0.906	0.554	-8.556	4.451	0.421	0.085	0.383	0.9525	0.342	1.186	-0.7369	9.17e-05
	CorePowerEClassPCLit	1.169	0.284	-0.533	0.372	-4.081	2.955	0.424	0.05	0.434	0.924	0.263	1.14	-0.5672	4.21e-06
	CorePowerEClassPCSBars	1.424	0.296	-0.698	0.395	-6.752	3.08	0.426	0.048	0.441	0.9602	-0.822	0.663	-0.5044	3.4e-05
	PowerE	1.088	0.681	-0.294	0.99	-3.359	6.986	0.574	0.148	0.458	0.6266	3.548	5.894	-0.3088	0.244
	PowerEClass	1.355	0.285	-0.887	0.382	-6.01	2.971	0.431	0.06	0.42	0.9892	-2.91	0.233	-0.6947	6.58e-07
	PowerEClassPC	1.342	0.251	-0.862	0.339	-5.883	2.609	0.424	0.054	0.426	0.994	-4.064	0.131	-0.7504	1.93e-09
	Pseudo	-0.254	0.727	0.38	0.833	9.613	7.395	0.549	0.123	0.47	0.6899	3.05	4.594	0.3035	0.207
	Pseudo	0.307	0.999	3.935	0.599	-4.073	0.599	0.395	0.036	0.426	0.9999	-7.502	0.023	0.5157	7.59e-08
	Pseudo	0.105	0.315	4.466	1.358	-2.95	2.211	0.336	0.062	0.362	0.9667	2.538	3.558	0.141	0.449
$M_B H \cdot M_B u \cdot \sigma$	All	0.105	0.315	4.466	1.358	-2.95	2.211	0.336	0.062	0.362	0.9667	2.538	3.558	0.141	0.449
	CoreE	0.105	0.315	4.466	1.358	-2.95	2.211	0.336	0.062	0.362	0.9667	2.538	3.558	0.141	0.449
	CorePowerE	0.357	0.192	3.365	0.859	-3.219	1.173	0.361	0.048	0.377	0.9666	-1.047	0.592	0.4339	0.00231
	CorePowerEClass	0.319	0.114	3.309	0.547	-2.654	0.757	0.323	0.035	0.353	0.9971	-5.583	0.061	0.4729	3.12e-05
	CorePowerEClassPC	0.368	0.094	3.186	0.518	-2.927	0.658	0.332	0.033	0.36	0.9999	-13.19	0.001	0.5819	2.86e-08
	CorePowerEClassPCSFONFI	0.588	0.211	2.242	1.147	-3.026	1.41	0.409	0.079	0.359	0.9955	-4.737	0.094	0.7899	1.23e-05
	CorePowerEClassPCLit	0.305	0.102	3.396	0.589	-2.706	0.755	0.296	0.04	0.346	0.9988	-6.574	0.037	0.4514	0.000425
	CorePowerEClassPCSBars	0.266	0.141	3.564	0.638	-2.663	0.856	0.334	0.039	0.362	0.9689	-1.395	0.523	0.4019	0.00132
	PowerE	0.36	0.341	2.759	1.433	-2.15	2.206	0.438	0.127	0.388	0.8753	2.392	3.307	0.2091	0.437
	PowerEClass	0.261	0.146	3.021	0.61	-1.422	1.1	0.329	0.048	0.333	0.9615	-0.719	0.698	0.2897	0.0698
	PowerEClassPC	0.357	0.111	2.876	0.574	-2.159	0.909	0.347	0.046	0.351	0.9985	-8.005	0.018	0.5019	0.000379
	Pseudo	-0.158	0.32	2.391	1.632	3.54	3.407	0.485	0.119	0.448	0.7002	3.014	4.514	-0.207	0.395

Column 1: Fit type; Column 2: Sample type; see Table 8; Column 3 and 4: first variable slope of the correlation and its error; Column 5 and 6: second variable slope of the correlation and its error; Column 7 and 8: zero-point of the correlation and its errors; Column 9 and 10: intrinsic scatter and its errors; Column 11: measured scatter; Column 12: probability of the bivariate correlation; Column 13 and 14: $\Delta cAIC$ value and $RP = \exp(\Delta cAIC/2)$ (the relative probability of

the mono- and bivariate solutions), they are computed matching the bivariate solutions of this table to the monivariate solutions of Table 11 of the respective datasets. The pairings are: $M_{BH} \cdot \sigma \cdot \gamma_h$ with $M_{BH} \cdot \sigma$, $M_{BH} \cdot M_{Bu} \cdot \gamma_h$ with $M_{BH} \cdot M_{Bu} \cdot \sigma$, $M_{BH} \cdot M_{Bu} \cdot \sigma$ with $M_{BH} \cdot \sigma$, see Sect. 4, Column 15 and 16. Spearman coefficient and its probability.

We now discuss the effects of considering different samples. The exclusion of barred objects weakens only slightly the significance of all the bivariate correlations discussed above; we come back to this issue at the end of this section. If we just fit the 22 galaxies with SINFONI black hole mass determinations, we find good evidence for the bivariate correlations $M_{BH}-\sigma-\rho_h$, $M_{BH}-\sigma-r_h$ and $M_{BH}-M_{Bu}-\sigma$ ($P(\beta) \neq 0 > 0.97$, $\Delta cAIC < -0.9$), but weaker or no evidence ($P(\beta) \neq 0 > 0.95$ but positive $\Delta cAIC$) for the bivariate correlations $M_{BH}-M_{Bu}-\rho_h$, $M_{BH}-M_{Bu}-r_h$. Similar numbers are found if we fit only the 57 galaxies with black hole mass measurements from the literature. The results do not change if we minimize the correlated errors by setting $a_{BH} = f = 0$ for all galaxies in the equations of Table 4. Similar to what was noticed for the one-dimensional correlations, we do not see any statistically significant change in the fitted parameters of the $M_{BH}-M_{Bu}-\rho_h$, $M_{BH}-M_{Bu}-\sigma$, and $M_{BH}-\sigma-\rho_h$ correlations when we augment the errors on the bulge mass and density by 0.15 dex (see Sect. 3). Only the estimated intrinsic scatter is reduced by approximately 0.15 dex in quadrature.

We also repeat the one- and bivariate analysis by deleting from the sample NGC 2974, NGC 3414, NGC 4552, NGC 4621, NGC 5813 and NGC 5846, for which only uncertain BH mass determinations are available (Cappellari et al. 2008), and NGC 3079 and NGC 4151, for which Kormendy & Ho (2013) do not trust the black hole masses. The results are presented in Appendix D, Tables 36 and 37. The changes are not significant, therefore we prefer the values derived including these galaxies (Tables 11 and 12) to maximize the size of the sample.

Finally, we repeated the $M_{BH}-\sigma$, $M_{BH}-M_{Bu}$ and $M_{BH}-M_{Bu}-\sigma$ fits using the BH and bulge masses, plus velocity dispersions and errors of Kormendy & Ho (2013) for the KH45 sample to derive the solutions given in their Eqs. (5) and (10). The results are given in Table 13, third and fourth row, and demonstrate that our fit methodology recovers the results of Kormendy & Ho (2013) for the $M_{BH}-\sigma$ and $M_{BH}-M_{Bu}$ correlations in terms of coefficients and intrinsic scatter within the errors.² This remains true when we repeat the fits using our estimated covariance matrix (Tables 3 and 7), see the results quoted in the fifth and

sixth row of Table 13. Finally, using our bulge masses and errors (Table 1 and 4) for the KH45 sample, we get the results listed in the seventh and eighth row of Table 13. The coefficients agree at the 1- σ level, but the estimate of the measured and intrinsic scatter for the $M_{BH}-M_{Bu}$ correlation is larger.

Table 14 reports the results of the bivariate analysis on the same datasets. The first row shows that the $M_{BH}-M_{Bu}-\sigma$ relation is well established when using the data and errors of Kormendy & Ho (2013). The intrinsic and measured scatter are just 0.26 dex, the values of $P(\beta \neq 0)$, $\Delta cAIC$ and $RP = \exp(\Delta cAIC/2)$ all demonstrate the existence of the bivariate correlation. When we consider the Tables 3 and 7, we find results similar to the ones discussed above. The evidence for the $M_{BH}-M_{Bu}-\sigma$, $M_{BH}-\sigma-\rho_h$ and $M_{BH}-\sigma-r_h$ correlations is strong, while the $M_{BH}-M_{Bu}-\rho_h$ and $M_{BH}-M_{Bu}-r_h$ are only marginally detected (second to sixth row of Table 14). The same is true when we consider the bulge masses and errors (Table 1 and 4) for the KH45 sample (seventh to eleventh row of Table 14). Also in this case, the coefficients agree at the 1- σ levels, but the estimates of the measured and intrinsic scatter for the correlations involving M_{Bu} are larger.

These tests let us conclude that our large, combined SINFONI-plus-literature database establishes the Equations 24 to 28 convincingly for the entire population of galaxies where dynamical BH masses have been measured. The "best results" (i.e. lowest measured and intrinsic scatter) are obtained when the list of galaxies of Kormendy & Ho (2013) is considered and bulge masses derived from colour-based M/L_C are used.

To first order, these equations deliver a consistent, unifying description of the relations between black holes on the one hand and core and power-law ellipticals and classical bulges on the other.

The one- and two-dimensional correlations discussed above have substantial intrinsic scatter (≥ 0.3 dex), despite the increased number of structural parameters investigated. This is true even when we increase the errors on the bulge masses by 0.15 dex in quadrature or when we use the bulge masses derived from colors of Kormendy & Ho (2013). The correlations derived for the sample of core ellipticals tend to have the smallest intrinsic and measured scatter, broadly in agreement with the averaging effect described by Peng (2007).

²We note in passing that the zero-point errors quoted by Kormendy & Ho (2013) are not marginalized, but given at the best-fit value of the slope.

TABLE 13
ONE-DIMENSIONAL CORRELATIONS DERIVED USING THE KH45 SAMPLE.

Fit	Sample	a	da	ZP	dZP	ϵ	$d\epsilon$	rms
$M_{BH}-\sigma$	Eq. (5) Kormendy & Ho (2013)	4.41	0.3	-1.66	0.05	0.28	-	-
$M_{BH}-M_{Bu}$	Eq. (10) Kormendy & Ho (2013)	1.16	0.08	-4.07	0.10	0.29	-	-
$M_{BH}-\sigma$	Kormendy & Ho (2013)	4.342	0.323	-1.497	0.762	0.309	0.041	0.321
$M_{BH}-M_{Bu}$	Kormendy & Ho (2013)	1.153	0.088	-3.98	0.966	0.309	0.043	0.318
$M_{BH}-M_{Bu}^{0.5}\sigma^2$	Kormendy & Ho (2013)	1.19	0.073	-3.431	0.745	0.25	0.035	0.263
$M_{BH}-M_{Bu}\sigma^2$	Kormendy & Ho (2013)	0.796	0.05	-3.796	0.783	0.256	0.036	0.268
$M_{BH}-\sigma$	Table 3 and 7	4.404	0.348	-1.658	0.82	0.323	0.043	0.337
$M_{BH}-M_{Bu}$	Table 3 and 7	1.172	0.089	-4.186	0.98	0.289	0.046	0.321
$M_{BH}-M_{Bu}^{0.5}\sigma^2$	Table 3 and 7	1.204	0.073	-3.577	0.746	0.251	0.036	0.27
$M_{BH}-M_{Bu}\sigma^2$	Table 3 and 7	0.803	0.051	-3.898	0.806	0.256	0.038	0.273
$M_{BH}-\sigma$	Table 1 and 4	4.418	0.351	-1.693	0.826	0.325	0.045	0.337
$M_{BH}-M_{Bu}$	Table 1 and 4	0.952	0.095	-1.813	1.045	0.404	0.053	0.426
$M_{BH}-M_{Bu}^{0.5}\sigma^2$	Table 1 and 4	1.115	0.079	-2.687	0.813	0.296	0.042	0.324
$M_{BH}-M_{Bu}\sigma^2$	Table 1 and 4	0.715	0.056	-2.554	0.886	0.324	0.045	0.351

Column 1: Fit type; Column 2: Sample type, see text; Column 3 and 4: first variable slope of the correlation and its error; Column 5 and 6: zero-point of the correlation and its errors; Column 7 and 8: intrinsic scatter and its errors; Column 9: measured scatter.

TABLE 14
TWO-DIMENSIONAL CORRELATIONS DERIVED USING THE KH45 SAMPLE.

Fit	Sample	a	da	b	db	ZP	dZP	ϵ	$d\epsilon$	rms	$P(\beta \neq 0)$	$\Delta cAIC$	RP
$M_{BH}-M_{Bu}-\sigma$	Kormendy & Ho (2013)	0.621	0.164	2.275	0.614	-3.469	0.822	0.255	0.035	0.262	0.9997	-11.98	0.003
$M_{BH}-M_{Bu}-\sigma$	Table 3 and 7	0.701	0.188	2.027	0.716	-3.77	0.873	0.256	0.037	0.269	0.9995	-11.47	0.003
$M_{BH}-\sigma-\rho_h$	Table 3 and 7	4.02	0.338	-0.141	0.047	0.461	1.028	0.282	0.041	0.308	0.9965	-6.414	0.04
$M_{BH}-M_{Bu}-\rho_h$	Table 3 and 7	1.298	0.124	0.109	0.067	-6.508	1.807	0.294	0.046	0.312	0.9503	-0.251	0.882
$M_{BH}-\sigma-r_h$	Table 3 and 7	3.621	0.385	0.385	0.113	0	0.874	0.272	0.04	0.295	0.9993	-9.198	0.01
$M_{BH}-M_{Bu}-r_h$	Table 3 and 7	1.396	0.177	-0.318	0.202	-6.48	1.858	0.297	0.047	0.311	0.9471	-0.062	0.97
$M_{BH}-M_{Bu}-\sigma$	Table 1 and 4	0.345	0.136	3.157	0.594	-2.534	0.813	0.293	0.042	0.311	0.9951	-4.073	0.13
$M_{BH}-\sigma-\rho_h$	Table 1 and 4	3.91	0.331	-0.194	0.054	1.191	1.067	0.267	0.039	0.291	0.9996	-10.64	0.005
$M_{BH}-M_{Bu}-\rho_h$	Table 1 and 4	1.159	0.162	0.203	0.119	-5.841	2.681	0.415	0.056	0.41	0.958	-0.512	0.774
$M_{BH}-\sigma-r_h$	Table 1 and 4	3.616	0.386	0.386	0.116	0.011	0.876	0.275	0.04	0.295	0.999	-8.687	0.013
$M_{BH}-M_{Bu}-r_h$	Table 1 and 4	1.355	0.272	-0.599	0.362	-5.954	2.83	0.415	0.055	0.41	0.9546	-0.319	0.853

Column 1: Fit type; Column 2: Sample type, text; Column 3 and 4: first variable slope of the correlation and its error; Column 5 and 6: second variable slope of the correlation and its error; Column 7 and 8: zero-point of the correlation and its errors; Column 9 and 10: intrinsic scatter and its errors; Column 11: measured scatter; Column 12: probability of the bivariate correlation; Column 13 and 14: $\Delta cAIC$ value and $RP = exp(\Delta cAIC/2)$ (the relative probability of the mono- and bivariate solutions). They are computed matching the bivariate solutions of this table to the monovariate solutions of Table 13 of the respective datasets. The pairings are: $M_{BH}-M_{Bu}-\sigma$ with $M_{BH}-\sigma$, $M_{BH}-\sigma-\rho_h$ with $M_{BH}-\sigma$, $M_{BH}-M_{Bu}-\rho_h$ with $M_{BH}-M_{Bu}$, $M_{BH}-\sigma-r_h$ with $M_{BH}-\sigma$, $M_{BH}-M_{Bu}-r_h$ with $M_{BH}-M_{Bu}$, see Sect. 4.

We conclude by clarifying again the role of barred galaxies. In Table 11 and 12 we quote the results of fitting the CorePowerEClassnoBars sample, where we drop 16 barred galaxies contained in the CorePowerEClassPC sample. The coefficients and scatter of the one-dimensional correlations hardly change within the errors, in particular the ones of Eqs. 31 or 32. The same is true for the bivariate correlations, but their significance is slightly decreased. This effect is partly due to the reduced number of fitted galaxies. We conclude that the BH FP is not driven solely by barred galaxies, contrary to the suggestion of Graham (2008).

6. Discussion

6.1. Comparing $M_{Bu}^{a_{best}}\sigma^{b_{best}}$, $M_{Bu}^{0.5}\sigma^2$, $M_{Bu}\sigma^2$ and $M_{Bu}\sigma$

In Sect. 1 we reviewed the different physical interpretations proposed to explain the bivariate correlations with M_{BH} . Hopkins et al. (2007b,a) concluded that the bivariate correlations mirror the correlation between M_{BH} and $M_{Bu}^{0.5}\sigma^2$, which can be expected on simple physical grounds (see below). Feoli & Mele (2005), Aller & Richstone (2007) and Mancini & Feoli (2012) argued that the bulge's kinetic or gravitational energy $M_{Bu}\sigma^2$ of a galaxy sets its black hole mass. Finally, Soker & Meiron (2011) suggested the bulge's momentum $M_{Bu}\sigma$ as the key physical quantity.

We compare the three options $M_{Bu}^{0.5}\sigma^2$, $M_{Bu}\sigma^2$ and $M_{Bu}\sigma$ to our best fit solutions given in Eq. 26 and Table 14 (row 2 and 7) using the model comparison formalism. Similar to what is discussed in Sect. 4, we marginalize the posterior probability distribution $P(a, b, ZP, \epsilon)$ over the parameters ZP and ϵ and derive the equivalent of Eq. 11 as:

$$-2 \ln[P(a_{best}, b_{best})/P(a, b)] = (a - a_{best}, b - b_{best}) V^{-1} \begin{pmatrix} a - a_{best} \\ b - b_{best} \end{pmatrix}, \quad (29)$$

where

$$V = \begin{pmatrix} (\delta a_{best})^2 & < \delta a \delta b >_{best} \\ < \delta a \delta b >_{best} & (\delta b_{best})^2 \end{pmatrix}, \quad (30)$$

a_{best} , δa_{best} , b_{best} , δb_{best} are given in Tables 12 and 14 (as usual dropping the label *best*), and $< \delta a \delta b >_{best}$ (see Fig. 11) is listed in Table 15. The slopes a and b in Eq. 29 obey $a/b = 0.25, 0.5, 1$ for the cases $M_{Bu}^{0.5}\sigma^2$, $M_{Bu}\sigma^2$ and $M_{Bu}\sigma$, respectively. The values of a and b reported in Table 15 maximize Eq. 29

and are identical to the values quoted in Tables 12 and 13 for the $M_{Bu}^{0.5}\sigma^2$ and $M_{Bu}\sigma^2$ fits. Next, we compute $\Delta cAIC$ and $RP = \exp(\Delta cAIC/2)$. What are the correct values of k to be used in Eq. 10? Since a_{best} is different from zero, we can recast our best-fit solution $M_{BH} \sim (M_{Bu}^{a_{best}}\sigma^{b_{best}})$ as $M_{BH} \sim (M_{Bu}\sigma^{b_{best}/a_{best}})^{a_{best}}$ and argue that $k = 3$ for the four relations $M_{Bu}\sigma^{b_{best}/a_{best}}$, $M_{Bu}^{0.5}\sigma^2$, $M_{Bu}\sigma^2$ or $M_{Bu}\sigma$. The values of $RP^{(3)}$ given in Table 15 are computed following this reasoning. They stem directly from Eq. 29, since the terms involving k in Eq. 10 are all equal and cancel out. These relative probabilities assess which of the three models $M_{Bu}^{0.5}\sigma^2$, $M_{Bu}\sigma^2$ or $M_{Bu}\sigma$ is nearest to our best solution.

The values of $RP^{(4)}$ given in Table 15 assume instead that our best-fit solution $M_{BH} \sim (M_{Bu}^{a_{best}}\sigma^{b_{best}})$ has $k = 4$, while the $M_{Bu}^{0.5}\sigma^2$, $M_{Bu}\sigma^2$ or $M_{Bu}\sigma$ models have $k = 3$. They assess whether our 'complex' best-fit solution $M_{BH} \sim (M_{Bu}^{a_{best}}\sigma^{b_{best}})$ is really needed to describe the data, or whether the 'simpler' $M_{Bu}^{0.5}\sigma^2$, $M_{Bu}\sigma^2$ or $M_{Bu}\sigma$ models should be preferred.

If we use $RP^{(3)}$ to rank the $M_{Bu}^{0.5}\sigma^2$, $M_{Bu}\sigma^2$ or $M_{Bu}\sigma$ models with respect to $M_{Bu}\sigma^{b_{best}/a_{best}}$, we find that the $M_{Bu}^{0.5}\sigma^2$ model performs the best (i.e., it has the largest $RP^{(3)}$), when compared with our best fitting solution, whatever sample is considered (either our reference CorePowerEClassPC sample, or the KH45 sample with the color-based bulge masses, or the same sample with dynamical bulge masses). The $M_{Bu}\sigma$ model performs worst; when using dynamical bulge masses we get $RP^{(3)} < 10^{-4}$ and only for the KH45 sample with bulge masses derived from M/L_C $RP^{(3)}$ is not too low (0.33).

If we consider $RP^{(4)}$, we conclude that the model $M_{Bu}^{0.5}\sigma^2$ provides a description of the data as good as the one of our best fitting solution, with $RP^{(4)} = 0.41$ for our reference CorePowerEClassPC sample and $RP^{(4)} = 0.88$ for the KH45 sample with dynamical bulge masses. The model $M_{Bu}^{0.5}\sigma^2$ is statistically preferred with respect to our best fitting solution when the KH45 sample with color-based bulge masses is considered ($RP^{(4)} = 2.89$). For this sample the same applies to the $M_{Bu}\sigma^2$ model ($RP^{(4)} = 2.82$), while the $M_{Bu}\sigma$ model is statistically indistinguishable ($RP^{(4)} = 1.1$) from the bivariate best-fit model. This conclusion is partially driven by the smaller size (45 versus 77 galaxies) and larger errors (see Sect. 3) of the KP45 sample, compared to our reference CorePowerEClassPC sample. But it could also re-

flect the underlying physical difference between color-based and dynamical bulge masses.

In the following we give a closer look to the models that compare best to our best fitting bivariate solution, the $M_{Bu}^{0.5}\sigma^2$ and $M_{Bu}\sigma^2$ model.

Table 11 presents the results of fitting the relation $\log M_{BH} = a \log(M_{Bu}^{0.5}\sigma^2) + ZP$. For the sample without pseudo bulges we find:

$$\log M_{BH} = (1.09 \pm 0.06) \log(M_{Bu}^{0.5}\sigma^2) - (2.54 \pm 0.64), \quad (31)$$

with intrinsic and measured scatter slightly lower than the M_{BH} - σ relation, and slightly larger than the ones given by Eqs. 19, 20 or 21. Fig. 18 (left) shows the relative correlation plot. We recognize the features discussed above: core Es are slightly shifted upwards, while pseudo bulges have systematically lower black hole masses than predicted. This confirms that the picture presented by Hopkins et al. (2007b,a) is valid for ellipticals and classical bulges, but breaks down for pseudo bulges. The intrinsic scatter is reduced to just 0.25 dex, when the KH45 sample with color-based bulge masses is considered.

Fig. 18 (right) shows the correlations between the black hole mass and the kinetic energy of the bulge $M_{Bu}\sigma^2$ put forward by Feoli & Mele (2005), Aller & Richstone (2007), Feoli & Mancini (2009), and Mancini & Feoli (2012). Table 11 also presents the results of fitting the relation $\log M_{BH} = a \log(M_{Bu}\sigma^2) + ZP$. For the sample without pseudo bulges we find:

$$\log M_{BH} = (0.67 \pm 0.04) \log(M_{Bu}\sigma^2) - (1.96 \pm 0.65). \quad (32)$$

This is similar to the dependences found by Aller & Richstone (2007), Hopkins et al. (2007b) and Mancini & Feoli (2012). The correlation is strong with intrinsic scatter slightly better than the one of the M_{BH} - σ relation and slightly larger than the one given by Eq. 31. In both cases the differences are not statistically significant. When the KH45 sample with color-based bulge masses is considered, the intrinsic scatter is reduced to just 0.256 dex. Again, pseudo bulges are offset towards lower black hole masses.

To conclude, our analysis shows that the model $M_{Bu}^{0.5}\sigma^2$ is slightly preferred to explain our bivariate correlations, especially when dynamically determined bulge masses are considered. However, the bulge kinetic energy $M_{Bu}\sigma^2$ produces correlations with black hole masses with statistically equivalent intrinsic and measured scatter. The bulge momentum $M_{Bu}\sigma$ is

highly disfavoured in the case of dynamically determined bulge masses.

6.2. A simple interpretation framework

As discussed above, Fig. 18 points to some sort of gravitationally induced equilibrium configuration, coupled with a feedback mechanism, which lies behind our empirical findings. Indeed, one could naively expect a correlation between $M_{Bu}\sigma^2$ and M_{BH} as a consequence of an energy balance during the simultaneous growth of bulges and black holes. Why a correlation between $M_{Bu}^{0.5}\sigma^2$ and M_{BH} should exist is less obvious. Hopkins et al. (2007b,a) argue that one needs to equate the momentum of the galactic outflow $\dot{p} \sim M_{Bu}\sigma$ to the injection of momentum $\dot{p} \sim L_{Edd}/c \sim M_{BH}$ during the dynamical time $t_{soi}^{dyn} \sim R_{soi}/\sigma$ near the black hole sphere of influence with radius $R_{soi} \sim GM_{BH}/\sigma^2$. This gives $\dot{p} \times t_{soi}^{dyn} \sim M_{BH}^2/\sigma^3 \sim M_{Bu}\sigma$, or $M_{BH} \sim M_{Bu}^{0.5}\sigma^2$. Clearly this argument applies only if the Eddington luminosity L_{Edd} is high enough. This is probably the case during 'wet' mergers of gas-rich galaxies, or during violent instabilities in high-density, high redshift disks, where large amounts of gas could be funnelled to the center and accreted quickly while simultaneously forming a classical bulge (Bournaud et al. 2014; Menci et al. 2014). However, this mechanism should not work in the case of 'dry' mergers, when gas-poor galaxies coalesce, or for pseudo bulges formed by secular evolution of disks, where only small amounts of gas can flow towards the center at any time (due to, for example, bar torques). Only pseudo bulges with particularly high densities could be expected to have generated in the past with accretion luminosities approaching the Eddington limit. In the following we summarize these statements in a simple quantitative way.

Dry mergers are mergers of (elliptical and S0) galaxies without cold gas and therefore are dissipationless. Equal mass dry mergers preserve the velocity dispersion σ ($\sigma^f = \sigma^i$, where i and f indicate the initial and final state) of the resulting merged galaxy, double the size ($r_h^f/r_h^i = 2$) and reduce the average density by 1/4 ($\rho_h^f/\rho_h^i = 1/4$). They increase the central black hole masses through black hole merging by a factor 2 (if both merging galaxies obey the M_{BH} - M_{Bu} relation before the merging), see Naab et al. (2009). These effects are indicated by the red arrows in the Figures 12 to 18. Dry mergers are also responsible for the formation of the cores of core ellipticals

Table 15: Comparison of the $M_{Bu}^{a_{best}}\sigma^{b_{best}}$, $M_{Bu}^{0.5}\sigma^2$, $M_{Bu}\sigma^2$ and $M_{Bu}\sigma$ models.

Model	a	b	Subsample	$\langle \delta a \delta b \rangle_{best}$	$RP^{(3)}$	$\Delta cAIC$	$RP^{(4)}$
$M_{Bu}^{0.5}\sigma^2$	0.547	2.186	CorePowerEClassPC	-0.041	0.14	-1.78	0.41
	0.602	2.408	KH45 sample from Tables 3 and 7	-0.123	0.86	2.12	2.89
	0.558	2.230	as above, but from Tables 1 and 4	-0.068	0.26	-0.25	0.88
$M_{Bu}\sigma^2$	0.673	1.346	CorePowerEClassPC	-0.041	0.002	-10.6	0.005
	0.803	1.606	KH45 sample from Tables 3 and 7	-0.123	0.84	2.07	2.82
	0.715	1.430	as above, but from Tables 1 and 4	-0.068	0.013	-6.31	0.04
$M_{Bu}\sigma$	0.757	0.757	CorePowerEClassPC	-0.041	1.5×10^{-5}	-19.9	4.7×10^{-5}
	0.965	0.965	KH45 sample from Tables 3 and 7	-0.123	0.33	0.2	1.1
	0.825	0.825	as above, but from Tables 1 and 4	-0.068	4×10^{-4}	-13.2	1.4×10^{-3}

Column 1: tested model; Column 2 and 3: best-fitting values of a and b ; Column 4: dataset used; Column 5: see Eq. 30; Column 6: the probabilities relative to the best-fitting $M_{BH}-M_{Bu}-\sigma$ correlation, see Sect. 6.1; Column 7: values of $\Delta cAIC$ computed matching the models of this table to the $M_{Bu}^{a_{best}}\sigma^{b_{best}}$ model of the corresponding dataset, see Tables 12 and 14; Column 8: $RP^{(4)} = \exp(\Delta cAIC/2)$ gives the probability of the models of this table relative to the $M_{Bu}^{a_{best}}\sigma^{b_{best}}$ model of the corresponding dataset.

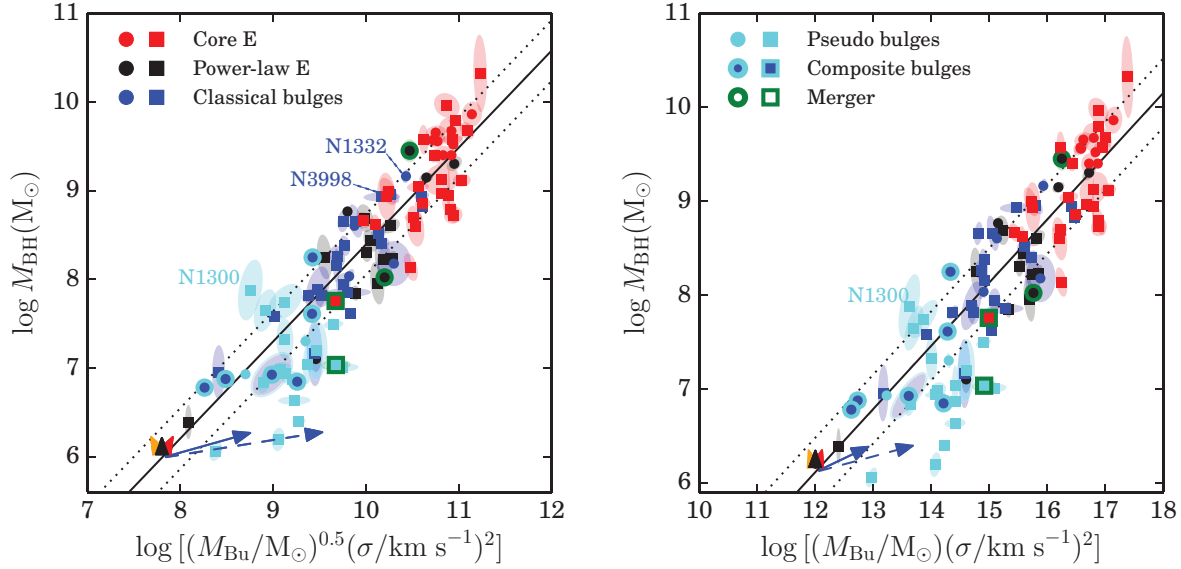


Fig. 18.— The correlation between $\log M_{BH}$ and $\log M_{Bu}^{0.5}\sigma^2$ (left) and between $\log M_{BH}$ and $\log M_{Bu}\sigma^2$ (right). The corresponding best-fit relations for the CorePowerEClassPC sample are shown using full lines, with the dotted lines showing estimated intrinsic scatter. The ellipses show the 1σ errors. Colors, arrows and point types as in Fig. 14.

through the binary black hole scouring mechanism. The absence of gas implies that the central cusp cannot be reformed after the merging event.

Several minor dry mergers (orange arrows in the Figures 12 to 18) can enlarge sizes and lower average densities even more (for a sequence of minor mergers doubling the mass, the size is increased by 4 and the density is decreased by $1/32$), while keeping M_{BH}/M_{Bu} ratio constant and reducing σ by a factor $1/2^{0.5}$ (Naab et al. 2009). These combined effects can qualitatively explain the position of the most massive, largest, and least dense core ellipticals in the Figures 12, 14, 16 and 18 and the “saturation effect” discussed in Kormendy & Bender (2013). These objects appear to have BH masses ≈ 0.3 dex larger than the rest of the CorePowerEClassPC sample and could well be the result of dry merging of pre-existing power-law or core ellipticals. Moreover, the intrinsic and measured scatter of the correlations defined by core ellipticals alone tend to be the smallest, in line with the averaging effect expectations discussed by Peng (2007).

Wet mergers are mergers of (disk) galaxies with cold gas. Measuring M_{BH} in local galaxies known to be recent mergers of disk galaxies allows one to sketch what could be the evolution with time of these class of objects (Kormendy & Ho 2013). If the merging progenitors follow a black hole scaling relation and the black hole(s) do not accrete substantial amounts of gas during the merging process, the merger remnant would now fall below the relation by a factor corresponding to the mean bulge-to-total (B/T) ratio of the progenitors. This is indicated by the blue arrows in the Figures 12 to 18 for an equal mass merger of spirals with $B/T = 0.2$ and a factor 3 increase in bulge size. The velocity dispersion will change according to the Virial Theorem $r_h^f \sigma^f{}^2 = 2r_h^i \sigma^i{}^2 / (B/T)$, while the scale length of the bulge will change by a factor $r_h^f / r_h^i = k$. Naab & Trujillo (2006) argue that k can vary between 0.5 and 3 in disk plus bulge mergers without gas. As a consequence, bulge masses and velocity dispersions will generally increase, while scale radii or densities might either increase or decrease. Therefore we could expect recent mergers to lie generically below the black hole correlations. This is indeed what we see for NGC 1316, NGC 2960, NGC 5018, and NGC 5128 (plotted in green in the Figures 12 to 18), all rather young, gas-rich, merger remnants. NGC 3923 is likely to be (the late phase of) a merger between an existing elliptical with a low velocity dispersion dwarf galaxy. In general, the distribution of

power-law ellipticals and classical bulges in the Figures 12 to 18 is better explained by the full blue arrow, i.e. when the scale length of the bulge resulting from the merger is larger than the original value.

Finally, the BH can increase its mass by accretion. This process has been also proposed for changing sizes and velocity dispersions of galaxies through its feedback (Fan et al. 2008), but it fails to explain the redshift evolution of sizes of early-type galaxies (Saglia et al. 2010). For simplicity we therefore neglect this possible effect on sizes and densities and just mark the importance of BH accretion in itself. The black arrows in the Figs. 13 to 18 indicate accretion that doubles the mass of the BH. Table 16 summarizes the mechanisms discussed above. Ultimately the feedback produced during the accretion event will set the galaxy back to the black hole correlations as discussed above.

The distribution of power-law ellipticals and classical bulges in Figures 13, 14 and 16 can be seen as the result of the combined effects of wet mergers, black hole accretion and feedback mechanisms. The exact steepness of the blue arrows depends on B/T and the relative amount of (dissipative) gas available. Some gas will be accreted on the BH. Some gas will generate new stars, increasing the density of the newly formed bulge and possibly forming a central power-law cusp.

As the average gas fraction of galaxies decreases with cosmic time, it is plausible that galaxies that merged earlier had a better chance to grow their black holes in lock-step (or even over-grow) with the spheroid than is possible for present-day mergers. Thus, we would expect the M_{BH}/M_{Bu} ratio to increase with increasing redshift (Sijacki et al. 2015). This is indeed observed in various samples of quasars at $z > 2$ (see review in Kormendy & Ho 2013 and references therein).

We can further speculate that those objects that were assembled early and did not undergo late major mergers today harbour the most massive black holes for a given bulge mass. These objects should have formed from very gas-rich material that allowed their black holes to grow efficiently. They also should have high stellar densities because earlier formation implies higher dark matter and gas densities (Thomas et al. 2009). As dry mergers decrease the mean stellar density, a high density today also implies that the objects did not undergo such events more recently. Examples for such objects could be very compact bulges in old S0s or early-type spirals, where the existence of a substantial disk indicates the lack of late major mergers.

Table 16: The fractional changes in M_{BH} , M_{Bu} , σ , r_h , ρ_h expected after a major or a minor ‘dry’ merger that double the galaxy and BH mass, a ‘wet’ merger with initial bulge-to-total ratio B/T and final-to-initial bulge-scales ratios k , and gas accretion on the BH.

Process	M_{BH}^f/M_{BH}^i	M_{Bu}^f/M_{Bu}^i	r_h^f/r_h^i	ρ_h^f/ρ_h^i	σ^f/σ_i
Major dry merger	2	2	2	1/4	1
Minor dry merger	2	2	4	1/32	$1/2^{0.5}$
Wet merger	2	$\frac{2}{(B/T)}$	κ	$\frac{2}{k^3(B/T)}$	$\left[\frac{2}{k(B/T)}\right]^{0.5}$
BH Accretion	2	1	1	1	1

In fact, some of the most compact bulges known (we include NGC 1332, NGC 3998, and NGC 4486b) do harbour unusually large black holes for their bulge mass (see Fig. 13). M32 (NGC 221) is also extremely dense, but with a normal black hole for its bulge mass. Except for NGC 4486b, these galaxies are not particularly deviant when the M_{BH} - σ relation is considered, an indication that the velocity dispersion (through the M_{BH} - σ relation) is a more robust black hole mass predictor than the bulge mass (through the M_{BH} - M_{Bu} relation).

Pseudo bulges with spherical densities $\rho_h \approx 10^{10} M_\odot/\text{kpc}^3$ such as NGC 4501 (where we detect molecular gas in non-circular motions, see Mazzei et al. 2013, 2014) or NGC 3227 (where an active nucleus is present and a recent episode of star formation took place, see Davies et al. 2006) have BHs with masses similar to those predicted by the M_{BH} - σ or the M_{BH} - M_{Bu} relations of ellipticals and classical bulges. Pseudo bulges with lower densities have smaller black holes than the classical-bulges prediction. Therefore, the growth of black holes in galaxies that did not undergo mergers, and therefore do not have a classical bulge, follows a path decoupled from the rest of the galaxy and set by the amount of gas that secular processes (such as bars) manage to funnel towards the galaxy centers. The resulting black hole masses are much smaller than the ones measured in early-type galaxies or classical bulges. We speculate that only when the densities involved are above a certain threshold are pseudo bulges able to fuel the black holes efficiently enough to approach the feedback mechanism (see above) that sets M_{BH}/M_{Bu} in classical bulges. The exact value of the density threshold is, however, uncertain by an order of magnitude, as it depends on the unknown geometry of pseudo bulges.

Finally, we also find composite systems where both a classical and a pseudo bulge co-exist. In the Figures 13, 14 and 16 we plot the position of NGC 1068,

NGC 2787, NGC 3368, NGC 3489, NGC 4371 and NGC 4699, all galaxies with composite bulges, using the mass of their small classical bulges. These high-density components form the high density, small size end of the power law and classical bulge bivariate correlations. We speculate that they formed together with their BH at high redshifts. Possibly *every* pseudo bulge has a small classical component at its center: Erwin et al. (2015) argue that it is not (yet) possible to present a clear case of a pure pseudo bulge where the presence of a small classical component can be excluded without doubt.

As noted in Section 5, all our one- and two-dimensional correlations have sizeable intrinsic scatter. The smallest intrinsic scatter (0.26 dex) is derived for the KH45 sample, using mass-to-light ratios derived from colors. On one hand, this could indicate that BH masses correlate best with the baryonic mass of classical bulges. On the other hand, having now explored the influence of all galaxy structure parameters and their errors, we have to conclude that the remaining factor ≈ 2 uncertainty in the black hole mass must stem from the unknown details of the accretion and feedback mechanisms.

7. Conclusions

We produced a merged SINFONI-plus-literature database of BH masses for 97 galaxies. For this sample we computed dynamical bulge mass estimates M_{Bu} , and determined the bulge spherical half-luminosity radius r_h and averaged spherical density ρ_h within r_h , collecting bulge-plus-disk decompositions from the literature or performing them ourselves (for 16 galaxies). We confirm that there is an almost linear relation between BH mass and the mass of the classical bulge of a galaxy. The quadratic relation suggested by Graham & Scott (2013) for ‘Sersic galaxies’ is driven by the inclusion of pseudo bulges and possibly uncertain

bulge masses.

Densities and sizes of classical bulges turn out to be important. We showed that BH masses correlate directly with both densities and sizes, although with larger scatter than the more usual $M_{BH}-\sigma$ or $M_{BH}-M_{Bu}$ relations. We established significant bivariate correlations involving σ , $M_{BH}-\sigma-\rho_h$, $M_{BH}-\sigma-r_h$, and $M_{BH}-\sigma-M_{Bu}$, valid for all classical bulges (core and power-law ellipticals, classical bulges of disk galaxies) with low intrinsic (≤ 0.34 dex) and measured (≤ 0.37 dex) scatter. Two further bivariate correlations involving $M_{Bu} - M_{BH}-M_{Bu}-\rho_h$ and $M_{BH}-M_{Bu}-r_h$ - are also robustly detected, but with larger intrinsic (≈ 0.43 dex) and measured (≈ 0.44 dex) scatter and with core elliptical galaxies slightly offset. The five bivariate correlations are robustly detected also when the KH45 sample is considered. For this sample, with bulge masses scaled from M/Ls derived from colors, the estimated intrinsic scatter is as low as 0.26 dex. Contrary to the suggestion of Graham (2008), none of these bivariate correlations are driven by the inclusion of barred galaxies. The relations are point to a link between black hole mass and $M_{Bu}^{0.5}\sigma^2$, as proposed by Hopkins et al. (2007b,a), or the bulge kinetic energy $M_{Bu}\sigma^2$, as first suggested by Feoli & Mele (2005). In contrast, pseudo bulges have systematically lower black hole masses, but approach the predictions of all the above relations at (spherical) densities $\rho_h \geq 10^{10} M_\odot/kpc^3$ or scale lengths $r_h \leq 1$ kpc. These thresholds are rather uncertain, because we do not know the true geometry of pseudo bulges.

High densities and small sizes imply a large baryonic concentration near the centre and make very efficient mass accretion onto the black hole likely. Classical bulge densities/sizes, in turn, are set mainly by two factors: (1) the formation redshift - earlier formation implies higher halo and gas densities - and (2) the merging history - gas poor mergers reduce the density and increase the size in each merger generation. (1) could explain why compact classical bulges of S0 galaxies have the highest BH masses for their bulge mass; (2) implies that slow-rotator, core ellipticals of a given mass have slightly more massive black holes the lower their average density is or the larger their size is. The averaging effect of a series of gas-free mergers (Peng 2007) would also make plausible why the correlations derived for the sample of core ellipticals only tend to have the smallest intrinsic and measured scatter. Power-law, fast-rotator early-types and classical bulges are the results of dissipational, gas-rich mergers

of disk-dominated progenitors. The feedback mechanism triggered by black hole accretion, coupled with the gravitationally induced virial equilibrium, creates the correlations between black hole mass and galaxy structural parameters. In this case at a given M_{Bu} or σ objects with larger average densities or smaller sizes have larger M_{BH} . The bivariate correlations, however, are not as tight as the mass Fundamental Plane of early-type galaxies (e.g., Hyde & Bernardi 2009). The tightest relation we derive is the $M_{BH}-M_{Bu}-\sigma$ for the KH45 sample, where the estimated intrinsic scatter is 0.26 dex. The unknown details of the black hole accretion physics and feedback mechanisms are probably responsible for this sizeable intrinsic and measured scatter.

Disk galaxies that do not experience major mergers might develop a pseudo bulge through secular instabilities such as bars. These may drive gas towards the center and feed the central black hole. However, the lack of correlation between M_{BH} and the structural parameters of pseudo bulges shows that no efficient consistent feedback mechanism is at work in these objects. Only pseudo bulges with extremely high densities/small sizes manage to form black holes with masses approaching those of classical-bulges.

Acknowledgements

We thank the first referee of the paper, John Kormendy, for a careful proof of Table 1; we thank the statistics editor of ApJ for his valuable suggestions on model comparison; we thank the second anonymous referee for comments that helped us improving the presentation of the results. MO acknowledges support by the Trans-regional Collaborative Research Centre TR22 “The Dark Universe” of the Deutsche Forschungsgemeinschaft (DFG) and the DFG Cluster of Excellence “Origin and Structure of the Universe”. SPR was supported by the DFG Cluster of Excellence “Origin and Structure of the Universe”. PE was supported by the DFG Priority Programme 1177 “Galaxy Evolution”. Funding for the creation and distribution of the SDSS Archive has been provided by the Alfred P. Sloan Foundation, the Participating Institutions, the National Aeronautics and Space Administration, the National Science Foundation, the US Department of Energy, the Japanese Monbukagakusho and the Max Planck Society. The SDSS website is <http://www.sdss.org/>. The SDSS is managed by the Astrophysical Research Consortium

(ARC) for the Participating Institutions. The Participating Institutions are The University of Chicago, Fermilab, the Institute for Advanced Study, the Japan Participation Group, The Johns Hopkins University, the Korean Scientist Group, Los Alamos National Laboratory, the Max-Planck-Institute for Astronomy (MPIA), the Max-Planck-Institute for Astrophysics (MPA), New Mexico State University, University of Pittsburgh, University of Portsmouth, Princeton University, the United States Naval Observatory and the University of Washington. This research made use of the of the NASA/IPAC Infrared Science Archive and the NASA/IPAC Extragalactic Database (NED) which are operated by the Jet Propulsion Laboratory, California Institute of Technology, under contract with the National Aeronautics and Space Administration. It also made use of the Lyon-Meudon Extragalactic Database (LEDa; part of HyperLeda at <http://leda.univ-lyon1.fr/>).

REFERENCES

- Akaike, H. 1973, in 2nd International Symposium on Information Theory, ed. B. Petrov & F. Csaki, 267–281
- Aller, M. C. & Richstone, D. O. 2007, *ApJ*, 665, 120
- Arnold, J. A., Romanowsky, A. J., Brodie, J. P., Forbes, D. A., Strader, J., Spitler, L. R., Foster, C., Blom, C., Kartha, S. S., Pastorello, N., Pota, V., Usher, C., & Woodley, K. A. 2014, *ApJ*, 791, 80
- Athanassoula, E. & Beaton, R. L. 2006, *MNRAS*, 370, 1499
- Atkinson, J. W., Collett, J. L., Marconi, A., Axon, D. J., Alonso-Herrero, A., Batcheldor, D., Binney, J. J., Capetti, A., Carollo, C. M., Dressel, L., Ford, H., Gerssen, J., Hughes, M. A., Macchetto, D., Maciejewski, W., Merrifield, M. R., Scarlata, C., Sparks, W., Stiavelli, M., Tsvetanov, Z., & van der Marel, R. P. 2005, *MNRAS*, 359, 504
- Barway, S. & Kembhavi, A. 2007, *ApJ*, 662, L67
- Batcheldor, D., Axon, D., Merritt, D., Hughes, M. A., Marconi, A., Binney, J., Capetti, A., Merrifield, M., Scarlata, C., & Sparks, W. 2005, *ApJS*, 160, 76
- Beifiori, A. 2010, PhD thesis, University of Padova
- Beifiori, A., Courteau, S., Corsini, E. M., & Zhu, Y. 2012, *MNRAS*, 419, 2497
- Beifiori, A., Sarzi, M., Corsini, E. M., Dalla Bontà, E., Pizzella, A., Coccato, L., & Bertola, F. 2009, *ApJ*, 692, 856
- Bender, R. 1988, *A&A*, 193, L7
- Bender, R., Rusli, S. P., Thomas, J., Saglia, R. P., Erwin, P., Fabricius, M., & Nowak, N. 2016, *ApJ*, in prep.
- Bender, R., Saglia, R. P., & Gerhard, O. E. 1994, *MNRAS*, 269, 785
- Bertola, F., Cinzano, P., Corsini, E. M., Rix, H.-W., & Zeilinger, W. W. 1995, *ApJ*, 448, L13
- Bettoni, D. & Galletta, G. 1997, *A&AS*, 124, 61
- Bonnet, H., Ströbele, S., Biancat-Marchet, F., Brynnel, J., Conzelmann, R. D., Delabre, B., Donaldson, R., Farinato, J., Fedrigo, E., Hubin, N. N., Kasper, M. E., & Kissler-Patig, M. 2003, in Society of Photo-Optical Instrumentation Engineers (SPIE) Conference Series, Vol. 4839, Adaptive Optical System Technologies II, ed. P. L. Wizinowich & D. Bonaccini, 329–343
- Bournaud, F., Perret, V., Renaud, F., Dekel, A., Elmegreen, B. G., Elmegreen, D. M., Teyssier, R., Amram, P., Daddi, E., Duc, P.-A., Elbaz, D., Epinat, B., Gabor, J. M., Juneau, S., Kraljic, K., & Le Floch, E. 2014, *ApJ*, 780, 57
- Bower, G. A., Green, R. F., Bender, R., Gebhardt, K., Lauer, T. R., Magorrian, J., Richstone, D. O., Danks, A., Gull, T., Hutchings, J., Joseph, C., Kaiser, M. E., Weistrop, D., Woodgate, B., Nelson, C., & Malumuth, E. M. 2001, *ApJ*, 550, 75
- Cappellari, M., Bacon, R., Bureau, M., et al. 2006, *MNRAS*, 366, 1126
- Cappellari, M., Bacon, R., Davies, R. L., de Zeeuw, P. T., Emsellem, E., Falcón-Barroso, J., Krajnović, D., Kuntschner, H., McDermid, R. M., Peletier, R. F., Sarzi, M., van den Bosch, R. C. E., & van de Ven, G. 2008, in IAU Symposium, Vol. 245, IAU Symposium, ed. M. Bureau, E. Athanassoula, & B. Barbuy, 215–218
- Cappellari, M., Neumayer, N., Reunanen, J., van der Werf, P. P., de Zeeuw, P. T., & Rix, H.-W. 2009, *MNRAS*, 394, 660

- Cappellari, M., Scott, N., Alatalo, K., Blitz, L., Bois, M., Bournaud, F., Bureau, M., Crocker, A. F., Davies, R. L., Davis, T. A., de Zeeuw, P. T., Duc, P.-A., Emsellem, E., Khochfar, S., Krajnović, D., Kuntschner, H., McDermid, R. M., Morganti, R., Naab, T., Oosterloo, T., Sarzi, M., Serra, P., Weijmans, A.-M., & Young, L. M. 2013, *MNRAS*, 432, 1709
- Dalla Bontà, E., Ferrarese, L., Corsini, E. M., Miralda-Escudé, J., Coccato, L., Sarzi, M., Pizzella, A., & Beifiori, A. 2009, *ApJ*, 690, 537
- Davies, R. I., Thomas, J., Genzel, R., Müller Sánchez, F., Tacconi, L. J., Sternberg, A., Eisenhauer, F., Abuter, R., Saglia, R., & Bender, R. 2006, *ApJ*, 646, 754
- Davis, T. A., Bureau, M., Cappellari, M., Sarzi, M., & Blitz, L. 2013, *Nature*, 494, 328
- de Francesco, G., Capetti, A., & Marconi, A. 2006, *A&A*, 460, 439
- Dressler, A. 1989, in *IAU Symposium*, Vol. 134, *Active Galactic Nuclei*, ed. D. E. Osterbrock & J. S. Miller, 217
- Ebisuzaki, T., Makino, J., & Okumura, S. K. 1991, *Nature*, 354, 212
- Eisenhauer, F., Abuter, R., Bickert, K., Biancat-Marchet, F., Bonnet, H., Brynnel, J., Conzelmann, R. D., Delabre, B., Donaldson, R., Farinato, J., Fedrigo, E., Genzel, R., Hubin, N. N., Iserlohe, C., Kasper, M. E., Kissler-Patig, M., Monnet, G. J., Roehrle, C., Schreiber, J., Stroebele, S., Tecza, M., Thatte, N. A., & Weisz, H. 2003, in *Society of Photo-Optical Instrumentation Engineers (SPIE) Conference Series*, Vol. 4841, *Instrument Design and Performance for Optical/Infrared Ground-based Telescopes*, ed. M. Iye & A. F. M. Moorwood, 1548–1561
- Emsellem, E. 2013, *MNRAS*, 433, 1862
- Emsellem, E., Cappellari, M., Krajnović, D., van de Ven, G., Bacon, R., Bureau, M., Davies, R. L., de Zeeuw, P. T., Falcón-Barroso, J., Kuntschner, H., McDermid, R., Peletier, R. F., & Sarzi, M. 2007, *MNRAS*, 379, 401
- Emsellem, E., Cappellari, M., Peletier, R. F., McDermid, R. M., Bacon, R., Bureau, M., Copin, Y., Davies, R. L., Krajnović, D., Kuntschner, H., Miller, B. W., & de Zeeuw, P. T. 2004, *MNRAS*, 352, 721
- Emsellem, E., Fathi, K., Wozniak, H., Ferruit, P., Mundell, C. G., & Schinnerer, E. 2006, *MNRAS*, 365, 367
- Erwin, P. 2004, *A&A*, 415, 941
- . 2005, *MNRAS*, 364, 283
- . 2015, *ApJ*, 799, 226
- Erwin, P. & Debattista, V. P. 2013, *MNRAS*, 431, 3060
- Erwin, P., Pohlen, M., & Beckman, J. E. 2008, *AJ*, 135, 20
- Erwin, P., Saglia, R. P., Fabricius, M., Thomas, J., Nowak, N., Rusli, S., Bender, R., Vega Beltrán, J. C., & Beckman, J. E. 2015, *MNRAS*, 446, 4039
- Erwin, P. & Sparke, L. S. 2003, *ApJS*, 146, 299
- Erwin, P., Thomas, J., Bender, R., Rusli, S. P., Saglia, R. P., Fabricius, M., & Nowak, N. 2016, *ApJ*, in prep.
- Erwin, P., Vega Beltrán, J. C., Graham, A. W., & Beckman, J. E. 2003, *ApJ*, 597, 929
- Faber, S. M., Tremaine, S., Ajhar, E. A., Byun, Y.-I., Dressler, A., Gebhardt, K., Grillmair, C., Kormendy, J., Lauer, T. R., & Richstone, D. 1997, *AJ*, 114, 1771
- Fabricius, M. H., Saglia, R. P., Fisher, D. B., Drory, N., Bender, R., & Hopp, U. 2012, *ApJ*, 754, 67
- Fan, L., Lapi, A., De Zotti, G., & Danese, L. 2008, *ApJ*, 689, L101
- Feoli, A. & Mancini, L. 2009, *ApJ*, 703, 1502
- Feoli, A. & Mele, D. 2005, *International Journal of Modern Physics D*, 14, 1861
- Ferrarese, L. & Merritt, D. 2000, *ApJ*, 539, L9
- Fisher, D. B. & Drory, N. 2008, *AJ*, 136, 773
- . 2010, *ApJ*, 716, 942
- Gadotti, D. A. 2008, *MNRAS*, 384, 420

- Gebhardt, K., Bender, R., Bower, G., Dressler, A., Faber, S. M., Filippenko, A. V., Green, R., Grillmair, C., Ho, L. C., Kormendy, J., Lauer, T. R., Magorrian, J., Pinkney, J., Richstone, D., & Tremaine, S. 2000, *ApJ*, 539, L13
- Gebhardt, K., Richstone, D., Tremaine, S., Lauer, T. R., Bender, R., Bower, G., Dressler, A., Faber, S. M., Filippenko, A. V., Green, R., Grillmair, C., Ho, L. C., Kormendy, J., Magorrian, J., & Pinkney, J. 2003, *ApJ*, 583, 92
- Gebhardt, K. & Thomas, J. 2009, *ApJ*, 700, 1690
- Goudfrooij, P., Hansen, L., Jorgensen, H. E., Norgaard-Nielsen, H. U., de Jong, T., & van den Hoek, L. B. 1994, *A&AS*, 104, 179
- Graham, A. W. 2008, *ApJ*, 680, 143
- Graham, A. W., Erwin, P., Caon, N., & Trujillo, I. 2001, *ApJ*, 563, L11
- Graham, A. W. & Scott, N. 2013, *ApJ*, 764, 151
- Greene, J. E., Peng, C. Y., Kim, M., Kuo, C.-Y., Braatz, J. A., Violette Impellizzeri, C. M., Condon, J. J., Lo, K. Y., Henkel, C., & Reid, M. J. 2010, *ApJ*, 721, 26
- Greenhill, L. J., Moran, J. M., & Herrnstein, J. R. 1997, *ApJ*, 481, L23
- Gültekin, K., Richstone, D. O., Gebhardt, K., Lauer, T. R., Pinkney, J., Aller, M. C., Bender, R., Dressler, A., Faber, S. M., Filippenko, A. V., Green, R., Ho, L. C., Kormendy, J., & Siopis, C. 2009a, *ApJ*, 695, 1577
- Gültekin, K., Richstone, D. O., Gebhardt, K., Lauer, T. R., Tremaine, S., Aller, M. C., Bender, R., Dressler, A., Faber, S. M., Filippenko, A. V., Green, R., Ho, L. C., Kormendy, J., Magorrian, J., Pinkney, J., & Siopis, C. 2009b, *ApJ*, 698, 198
- Gutiérrez, L., Erwin, P., Aladro, R., & Beckman, J. E. 2011, *AJ*, 142, 145
- Häring, N. & Rix, H.-W. 2004, *ApJ*, 604, L89
- Héraudeau, P. & Simien, F. 1998, *A&AS*, 133, 317
- Ho, L. C. & Kim, M. 2014, *ApJ*, 789, 17
- Hopkins, P. F., Hernquist, L., Cox, T. J., Robertson, B., & Krause, E. 2007a, *ApJ*, 669, 45
- . 2007b, *ApJ*, 669, 67
- Hurvich, C. & Tsai, C.-L. 1989, *Biometrika*, 76, 297
- Hyde, J. B. & Bernardi, M. 2009, *MNRAS*, 396, 1171
- Jardel, J. R., Gebhardt, K., Shen, J., Fisher, D. B., Kormendy, J., Kinzler, J., Lauer, T. R., Richstone, D., & Gültekin, K. 2011, *ApJ*, 739, 21
- Jordi, K., Grebel, E. K., & Ammon, K. 2006, *A&A*, 460, 339
- Jorgensen, I. & Franx, M. 1994, *ApJ*, 433, 553
- Kelly, B. C. 2007, *ApJ*, 665, 1489
- King, A. 2003, *ApJ*, 596, L27
- Kondratko, P. T., Greenhill, L. J., & Moran, J. M. 2005, *ApJ*, 618, 618
- Kormendy, J. 1993, in *The Nearest Active Galaxies*, ed. J. Beckman, L. Colina, & H. Netzer, 197–218
- Kormendy, J. 2013, *Secular Evolution in Disk Galaxies*, ed. J. Falcón-Barroso & J. H. Knapen (Cambridge University Press), 1
- Kormendy, J. & Bender, R. 1996, *ApJ*, 464, L119
- . 1999, *ApJ*, 522, 772
- . 2009, *ApJ*, 691, L142
- . 2013, *ApJ*, 769, L5
- Kormendy, J., Bender, R., & Cornell, M. E. 2011, *Nature*, 469, 374
- Kormendy, J., Bender, R., Magorrian, J., Tremaine, S., Gebhardt, K., Richstone, D., Dressler, A., Faber, S. M., Grillmair, C., & Lauer, T. R. 1997, *ApJ*, 482, L139
- Kormendy, J., Fisher, D. B., Cornell, M. E., & Bender, R. 2009, *ApJS*, 182, 216
- Kormendy, J. & Gebhardt, K. 2001, in *American Institute of Physics Conference Series*, Vol. 586, 20th Texas Symposium on relativistic astrophysics, ed. J. C. Wheeler & H. Martel, 363–381
- Kormendy, J. & Ho, L. C. 2013, *ARA&A*, 51, 511
- Kormendy, J. & Richstone, D. 1995, *ARA&A*, 33, 581

- Krajnović, D., McDermid, R. M., Cappellari, M., & Davies, R. L. 2009, *MNRAS*, 399, 1839
- Kronawitter, A., Saglia, R. P., Gerhard, O., & Bender, R. 2000, *A&AS*, 144, 53
- Läsker, R., Ferrarese, L., & van de Ven, G. 2014, *ApJ*, 780, 69
- Lauer, T. R. 2012, *ApJ*, 759, 64
- Laurikainen, E., Salo, H., Buta, R., & Knapen, J. H. 2011, *MNRAS*, 418, 1452
- Laurikainen, E., Salo, H., Buta, R., Knapen, J. H., & Comerón, S. 2010, *MNRAS*, 405, 1089
- Magorrian, J., Tremaine, S., Richstone, D., Bender, R., Bower, G., Dressler, A., Faber, S. M., Gebhardt, K., Green, R., Grillmair, C., Kormendy, J., & Lauer, T. 1998, *AJ*, 115, 2285
- Maiolino, R., Krabbe, A., Thatte, N., & Genzel, R. 1998, *ApJ*, 493, 650
- Mancini, L. & Feoli, A. 2012, *A&A*, 537, A48
- Maraston, C. 2005, *MNRAS*, 362, 799
- Marconi, A. & Hunt, L. K. 2003, *ApJ*, 589, L21
- Mathur, S., Fields, D., Peterson, B. M., & Grupe, D. 2012, *ApJ*, 754, 146
- Mazzalay, X., Thomas, J., Saglia, R. P., Wegner, G., Bender, R., Erwin, P., Fabricius, M. H., Nowak, N., & Rusli, S. P. 2016, *MNRAS*, submitted
- Mazzalay, X., Maciejewski, W., Erwin, P., Saglia, R. P., Bender, R., Fabricius, M. H., Nowak, N., Rusli, S. P., & Thomas, J. 2014, *MNRAS*, 438, 2036
- Mazzalay, X., Saglia, R. P., Erwin, P., Fabricius, M. H., Rusli, S. P., Thomas, J., Bender, R., Opitsch, M., Nowak, N., & Williams, M. J. 2013, *MNRAS*, 428, 2389
- McConnell, N. J. & Ma, C.-P. 2013, *ApJ*, 764, 184
- McConnell, N. J., Ma, C.-P., Gebhardt, K., Wright, S. A., Murphy, J. D., Lauer, T. R., Graham, J. R., & Richstone, D. O. 2011, *Nature*, 480, 215
- McConnell, N. J., Ma, C.-P., Murphy, J. D., Gebhardt, K., Lauer, T. R., Graham, J. R., Wright, S. A., & Richstone, D. O. 2012, *ApJ*, 756, 179
- McMillan, P. J. 2011, *MNRAS*, 414, 2446
- Menci, N., Gatti, M., Fiore, F., & Lamastra, A. 2014, *A&A*, 569, A37
- Merloni, A., Heinz, S., & di Matteo, T. 2003, *MNRAS*, 345, 1057
- Milosavljević, M. & Merritt, D. 2001, *ApJ*, 563, 34
- Moellenhoff, C., Matthias, M., & Gerhard, O. E. 1995, *A&A*, 301, 359
- Naab, T., Johansson, P. H., & Ostriker, J. P. 2009, *ApJ*, 699, L178
- Naab, T. & Trujillo, I. 2006, *MNRAS*, 369, 625
- Nieto, J.-L. & Bender, R. 1989, *A&A*, 215, 266
- Nieto, J.-L., Bender, R., & Surma, P. 1991, *A&A*, 244, L37
- Nowak, N., Saglia, R. P., Thomas, J., Bender, R., Davies, R. I., & Gebhardt, K. 2008, *MNRAS*, 391, 1629
- Nowak, N., Saglia, R. P., Thomas, J., Bender, R., Pannella, M., Gebhardt, K., & Davies, R. I. 2007, *MNRAS*, 379, 909
- Nowak, N., Thomas, J., Erwin, P., Saglia, R. P., Bender, R., & Davies, R. I. 2010, *MNRAS*, 403, 646
- Oliva, E., Origlia, L., Kotilainen, J. K., & Moorwood, A. F. M. 1995, *A&A*, 301, 55
- Onken, C. A., Valluri, M., Peterson, B. M., Pogge, R. W., Bentz, M. C., Ferrarese, L., Vestergaard, M., Crenshaw, D. M., Sergeev, S. G., McHardy, I. M., Merritt, D., Bower, G. A., Heckman, T. M., & Wandel, A. 2007, *ApJ*, 670, 105
- Paturel, G., Petit, C., Prugniel, P., Theureau, G., Rousseau, J., Brouty, M., Dubois, P., & Cambrésy, L. 2003, *A&A*, 412, 45
- Peletier, R. F. 1993, *A&A*, 271, 51
- Peletier, R. F., Knapen, J. H., Shlosman, I., Pérez-Ramírez, D., Nadeau, D., Doyon, R., Rodríguez Espinosa, J. M., & Pérez García, A. M. 1999, *ApJS*, 125, 363
- Peng, C. Y. 2007, *ApJ*, 671, 1098

- Pizzella, A., Amico, P., Bertola, F., Buson, L. M., Danziger, I. J., Dejonghe, H., Sadler, E. M., Saglia, R. P., de Zeeuw, P. T., & Zeilinger, W. W. 1997, *A&A*, 323, 349
- Portail, M., Wegg, C., Gerhard, O., & Martinez-Valpuesta, I. 2015, *MNRAS*, 448, 713
- Prugniel, P., Bica, E., Klotz, A., & Alloin, D. 1993, *A&AS*, 98, 229
- Prugniel, P. & Heraudeau, P. 1998, *A&AS*, 128, 299
- Prugniel, P., Zeilinger, W., Koleva, M., & de Rijcke, S. 2011, *A&A*, 528, A128
- Rusli, S. P., Erwin, P., Saglia, R. P., Thomas, J., Fabricius, M., Bender, R., & Nowak, N. 2013a, *AJ*, 146, 160
- Rusli, S. P., Thomas, J., Erwin, P., Saglia, R. P., Nowak, N., & Bender, R. 2011, *MNRAS*, 410, 1223
- Rusli, S. P., Thomas, J., Saglia, R. P., Fabricius, M., Erwin, P., Bender, R., Nowak, N., Lee, C. H., Riffeser, A., & Sharp, R. 2013b, *AJ*, 146, 45
- Saglia, R. P., Bertin, G., Bertola, F., Danziger, J., Dejonghe, H., Sadler, E. M., Stiavelli, M., de Zeeuw, P. T., & Zeilinger, W. W. 1993, *ApJ*, 403, 567
- Saglia, R. P., Kronawitter, A., Gerhard, O., & Bender, R. 2000, *AJ*, 119, 153
- Saglia, R. P., Sánchez-Blázquez, P., Bender, R., Simard, L., Desai, V., Aragón-Salamanca, A., Milvang-Jensen, B., Halliday, C., Jablonka, P., Noll, S., Poggianti, B., Clowe, D. I., De Lucia, G., Pelló, R., Rudnick, G., Valentinuzzi, T., White, S. D. M., & Zaritsky, D. 2010, *A&A*, 524, A6
- Sandage, A. & Visvanathan, N. 1978, *ApJ*, 223, 707
- Sani, E., Marconi, A., Hunt, L. K., & Risaliti, G. 2011, *MNRAS*, 413, 1479
- Savorgnan, G., Graham, A. W., Marconi, A., Sani, E., Hunt, L. K., Vika, M., & Driver, S. P. 2013, *MNRAS*, 434, 387
- Schlegel, D. J., Finkbeiner, D. P., & Davis, M. 1998, *ApJ*, 500, 525
- Schmitt, H. R. & Kinney, A. L. 2000, *ApJS*, 128, 479
- Schulze, A. & Gebhardt, K. 2011, *ApJ*, 729, 21
- Schwarz, G. 1978, *Annals of Statistics*, 6, 461
- Scorza, C., Bender, R., Winkelmann, C., Capaccioli, M., & Macchetto, D. F. 1998, *A&AS*, 131, 265
- Scott, N., Graham, A. W., & Schombert, J. 2013, *ApJ*, 768, 76
- Seifert, W. & Scorza, C. 1996, *A&A*, 310, 75
- Shaw, M., Wilkinson, A., & Carter, D. 1993, *A&A*, 268, 511
- Sijacki, D., Vogelsberger, M., Genel, S., Springel, V., Torrey, P., Snyder, G. F., Nelson, D., & Hernquist, L. 2015, *MNRAS*, 452, 575
- Simien, F. & Prugniel, P. 2000, *A&AS*, 145, 263
- Soker, N. & Meiron, Y. 2011, *MNRAS*, 411, 1803
- Stephens, A. W., Frogel, J. A., Ortolani, S., Davies, R., Jablonka, P., Renzini, A., & Rich, R. M. 2000, *AJ*, 119, 419
- Theureau, G., Hanski, M. O., Coudreau, N., Hallet, N., & Martin, J.-M. 2007, *A&A*, 465, 71
- Thomas, J., Bender, R., Rusli, S. P., Thomas, J., Saglia, R. P., Erwin, P., Fabricius, M., & Nowak, N. 2016, *ApJ*, in prep.
- Thomas, J., Saglia, R. P., Bender, R., Erwin, P., & Fabricius, M. 2014, *ApJ*, 782, 39
- Thomas, J., Saglia, R. P., Bender, R., Thomas, D., Gebhardt, K., Magorrian, J., Corsini, E. M., & Wegner, G. 2005, *MNRAS*, 360, 1355
- . 2009, *ApJ*, 691, 770
- Thomas, J., Saglia, R. P., Bender, R., Thomas, D., Gebhardt, K., Magorrian, J., Corsini, E. M., Wegner, G., & Seitz, S. 2011, *MNRAS*, 415, 545
- Thomas, J., Saglia, R. P., Bender, R., Thomas, D., Gebhardt, K., Magorrian, J., & Richstone, D. 2004, *MNRAS*, 353, 391
- Trujillo, I., Erwin, P., Asensio Ramos, A., & Graham, A. W. 2004, *AJ*, 127, 1917
- Tully, R. B., Rizzi, L., Shaya, E. J., Courtois, H. M., Makarov, D. I., & Jacobs, B. A. 2009, *AJ*, 138, 323

van den Bosch, R. C. E., Gebhardt, K., Gültekin, K., van de Ven, G., van der Wel, A., & Walsh, J. L. 2012, *Nature*, 491, 729

Vika, M., Driver, S. P., Cameron, E., Kelvin, L., & Robotham, A. 2012, *MNRAS*, 419, 2264

Yamauchi, A., Nakai, N., Sato, N., & Diamond, P. 2004, *PASJ*, 56, 605

York, D. G., Adelman, J., Anderson, J., et al. 2000, *AJ*, 120, 1579

Appendix A: The effective velocity dispersion for SINFONI galaxies

We determined the effective velocity dispersion σ for the SINFONI sample using long-slit or integral field stellar kinematics and total half-luminosity radii R_{eT} taken from the Hyperleda or RC3 (see Table 17) for consistency with previous studies, in combination with the photometry we used for the dynamical modeling. These radii refer to the galaxy as a whole; the half-luminosity radii of the bulge component of a galaxy can be much smaller, see Sect. 2. The σ values given in Table 1 were obtained by averaging the quantity:

$$v(R) = \sqrt{V(r)^2 + \sigma(R)^2}, \quad (33)$$

out to $R = R_{eT}$, where $V(R)$ and $\sigma(R)$ are the stellar line-of-sight mean velocity and velocity dispersion at a distance R from the center:

$$\sigma = \frac{\sum_{R \leq R_{eT}} v(R)w(R)}{\sum_{R \leq R_{eT}} w(R)} \quad (34)$$

We weighted each data point with its light contribution. When integral field data were available, this means we set $w(R) = I_c(R)$, where $I_c(R)$ is the circularized surface brightness at the distance R . When only long-slit data were available, we multiplied $I_c(R)$ by the corresponding circumference, $2\pi R$, i.e. $w(R) = 2\pi R I_c(R)$. The errors given in Table 1 for the SINFONI galaxies are the rms of the simple mean of the $v(R)$ (σ^s , obtained by setting $w(R) = 1$ in Eq. 34), divided by the square root of the number of points.

In Table 17 we also list the following quantities:

σ_{col} : the velocity dispersion derived by fitting the spectrum obtained by summing together the spectra of the SINFONI datacube

σ_{SIN} : the velocity dispersion derived by applying Eq. 34 to the SINFONI kinematics.

σ_{SIN}^s : the velocity dispersion derived by applying Eq. 34 with $w(R) = 1$ to the SINFONI kinematics.

$\sigma_{e/2}$: the velocity dispersion derived by applying Eq. 34 out to $R_{eT}/2$.

$\sigma_{e/2}^s$: the velocity dispersion derived by applying Eq. 34 with $w(R) = 1$ out to $R_{eT}/2$.

Fig. 19 compares the quantities listed in Tab. 17 to σ . On one hand, the velocity dispersion σ_{col} derived from spectrum obtained by summing together the spectra of the SINFONI datacube reproduces within 5% σ_{SIN} and within 8% σ_{SIN}^s with mean deviations less than 1%. So, averaging resolved kinematics according to Eq. 33 is equivalent to deriving the velocity dispersion from an integrated spectrum of a galaxy. On the other hand, σ matches the other estimates σ_e^s , $\sigma_{e/2}^s$, $\sigma_{e/2}$ within less than 3% scatter and with mean deviations less than 0.8%. So neither the exact choice of the cutoff radius, nor the weighting scheme plays a big role in the determination of the average velocity dispersion. Moreover, the average fractional error is 0.02, which matches the scatter well. Not surprisingly, the scatter obtained comparing σ_{col} to σ is much larger (14% with a mean difference of 2%), as σ_{col} probes the inner regions of the galaxies, where the presence of the supermassive black hole and/or the influence of a compact classical bulge becomes dynamically important.

Kormendy & Ho (2013) give discrepant velocity dispersions for three galaxies of our SINFONI sample. For NGC 1332 they have 328 km/s (from our previous determination in Rusli et al. 2011), that we now revise to 293.1 km/s (see Appendix B). For NGC 4486a they quote 111 km/s while we get 144.5 km/s using the profiles of Prugniel et al. (2011). For NGC 4486b their value is larger (185 km/s compared to 148.6 km/s), but the combination of a steep surface brightness and velocity dispersion radial gradient makes the measurement difficult (see Appendix B).

Appendix B: The luminosity profiles and the bulge mass-to-light ratios.

Many of the profiles come from the ESO Key Programme described in Scorza et al. (1998, hereafter KeyProg) or were derived from images from the Sloan Digital Sky Survey (York et al. 2000, hereafter SDSS).

This 2-column preprint was prepared with the AAS L^AT_EX macros v5.2.

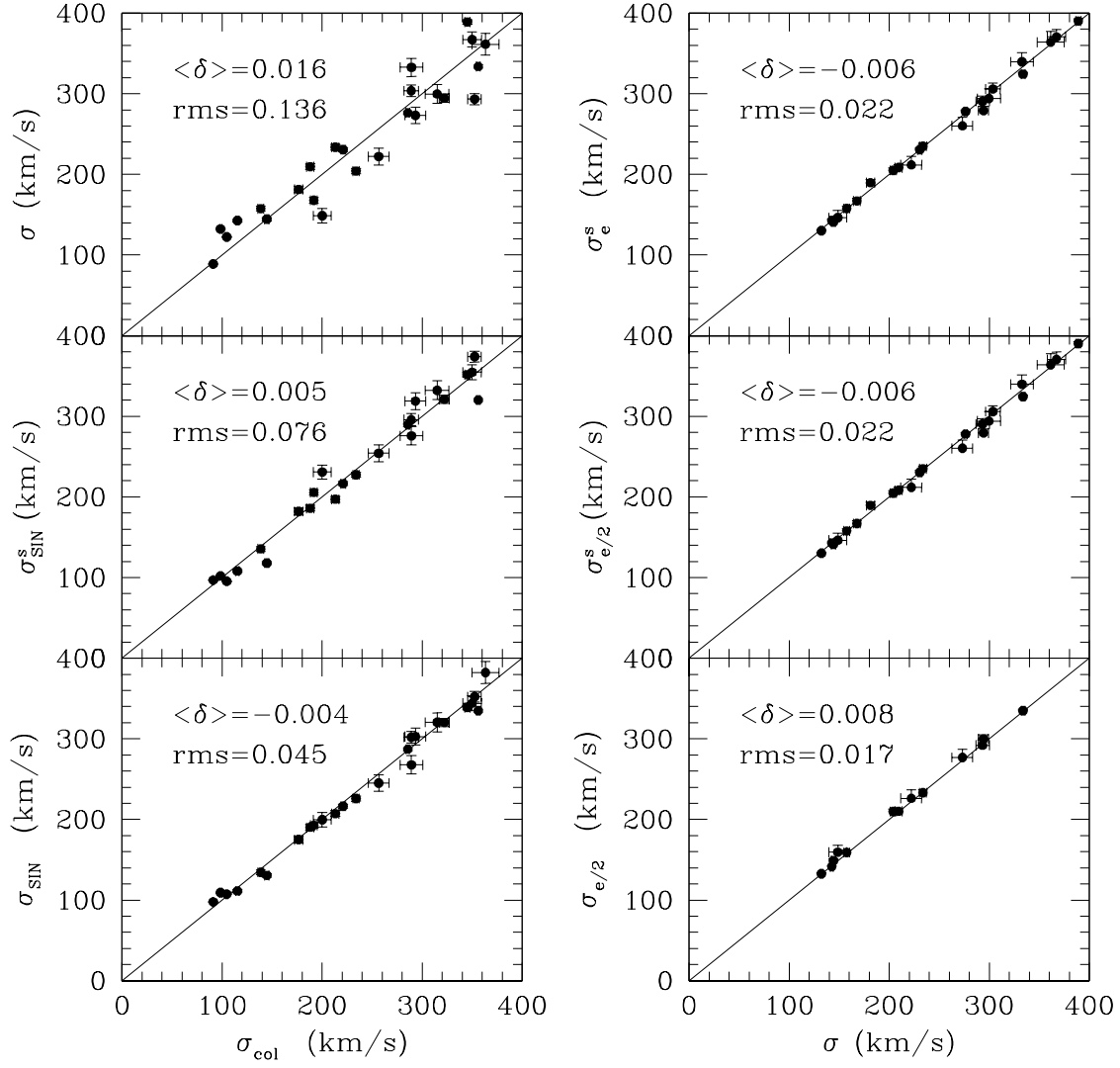


Fig. 19.— The comparison between the different estimates of the average velocity dispersion of a galaxy and σ for the SINFONI sample.

Table 17: Velocity dispersions of the SINFONI sample.

Galaxy	R_{eT} ($''$)	R_{max}^{kin}/R_{eT} -	σ_{col} ($km s^{-1}$)	σ_{SIN} ($km s^{-1}$)	σ_{SIN}^s ($km s^{-1}$)	$\sigma_{e/2}$ ($km s^{-1}$)	$\sigma_{e/2}^s$ ($km s^{-1}$)	σ_e^s ($km s^{-1}$)
NGC0307	4.755	1.942	233.9	225.9	227.6	209.9	204.9	204.9
NGC1316	80.75	0.6128	221	216.4	216.5	230.6	230.4	230.4
NGC1332	28	0.7178	352.4	352.3	373.9	292	290.4	290.4
NGC1374	24.38	0.4825	191.7	192.9	205.6	167.8	167	167
NGC1398	52.13	0.693	213.1	207.3	197.1	233.2	235	235
NGC1407	70.33	0.5436	285.6	287.2	289.4	276.4	277.9	277.9
NGC1550	25.53	0.965	293.3	302.8	318.8	276.9	260.2	260.2
NGC3091	32.89	0.3684	315	320.5	332.3	299.7	294.1	294.1
NGC3368	73.64	1.058	98.5	109.2	102	132.8	130.2	130.2
NGC3489	20.3	-	91.1	97.72	96.85	-	-	-
NGC3627	67.16	0.4754	104.7	107.3	95.43	122.4	122.4	122.4
NGC3923	49.79	0.7626	256.6	245.2	254.1	226.3	211.8	211.8
NGC4371	23.29	1.099	115.4	111.3	108.1	141.5	142.8	142.8
NGC4472	225.5	0.3036	289.1	302.1	295.9	303.7	305.9	305.9
NGC4486a	5.459	1.952	144.8	130.7	118	149.1	141.1	141.1
NGC4486b	2.495	1.2	200.1	199.8	230.8	159.4	146.3	146.3
NGC4501	77.11	0.8222	138.7	134.5	135.5	159.1	157.8	157.8
NGC4699	30.7	0.5416	176.5	175	182	181.3	189.6	189.6
NGC4751	22.76	0.3563	363.3	382.3	416.7	361.4	363.9	363.9
NGC5018	22.76	0.9905	188.1	190.3	186	210.1	208.4	208.4
NGC5328	22.24	1.27	356.1	335	320.1	335	324.3	324.3
NGC5419	43.36	0.3201	349.9	344.1	354.6	367.2	370.4	370.4
NGC5516	22.09	0.3944	289.3	267.7	275.7	332.7	339.7	339.7
NGC6861	17.67	0.4878	345.3	338.8	351.7	389	390.2	390.2
NGC7619	36.91	1.837	322.2	320.3	321.1	299.9	279.3	279.3

Column 1: galaxy name; column 2: total half-luminosity radius $R_{e,T}$; column 3: ratio between R_{max}^{kin} and $R_{e,T}$, where R_{max}^{kin} is the distance from the center of the most distant available stellar kinematic point; column 4 to 9: see text in Appendix A.

We corrected luminosity profiles and colors for Galactic extinction (hereafter G.E.) following Schlegel et al. (1998); however we quote the results of the fits in the Tables 20 to 33 without correction for G.E.. The zero-points of the profiles derived from SDSS images and corrected for G.E. are moved to the Johnson-Cousin bands when necessary using the equations of Jordi et al. (2006) and extinction corrected colors. Most of the colors used in the conversions from one band to the other come from the Hyperleda database (Paturel et al. 2003). For three galaxies we also use the colors of the Simple Stellar Populations (SSP) of Maraston (2005). We discuss how we addressed these cases and how we obtained the bulge luminosity profiles (which coincide with the total luminosity profile in the case of elliptical galaxies) below.

For all the galaxies we managed either to collect the dynamically determined bulge mass-to-light ratios from the literature or to compute our own dynamical estimate by fitting available stellar kinematics (see Appendix C). The ratios and their sources are quoted in Table 34. In most of the cases the literature values do not include a correction for G.E., which we apply here following Schlegel et al. (1998). Exceptions are Saglia et al. (1993, 2000), Moellenhoff et al. (1995), Kronawitter et al. (2000), Bower et al. (2001), Cappellari et al. (2006), Dalla Bontà et al. (2009), Krajnović et al. (2009), Rusli et al. (2013a) who already published M/L values corrected for G.E. The photometric band for which the M/L values were computed does not always coincide with the photometric band we used to derive the bulge luminosity profile (see Table 34). Finally, we adjust distances by adopting the ones given by Kormendy & Ho (2013), or Sani et al. (2011) for the remaining objects.

In general we scale the M/L ratios to our distances and bands using the equation

$$M/L_{us} = M/L_{lit} \times \frac{D_{lit}}{D_{us}} \times 10^{0.4(m_{us}-m_{lit})} \times 10^{0.4(m_{\odot,lit}-m_{\odot,us})}. \quad (35)$$

The solar magnitudes used below are listed in Table 18. The original M/L values and distances, together with colors and G.E. values used to transform or compute the M/L s are given in Table 19.

Fig. 20 shows the derived M/L ratios in the 9 bands with more than one galaxy as a function of the dynamical bulge mass. In general, they increase with bulge mass; a comparison with the models of Maraston (2005) shows that simple stellar populations with

a Kroupa IMF, solar metallicity and ages ranging from 2 to 12 Gyr roughly bracket the observed range.

Table 18: The solar magnitudes used in the conversion of the M/L .

$m_{\odot,B}$	5.48
$m_{\odot,V}$	4.83
$m_{\odot,g}$	5.36
$m_{\odot,R}$	4.42
$m_{\odot,r}$	4.67
$m_{\odot,I}$	4.08
$m_{\odot,i}$	4.57
$m_{\odot,z}$	4.52
$m_{\odot,zACS}$	3.98
$m_{\odot,H}$	3.32
$m_{\odot,K}$	3.28
$m_{\odot,3.6\mu}$	3.24

TABLE 19

THE ORIGINAL M/L AND DISTANCES, WITH COLORS AND GALACTIC EXTINCTION (G.E.) VALUES USED IN THE M/L CONVERSIONS FOR THE LITERATURE SAMPLE.

Galaxy	Comment
Circinus	$M/L_{3.6mu}$ derived fitting the stellar kinematics of Maiolino et al. (1998), $A_{3.6mu} = 0.107$
A1836	$M/L_I = 5M_\odot/L_\odot$, D=147.2 Mpc from Dalla Bontà et al. (2009), G.E. corrected $A_i = 0.134$, $A_r = 0.176$, $(r - i) = 0.482$, $(I - i) = -0.247 \times [(r - i)_0 + 0.236]/1.007$
IC1459	$M/L_R = 4.2M_\odot/L_\odot$, D=29.2 Mpc from Häring & Rix (2004), not corrected for G.E. $A_R = 0.042$, $A_V = 0.053$, $(V - R) = 0.621$
IC2560	$M/L_{3.6mu}$ derived fitting the central σ of Greene et al. (2010), $A_{3.6mu} = 0.015$
IC4296	$M/L_B = 5.6M_\odot/L_\odot$, D=75 Mpc from Saglia et al. (1993), G.E. corrected $A_B = 0.265$, $A_I = 0.119$, $(B - I) = 2.41$
NGC0221	$M/L_V = 2.16M_\odot/L_\odot$, D=0.8 Mpc from Magorrian et al. (1998), not corrected for G.E. $A_V = 0.206$, $A_R = 0.166$, $(V - R) = 0.641$
NGC0224	$M/L_V = 4.83M_\odot/L_\odot$, D=0.8 Mpc from Magorrian et al. (1998), not corrected for G.E., $A_V = 0.206$
NGC0524	$M/L_I = 4.99M_\odot/L_\odot$, D=23.3 Mpc from Cappellari et al. (2006), G.E. corrected
NGC0821	$M/L_I = 3.08M_\odot/L_\odot$, D=23.44 Mpc from Cappellari et al. (2006), G.E. corrected $A_R = 0.294$, $A_I = 0.213$, $(R - I) = 0.6923$
NGC1023	$M/L_V = 5.56M_\odot/L_\odot$, D=10.2 Mpc from Bower et al. (2001), G.E. corrected $A_V = 0.201$, $A_{3.6mu} = 0.009$, $(V - 3.6mu) = 3.695$
NGC1068	M/L_K derived fitting the stellar kinematics of Emsellem et al. (2006), $A_K = 0.012$
NGC1194	M/L_r derived fitting the stellar kinematics of Greene et al. (2010), $A_r = 0.21$
NGC1300	$M/L_{F606W} = 2.29M_\odot/L_\odot$, D=18.8 Mpc from Atkinson et al. (2005), not corrected for G.E., $A_V = 0.1$, $A_R = 0.081$, $(V - F606W) = 0.36$
NGC1399	$M/L_B = 10.2M_\odot/L_\odot$, D=21.1 Mpc from Kronawitter et al. (2000), G.E. corrected
NGC2273	M/L_R derived fitting the stellar kinematics of Greene et al. (2010), $A_R = 0.189$
NGC2549	M/L_R from Krajnović et al. (2009), G.E. corrected $A_V = 0.22$, $A_R = 0.175$, $(V - R)_{SV} = 0.567$, $(R_{SV} - r) = -0.267 \times (V - R)_{SV} - 0.088$ $(R - R_{SV}) = 0.27 \times (R - V)_{SV} - 0.22$
NGC2748	$M/L_{3.6mu}$ derived fitting the stellar kinematics of Batcheldor et al. (2005), $A_{3.6mu} = 0.004$
NGC2778	$M/L_V = 8M_\odot/L_\odot$, D=22.9 Mpc from Gebhardt et al. (2003), not corrected for G.E. $A_V = 0.069$, $(V - R) = 0.643$, $(B - V) = 0.958$, $(V - r)_0 = -0.63(B - V) + 1.646(V - R) + 0.124 - A_V$
NGC2787	$M/L_{3.6mu}$ derived fitting the stellar kinematics of Bertola et al. (1995), $A_{3.6mu} = 0.020$
NGC2960	M/L_r derived fitting the stellar kinematics of Greene et al. (2010), $A_r = 0.123$
NGC2974	$M/L_I = 4.52M_\odot/L_\odot$, D=20.89 Mpc from Cappellari et al. (2006), corrected for G.E. $A_I = 0.106$, $A_{3.6mu} = 0.008$, $(I - 3.6mu) = 2.374$
NGC3031	M/L_i derived fitting the stellar kinematics of Fabricius et al. (2012), $A_i = 0.167$
NGC3079	$M/L_{3.6mu}$ derived fitting the stellar kinematics of Shaw et al. (1993), $A_{3.6mu} = 0.002$
NGC3115	$M/L_V = 8.04M_\odot/L_\odot$, D=8.4 Mpc from Magorrian et al. (1998), not corrected for G.E., $A_V = 0.157$
NGC3227	M/L_{Kp} from Davies et al. (2006), G.E. corrected, narrow band definition
NGC3245	$M/L_R = 3.7M_\odot/L_\odot$, D=20.9 Mpc from Häring & Rix (2004), not corrected for G.E.

TABLE 19—*Continued*

Galaxy	Comment
	$A_B = 0.108, A_V = 0.083, A_R = 0.067, A_i = 0.052, (B - V) = 0.8367,$ $(V - R)_{SSP} = 0.508, (R - I)_{SSP} = 0.48,$ $(R - i) = 1.007 \times (R - I)_{SSP} - 0.267 \times (V - R)_{SSP} - 0.236 - 0.088$
NGC3377	$M/L_I = 2.22M_\odot/L_\odot, D=10.91$ Mpc from Cappellari et al. (2006), G.E. corrected $A_R = 0.091, A_I = 0.066, (R - I) = 0.629$
NGC3379	$M/L_I = 2.8M_\odot/L_\odot, D=10.57$ Mpc, from Cappellari et al. (2006), G.E. corrected
NGC3384	$M/L_V = 2.2M_\odot/L_\odot, D=11.7$ Mpc from Schulze & Gebhardt (2011), not corrected for G.E., $A_V = 0.088, A_R = 0.071, A_I = 0.052, A_i = 0.052, (R - I) = 0.624,$ $(V - I) = 1.18, (I - i) = -0.247 \times (R - I)_0 - 0.329$
NGC3393	M/L_I fitting the stellar velocity dispersion of Greene et al. (2010), $A_I = 0.146$
NGC3414	$M/L_I = 4.26M_\odot/L_\odot, D=24.55$ Mpc from Cappellari et al. (2006), G.E. corrected $A_r = 0.067, A_i = 0.051, (r - i) = 0.419, (R - I) = [0.236 + (r - i)_0]/1.007,$ $(i - I) = -0.247 \times (R - I) - 0.329$
NGC3585	$M/L_V = 3.4M_\odot/L_\odot, D=21.2$ Mpc from Gültekin et al. (2009a), not corrected for G.E., $A_V = 0.212$
NGC3607	$M/L_V = 7.5M_\odot/L_\odot, D=19.9$ Mpc from Gültekin et al. (2009a), not corrected for G.E. $A_B = 0.09, A_V = 0.069, A_g = 0.079, (B - V) = 0.921,$ $(V - g) = -0.63 \times (B - V)_0 + 0.124$
NGC3608	$M/L_V = 3.1M_\odot/L_\odot, D=23$ Mpc from Rusli et al. (2013a), G.E. corrected $A_V = 0.069, A_I = 0.041, (V - I) = 1.24$ $A_R = 0.056, A_I = 0.041, A_i = 0.044, (R - I) = 0.608,$ $(I - i) = -0.247 \times (R - I)_0 - 0.329$
NGC3842	M/L_V from Rusli et al. (2013a), G.E. corrected
NGC3998	$M/L_V = 6.5M_\odot/L_\odot, D=17$ Mpc from de Francesco et al. (2006), not corrected for G.E. $A_B = 0.069, A_V = 0.053, A_I = 0.031, A_i = 0.034, (B - V) = 0.966,$ $(V - I)_{SSP} = 1.135, (R - I)_{SSP} = 0.555, (I - i) = -0.247 \times (R - I)_{SSP} - 0.329$
NGC4026	$M/L_V = 4.89M_\odot/L_\odot$ from Gültekin et al. (2009a), not corrected for G.E. $A_B = 0.095, A_V = 0.073, A_g = 0.084, (B - V) = 0.962,$ $(V - g) = -0.63 \times (B - V)_0 + 0.124$
NGC4151	$M/L_R = 1.4M_\odot/L_\odot, D=13.9$ Mpc from Onken et al. (2007), not corrected for G.E., $A_R = 0.074$
NGC4258	$M/L_V = 3.6M_\odot/L_\odot, D=7.28$ Mpc from Häring & Rix (2004), not corrected for G.E. $A_V = 0.053, A_{3.6\mu} = 0.002, (V - 3.6\mu) = 3.629$
NGC4261	$M/L_V = 9.1M_\odot/L_\odot, D=31.6$ Mpc from Rusli et al. (2013a), G.E. corrected
NGC4291	$M/L_V = 5.4M_\odot/L_\odot, D=25$ Mpc from Rusli et al. (2013a), G.E. corrected
NGC4342	$M/L_I = 6.3M_\odot/L_\odot, D=15$ Mpc from Cappellari et al. (2006), G.E. corrected $A_r = 0.056, A_i = 0.043, A_I = 0.04, (r - i) = 0.426, (R - I) = [(r - i)_0 + 0.236]/1.007,$ $(I - i) = -0.247 \times (R - I) - 0.329$
NGC4374	$M/L_I = 4.36M_\odot/L_\odot, D=17.86$ Mpc from Cappellari et al. (2006), G.E. corrected $A_V = 0.134, A_I = 0.078, (V - I) = 1.26$
NGC4388	$M/L_{3.6\mu}M_\odot/L_\odot$ fitting the stellar velocity dispersion Greene et al. (2010),

TABLE 19—*Continued*

Galaxy	Comment
	$A_{3.6\mu} = 0.005$
NGC4459	$M/L_I = 2.51M_\odot/L_\odot$, D=15.7 Mpc from Cappellari et al. (2006), G.E. corrected $A_V = 0.153$, $A_I = 0.09$, $(V - I) = 1.306$
NGC4473	$M/L_V = 6.8M_\odot/L_\odot$, D=17 Mpc from Schulze & Gebhardt (2011), not corrected for G.E., $A_V = 0.094$
NGC4486	$M/L_V = 6.3M_\odot/L_\odot$, D=17.9 Mpc from Gebhardt & Thomas (2009), not corrected for G.E., $A_V = 0.074$
NGC4526	$M/L_I = 2.65M_\odot/L_\odot$, D=16.5 Mpc from Davis et al. (2013), corrected for G.E. $A_I = 0.043$, $A_{3.6\mu} = 0.003$, $(I - 3.6\mu) = 2.47$
NGC4552	$M/L_V = 7.1M_\odot/L_\odot$, D=15.85 Mpc from Rusli et al. (2013a), G.E. corrected
NGC4564	M/L_V fitting the stellar kinematics of Bender et al. (1994), $A_V = 0.116$
NGC4594	$M/L_I = 3.4M_\odot/L_\odot$, D=9.8 Mpc from Jardel et al. (2011), not corrected for G.E. $A_I = 0.099$
NGC4596	$M/L_K M_\odot/L_\odot$ fitting the stellar kinematics of Bettoni & Galletta (1997), $A_K = 0.008$
NGC4621	$M/L_I = 3.03M_\odot/L_\odot$, D=17.78 Mpc from Cappellari et al. (2006), G.E. corrected $A_I = 0.064$, $A_{3.6\mu} = 0.005$, $(I - 3.6\mu) = 2.515$
NGC4649	$M/L_V = 7.3M_\odot/L_\odot$, D=17.3 Mpc from Rusli et al. (2013a), G.E. corrected
NGC4697	$M/L_V = 4.3M_\odot/L_\odot$, D=12.4 Mpc from Schulze & Gebhardt (2011), not corrected for G.E., $A_V = 0.101$, $A_R = 0.081$, $(V - R) = 0.59$
NGC4736	$M/L_B = 1.8M_\odot/L_\odot$, D=6.6 Mpc from Moellenhoff et al. (1995), G.E. corrected $A_B = 0.076$, $A_V = 0.059$, $A_R = 0.047$, $A_I = 0.034$, $A_z = 0.026$, $(B - V) = 0.9$, $(V - R) = 0.84$, $(R - I) = 0.74$, $(g - r) = 1.646 \times (V - R)_0 - 0.139$, $(g - B) = -0.37 \times (B - V)_0 - 0.124$, $(r - z) = 1.586 \times (R - I)_0 - 0.386$, $(z - B) = (g - B) - (g - r) - (r - z)$
NGC4826	M/L_i fitting the stellar kinematics of Héraudeau & Simien (1998), $A_i = 0.086$
NGC4889	$M/L_r = 6.025M_\odot/L_\odot$, D=103.2 Mpc from McConnell et al. (2012), not corrected for G.E., $A_R = 0.026$, $A_V = 0.032$, $(V - R) = 0.724$, $(r - R) = -0.267 \times (V - R)_0 - 0.088$
NGC5077	$M/L_B = 4M_\odot/L_\odot$, D=56 Mpc from Pizzella et al. (1997), not corrected for G.E. $A_B = 0.21$, $A_V = 0.161$, $(B - V) = 1.04$
NGC5128	$M/L_K = 0.65M_\odot/L_\odot$, D=3.5 Mpc from Cappellari et al. (2009), G.E. corrected
NGC5576	$M/L_V = 3.7M_\odot/L_\odot$, D=27.1 Mpc from Gültekin et al. (2009a), not corrected for G.E. $A_V = 0.104$, $A_R = 0.084$, $(V - R) = 0.553$
NGC5813	$M/L_V = 4.7M_\odot/L_\odot$, D=32.2 Mpc from Rusli et al. (2013a), G.E. corrected
NGC5845	$M/L_V = 5.1M_\odot/L_\odot$, D=28.7 Mpc from Schulze & Gebhardt (2011), not corrected for G.E., $A_V = 0.177$
NGC5846	$M/L_I = 5.2M_\odot/L_\odot$, D=24.9 Mpc from Rusli et al. (2013a), G.E. corrected
NGC6086	$M/L_R = 4.2M_\odot/L_\odot$, D=133 Mpc from Rusli et al. (2013a), G.E. corrected
NGC6251	$M/L_R = 6M_\odot/L_\odot$, D=106 Mpc from Häring & Rix (2004), not corrected for G.E. $A_V = 0.29$, $A_R = 0.234$, $A_I = 0.17$, $(R - I) = 0.626$, $(R - I)_{SSP} = 0.643$, $(V - I) = 1.408$

In the following two subsections we discuss in detail the galaxies with black hole masses from the literature and from our SINFONI survey.

Literature Sample

The surface brightness values reported in the Tables 20 to 33 are in the Vega system, when Johnson and the 3.6μ filters are used, or in the AB system, when SDSS filters are used.

Milky Way: We adopt the axisymmetric bulge density profile of McMillan (2011) scaled as follows. Portail et al. (2015) compute the total mass in the bulge volume ($\pm 2.2 \times \pm 1.4 \times \pm 1.2$) kpc to be $1.84 \times 10^{10} M_{\odot}$. A sphere with a 1.92 kpc radius has the same volume. Using the spherically averaged density profile of McMillan (2011) we get a mass within this radius of $7.2 \times 10^9 M_{\odot}$, so we scale up this profile by a factor 2.54.

Circinus: The bulge photometry in 3.6μ -band is taken from the decomposition published by Sani et al. (2011). The M/L is derived as in Appendix C and Fig. 37 to match the kinematic profiles of Maiolino et al. (1998). We follow Kormendy & Ho (2013) in classifying the galaxy as barred.

A1836: The M/L is scaled to the distance of Kormendy & Ho (2013) and the i -band image is calibrated to the Cousins I using the $(r - i)$ color and the equations in Jordi et al. (2006). McConnell & Ma (2013) and Kormendy & Ho (2013) consider the galaxy a core elliptical; we accept their classification, although strong nuclear dust makes it difficult to determine its core properties (see discussion in Rusli et al. 2013a).

IC 1459: We correct the M/L for G.E., scaled it from R to V -band using the $(V - R)$ color from Hyperleda and adjust it to the distance of Kormendy & Ho (2013). The galaxy is a core elliptical (Rusli et al. 2013a), despite the classification of Kormendy & Ho (2013). We use the profile of Rusli et al. (2013a) and derive $R_e = 18.6''$, while their $n = 7.6$ Core-Sersic fit profile has $R_e = 45.4''$ (see Fig. 2). The difference is driven by the extrapolation. The same applies to the result of Sani et al. (2011) who measure $R_e = 53.3''$, and Läscher et al. (2014),

who quote $R_e = 38.4''$ for the 'classical' fit and $R_e = 51.9''$ for the best fit.

IC 4296: McConnell & Ma (2013) and Kormendy & Ho (2013) consider the galaxy a core elliptical; we accept their classification, although strong nuclear dust makes it difficult to determine its core properties (see discussion in Rusli et al. 2013a). We measure the profile from I -band FORS images that we calibrate to Cousins I using the photometry of Prugniel & Heraudeau (1998) and finally to the B band using the mean $(B - I) = 2.41$ color derived from Goudfrooij et al. (1994) and $A_B = 0.265$. From this profile we measure $R_e = 68.1''$, in agreement with Läscher et al. (2014, $R_e = 70.9''$) 'best fit', but disagreeing with their 'classical fit' ($R_e = 28.9''$) or the value reported by Sani et al. (2011, $32.3''$). The M/L (from the model with dark matter and already corrected for G.E.) is scaled to the distance of Kormendy & Ho (2013).

NGC 221: The M/L is scaled from V to R -band using the $(V - R)$ color from Hyperleda and to the distance of Kormendy & Ho (2013).

NGC 224: The M/L is scaled to the distance of Kormendy & Ho (2013). We classify it as barred following Athanassoula & Beaton (2006).

NGC 524: The M/L is scaled to the distance of Kormendy & Ho (2013). We classify this galaxy with $T = 2$ (a classical bulge). Although the galaxy is circular, significant stellar rotation is nonetheless seen (Simien & Prugniel 2000; Emself et al. 2004); therefore the S0 classification is dubious and the galaxy could be a core elliptical (McConnell & Ma 2013). We deproject the multi-gaussian expansion of the photometry profile as given in Cappellari et al. (2006) and get $R_e = 47.1''$. We ignore the possible small disk detected by Sani et al. (2011) ($B/T \approx 0.83$); Kormendy & Ho (2013) give $B/T = 0.92$. Finally, we conclude that the bulge plus disk decomposition with $B/T = 0.28$ and $R_e = 8.9''$ of Laurikainen et al. (2010) does not describe the nature of the galaxy.

NGC 821: Kormendy & Ho (2013) quote $B/T = 0.95$, therefore we ignore the possible disk component and use the whole galaxy profile (Graham et al. 2001), getting $R_e = 34.8''$. Beifiori

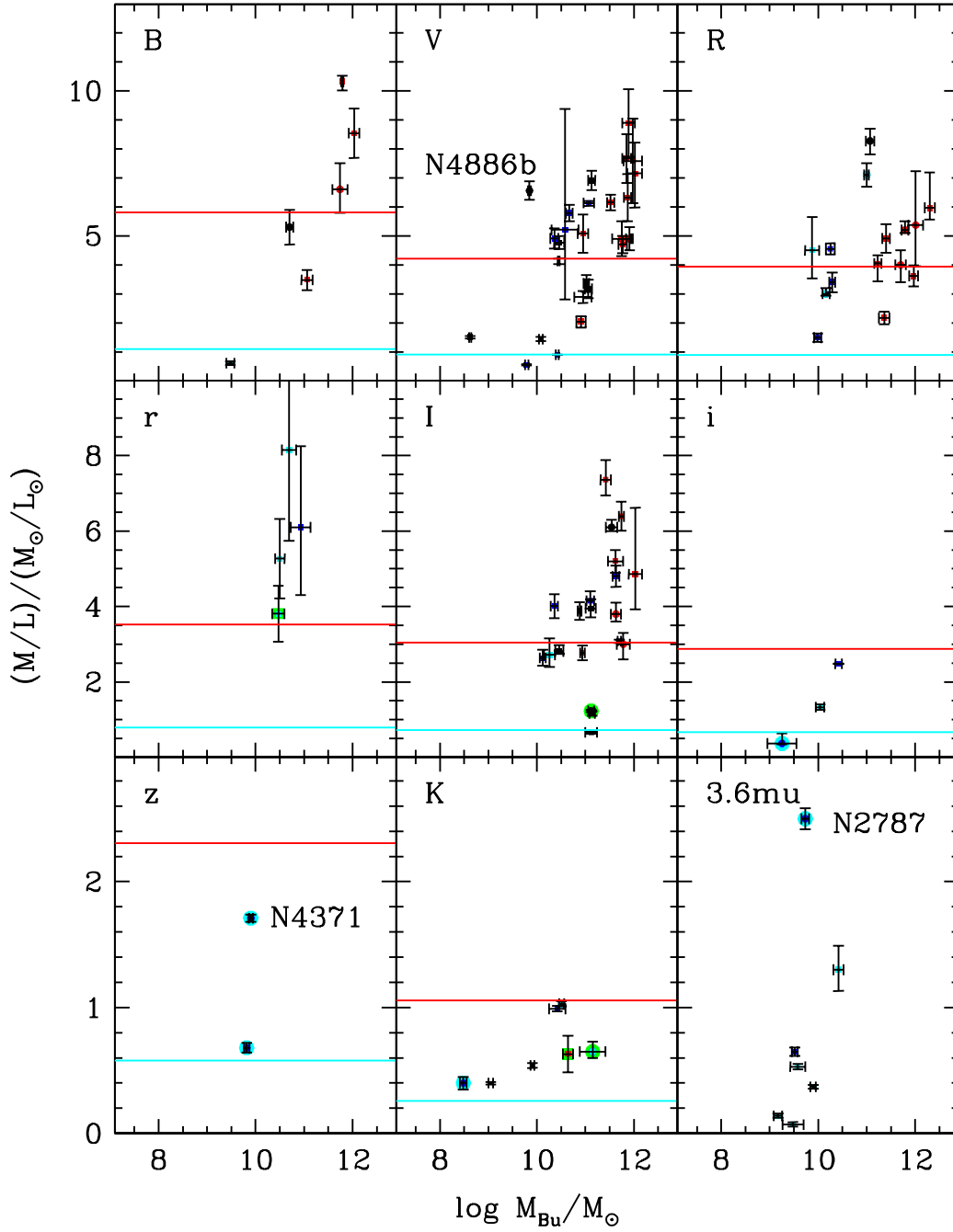


Fig. 20.— The M/L ratios in the 9 bands with more than one galaxy as a function of the dynamical bulge mass. Colors and point types as in Fig. 14. The lines show the values predicted by the simple stellar population models of Maraston (2005) for a Kroupa IMF, solar metallicity and age of 2 (cyan) and 12 (red) Gyr.

TABLE 19—*Continued*

Galaxy	Comment
NGC6264	M/L_r fitting Greene et al. (2010) minor axis velocity dispersion, $A_r = 0.178$
NGC6323	M/L_r fitting Greene et al. (2010) velocity dispersion, $A_r = 0.047$
NGC7052	$M/L_R = 3.5M_\odot/L_\odot$, $D = 58.7$ Mpc from Häring & Rix (2004), not corrected for G.E. $A_R = 0.324$
NGC7457	$M/L_{3.6mu}$ fitting the stellar kinematics of Emsellem et al. (2004), $A_{3.6mu} = 0.008$
NGC7582	$M/L_{3.6mu}$ fitting the stellar kinematics of Oliva et al. (1995), $A_{3.6mu} = 0.002$
NGC7768	$M/L_V = 7.8M_\odot/L_\odot$, $D = 112.8$ Mpc from Rusli et al. (2013a), G.E. corrected
UGC3789	M/L_H fitting the stellar velocity dispersion of Greene et al. (2010), $A_H = 0.037$

et al. (2012) report $R_e = 85.4''$ and Läsker et al. (2014) ‘best fit’ gives $3.5''$. The fit of Beifiori et al. (2012) overestimates the measured profile at radii larger than $70''$ by 0.4 mag. Läsker et al. (2014) consider a bulge, a (faint) disk and a halo and it is not clear that bulge and halo should be treated as separate components. The M/L is scaled to the distance of Kormendy & Ho (2013) and from I to R -band using the mean $(R - I)$ color from Hyperleda.

NGC 1023: The M/L of Bower et al. (2001) is already corrected for G.E.; we scale it to the distance of Kormendy & Ho (2013) and calibrate it from the V -band to $3.6mu$ using the V -band aperture photometry from Hyperleda. The Spitzer images come from Program 69, PI Giovanni Fazio, Observer ID 2. We perform a Sérsic bulge plus exponential disk decomposition along the major axis of the galaxy following Fisher & Drory (2008) and masking the region where the bar is present (see Fig. 21 and Table 20). This gives $R_e = 7.5''$, which agrees with Fisher & Drory (2010). The 2-dimensional fit (including a bar) of Sani et al. (2011) gives $R_e = 18.8''$, but the peculiar fit residuals suggest that the bar has not been modeled correctly.

NGC 1068: We consider the small classical component of the composite bulge, getting $R_e = 0.5''$ (Erwin et al. 2015). This explains the large difference with Sani et al. (2011), who derive $R_e = 8.4''$ for the pseudo bulge of the galaxy. The M/L is derived using the distance of Kormendy & Ho (2013) and fitting the major-axis kinematic profile $\sqrt{\sigma^2 + V^2}$ of Fig. 5 of Emsellem et al. (2006), summing the bulge and disk

contributions (see App. C and Fig. 37). The value $M/L_K = 0.7$ derived by Erwin et al. (2015) for the stellar population of the classical bulge is a factor 1.9 larger. We adopt this as the upper error estimate. The lower error estimate comes from the spherical mass profile derived from Fig. 13 of Emsellem et al. (2006) evaluated at $20''$ from the center. We classify the galaxy as “barred” following Erwin (2004). Kormendy & Ho (2013) call it a prototypical oval galaxy.

NGC 1194: The SDSS r -band bulge photometry is taken from the decomposition given in Greene et al. (2010). The M/L is derived following Appendix C to match the velocity dispersion within the effective aperture radius of $1.38''$, using the distance of Kormendy & Ho (2013).

NGC 1300: The bulge model is taken from Fisher & Drory (2008), who correctly discard the bar contribution. The huge difference between our R_e ($4''$) and the value quoted by Sani et al. (2011), $45.98''$, stems from the fact that they do not separately fit the strong bar of the galaxy and thus include it in the bulge component. The M/L is derived by converting the average of the two values in the F160W band given in Table 4 of Atkinson et al. (2005), using the color of Hyperleda. We adopt the distance of Kormendy & Ho (2013).

NGC 1399: The galaxy is a core elliptical (Rusli et al. 2013a); we use their profile and subtract the outer exponential component before deprojecting the galaxy, getting $R_e = 103.7''$. The ‘classical’ best fit of Läsker et al. (2014) gives $R_e = 49.3''$, the ‘best’ one $R_e = 147''$. The

M/L is scaled to the distance of Kormendy & Ho (2013). Errors are taken from Kronawitter et al. (2000).

NGC 2273: We performed a bulge plus disk decomposition on an R -band image from Erwin & Sparke (2003) using the IMFIT software of Erwin (2015). A Sersic bulge (function *Sersic* of IMFIT), a bar (function *Sersic-GenEllipse* of IMFIT), an exponential disk (function *Exponential* of IMFIT) and an outer ring (function *GaussianRing2Side* of IMFIT) were fit to the image; see Erwin (2015) for a definition of the function parameters. We set $\mu_e = -2.5 \log I_e$ and $\mu_0 = -2.5 \log I_0$. The parameter values of the fit are given in Table 21. Model images of the bar, disk and inner ring components (see Figs. 22 and 35) were subtracted from the original image and the bulge photometry was derived on the residual image. The M/L is computed as in Appendix C to match the velocity dispersion of Greene et al. (2010) within the effective aperture radius of $1.38''$, using the distance of Kormendy & Ho (2013).

NGC 2549: The M/L (already corrected for G.E.) is scaled to the distance of Kormendy & Ho (2013). The SDSS r -band image is calibrated to the R -band using the aperture photometry in the R_{SV} and V_{SV} -band of Sandage & Visvanathan (1978), using the color transformations of Prugniel et al. (1993) and Jordi et al. (2006). We performed an IMFIT bulge (function *Sersic*) plus disk (function *EdgeOnDisk*) decomposition (see Figs. 23 and 35). The parameters of this fit are given in Table 22.

NGC 2748: We performed an IMFIT bulge (function *Sersic*) plus disk (function *Exponential*) plus double ring (functions *GaussianRing*) decomposition of the 3.6μ band Spitzer image (see Figs. 24 and 35). The resulting values of the parameters of the fit are listed in Table 23. The residual image shows that the galaxy has a low surface brightness polar ring, that we masked while fitting the main galaxy. The position angle of the bulge component (which contributes 15% of the total light) is different from the rest of the galaxy; this probably stems from the modeling of the combination of a small bar (in which case the two rings make sense as an inner ring and an outer ring) and whatever small pseudobulge the

galaxy may have. The Spitzer image does not really have the resolution to be sure about that. The 'bulge' model of Sani et al. (2011) is 0.8 mag brighter and 3.5 times larger in size than our solution. The $M/L = 0.5 \pm 0.02 M_\odot/L_\odot$ in the 3.6μ band is derived as in Appendix C and Fig. 37 using the (circularized) surface brightness of the entire galaxy (i.e. with the polar ring component) to match the kinematic profile of Batcheldor et al. (2005). The distance comes from Kormendy & Ho (2013). If we convert the best-fit value in the F160W-band given in the Table 4 of Atkinson et al. (2005) to the 3.6μ band using 2MASS J , H , K aperture magnitudes and the conversion equation given in Stephens et al. (2000), we get $M/L_{3.6\mu} = 0.4 \pm 0.05 M_\odot/L_\odot$. Since the galaxy is too dusty and edge-on to be sure about the presence or absence of a bar, we set $b = 0.5$ in Table 1.

NGC 2787: Erwin et al. (2003) presented evidence for a composite bulge in this galaxy. Although their "inner disk" may perhaps be better understood as the projected box/peanut structure of the bar (rather than a "disky pseudo bulge"), we use the parameters of their decomposition (their Table 5) giving $R_e = 3.5''$, but shift the resulting total surface brightness to the 3.6μ band to match the total profile derived from Spitzer images (coming from Program 30318, PI Giovanni Fazio, Observer ID 2; Fig. 21). Sani et al. (2011) derive $R_e = 12.3''$, not distinguishing between the classical and the pseudo component of the bulge. The M/L is computed by fitting the kinematics of Bertola et al. (1995) (see Appendix C and Fig. 37), using the sum of the bulge and disk profiles derived above. The distance comes from Kormendy & Ho (2013).

NGC 2960: We use the bulge plus disk decomposition of Greene et al. (2010) in the r -band, ignoring the E2 morphology of Kormendy & Ho (2013), but accepting the merger appearance of the galaxy. The M/L is computed as in Appendix C to match the velocity dispersion of Greene et al. (2010) within an effective aperture radius of $1.6''$, using the distance of Kormendy & Ho (2013).

NGC 2974: The M/L is scaled to the distance of Sani et al. (2011) and from I to 3.6μ -band using the $(I - 3.6\mu)$ color from Hyperleda. The

Spitzer images come from Program 30318, PI Giovanni Fazio, Observer ID 2. The BH mass comes from the uncertain determination of Cappellari et al. (2008). We exclude this galaxy from the fits reported in Tables 36 and 37.

NGC 3031: The SDSS i -band decomposed bulge profile comes from Beifiori et al. (2012), which gives $R_e = 41.4''$. Sani et al. (2011) quote $R_e = 100.2''$, probably overestimating the size of the bulge by including the bar of the galaxy as part of the bulge in the fit. Fisher & Drory (2010) are in better agreement with our adopted solution. The M/L is determined using the distance of Kormendy & Ho (2013) and by fitting the kinematics of Fabricius et al. (2012) (see Appendix C and Fig. 37), summing the disk and the bulge profiles. We classify the galaxy as barred following Gutiérrez et al. (2011) and Erwin & Debattista (2013). Following Fabricius et al. (2012) we classify the galaxy bulge as classical, even if it is most likely a composite (pseudo plus classical) system.

NGC 3079: We model the Spitzer 3.6μ -band image of this pseudo bulge galaxy with four components using IMFIT: a pseudo bulge (function *Sersic*), a disk (function *Exponential*), a bar (a second *Sersic* function) and a ring (function *GaussianRing*). The results are shown in Fig. 25 and 35. The parameters of the fit are listed in Table 24. All four components are very flattened and have almost the same position angle. The small ($a_e = 4.5''$) pseudo bulge component contributes 26% of the total light of the galaxy. This is in contrast to the fit of Sani et al. (2011), who claim the existence of an unrealistically large ($R_e = 74''$) bulge with $B/T = 0.87$. The M/L is computed as in Appendix C to match the stellar kinematic profile of Shaw et al. (1993) (see Fig. 37) using the distance of Sani et al. (2011). Kormendy & Ho (2013) judge the black hole mass determination of Kondratko et al. (2005) unreliable, which however agrees with Yamauchi et al. (2004) and matches the value quoted by Sani et al. (2011) we used here. We exclude this galaxy from the fits reported in Tables 36 and 37.

NGC 3115: For this edge-on S0 we prefer the decomposition of Seifert & Scorza (1996) and Scorza et al. (1998), which gives $R_e = 42''$, to the one

of Sani et al. (2011, $R_e = 15.7''$) that shows systematic residuals. The M/L is scaled to the distance of Kormendy & Ho (2013) and corrected for G.E..

NGC 3227: The bulge component is determined in Davies et al. (2006) from a high-resolution SINFONI image, giving $R_e = 3.1''$. The 'classical fit' of Läscher et al. (2014) delivers $R_e = 1.4''$, the 'best fit' $R_e = 0.5''$, both results are probably affected by insufficient resolution (FWHM=0.9''). Sani et al. (2011) quote $R_e = 58''$, which is definitely too large. The K -band M/L (scaled to the distance of Kormendy & Ho 2013) is given in the unusual units quoted by Davies et al. (2006). We mark the 'peculiarity' of this definition by referring to the band as 'Kp' in Table 34 and by not plotting the galaxy in Fig. 20. Kormendy & Ho (2013) exclude the galaxy from their fits, arguing that the active nucleus makes the dynamical modeling challenging.

NGC 3245: We use the decomposition of Beifiori et al. (2012) in the i -band, which gives $R_e = 3.5''$ (with $B/T = 0.27$) and agrees with the 'classical fit' of Läscher et al. (2014). The 'best fit' of Läscher et al. (2014), which includes a bar, gives $R_e = 1.5''$. Since what Läscher et al. (2014) call a 'bar' could also be an 'oval' component, we stick to the decomposition of Beifiori et al. (2012). We calibrate the fit to the R -band from the original SDSS i -band using the $(R - I)$ color estimated as follows and the $(i - R)$ conversion equation in Jordi et al. (2006). Since only the $(B - V)$ color was available in Hyperleda, we derived $(R - I)$ by linearly fitting the $(V - I)$ vs. $(B - V)$ correlation of the simple stellar population models of Maraston (2005). The M/L is corrected for G.E. and scaled to the distance of Kormendy & Ho (2013).

NGC 3377: For this E6 galaxy we use a single profile, which gives $R_e = 39.1''$, roughly consistent with Arnold et al. (2014). The multi-component fit of Läscher et al. (2014) delivers $R_e = 7''$, but their disk component is faint and the envelope could well be part of the bulge. The M/L is scaled to the distance of Kormendy & Ho (2013) and from I to R -band using the $(R - I)$ color from Hyperleda.

NGC 3379: The galaxy is a core elliptical (Rusli et al.

2013a). We use their profile and M/L , which is scaled to the distance of Kormendy & Ho (2013).

NGC 3384: The decomposed SDSS i -band bulge profile comes from Beifiori et al. (2012). We calibrated it to the I -band using the equation of Jordi et al. (2006) and the $(R-I)$ color from Hyperleda. We get $R_e = 7.6''$, while Laurikainen et al. (2010) quote $R_e = 3.6''$ from a complex fit involving 2 bars. But Erwin (2004) classified the object as a barred galaxy with an inner disk, rather than double-barred. Moreover, the residuals of the fit of Laurikainen et al. (2010) are not shown, so we keep our reasonable solution. We correct the M/L of the model with dark matter of Schulze & Gebhardt (2011) for G.E., and scale it from V to I -band using the $(V-I)$ color of Hyperleda, using the distance of Kormendy & Ho (2013).

NGC 3393: We performed an IMFIT bulge (function *Sersic*) plus bar (function *Sersic_GenEllipse*) plus disk (function *Exponential*) decomposition (see Fig. 26 and 35) on an I -band image observed with the 0.9 m CTIO telescope by Schmitt & Kinney (2000). The parameters of the decomposition are given in Table 25. The M/L is computed as in Appendix C to match the velocity dispersion of Greene et al. (2010) within an effective aperture of radius of $1.6''$, using the distance of Kormendy & Ho (2013).

NGC 3414: We performed an IMFIT bulge (function *Sersic*) plus bar (function *Sersic_GenEllipse*) plus disk (function *Exponential*) decomposition on the SDSS i -band image of the galaxy (see Figs. 27 and 35). The parameters are listed in Table 26. We converted the i -band zeropoint into a Cousins I -band using two equations in Jordi et al. (2006) and the $(r-i)$ SDSS color. The M/L of Cappellari et al. (2006) is scaled to the distance of Sani et al. (2011). Our decomposition gives $R_e = 23''$ and agrees with Sani et al. (2011). Laurikainen et al. (2010) obtain $R_e = 3.2''$ and classify the galaxy as 'spindle'. Given the impossibility of verifying the quality of the fit of Laurikainen et al. (2010), we stick to our solution but acknowledge that the galaxy is complex. For consistency with our fit that contains a bar we set $b = 1$ in Table 1. The BH mass comes from the uncertain determination of

Cappellari et al. (2008). We exclude this galaxy from the fits reported in Tables 36 and 37.

NGC 3585: For this edge-on S0 we prefer the decomposition of Scorza et al. (1998), giving $R_e = 27.4''$, to the one of Sani et al. (2011, $R_e = 11.5''$), which shows systematic residuals. The M/L is corrected for G.E. and scaled to the distance of Kormendy & Ho (2013).

NGC 3607: We calibrate the g -band SDSS image to the V -band using the $(B-V)$ color from Hyperleda and the $(g-V)$ transformation of Jordi et al. (2006). McConnell & Ma (2013) and Kormendy & Ho (2013) consider the galaxy a core elliptical; we accept their classification, although strong nuclear dust makes it difficult to determine its core properties (see discussion in Rusli et al. 2013a). From the profile we measure $R_e = 45.0''$, in fair agreement with Beifiori et al. (2012) who measure $R_e = 56.34''$ from a Sersic fit to the SDSS i -band image. In contrast, Laurikainen et al. (2010) perform a bulge plus disk decomposition, deriving $R_e = 6.1''$ with $B/T = 0.32$. We do not think that this is a good description of the galaxy. The M/L is corrected for G.E. and scaled to the distance of Kormendy & Ho (2013).

NGC 3608: The galaxy is a core elliptical (Rusli et al. 2013a). We calibrate the i -band SDSS image to the I -band using the $(R-I)$ color from Hyperleda and the transformation of Jordi et al. (2006). This gives a more extended profile than the one derived by Rusli et al. (2013a), which comes from the g -band image. We transform the M/L_V of Rusli et al. (2013a) to the I -band using the $(V-I)$ color of Hyperleda and scaling it to the distance of Kormendy & Ho (2013). We measure $R_e = 43''$, while Beifiori et al. (2012) obtain $R_e = 161.9''$. This stems from the systematic overestimation (by 0.4 mag) of the light of the galaxy at radii larger than $60''$ in Beifiori et al. (2012)'s fit.

NGC 3842: The galaxy is a core elliptical (Rusli et al. 2013a). We use their profile and M/L , scaled to the distance of Kormendy & Ho (2013).

NGC 3998: The SDSS i -band decomposed bulge profile comes from Beifiori et al. (2012), is calibrated to the I -band using the equation of Jordi

et al. (2006) and gives $R_e = 5.2''$. This roughly agrees with the $R_e = 3.4''$ of Laurikainen et al. (2010). We prefer this solution to the multi-component 'best-fit' of Läscher et al. (2014), which delivers $R_e = 1.8''$, since the size of the fitted bar seems implausible. Since only the $(B - V)$ color was available in Hyperleda, we derived the $(V - I)$ and the $(R - I)$ colors by linearly fitting the $(V - I)$ vs. $(B - V)$ and $(R - I)$ vs. $(B - V)$ correlation of the simple stellar population models of Maraston (2005). We correct the M/L for G.E. and scaled it to the distance of Kormendy & Ho (2013); moreover, we adapt it to the I -band using the above colors. Errors on M/L are half of the 2σ values. We classify the galaxy as "barred" following Gutiérrez et al. (2011).

NGC 4026: We correct the M/L for G.E. and scale it to the distance of Kormendy & Ho (2013). The SDSS g -band image was calibrated to the V -band using the transformation of Jordi et al. (2006) and the mean $(B - V)$ colors from Hyperleda. We performed an IMFIT bulge (function *Sersic*) plus disk (function *EdgeOnDisk*) decomposition (see Figs. 28 and 35). The best fit parameters are given in Table 27. We set $b = 0.5$ in Table 1, since the galaxy is too edge-on to be certain about the presence or the absence of a bar.

NGC 4151: We take the R -band bulge plus bar plus disk decomposition of Gadotti (2008) and set $b = 1$ in Table 1 (Erwin 2005). Sani et al. (2011) ignore the bar of the galaxy in their fit. We use the R -band M/L value (and black hole mass) of Onken et al. (2007), which we correct for G.E. We follow Ho & Kim (2014) and classify its bulge as classical, but Kormendy (2013) disagrees. Kormendy & Ho (2013) exclude the galaxy from their fits, arguing that the active nucleus makes the dynamical modeling challenging. We exclude this galaxy from the fits reported in Tables 36 and 37.

NGC 4258: The Spitzer 3.6μ images come from Program 20801, PI Seppo Laine, Observer ID 14916. The Sersic bulge plus exponential disk decomposition is performed using the technique of Fisher & Drory (2008), fitting the major axis profile. The result is shown in Fig. 21 and listed in Table 20. This gives $R_e = 13.3''$.

The fit of Sani et al. (2011) has $R_e = 75.8''$ with strong residuals; Läscher et al. (2014) quote $R_e = 118.9''$ for the 'classical' decomposition with strong residuals and $R_e = 4.1''$ for the 6 component fit; we prefer our simpler approach. The M/L is scaled to the distance of Kormendy & Ho (2013) and from V to 3.6μ -band using the $(V - 3.6\mu)$ color using the V -band photometry of Hyperleda.

NGC 4261: The galaxy is a core elliptical (Rusli et al. 2013a). We use their profile and derive $R_e = 54.2''$, in fair agreement with Beifiori et al. (2012), who measure $R_e = 45.82''$ from a Sersic fit to the i -band SDSS image. In contrast, Sani et al. (2011) get $R_e = 20''$ from an improbable bulge plus disk decomposition, given the galaxy type, and Vika et al. (2012) derive $R_e = 21.6''$ from a fit with low n_{Sersic} . The M/L is scaled to the distance of Kormendy & Ho (2013).

NGC 4291: The galaxy is a core elliptical (Rusli et al. 2013a). We use their profile and M/L scaled to the distance of Kormendy & Ho (2013).

NGC 4342: We performed an IMFIT bulge (function *Sersic*) plus disk (function *Exponential*) decomposition on a SDSS i -band image (see Figs. 29 and 35), converting the zero-point to the Cousins I -band using the SDSS $(r - i)$ color and two equations from Jordi et al. (2006). The parameters of the decomposition are given in Table 28. Our fit gives $R_e = 4.9''$, while Vika et al. (2012) quote $R_e = 0.6''$ and Läscher et al. (2014) derive $R_e = 1.1''$ for the classical fit and $R_e = 0.7''$ for the 'best' fit. All fits have systematic residuals, but given that the resolution of the images considered by Vika et al. (2012) (FWHM=0.5'' or 1.1 pixels) and Läscher et al. (2014) (FWHM=0.6'') is too near their quoted R_e , we prefer our solution. The M/L is corrected for G.E. and scaled to the distance of Kormendy & Ho (2013).

NGC 4374: The galaxy is a giant core elliptical (Rusli et al. 2013a). We measure $R_e = 84.0''$, while Vika et al. (2012) derive implausibly small bulge radii from one-component ($R_e = 26.8''$) or bulge plus disk ($R_e = 7.2''$) fits. The M/L is scaled to the distance of Kormendy & Ho (2013).

and from I to V -band using the $(V - I)$ Hyperleda color.

NGC 4388: Our best IMFIT decomposition of this pseudo bulge galaxy is achieved by fitting a central point source (function *Gaussian*), a pseudo bulge (function *Sersic*), a disk (function *Exponential*) plus a ring (function *GaussianRing2Side*) (see Figs. 30 and 35). The parameters of the fit are listed in Table 29. The pseudo bulge component contributes 38% of the total light of the galaxy; Greene et al. (2010) give $B/T = 0.5$, while Kormendy & Ho (2013) quote $B/T = 0.096$, which explains most of the discrepancy observed in Fig. 6. Despite the use of four components, there are still significant residuals, stemming from the strong non-axisymmetric galaxy features. The M/L is computed as in Appendix C to match the velocity dispersion of Greene et al. (2010) within an effective aperture radius of $1.6''$, by considering the circularized surface brightness of the galaxy without the central point source and using the distance of Kormendy & Ho (2013). We classify the galaxy as barred following Kormendy & Ho (2013). In our decomposition the bar is described by the ring component.

NGC 4459: For this E2 galaxy we measure $R_e = 35.2''$ from the whole profile. Beifiori et al. (2012) quote $140.5''$, Sani et al. (2011) give $9.4''$, and Laurikainen et al. (2010) report $5.2''$. The large value of Beifiori et al. (2012) stems from a fit overestimating by 0.4 mag the light of the galaxy at radii larger than $100''$; the fit to a K -band image of the galaxy described by Beifiori (2010) agrees with our value. The discrepancy with the R_e of Sani et al. (2011) and Laurikainen et al. (2010) is driven by their (unplausible large) disk component, that we ignore following Kormendy & Ho (2013). The M/L is scaled to the distance of Kormendy & Ho (2013) and from I to V -band using $(V - I)$ from Hyperleda.

NGC 4473: Contrary to the classification of McConnell & Ma (2013), the galaxy is not a core elliptical (see discussion in Rusli et al. 2013a). We derive $R_e = 35.7''$ using a single profile extending to $261.5''$. Vika et al. (2012) quote $R_e = 16.3''$, fitting a single Sérsic profile to just the inner $70''$. Beifiori et al. (2012) fit two

components, which we do not believe to be real, getting $R_e = 8''$. On the other hand, they derive $R_e = 34''$, in agreement with our value, from the isophotal profile (their Table 3). We correct the M/L for G.E. and scale it to the distance of Kormendy & Ho (2013).

NGC 4486: The galaxy is a giant core elliptical (Rusli et al. 2013a). We derive $R_e = 158.4''$, in disagreement with the 'classical fit' of Läsker et al. (2014) giving $R_e = 59.1''$ and with the fit of Vika et al. (2012), who quote an even smaller $R_e = 34.6''$. The M/L is scaled to the distance of Kormendy & Ho (2013) and corrected for G.E..

NGC 4526: We considered a Spitzer 3.6μ -band image that we calibrated to the I -band using the aperture photometry of Hyperleda. We performed an IMFIT decomposition with 5 structures: a classical bulge (function *Sersic*), an inner disk (function *Exponential*), a bar (function *Sersic_GenEllipse*), an outer (edge-on and diamond-shaped) disk (function *Exponential_GenEllipse*), and two off-center spurs (function *Sersic*), see Figs. 31 and 35). The parameters of the decomposition are given in Table 30. Our B/T (0.11) is much smaller than the value (0.65) quoted by Kormendy & Ho (2013). The M/L is scaled to the distance of Kormendy & Ho (2013).

NGC 4552: The galaxy is a core elliptical (Rusli et al. 2013a). We use their profile extending to $445.8''$ and their M/L scaled to the distance of Sani et al. (2011). We measure $R_e = 82.6''$. Sani et al. (2011) and Vika et al. (2012) derive shorter scale lengths ($R_e = 23.3''$ and $16.5''$ respectively) from a dubious bulge plus disk decomposition (Sani et al. 2011), given the galaxy type, or a fit to a too small ($\approx 100''$) image (Vika et al. 2012). The BH mass comes from the uncertain determination of Cappellari et al. (2008). We exclude this galaxy from the fits reported in Tables 36 and 37.

NGC 4564: We take the bulge profile as decomposed by Kormendy et al. (2009). This gives $R_e = 15.32''$. We prefer it to the result of Vika et al. (2012, $R_e = 2.2''$), who fit a bulge and a bar (without a disk) to an image of average ($1.5''$) seeing. The M/L is computed as in Appendix C

to match the stellar kinematic profiles of Bender et al. (1994) (see Fig. 37), using the distance of Kormendy & Ho (2013).

NGC 4594: We use the Sersic bulge fit of Jardel et al. (2011) and correct their M/L for G.E., scaling it to the distance of Kormendy & Ho (2013). Our $R_e = 133.6''$ is much larger than the unreliable value of Sani et al. (2011, $33.7''$). We set $b = 0.5$ in Table 1, since the galaxy is too edge-on to be sure about the presence or absence of a bar.

NGC 4596: We use the bulge plus disk plus bar decomposition of Vika et al. (2012), which gives $R_e = 11.9''$ with small residuals. We prefer this to Laurikainen et al. (2010), who quote $R_e = 3.2''$ but do not show the fit. The fit of Beifiori et al. (2012) gives $R_e = 44.9''$ without a bar component. The M/L is computed as in Appendix C to match the stellar kinematic profiles of Bettoni & Galletta (1997), summing the disk, bulge and bar profiles (see Fig. 37) and using the distance of Kormendy & Ho (2013).

NGC 4621: The M/L is scaled to the distance of Sani et al. (2011) and calibrated from the I -band to 3.6μ using the I -band aperture photometry from Hyperleda. The Spitzer images come from Program 13649, PI Patrick Cote, Observer ID 522. The BH mass comes from the uncertain determination of Cappellari et al. (2008). We exclude this galaxy from the fits reported in Tables 36 and 37.

NGC 4649: The galaxy is a core elliptical (Rusli et al. 2013a). We use their profile and get $R_e = 99.5''$. Beifiori et al. (2012) quote $R_e = 13.7''$, from a fit with two components, which we do not believe are real, given the galaxy type. The same applies to the decompositions put forward by Sani et al. (2011), who quote $R_e = 42.7''$, Vika et al. (2012), who get $R_e = 41.2''$, or the 'best fit' of Läsker et al. (2014), who derive $R_e = 46.8''$. The M/L of Rusli et al. (2013a) is scaled to the distance of Kormendy & Ho (2013).

NGC 4697: The profile is measured on R -band images taken during the observations described in Erwin et al. (2008). From this we derive $R_e = 65.8''$, in rough agreement with Sani et al. (2011, $R_e = 81''$), Beifiori et al. (2012,

$R_e = 107''$) and the 'classical' fit of Läsker et al. (2014, $R_e = 118''$). The 'best fit' of Läsker et al. (2014) has a bulge with a short scale-length ($R_e = 4.8''$) but adds an envelope component. The M/L is scaled to the distance of Kormendy & Ho (2013), calibrated to the R band using $(V - R) = 0.59$ from the aperture photometry in Hyperleda and corrected for G.E.

NGC 4736: An IMFIT bulge (function *Sersic*) plus disk (function *Exponential*) plus outer ring (function *GaussianRing2Side*) decomposition was performed on a z -band image from SDSS (see Fig. 32 and 35). The parameters of the fit are given in Table 31. A model image of the disk and the outer ring was created, which was then subtracted from the original image. On the residual image an ellipse fit was performed with IRAF to get the bulge profile. The M/L of the bulge calculated by Moellenhoff et al. (1995) was converted to the z -band using the equations of Jordi et al. (2006) and the B, V, R, I aperture magnitudes provided by Hyperleda, and scaled to the distance of Kormendy & Ho (2013). We classify the galaxy as "barred" following Moellenhoff et al. (1995).

NGC 4826: We performed an IMFIT bulge (function *Sersic*) plus disk (function *Exponential*) decomposition on a SDSS i -band image (see Fig. 33) after masking the very strong dust lane. The parameters for the fit are given in Table 32. We subtracted a model image of the disk and performed an ellipse fit on the residual image for the bulge profile. From this we derive $R_e = 31.3''$, while Beifiori et al. (2012) get $R_e = 4''$. The fit of Beifiori et al. (2012) fails to reproduce the photometry at large radii, where the disk dominates. Beifiori (2010) discusses an alternative fit to a K -band image of the galaxy that agrees with us. The M/L is computed as in Appendix C to match the stellar kinematic profiles of Héraudeau & Simien (1998), summing the disk and the bulge profiles (see Fig. 37) and using the distance of Kormendy & Ho (2013).

NGC 4889: The Gunn r -band photometry of Jorgensen & Franx (1994) was calibrated to Cousins R using the transformation of Jordi et al. (2006) and the $(V - R)$ colors from Hyperleda. The galaxy is a core elliptical (Rusli et al. 2013a). We derive $R_e = 47.1''$, while Rusli et al.

(2013a) quote $R_e = 169.2''$ fitting a $n = 9.8$ Core-Sersic profile. The difference is driven by the extrapolation (see Fig. 2). The M/L_R value (scaled to the distance of Kormendy & Ho 2013) is the average of the results for four quadrants given by McConnell et al. (2012) corrected for G.E. Rusli et al. (2013a) get $M/L_R = 5.8$ correcting for G.E., which is the value quoted in the Conclusions of McConnell et al. (2012).

NGC 5077: The surface brightness profile comes from the observations described in Scorza et al. (1998). The M/L is scaled to the distance of Kormendy & Ho (2013), corrected for G.E. and converted from the B to the V -band using the $(B - V)$ color from Hyperleda. We follow McConnell & Ma (2013) and Kormendy & Ho (2013) and consider the galaxy a core elliptical, even though the classification is uncertain (see discussion in Rusli et al. 2013a).

NGC 5128 (Cen A): We deprojected the multi-gaussian expansion of the photometry profile as given in Cappellari et al. (2009) and their M/L_K scaled to the distance of Kormendy & Ho (2013). Despite the strong dust lane and the decomposition proposed by Sani et al. (2011), CenA does not have a strong stellar disk. McConnell & Ma (2013) and Kormendy & Ho (2013) consider the galaxy a core elliptical; we accept their classification, although the strong nuclear dust makes it difficult to determine its core properties (see discussion in Rusli et al. 2013a).

NGC 5576: We used an r -band SDSS image calibrated to the R -band. For this E6 galaxy we derive $R_e = 26.1''$ from a profile extending to $200''$, while Beifiori et al. (2012) quote $64''$ fitting a Sersic model to an image extending to $120''$. Their isophotal profile (Table 3) gives $R_e = 49''$. Our result agrees with Trujillo et al. (2004). Contrary to the classification of McConnell & Ma (2013) and Kormendy & Ho (2013), the galaxy is not a core elliptical (see discussion in Rusli et al. 2013a). The M/L is corrected for G.E., scaled from the V to the R -band using the Hyperleda $(V - R)$ color and using the distance of Kormendy & Ho (2013).

NGC 5813: The galaxy is a core elliptical (Rusli et al. 2013a), we use their profile and M/L , scaled to

the distance of Sani et al. (2011). The large discrepancy between our $R_e = 42.43''$ and the values reported by Sani et al. (2011, $R_e = 98.33''$) and Vika et al. (2012, $R_e = 106.8''$) stem from the outer component of the galaxy (Rusli et al. 2013a)³. The BH mass comes from the uncertain determination of Cappellari et al. (2008). We exclude this galaxy from the fits reported in Tables 36 and 37.

NGC 5845: The surface brightness profile comes from the observations described in Scorza et al. (1998). The M/L is corrected for G.E. and scaled to the distance of Kormendy & Ho (2013).

NGC 5846: The galaxy is a core elliptical (Rusli et al. 2013a). We use their M/L_i and profile extending to $214.5''$ from the center and measure $R_e = 89.4''$. Sani et al. (2011) derive $R_e = 36.5''$ by fitting (with systematic residuals) an image extending to $\approx 160''$ from the center. Laurikainen et al. (2010) perform an unrealistic bulge plus disk decomposition with $B/T = 0.46$ which delivers $R_e = 15.6''$. The BH mass comes from the uncertain determination of Cappellari et al. (2008). We exclude this galaxy from the fits reported in Tables 36 and 37.

NGC 6086: The galaxy is a core elliptical (Rusli et al. 2013a). We use their profile and M/L_R , scaled to the distance of Kormendy & Ho (2013), after subtracting the outer halo component fitted there.

NGC 6251: We confirm the core elliptical classification of the galaxy given by Kormendy & Ho (2013). We derive $R_e = 16.5''$, while Sani et al. (2011) quote $R_e = 38.9''$ from a Sersic fit (with $n_{Ser} = 7$) and a small central point source. The difference is driven by the different amounts of extrapolation. The M/L is corrected for G.E. and scaled from R to I -band using $(R - I) = 0.63$, using the distance of Kormendy & Ho (2013). There are no $(R - I)$ colors measured for this galaxy, but Hyperleda provides $(V - I)$. So we searched for elliptical galaxies with velocity dispersions and $(V - I)$

³We note that Table 3 of Rusli et al. (2013a) reports wrong values for n , r_e and μ_e . The parameters corresponding to the fits presented in their Fig. 2 there are $n = 2.07$, $r_e = 55.98''$ and $\mu_e = 21.57$ mag/arcsec².

colors similar to NGC 6251 and adopted their mean $(R - I)$ value. This matches the predictions of the models of Maraston (2005) for old and metal rich simple stellar populations.

NGC 6264: We took the bulge plus disk decomposition of Kormendy (in prep.), based on the r -band profile of Greene et al. (2010). The M/L is computed by fitting the Jeans equations as in Appendix C to match the average velocity dispersion measured along the minor axis (118 ± 10 km/s) within an effective aperture radius of $1.6''$, with a 20% error and using the distance of Kormendy & Ho (2013). The velocity dispersion along the major axis is much higher (166 km/s) and would give a M/L almost a factor 2 larger.

NGC 6323: We use the bulge plus bar plus disk decomposition of Greene et al. (2010). The M/L is derived as described in Appendix C, by matching the velocity dispersion of Greene et al. (2010) within an effective aperture radius of $1.38''$ and using the distance of Kormendy & Ho (2013). In this process we summed the density contributions of the small bulge and the prominent bar. The resulting M/L ($8.15 M_{\odot}/L_{\odot}$ in the r -band) is suspiciously high, which might explain the discrepancy observed in Fig. 6. We classify the galaxy as barred following Graham & Scott (2013).

NGC 7052: McConnell & Ma (2013) and Kormendy & Ho (2013) consider the galaxy a core elliptical, we accept their classification, although strong nuclear dust makes it difficult to determine its core properties (see discussion in Rusli et al. 2013a). We derive $R_e = 17.4''$ in agreement with Läsker et al. (2014, $R_e = 18.6''$) and the one-component fit of Vika et al. (2012, $R_e = 15.7''$), and compatible with Sani et al. (2011, $R_e = 27.5''$), but different from the two-component fit of Vika et al. (2012, $R_e = 3''$). The M/L is scaled to the distance of Kormendy & Ho (2013) and corrected for G.E.

NGC 7457: The Spitzer images come from Program 30318, PI Giovanni Fazio, Observer ID 2. We perform a Sersic bulge plus exponential disk decomposition along the major axis, following Fisher & Drory (2008); the results are given in Fig. 21 and Table 21. This gives $R_e = 8.7''$,

which agrees with Erwin et al. (2015), Laurikainen et al. (2010) and Sani et al. (2011). The 'classical fit' of Läsker et al. (2014) is clearly too large a bulge ($R_e = 39.4''$), while their multicomponent 'best fit' giving $R_e = 2.3''$ is possibly affected by insufficient resolution ($FWHM = 1.1''$). The M/L is computed as in Appendix C to match the stellar kinematic profiles along the major axis of Emsellem et al. (2004), summing the bulge and the disk profiles (see Fig. 37) and using the distance of Kormendy & Ho (2013).

NGC 7582: We perform a (pseudo) bulge plus bar plus disk decomposition using IMFIT and the 3.6μ Spitzer image. A Sersic bulge (function *Sersic*), a bar (function *Sersic.GenEllipse*), and an exponential disk (function *Exponential*) were fit to the image (see Figs. 34 and 35). The parameters of the fits are given in Table 33. The inclusion of a central point source does not improve the fit. The pseudo bulge contributes 29% of the total light of the galaxy. The large discrepancy with the bulge luminosity and size fitted by Sani et al. (2011) stems from their inclusion in the bulge of the peanut bar present there. The M/L is computed as in Appendix C to match the velocity dispersion of Oliva et al. (1995), measured inside an equivalent $2.48''$ aperture radius, and considering the sum of the bulge, the disk and the bar profiles. The distance is taken from Kormendy & Ho (2013).

NGC 7768: The galaxy is a core elliptical (Rusli et al. 2013a). We use their profile and M/L , scaled to the distance of Kormendy & Ho (2013).

UGC 3789: We use the bulge-disk decomposition of Kormendy (in prep.), based on the H -band profile of Peletier et al. (1999). The M/L is computed as in Appendix C to match the average velocity dispersion measured by Greene et al. (2010) within a radius of $1.4''$ (107 ± 12 km/s) and using the distance of Kormendy & Ho (2013). We classify the galaxy as barred following Graham & Scott (2013); Kormendy & Ho (2013) disagree.

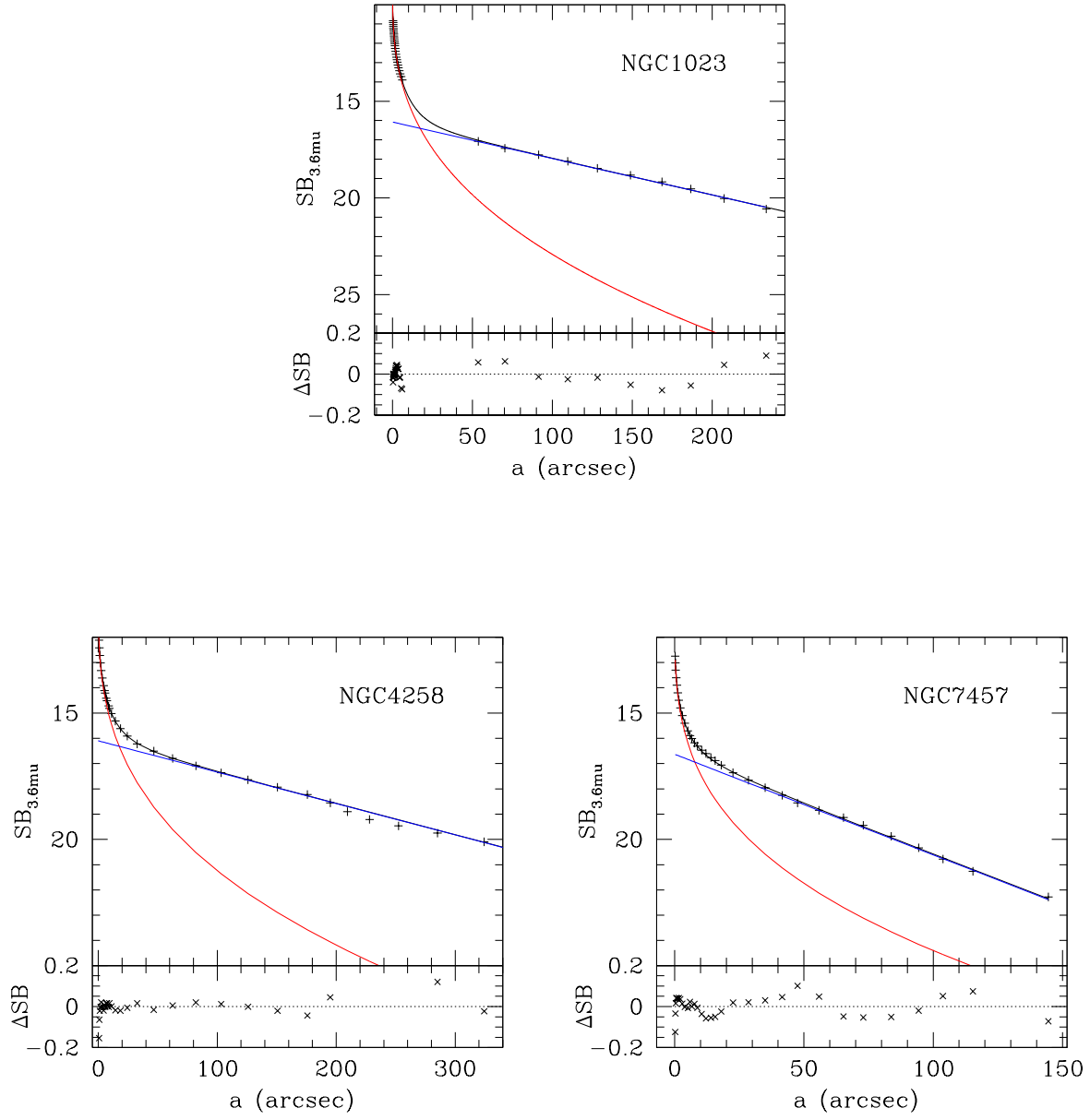


Fig. 21.— The major-axis bulge plus disk fits to the Spitzer 3.6 μ m profiles of NGC 1023, NGC 4258 and NGC 7457 (see text and Table 20).

Table 20: Bulge plus disk fits to the galaxies of Fig. 21.

Galaxy	b/a	n_{Ser}^B	a_e^B (arcsec)	μ_{a_e} (mag arcsec $^{-2}$)	m_{tot}^B (mag)	h^D (arcsec)	μ_0^D (mag arcsec $^{-2}$)	m_{tot}^D (mag)	Bu/T
NGC1023	0.75	2.71 ± 0.02	8.61 ± 0.19	14.8 ± 0.03	7.249 ± 0.04	57.6 ± 0.8	16.08 ± 0.04	5.59 ± 0.04	0.18
NGC4258	0.6	2.91 ± 0.01	17.12 ± 0.21	16.27 ± 0.02	7.43 ± 0.03	87.6 ± 1.05	16.10 ± 0.02	4.95 ± 0.02	0.09
NGC7457	0.75	3.14 ± 0.02	10.1 ± 0.4	17.43 ± 0.05	9.47 ± 0.07	27.3 ± 0.04	16.63 ± 0.04	7.77 ± 0.04	0.17

We list the galaxy name, Column 1; the flattening of the system, Column 2; the parameters of the bulge (major axis half-light radius a_e , Column 4; surface brightness at a_e , Column 5; bulge magnitude, Column 6; exponential scale length of the disk, Column 7; disk central surface brightness, Column 8; disk magnitude, Column 9) and bulge-to-total ratio, Column 10. Surface brightnesses and magnitudes are given in the $3.6mu$ band.

Table 21: Parameters of the bulge plus disk decomposition of NGC 2273.

Bulge	PA[$^\circ$]	ell	n	μ_e [mag/arcsec 2 , R]	a_e [arcsec]	m_{Bu} [R mag]	Bu/T
	34.50 ± 0.03	0.3616 ± 0.0003	0.7937 ± 0.0008	17.2699 ± 0.0008	1.7801 ± 0.0007	13.91	0.08
Bar	PA[$^\circ$]	ell	c_0	μ_e [mag/arcsec 2 , R]	a_e [arcsec]	m_{Bar} [R mag]	Bar/T
	105.08 ± 0.02	0.4022 ± 0.0003	-0.305 ± 0.002	20.2888 ± 0.0009	14.67 ± 0.01	12.43	0.31
Disk	PA[$^\circ$]	ell		μ_0 [mag/arcsec 2 , R]	h [arcsec]	m_{Di} [R mag]	Di/T
	63.76 ± 0.03	0.3919 ± 0.0004		20.868 ± 0.002	33.94 ± 0.03	11.76	0.57
Inner Ring	PA[$^\circ$]	ell		μ_0 [mag/arcsec 2 , R]	r_{ring} [arcsec]	m_{Ri} [R mag]	Ri/T
	64.65 ± 0.05	0.3069 ± 0.0004		21.884 ± 0.002	20.45 ± 0.02	14.65	0.04
	σ_{in} [arcsec]	σ_{out} [arcsec]					
	2.14 ± 0.02	4.31 ± 0.01					

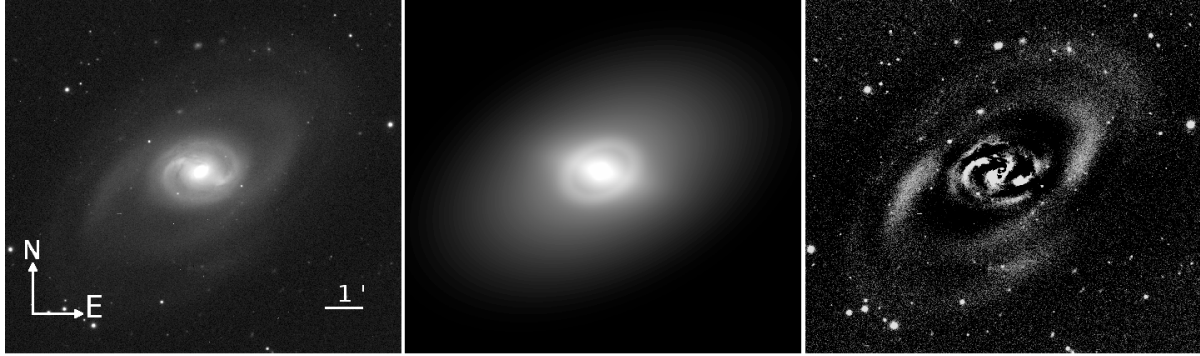


Fig. 22.— The IMFIT model for NGC 2273: the galaxy R -band image (left), the model (middle) and the residuals (right); see also Fig. 35.

Table 22: Parameters of the bulge plus disk decomposition of NGC 2549.

Bulge	PA[$^\circ$]	ell	n	μ_e [mag/arcsec 2 , R]	a_e [arcsec]	m_{Bu} [R mag]	Bu/T
	179.73 ± 0.02	0.5055 ± 0.0002	3.467 ± 0.004	19.23 ± 0.003	13.09 ± 0.003	11.1	0.77
Edge-On-Disk	PA[$^\circ$]	μ_0 [mag/arcsec 2 , R]	h [arcsec]	$\alpha = 2/n$	z_0 [arcsec]	m_{Di} [R mag]	Di/T
	179.31 ± 0.01	20.14 ± 0.002	26.43 ± 0.03	2.38 ± 0.04	5.07 ± 0.03	12.39	0.23

Table 23: Parameters of the bulge-bar-disk decomposition of NGC 2748.

Bulge	PA[$^\circ$]	ell	n	μ_e [mag/arcsec 2 , 3.6mu]	a_e [arcsec]	m_{Bu} [3.6mu mag]	Bu/T
	13.68 ± 0.07	0.386 ± 0.001	1.419 ± 0.003	15.99 ± 0.01	4.447 ± 0.007	10.42	0.15
Disk	PA[$^\circ$]	ell		μ_0 [mag/arcsec 2 , 3.6mu]	h [arcsec]	m_{Di} [3.6mu mag]	Di/T
	41.27 ± 0.01	0.719 ± 0.001		15.50 ± 0.01	16.75 ± 0.01	8.35	0.69
Inner Ring	PA[$^\circ$]	ell		μ_0 [mag/arcsec 2 , 3.6mu]	r_{ring} [arcsec]	m_{Ri} [3.6mu mag]	Ri/T
	44.28 ± 0.04	0.589 ± 0.001		17.30 ± 0.01	10.73 ± 0.01	11.87	0.04
	σ_{ring} [arcsec]						
	2.126 ± 0.009						
Outer Ring	PA[$^\circ$]	ell		μ_0 [mag/arcsec 2 , 3.6mu]	r_{ring} [arcsec]	m_{Ro} [3.6mu mag]	Ro/T
	43.3 ± 0.005	0.822 ± 0.001		17.49 ± 0.01	28.80 ± 0.01	9.09	0.12
	σ_{ring} [arcsec]						
	6.90 ± 0.01						



Fig. 23.— The IMFIT model for NGC 2549: the galaxy r -band image (left), the model (middle) and the residuals (right), see also Fig. 35.

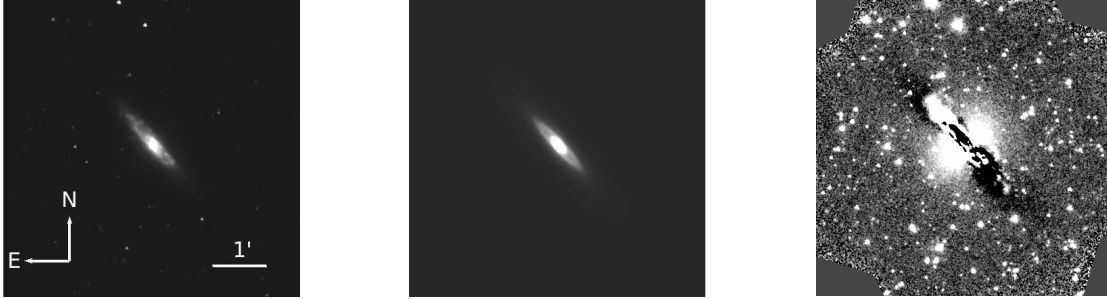


Fig. 24.— The IMFIT model for NGC 2748: the galaxy 3.6μ -band image (left), the model (middle) and the residuals (right); see also Fig. 35.

Table 24: Parameters of the bulge-bar-disk-ring decomposition of NGC 3079.

Bulge	PA[$^{\circ}$] 169.4 ± 0.1	ell 0.79 ± 0.01	n 2.724 ± 0.002	μ_e [mag/arcsec 2 , 3.6μ] 13.00 ± 0.011	a_e [arcsec] 4.50 ± 0.01	m_{Bu} [3.6μ mag] 8.24	Bu/T 0.26
Bar	PA[$^{\circ}$] 171.6 ± 0.1	ell 0.69 ± 0.01	n 0.37 ± 0.01	μ_e [mag/arcsec 2 , 3.6μ] 17.43 ± 0.01	a_e [arcsec] 40.77 ± 0.01	m_{Bar} [3.6μ mag] 8.35	Bar/T 0.24
Disk	PA[$^{\circ}$] 166.9 ± 0.1	ell 0.86 ± 0.01		μ_0 [mag/arcsec 2 , 3.6μ] 16.35 ± 0.01	h [arcsec] 52.87 ± 0.01	m_{Di} [3.6μ mag] 7.83	Di/T 0.38
Ring	PA[$^{\circ}$] 169.2 ± 0.01	ell 0.90 ± 0.01	μ [mag/arcsec 2 , 3.6μ] 16.66 ± 0.01	r_{ring} [arcsec] 52.74 ± 0.01	σ_{ring} [arcsec] 13.11 ± 0.01	m_{Ri} [3.6μ mag] 9.09	Ri/T 0.12



Fig. 25.— The IMFIT model for NGC 3079: the galaxy 3.6 μ -band image (left), the model (middle) and the residuals (right); see also Fig. 35.

Table 25: Parameters of the bulge plus disk decomposition of NGC 3393.

Bulge	PA[$^{\circ}$]	ell		n	μ_e [mag/arcsec 2 , I]	a_e [arcsec]	m_{Bu} [I mag]	Bu/T
	142.1 ± 0.5	0.107 ± 0.002		1.45 ± 0.01	17.27 ± 0.01	1.91 ± 0.01	13.12	0.17
Bar	PA[$^{\circ}$]	ell	c_0	n	μ_e [mag/arcsec 2 , I]	a_e [arcsec]	m_{Bar} [I mag]	Bar/T
	160.5 ± 0.1	0.429 ± 0.002	-0.35 ± 0.01	0.352 ± 0.004	19.632 ± 0.007	9.98 ± 0.03	13.08	0.18
Disk	PA[$^{\circ}$]	ell			μ_0 [mag/arcsec 2 , I]	h [arcsec]	m_{Di} [I mag]	Di/T
	29 ± 4	0.022 ± 0.003			20.022 ± 0.005	18.98 ± 0.06	11.66	0.65

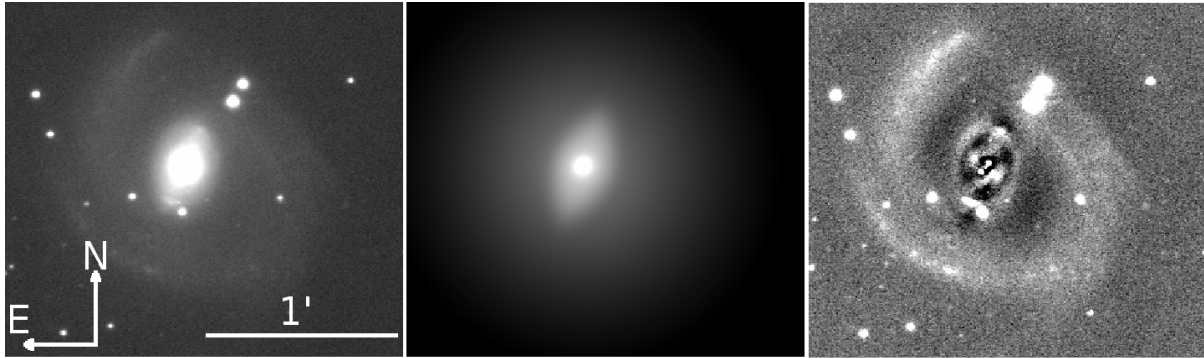


Fig. 26.— The IMFIT model for NGC 3393: the galaxy I -band image (left), the model (middle) and the residuals (right); see also Fig. 35.

Table 26: Parameters of the bulge plus disk decomposition of NGC 3414.

Bulge	PA[°]	ell	n	μ_e [mag/arcsec ² , <i>I</i>]	a_e [arcsec]	m_{Bu} [<i>I</i> mag]	Bu/T
	176.01 ± 0.01	0.1918 ± 0.0005	5.13 ± 0.01	20.827 ± 0.008	28.04 ± 0.14	9.9	0.79
Bar	PA[°]	ell	c_0	μ_e [mag/arcsec ² , <i>I</i>]	a_e [arcsec]	m_{Bar} [<i>I</i> mag]	Bar/T
	199.48 ± 0.04	0.8527 ± 0.0006	0.478 ± 0.006	22.177 ± 0.006	40.59 ± 0.14	13.2	0.04
Disk	PA[°]	ell		μ_0 [mag/arcsec ² , <i>I</i>]	h [arcsec]	m_{Di} [<i>I</i> mag]	Di/T
	35.7 ± 0.3	0.307 ± 0.003		21.152 ± 0.007	33.2 ± 0.1	11.54	0.17



Fig. 27.— The IMFIT model for NGC 3414: the galaxy *I*–band image (left), the model (middle) and the residuals (right); see also Fig. 35.

Table 27: Parameters of the bulge plus disk decomposition of NGC 4026.

Bulge	PA[°]	ell	n	μ_e [mag/arcsec ² , <i>V</i>]	a_e [arcsec]	m_{Bu} [<i>V</i> mag]	Bu/T
	180.9 ± 0.1	0.402457 ± 0.0004	3.242 ± 0.004	19.222 ± 0.003	10.67 ± 0.02	11.36	0.59
Edge-On-Disk	PA[°]	μ_0 [mag/arcsec ² , <i>V</i>]	h [arcsec]	$\alpha = 2/n$	z_0 [arcsec]	m_{Di} [<i>V</i> mag]	Di/T
	177.5 ± 0.1	19.893 ± 0.003	34.34 ± 0.03	1.50 ± 0.01	4.83 ± 0.02	11.76	0.41

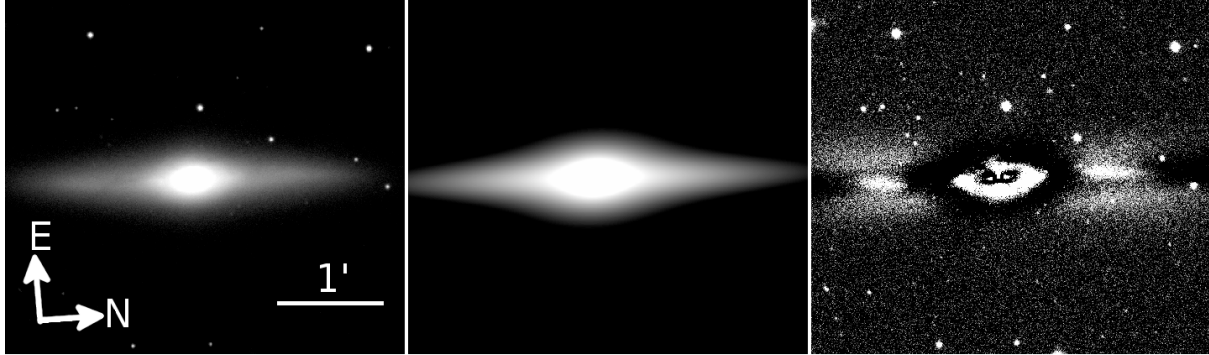


Fig. 28.— The IMFIT model for NGC 4026: the galaxy *V*–band image (left), the model (middle) and the residuals (right); see also Fig. 35.

Table 28: Parameters of the bulge plus disk decomposition of NGC 4342.

Bulge	PA[°]	ell	n	μ_e [mag/arcsec ² , <i>I</i>]	a_e [arcsec]	m_{Bu} [<i>I</i> mag]	Bu/T
	164.99 ± 0.07	0.3420 ± 0.0009	7.51 ± 0.02	18.50 ± 0.008	5.79 ± 0.02	11.42	0.65
Disk	PA[°]	ell		μ_0 [mag/arcsec ² , <i>I</i>]	h [arcsec]	m_{Di} [<i>I</i> mag]	Di/T
	167.46 ± 0.01	0.7680 ± 0.0003		16.22 ± 0.002	5.581 ± 0.005	12.07	0.35

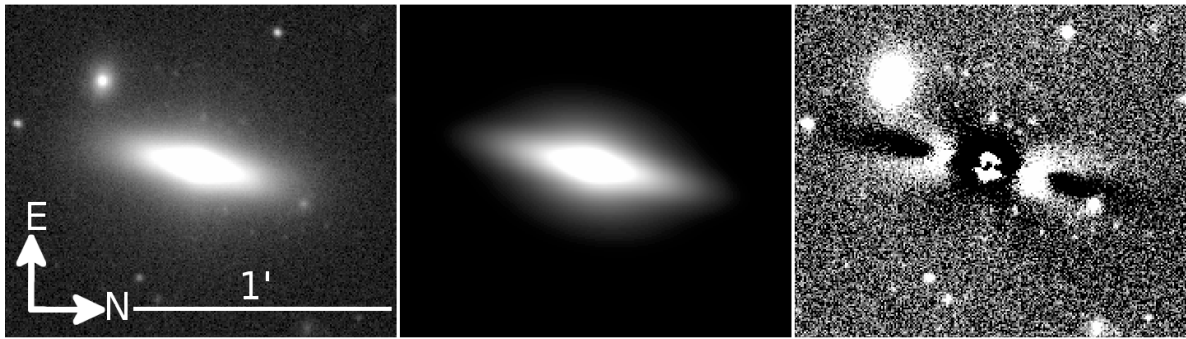


Fig. 29.— The IMFIT model for NGC 4342: the galaxy I -band image (left), the model (middle) and the residuals (right); see also Fig. 35.

Table 29: Parameters of the bulge–ring–disk plus point source decomposition of NGC 4388.

Bulge	PA ^[°] 93.3 ± 0.1	ell 0.494 ± 0.001	n 2.886 ± 0.002	μ_e [mag/arcsec ² , 3.6 <i>m u</i>] 18.23 ± 0.01	a_e [arcsec] 27.82 ± 0.01	m_{Bu} [3.6 <i>m u</i> mag] 8.53	Bu/T 0.38
Disk	PA ^[°] 88.75 ± 0.01	ell 0.830 ± 0.001		μ_0 [mag/arcsec ² , 3.6 <i>m u</i>] 17.29 ± 0.01	h [arcsec] 48.64 ± 0.01	m_{Di} [3.6 <i>m u</i> mag] 8.78	Di/T 0.31
Ring	PA ^[°] 90.97 ± 0.01 σ_{in} [arcsec] 7.39 ± 0.01	ell 0.82 ± 0.01 σ_{out} [arcsec] 12.28 ± 0.01		μ_0 [mag/arcsec ² , 3.6 <i>m u</i>] 16.78 ± 0.01	r_{ring} [arcsec] 28.99 ± 0.01	m_{Ri} [3.6 <i>m u</i> mag] 9.4	Ri/T 0.17
Point Source	PA ^[°] 63.55 ± 0.19	ell 0.649 ± 0.002		μ_0 [mag/arcsec ² , 3.6 <i>m u</i>] 8.392 ± 0.008	σ [arcsec] 0.38 ± 0.01	m_{PS} [3.6 <i>m u</i> mag] 9.63	PS/T 0.14


 Fig. 30.— The IMFIT model for NGC 4388: the galaxy 3.6*mu*–band image (left), the model (middle) and the residuals (right); see also Fig. 35.

Table 30: Parameters of the bulge plus disk decomposition of NGC 4526.

Bulge	PA ^[°] 10.7 ± 1.4	ell 0.15 ± 0.01	n 2.74 ± 0.03	μ_e [mag/arcsec ² , 3.6 <i>m u</i>] 15.84 ± 0.04	a_e [arcsec] 7.3 ± 0.2	m_{Bu} [3.6 <i>m u</i> mag] 8.51	Bu/T 0.11
Inner Disk	PA ^[°] 21.58 ± 0.05	ell 0.69 ± 0.02	n 12.23 ± 0.01	μ_0 [mag/arcsec ² , 3.6 <i>m u</i>] 3.78 ± 0.01	h [arcsec] 8.63	m_{Di} [3.6 <i>m u</i> mag] 0.10	Di/T 0.10
Bar	PA ^[°] 28.28 ± 0.07 c_0 1.55 ± 0.03	ell 0.368 ± 0.001	n 0.738 ± 0.005	μ_e [mag/arcsec ² , 3.6 <i>m u</i>] 16.33 ± 0.01	a_e [arcsec] 19.54 ± 0.04	m_{Bar} [3.6 <i>m u</i> mag] 7.66	Bar/T 0.25
Outer Disk	PA ^[°] 27.97 ± 0.09 c_0 −0.92 ± 0.01	ell 0.710 ± 0.003	n 1	μ_0 [mag/arcsec ² , 3.6 <i>m u</i>] 19.02 ± 0.02	h [arcsec] 154.9 ± 2.6	m_{Do} [3.6 <i>m u</i> mag] 7.83	Do/T 0.21
Spur1	PA ^[°] 16.08 ± 0.06 RA(Spur1)–RA(Center) [arcsec] 31.2 ± 0.1	ell 0.711 ± 0.001 DEC(Spur1)–DEC(Center) [arcsec] −18.1 ± 0.2	n 0.971 ± 0.004	μ_e [mag/arcsec ² , 3.6 <i>m u</i>] 18.99 ± 0.01	a_e [arcsec] 83.62 ± 0.35	m_{Sp1} [3.6 <i>m u</i> mag] 8.05	Sp1/T 0.18
Spur2	PA ^[°] 17.37 ± 0.06 RA(Spur2)–RA(Center) [arcsec] −29.7 ± 0.1	ell 0.710 ± 0.001 DEC(Spur2)–DEC(Center) [arcsec] −17.3 ± 0.2	n 0.756 ± 0.003	μ_e [mag/arcsec ² , 3.6 <i>m u</i>] 18.65 ± 0.01	a_e [arcsec] 67.8 ± 0.2	m_{Sp2} [3.6 <i>m u</i> mag] 8.27	Sp2/T 0.14

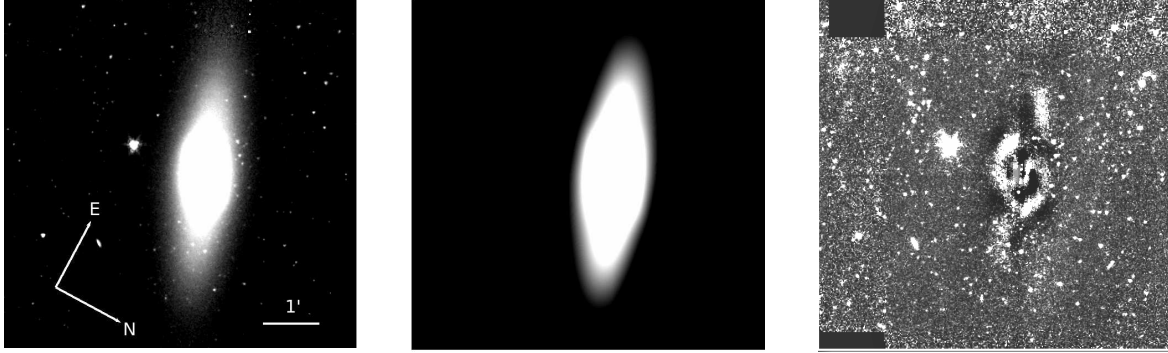


Fig. 31.— The IMFIT model for NGC 4526: the galaxy 3.6 μ -band image (left), the model (middle) and the residuals (right); see also Fig. 35.

Table 31: Parameters of the bulge plus disk decomposition of NGC 4736.

Bulge	PA[$^{\circ}$]	ell	n	μ_e [mag/arcsec 2 , z]	a_e [arcsec]	m_{Bu} [z mag]	Bu/T
	25.80 ± 0.06	0.1582 ± 0.0003	1.405 ± 0.001	16.004 ± 0.001	8.071 ± 0.007	8.8	0.26
Disk	PA[$^{\circ}$]	ell		μ_0 [mag/arcsec 2 , z]	h [arcsec]	m_{Di} [z mag]	Di/T
	106.14 ± 0.04	0.1850 ± 0.0003		16.674 ± 0.002	23.80 ± 0.02	8.02	0.54
Outer Ring	PA[$^{\circ}$]	ell		μ_0 [mag/arcsec 2 , z]	r_{ring} [arcsec]	m_{Ri} [z mag]	Ri/T
	94.44 ± 0.06	0.2497 ± 0.0005		21.011 ± 0.001	110.31 ± 0.09	9.1	0.2
	σ_{in} [arcsec]	σ_{out} [arcsec]					
	23.2 ± 0.1	51.01 ± 0.07					

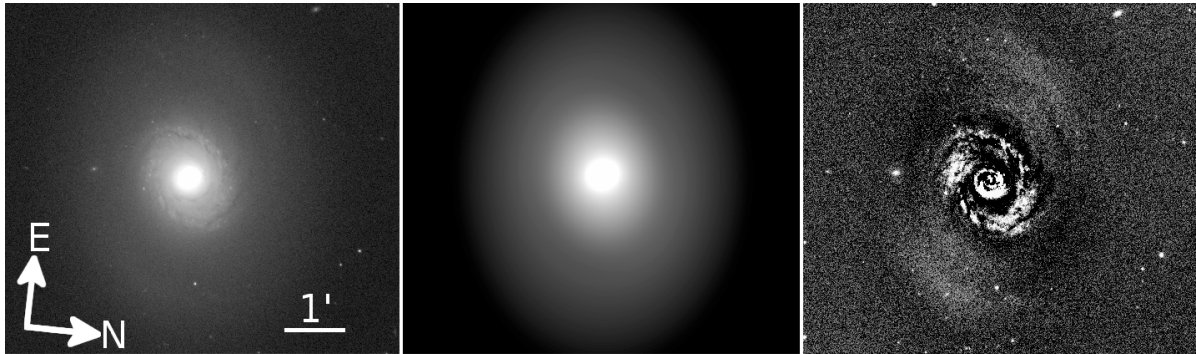


Fig. 32.— The IMFIT model for NGC 4736: the galaxy z -band image (left), the model (middle) and the residuals (right); see also Fig. 35.

Table 32: Parameters of the bulge plus disk decomposition of NGC 4826.

Bulge	PA[°]	ell	n	μ_e [mag/arcsec ² , <i>i</i>]	a_e [arcsec]	m_{Bu} [<i>i</i> mag]	Bu/T
	105.21 ± 0.04	0.2190 ± 0.0003	4.295 ± 0.005	20.106 ± 0.004	36.8 ± 0.1	9.12	0.28
Disk	PA[°]	ell		μ_0 [mag/arcsec ² , <i>i</i>]	h [arcsec]	m_{Di} [<i>i</i> mag]	Di/T
	111.399 ± 0.006	0.4556 ± 0.0001		18.1850 ± 0.0004	56.561 ± 0.009	8.08	0.72

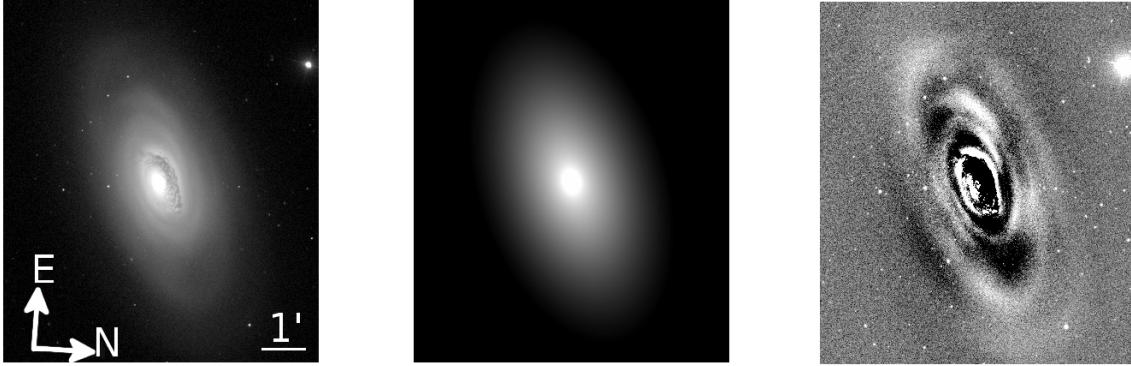


Fig. 33.— The IMFIT model for NGC 4826: the galaxy *i*-band image (left), the model (middle) and the residuals (right); see also Fig. 35.

Table 33: Parameters of the bulge plus bar plus disk decomposition of NGC 7582.

Bulge	PA[°]	ell		n	μ_e [mag/arcsec ² , 3.6 <i>m u</i>]	a_e [arcsec]	m_{Bu} [3.6 <i>m u</i> mag]	Bu/T
	134.6 ± 0.06	0.419 ± 0.001		2.59 ± 0.01	12.71 ± 0.01	2.38 ± 0.01	8.27	0.29
Bar	PA[°]	ell	c_0	n	μ_e [mag/arcsec ² , 3.6 <i>m u</i>]	a_e [arcsec]	m_{Bar} [3.6 <i>m u</i> mag]	Bar/T
	140 ± 0.01	0.869 ± 0.001	1.74 ± 0.02	0.211 ± 0.001	17.20 ± 0.01	51.76 ± 0.04	8.58	0.22
Disk	PA[°]	ell			μ_0 [mag/arcsec ² , 3.6 <i>m u</i>]	h [arcsec]	m_{Di} [3.6 <i>m u</i> mag]	Di/T
	141.4 ± 0.03	0.602 ± 0.001			16.54 ± 0.01	37.3 ± 0.04	7.69	0.49

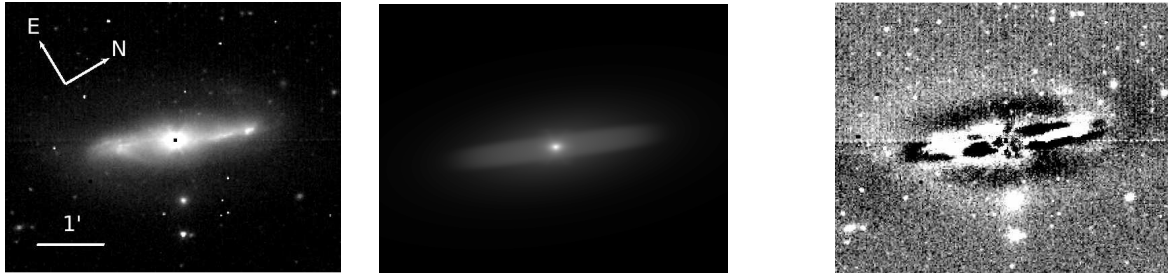


Fig. 34.— The IMFIT model for NGC 7582: the galaxy 3.6μ -band image (left), the model (middle) and the residuals (right); see also Fig. 35.

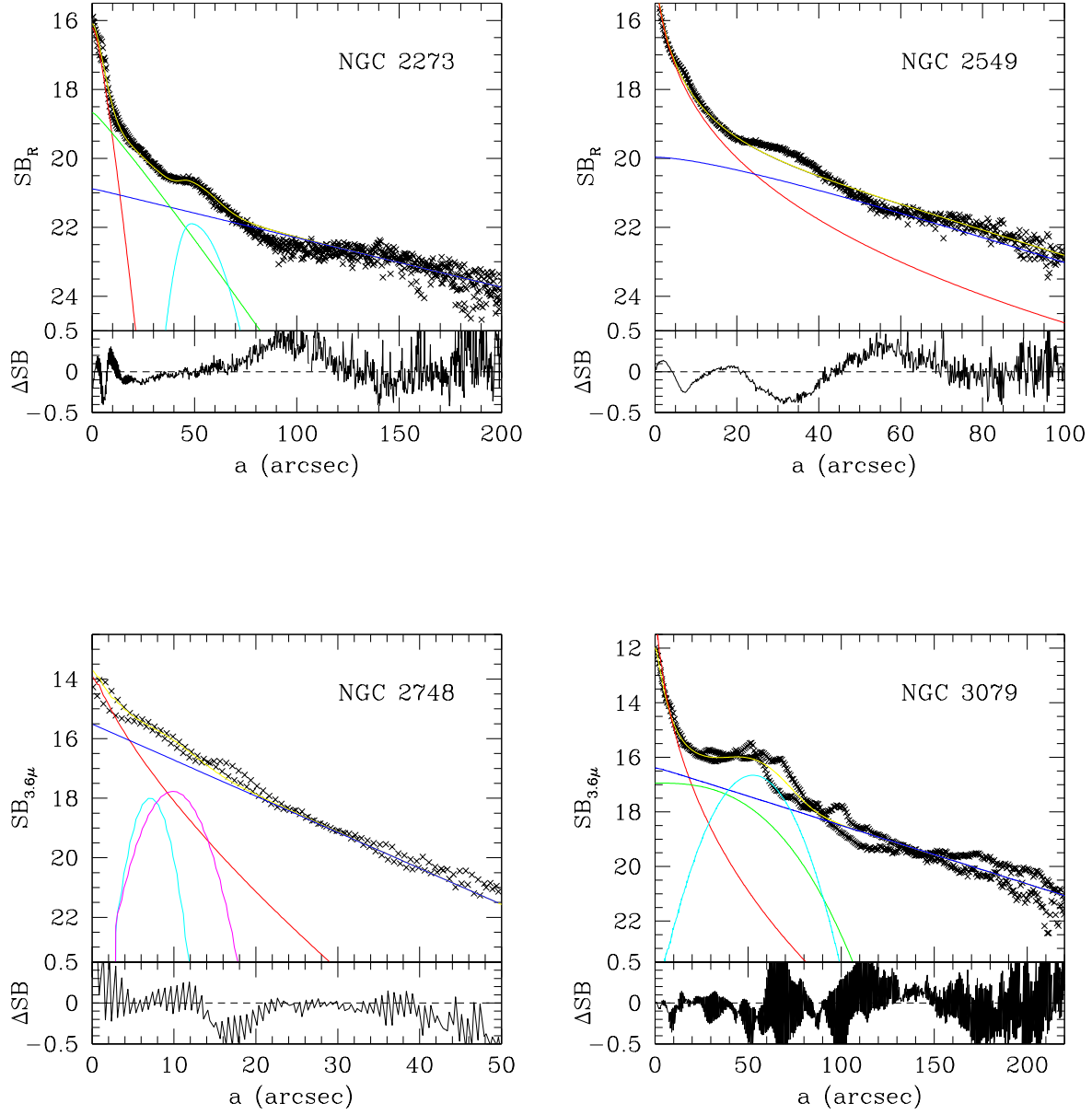


Fig. 35.— Cuts along the bulge major axis for the galaxies where we performed IMFIT decompositions. For each galaxy there are two plots. At the top we show the surface brightness along the bulge major axis (crosses), the resulting point spread function- (PSF-) convolved fitted profile (yellow line) and the unconvolved fitted components (red line: bulge; blue line: disk; green line: bar; cyan line: ring or spurs, magenta line: point source), as a function of the distance from the center. At the bottom we show the difference in surface brightness between measured and PSF-convolved fitted profiles.

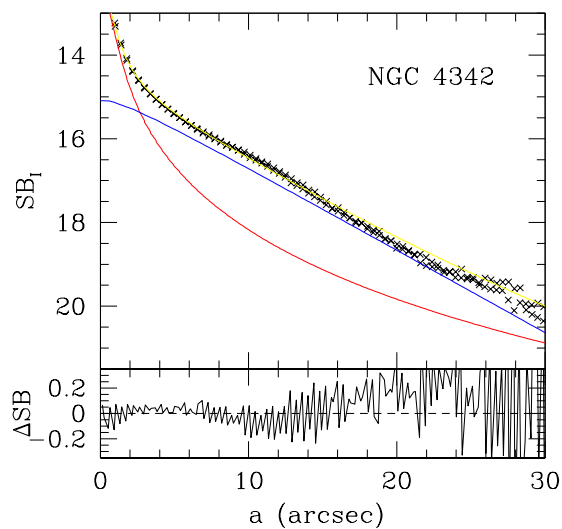
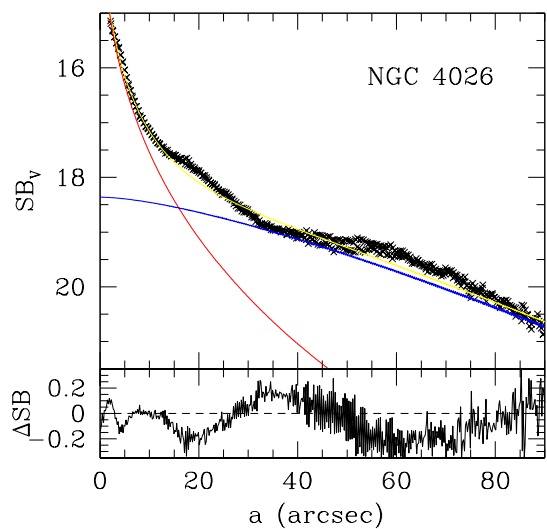
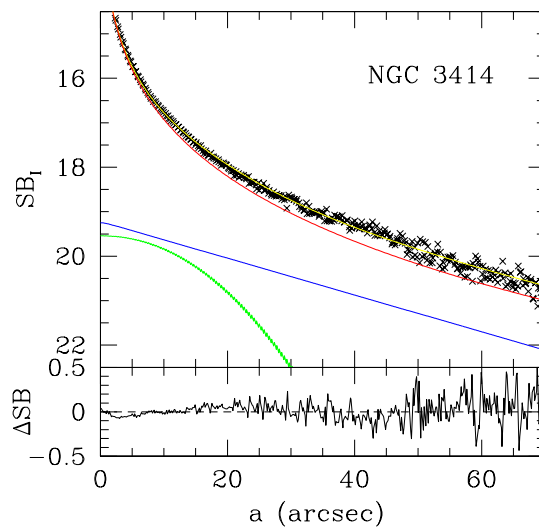
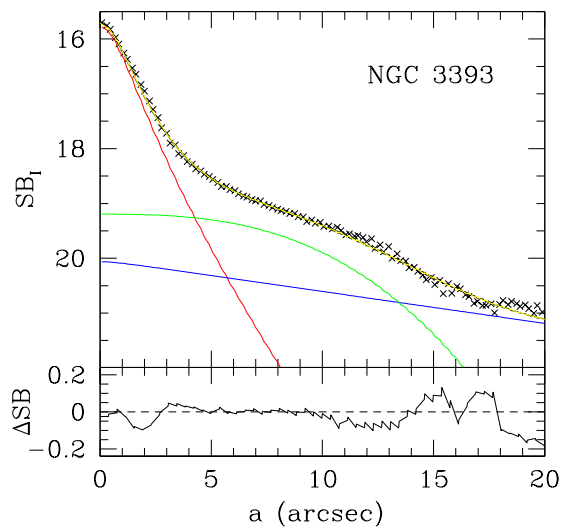


Fig. 35.— Continued.

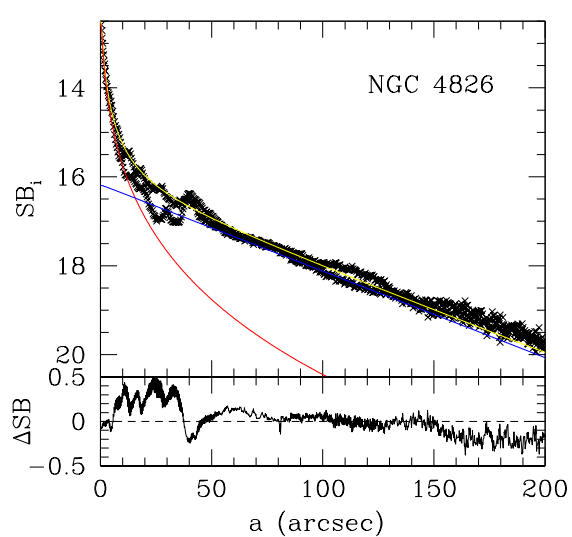
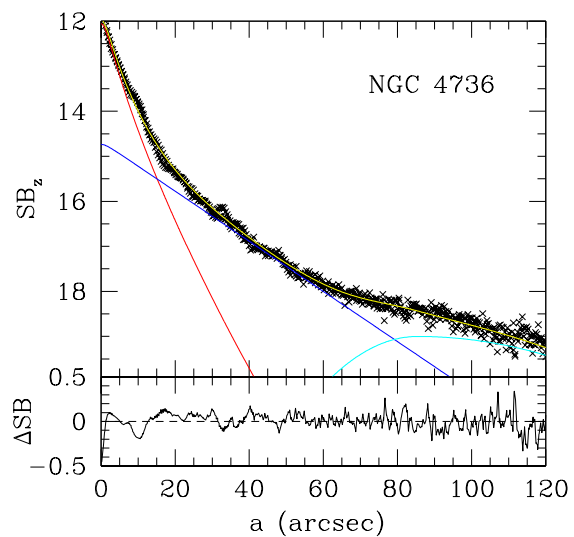
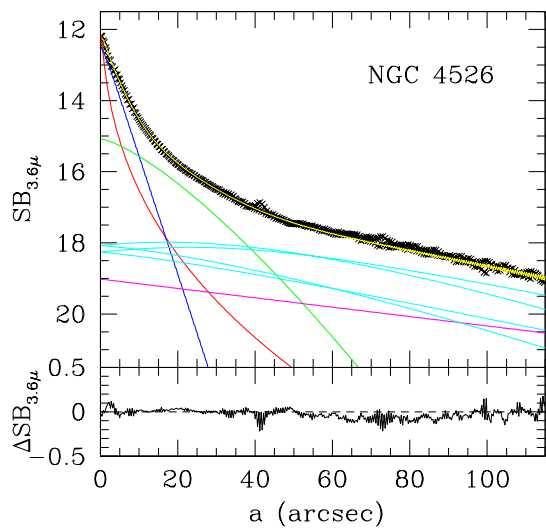
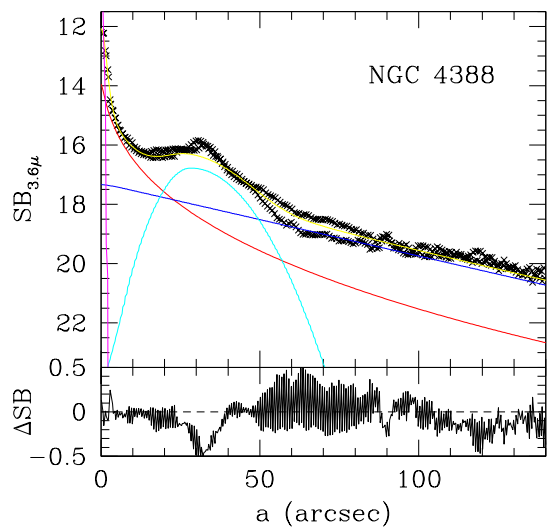


Fig. 35.— Continued.

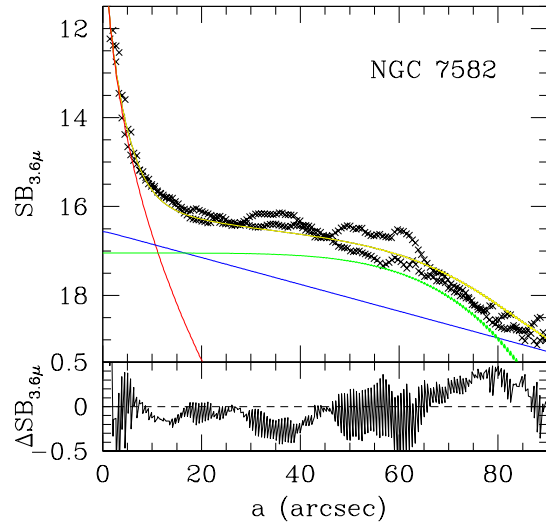


Fig. 35.— Continued.

TABLE 34
THE DYNAMICAL M/L RATIOS OF THE LITERATURE AND SINFONI SAMPLES.

Galaxy	M/L	Band of M/L	$(d \log M/L)^2$	Band of image	Reference
MW	1.00	-	0.001886	-	-
Circinus	0.14	3.6 μ	0.002651	3.6 μ	Sani et al. (2011)
A1836	4.86	I	0.01443	I	SDSS
IC1459	4.91	V	0.001961	V	Rusli et al. (2013a)
IC4296	8.54	B	0.001961	I	Erwin et al. (2016)
NGC221	1.50	R	0.0001532	R	Peletier (1993)
NGC224	4.13	V	0.0001061	V	Kormendy & Bender (1999)
NGC524	4.80	I	0.0006592	I	Cappellari et al. (2006)
NGC821	3.95	R	0.0006942	R	Graham et al. (2001)
NGC1023	0.90	3.6 μ	2.615e-06	3.6 μ	Spitzer
NGC1068	0.37	K	0.02909	K	Erwin et al. (2015)
NGC1194	6.10	r	0.01975	r	SDSS
NGC1300	2.13	V	1.451e-05	V	Fisher & Drory (2008)
NGC1399	10.32	B	0.0001133	B	Saglia et al. (2000)
NGC2273	4.50	R	0.01044	R	Erwin & Sparke (2003)
NGC2549	4.55	R	0.0003426	r	SDSS
NGC2748	0.53	3.6 μ	0.0003018	3.6 μ	Spitzer
NGC2787	2.50	3.6 μ	0.0002153	3.6 μ	Spitzer
NGC2960	3.81	r	0.007132	r	SDSS
NGC2974	1.17	3.6 μ	0.0005821	3.6 μ	Spitzer
NGC3031	2.48	i	9.922e-07	i	Beifiori et al. (2012)
NGC3079	0.37	3.6 μ	0.0003067	3.6 μ	Spitzer
NGC3115	6.13	V	3.643e-05	V	Scorza et al. (1998)
NGC3227	19.68	K	0.001961	K	Davies et al. (2006)
NGC3245	3.40	R	0.001961	i	Beifiori et al. (2012)
NGC3377	2.81	R	0.0003275	R	Graham et al. (2001)
NGC3379	2.77	I	0.0009665	I	Rusli et al. (2013a)
NGC3384	1.44	I	0.0004682	i	SDSS
NGC3393	2.72	I	0.003697	I	Schmitt & Kinney (2000)
NGC3414	4.15	I	0.0005544	i	SDSS
NGC3585	2.89	V	0.000959	V	Scorza et al. (1998)
NGC3607	6.15	V	0.000346	g	SDSS
NGC3608	2.04	I	0.001753	i	SDSS
NGC3842	7.15	V	0.004632	V	Rusli et al. (2013a)
NGC3998	5.21	I	0.07487	i	SDSS
NGC4026	4.91	V	0.0009635	g	SDSS
NGC4151	1.49	R	0.001961	R	Gadotti (2008)
NGC4258	0.55	3.6 μ	0.0002412	3.6 μ	Spitzer
NGC4261	8.89	V	0.003279	V	Rusli et al. (2013a)
NGC4291	5.08	V	0.003171	V	Rusli et al. (2013a)
NGC4342	4.01	I	0.00116	i	SDSS
NGC4374	6.39	V	0.000687	V	Kormendy et al. (2009)
NGC4388	1.30	3.6 μ	0.003625	3.6 μ	Spitzer
NGC4459	3.88	V	0.0006867	V	Kormendy et al. (2009)
NGC4473	6.91	V	0.0004416	V	Kormendy et al. (2009)
NGC4486	6.32	V	0.003142	V	Kormendy et al. (2009)
NGC4526	2.64	I	0.001193	3.6 μ	Spitzer
NGC4552	7.36	V	0.0007571	V	Kormendy et al. (2009)
NGC4564	5.78	V	0.0004514	V	Kormendy et al. (2009)
NGC4594	3.08	I	3.265e-05	I	Jardel et al. (2011)
NGC4596	0.99	K	9.111e-05	K	Vika et al. (2012)

SINFONI Sample

NGC 307: The galaxy has a classical bulge (Thomas et al. 2014; Erwin et al. 2016). We set $b = 0.5$ in Table 1 since the galaxy is too edge-on to be sure about the presence or absence of a bar. We derive its BH mass in Erwin et al. (2016), where we model the stellar kinematics allowing for different M/L for the bulge and the disk components, and no dark matter halo, see Fig. 36. We adopt the distance derived from the Hyperleda radial velocity corrected for Local Group infall onto Virgo and $H_0 = 75$.

NGC1316: We consider the galaxy as a merger remnant and power-law elliptical (Nowak et al. 2008). We derive its BH mass in Nowak et al. (2008).

NGC1332: The galaxy has a prototypical classical bulge (Erwin et al. 2015). We revised our previous velocity dispersion determination of 328 km/s in Rusli et al. (2011) to 293.1 km/s. This stems from the larger half-luminosity radius for the whole galaxy ($28''$) that we use now versus the bulge-only radius ($8.4''$) quoted in Rusli et al. (2011). We derive its BH mass in Rusli et al. (2011).

NGC1374: The galaxy is a power-law elliptical (Rusli et al. 2013a). We derive its BH mass in Rusli et al. (2013b).

NGC1398: The galaxy has a classical bulge (Erwin et al. 2016). We derive its BH mass in Erwin et al. (2016), where we model the stellar kinematics allowing for different M/L for the bulge and the disk components, and no dark matter halo, see Fig. 36. The distance comes from Tully et al. (2009).

NGC1407: The galaxy is a core elliptical (Rusli et al. 2013a). We derive its BH mass in Rusli et al. (2013b).

NGC1550: The galaxy is a core elliptical (Rusli et al. 2013a). We derive its BH mass in Rusli et al. (2013b).

NGC3091: The galaxy is a core elliptical (Rusli et al. 2013a). We derive its BH mass in Rusli et al. (2013b). We measure $R_e = 22.4''$ using the profile of Rusli et al. (2013a), who get $R_e = 90''$

fitting a $n = 9.3$ Core-Sersic profile. The difference is driven by the extrapolation (see Fig. 2).

NGC3368: The galaxy has a composite (classical plus pseudo) bulge (Nowak et al. 2010; Erwin et al. 2015). We derive its BH mass in Nowak et al. (2010).

NGC3489: Following Nowak et al. (2010), the galaxy has a composite (classical plus pseudo) bulge. We use that decomposition, although it is a bit uncertain (Erwin et al. 2015). We derive its BH mass and velocity dispersion in Nowak et al. (2010) and do not compute $\sigma_{e/2}, \sigma_{e/2}^S, \sigma_e^S$ in Table 17 (see discussion in Nowak et al. 2010).

NGC3627: The galaxy has a pseudo bulge (Erwin et al. 2016), that we fit without the box-peanut component. We derive its BH mass in Erwin et al. (2016), where we model the stellar kinematics allowing for different M/L for the bulge and the disk components, and no dark matter halo, see Fig. 36. We analyze its gas emission and kinematics in Mazzalay et al. (2013, 2014), from which we take the distance.

NGC3923: The galaxy is a merger remnant (Bender et al. 2016). We derive the BH mass by fitting the stellar kinematics without dark matter halo, see Fig. 36. We use the mean of the redshift-independent measurements given by the Nasa Extragalactic Database (NED).

NGC4371: The galaxy has a composite (classical plus pseudo) bulge (Erwin et al. 2015). We derive its BH mass in Erwin et al. (2016), where we model the stellar kinematics allowing for different M/L for the bulge and the disk components, and no dark matter halo, see Fig. 36.

NGC4472: The galaxy is a core elliptical (Rusli et al. 2013a). We derive its BH mass in Rusli et al. (2013b).

NGC4486a: The galaxy is a power-law elliptical (Nowak et al. 2007). We derive its BH mass in Nowak et al. (2007). We derive the velocity dispersions quoted in Table 1 and 17 using the profiles of Prugniel et al. (2011), see also Appendix A.

NGC4486b: The galaxy is a compact elliptical (Bender et al. 2016). We derive the black hole mass

TABLE 34—*Continued*

Galaxy	M/L	Band of M/L	$(d \log M/L)^2$	Band of image	Reference
NGC4621	0.66	3.6 μ	0.0006928	3.6 μ	Spitzer
NGC4649	7.67	V	0.002266	V	Rusli et al. (2013a)
NGC4697	3.36	R	0.001467	R	Erwin et al. (2008)
NGC4736	0.61	z	0.001961	z	SDSS
NGC4826	1.33	i	0.0005272	i	SDSS
NGC4889	5.97	R	0.003468	r	Jorgensen & Franx (1994)
NGC5077	3.48	V	0.001961	V	KeyProg
NGC5128	0.63	K	0.01004	K	Cappellari et al. (2009)
NGC5576	3.17	R	0.001889	r	SDSS
NGC5813	4.70	V	0.0007684	V	Rusli et al. (2013a)
NGC5845	4.77	V	0.0004076	V	KeyProg
NGC5846	5.20	I	0.0006278	i	Rusli et al. (2013a)
NGC6086	4.05	R	0.002363	R	Rusli et al. (2013a)
NGC6251	3.62	I	0.001961	I	Graham et al. (2001)
NGC6264	5.27	r	0.007546	r	Greene et al. (2010)
NGC6323	8.15	r	0.01908	r	Greene et al. (2010)
NGC7052	2.17	R	0.001961	R	Graham et al. (2001)
NGC7457	0.65	3.6 μ	0.0005046	3.6 μ	Spitzer
NGC7582	0.07	3.6 μ	0.01245	3.6 μ	Spitzer
NGC7768	7.58	V	0.006975	V	Rusli et al. (2013a)
U3789	0.50	H	0.008882	H	Peletier et al. (1999)
NGC307	1.03	K	6.695e-05	K	Erwin et al. (2016)
NGC1316	0.65	K	0.001886	K	Nowak et al. (2008)
NGC1332	7.10	R	0.0005986	R	Rusli et al. (2011)
NGC1374	5.30	B	0.002417	B	Rusli et al. (2013b)
NGC1398	3.00	R	0.0003303	R	Erwin et al. (2016)
NGC1407	6.60	B	0.003128	B	Rusli et al. (2013b)
NGC1550	4.00	R	0.003566	R	Rusli et al. (2013b)
NGC3091	3.80	I	0.0008164	I	Rusli et al. (2013b)
NGC3368	0.40	K	0.002947	K	Nowak et al. (2010)
NGC3489	0.44	H	0.0003723	H	Nowak et al. (2010)
NGC3627	0.40	K	0.0001181	K	Erwin et al. (2016)
NGC3923	4.22	z	0.003155	z	Bender et al. (2016)
NGC4371	1.71	z	5.221e-05	z	Erwin et al. (2016)
NGC4472	4.90	V	0.001257	V	Rusli et al. (2013b)
NGC4486a	4.00	$zACS$	0.0007368	$zACS$	Nowak et al. (2007)
NGC4486b	6.56	V	0.0004456	V	Bender et al. (2016)
NGC4501	0.54	K	0.0002495	K	Erwin et al. (2016)
NGC4699	0.68	z	0.0005982	z	Erwin et al. (2016)
NGC4751	8.27	R	0.0005339	R	Rusli et al. (2013b)
NGC5018	1.23	I	0.0001083	I	Bender et al. (2016)
NGC5328	4.90	V	0.002828	V	Rusli et al. (2013b)
NGC5419	5.37	R	0.01759	R	Mazzalay et al. (2016)
NGC5516	5.20	R	0.000279	R	Rusli et al. (2013b)
NGC6861	6.10	I	0.000114	I	Rusli et al. (2013b)
NGC7619	3.00	I	0.002567	I	Rusli et al. (2013b)

Column 1, the object name (both literature and SINFONI samples); Column 2 to 4: the dynamical M/L , its band, and its logarithmic error squared; Column 5: the band of the related image; Column 6: the references of the used profiles. When no errors are available, we set the errors to the average value of all the available errors.

by fitting the stellar kinematics without dark matter halo (Bender et al. 2016), see Fig. 36. Our SINFONI black hole mass is 30% smaller than the value used by Kormendy & Ho (2013). We do not use it in the fits, since it is the largest outlier in the correlations involving BH masses. We derive the velocity dispersions quoted in Table 1 and 17 using the profiles of Kormendy et al. (1997) determined at distances between 1.5 and 3 arcsec from the center. This leads to a value of σ different from the one used by Kormendy & Ho (2013), see above. We use the average of the three surface brightness fluctuation distances reported by NED.

NGC4501: The galaxy has a pseudo bulge (Erwin et al. 2016). We derive its BH mass in Erwin et al. (2016), where we model the stellar kinematics allowing for different M/L for the bulge and the disk components, and no dark matter halo, see Fig. 36. We analyze its gas emission and kinematics in Mazzalay et al. (2013, 2014).

NGC4699: The galaxy has a composite (classical plus pseudo) bulge (Erwin et al. 2015). We derive its BH mass in Erwin et al. (2016), where we model the stellar kinematics allowing for different M/L for the bulge and the disk components, and no dark matter halo, see Fig. 36.

NGC4751: The galaxy is a power-law elliptical (Rusli et al. 2013b). We derive its BH mass in Rusli et al. (2013b), but correct the M/L , having discovered that Rusli et al. (2013b) incorrectly used the magnitude of the sun in the V band instead of the R band.

NGC5018: The galaxy is a power-law elliptical, see Thomas et al. (2016) where we measure M_{BH} allowing for a dark matter halo as in Rusli et al. (2013b), see Fig. 36. We take the Tully-Fisher mean distance of Theureau et al. (2007).

NGC5328: The galaxy is a core elliptical (Rusli et al. 2013a). We derive its BH mass in Rusli et al. (2013b). We find $R_e = 29.4''$ using the profile of Rusli et al. (2013a), who get $R_e = 76.8''$ fitting a $n = 11.1$ Core-Sersic profile⁴. However, the difference is compatible with our estimated errors due to extrapolation.

NGC5419: The galaxy is a core elliptical (Mazzalay et al. 2016, where we measure its BH mass). We derive the distance from the radial velocity corrected for Local Group infall onto Virgo from Hyperleda using $H_0 = 72$.

NGC5516: The galaxy is a core elliptical (Rusli et al. 2013a). Kormendy & Ho (2013) use a black hole mass slightly different from our value published in Rusli et al. (2013b).

NGC6861: The galaxy is a power-law elliptical (Rusli et al. 2013b). We derive its BH mass in Rusli et al. (2013b).

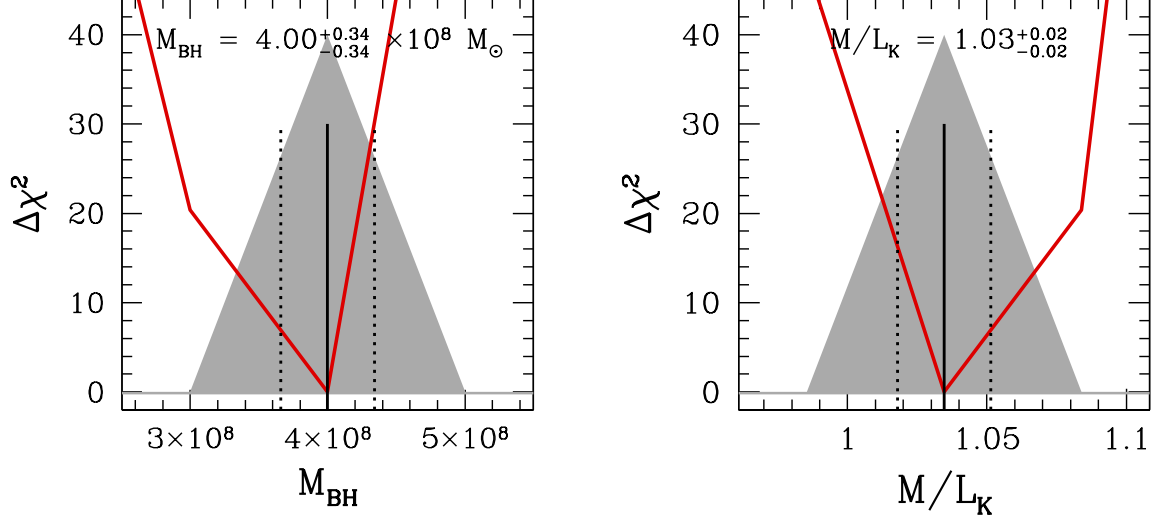
NGC7619: The galaxy is a core elliptical (Rusli et al. 2013a). We derive $R_e = 42''$ using the profile of Rusli et al. (2013a), who get $R_e = 100''$ fitting a $n = 9.3$ Core-Sersic profile. The difference is driven by the extrapolation (see Fig. 2). Kormendy & Ho (2013) use a black hole mass slightly different from our value published in Rusli et al. (2013b).

Appendix C: M/L from stellar kinematics

For a number of galaxies in Table 34 no dynamically determined M/L is available in the literature. Nevertheless, for all of these objects stellar kinematics of some sort is available, either as stellar velocity and velocity dispersion profiles or central velocity dispersions. In these cases we determine the M/L by solving the Jeans equations for a self-consistent, isotropic non-rotating spherical system, using the spherically deprojected surface brightness profiles determined in Sect. 2. If radially extended stellar kinematics is available, we fit $\sigma_{kin}(R) = \sqrt{v(R)^2 + \sigma(R)^2}$. Fig. 37 shows the resulting fits for the ten galaxies with extended kinematics. When the bulge and disk profiles are of similar luminosity in the radial range where the stellar kinematics is available, we solve the Jeans equations by summing the two deprojected contributions and determining the M/L value (equal for both components) that minimizes χ^2 . The errors on M/L are computed by looking at $\chi^2 = \chi^2_{min} + 1$. When only a “central” velocity dispersion is available, we select the M/L that predicts a line-of-sight velocity dispersion $\sigma_{ap} = \sqrt{\langle \sigma^2 L \rangle_{ap} / \langle L \rangle_{ap}}$, luminosity-averaged over the effective aperture with radius $r_{ap} = \sqrt{\text{slitwidth} \times \text{slitlength} / \pi}$, matching the observed value. The percentage error on M/L is twice the percentage error on the observed velocity dispersion.

⁴There is a mistake in their Table 2, where μ_b should read 16.73 instead of 17.07.

NGC307



NGC1398

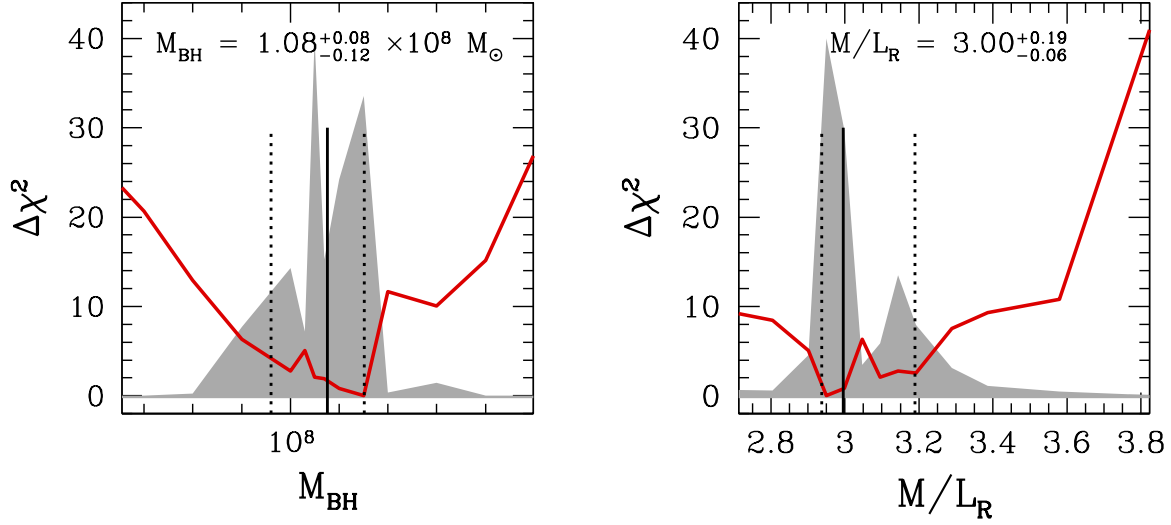
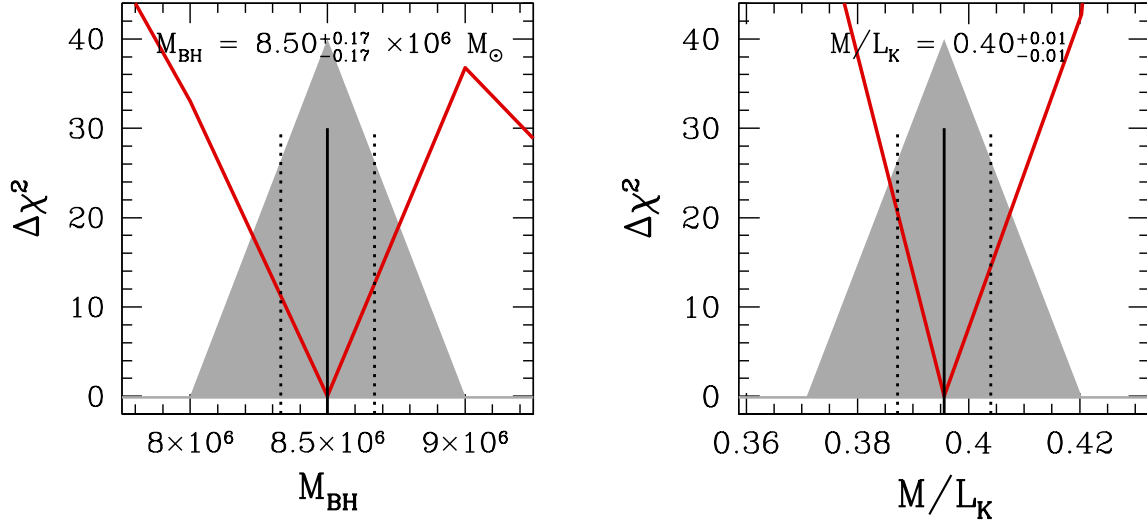


Fig. 36.— We show two plots for each SINFONI galaxy where we have not yet published a complete analysis of our data. The left plot shows the marginalized posterior probability P , scaled arbitrarily to a maximum value of 40 (shaded, see Eq. 4 of Rusli et al. 2013b) and $\Delta\chi^2$ (red lines) vs. M_{BH} ; the plot to the right shows P and $\Delta\chi^2$ as a function of M/L . The vertical solid lines show the derived values; the vertical dashed lines show the 1σ errors.

NGC3627



NGC3923

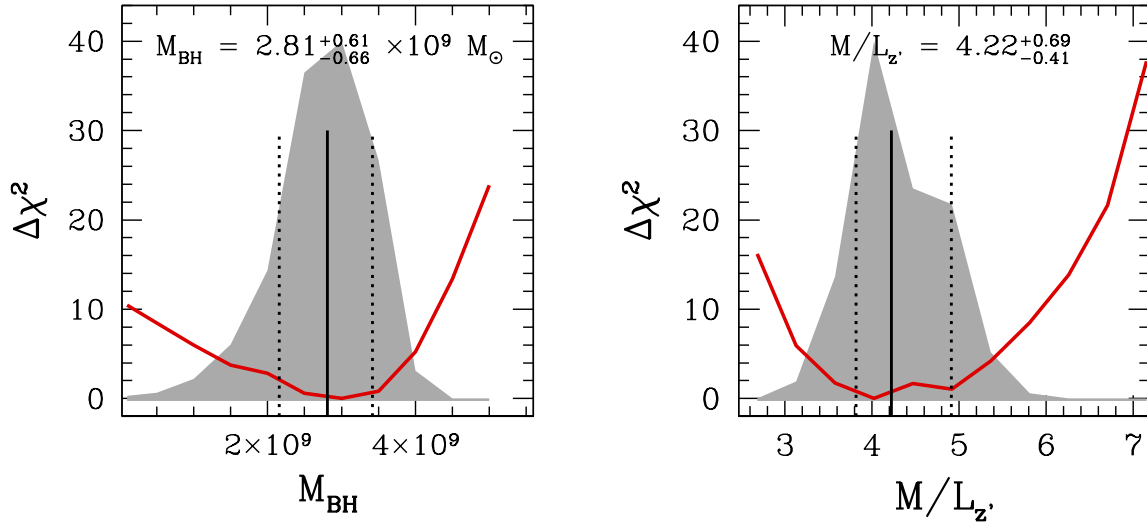
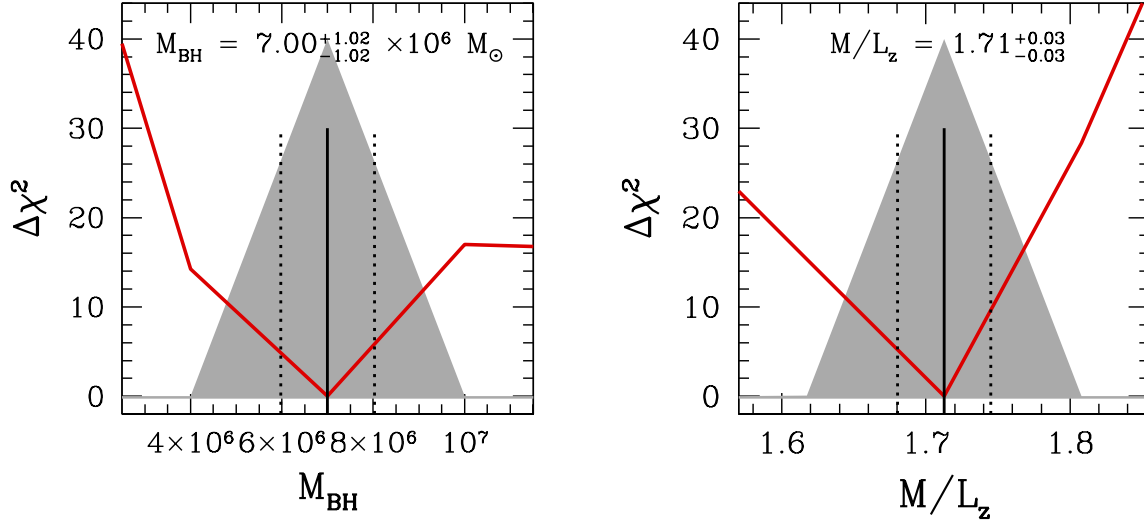


Fig. 36.— Continued

NGC4371



NGC4486B

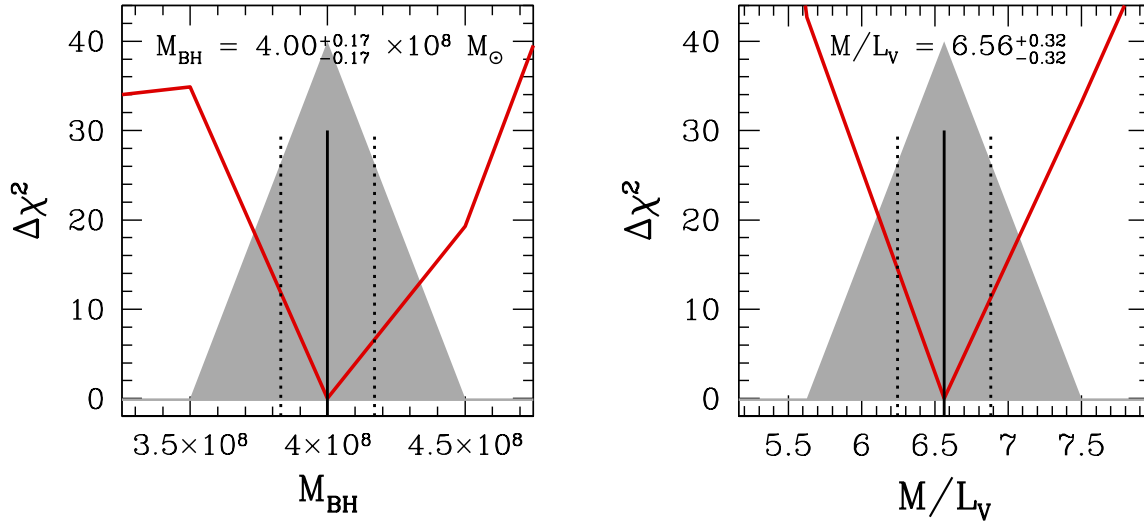
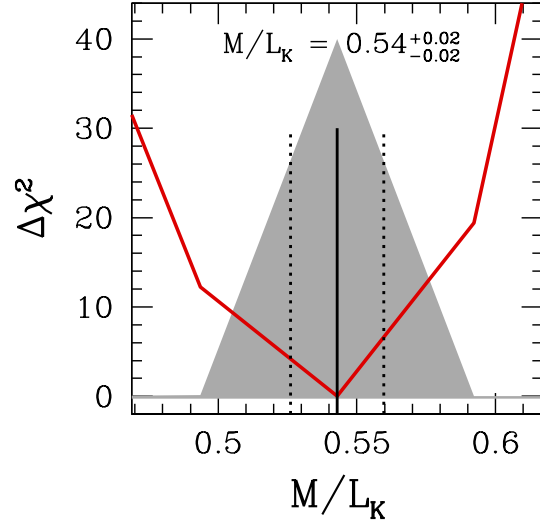
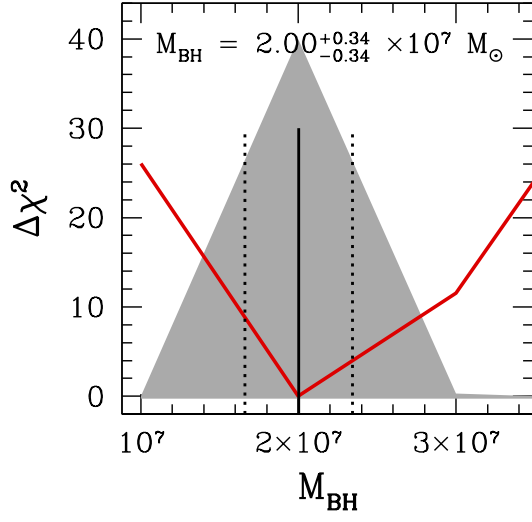


Fig. 36.— Continued

NGC4501



NGC4699

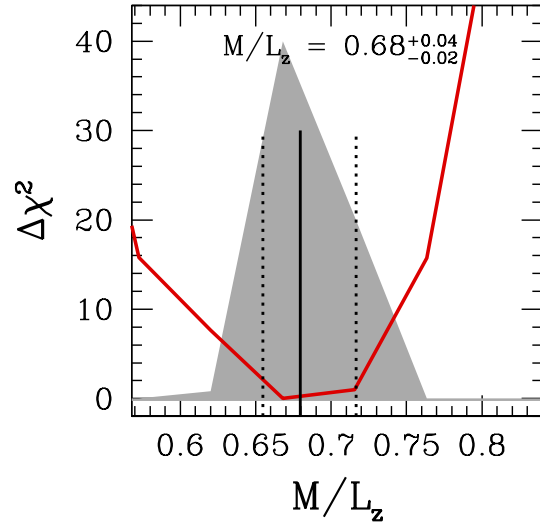
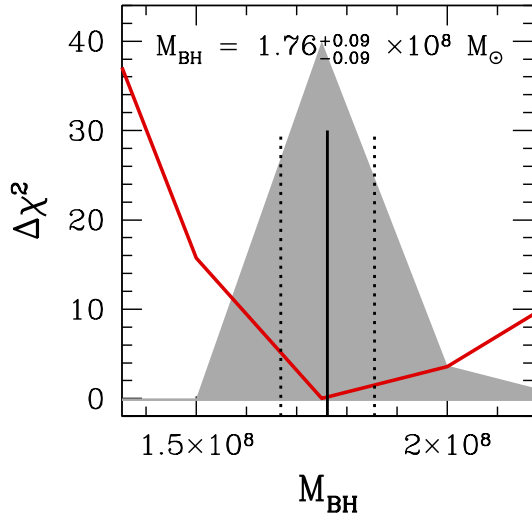


Fig. 36.— Continued

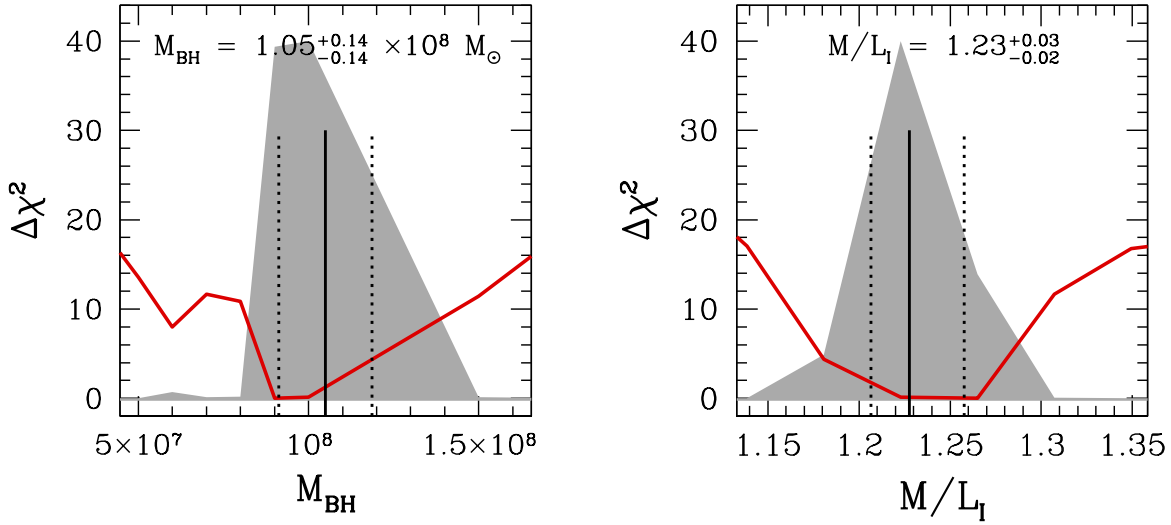


Fig. 36.— Continued

This approach is a drastic simplification of the appropriate dynamical modeling of the galaxies, which would need to take into account the geometry of the objects and the dynamical effects of the central black hole and dark matter halos, not to mention the presence of bars. In order to estimate how wrong our simple dynamical estimates of M/L can be, we apply both methods (i.e. $(M/L)_{\text{kin}}$ from the spherical Jeans modeling of $\sqrt{V^2 + \sigma^2}$, or $(M/L)_{\text{ap}}$ from modeling of the single aperture velocity dispersion) to the sample of SINFONI galaxies where we performed the full Schwarzschild modeling of the available extended stellar kinematics, deriving $(M/L)_{\text{best}}$. To compute M/L_{ap} we consider the σ_{col} of Table 17, obtained by fitting the SINFONI collapsed spectrum. Since the SINFONI field of view is $3 \times 3 \text{ arcsec}^2$, the radius of the equivalent aperture is $r_{\text{ap}} = 3/\pi^{1/2} = 1.7 \text{ arcsec}$.

In Table 35 we report the ratios $(M/L)_{\text{kin}}/(M/L)_{\text{best}}$ and $(M/L)_{\text{ap}}/(M/L)_{\text{best}}$. On average, our simple methods tend to overestimate the true M/L values by 40% with similar scatter ($\approx 0.15 \text{ dex}$). There are no trends with M_{BH} , σ , r_h or ρ_h .

Appendix D: Fits without NGC 2974, NGC 3079, NGC 3414, NGC 4151, NGC 4552, NGC 4621, NGC 5813, NGC 5846.

Tables 36 and 37 report the results of the mono- and bivariate correlations involving black hole masses, excluding the galaxies NGC 2974, NGC 3079, NGC 3414, NGC 4151, NGC 4552, NGC 4621, NGC 5813, NGC 5846, for which only uncertain black hole masses are available. No significant differences with the results reported for the full sample (see Tables 11 and 12) are found.

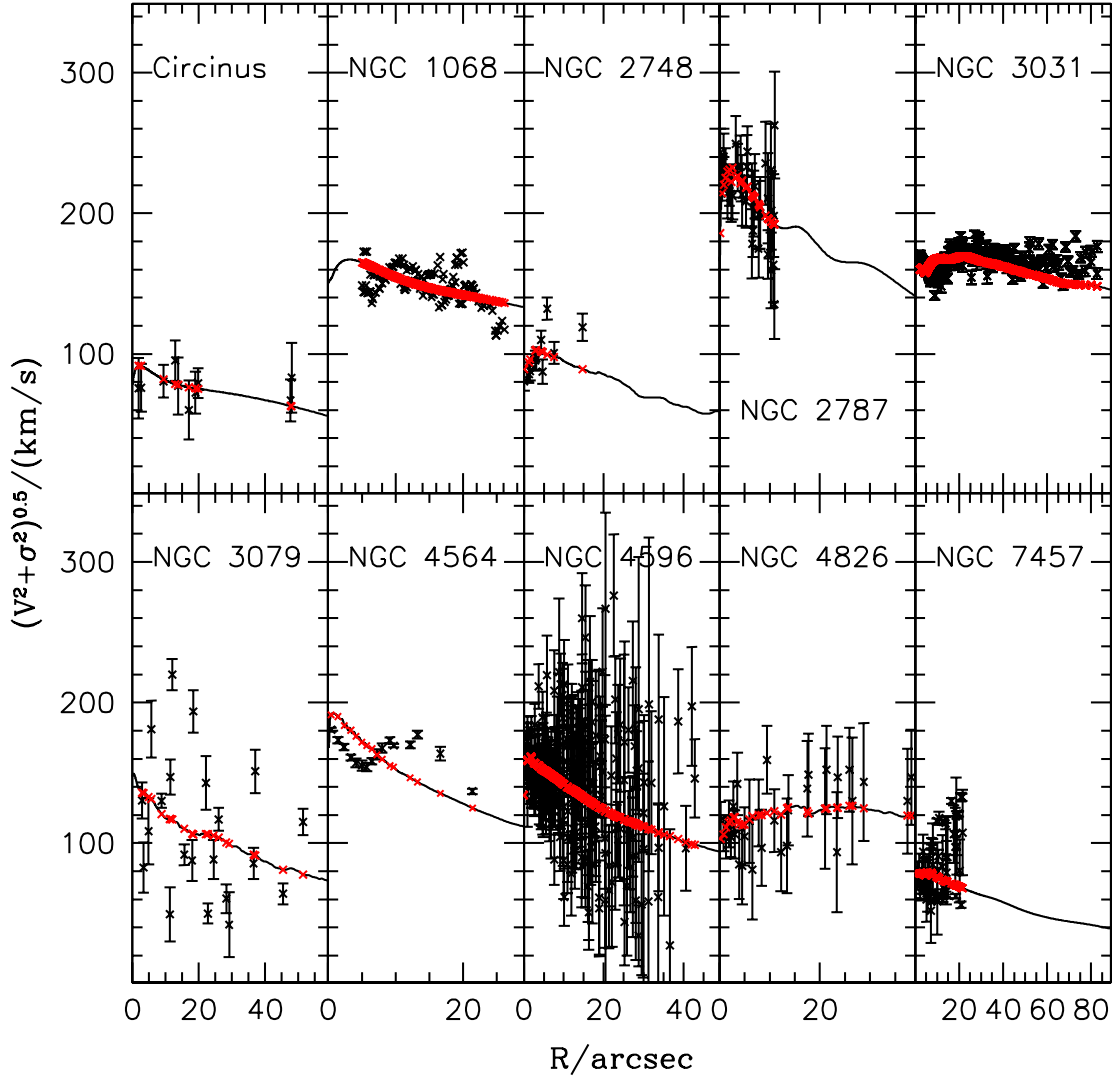


Fig. 37.— The spherical Jeans fits to the ten galaxies with extended stellar kinematics, but without dynamical M/L . The black crosses show the datapoints, the black line the model, and the red crosses the values of the model at the radii where data are available.

TABLE 36

ONE-DIMENSIONAL CORRELATIONS DERIVED WITHOUT THE GALAXIES NGC 2974, NGC 3079, NGC 3414, NGC 4151, NGC 4552, NGC 4621, NGC 5813, NGC 5846.

Fit	Sample	N	a	da	ZP	dZP	ϵ	d ϵ	rms	r_S	$P(r_S)$
$M_{BH}-\sigma$	All	88	5.175	0.274	-3.594	0.63	0.412	0.04	0.457	0.9111	7.33e-35
	CoreE	28	4.782	0.857	-2.499	2.102	0.351	0.068	0.379	0.6494	0.000185
	CorePowerE	42	4.696	0.48	-2.341	1.155	0.397	0.055	0.411	0.7838	8.33e-10
	CorePowerEClass	64	4.521	0.342	-1.961	0.81	0.365	0.041	0.392	0.8667	2.17e-20
	CorePowerEClassPC	70	4.864	0.333	-2.815	0.781	0.396	0.041	0.423	0.883	5.06e-24
	CorePowerEClassPCSINFONI	22	4.979	0.717	-3.032	1.714	0.501	0.092	0.446	0.7134	0.000194
	CorePowerEClassPCLit	50	4.805	0.393	-2.698	0.912	0.36	0.05	0.406	0.9051	1.88e-19
	CorePowerEClassnoBars	56	4.56	0.359	-2.026	0.855	0.352	0.044	0.388	0.8524	7.82e-17
	PowerE	14	4.052	0.939	-0.974	2.15	0.543	0.146	0.435	0.7231	0.00348
	PowerEClass	36	3.799	0.474	-0.396	1.088	0.369	0.055	0.364	0.817	1.22e-09
	PowerEClassPC	42	4.219	0.469	-1.431	1.067	0.418	0.056	0.417	0.8315	9.14e-12
	Pseudo	18	2.662	1.268	1.449	2.656	0.397	0.113	0.428	0.4556	0.0574
$M_{BH}-M_{Bu}$	All	88	0.963	0.07	-2.085	0.75	0.545	0.046	0.548	0.8503	1.07e-25
	CoreE	28	0.915	0.236	-1.418	2.744	0.442	0.078	0.431	0.5566	0.0021
	CorePowerE	42	0.991	0.118	-2.337	1.342	0.455	0.061	0.455	0.7321	3.59e-08
	CorePowerEClass	64	0.905	0.086	-1.342	0.951	0.441	0.047	0.458	0.7822	2.33e-14
	CorePowerEClassPC	70	0.864	0.067	-0.885	0.732	0.445	0.045	0.46	0.8214	3.07e-18
	CorePowerEClassPCSINFONI	22	0.943	0.119	-1.619	1.315	0.446	0.085	0.403	0.8557	3.84e-07
	CorePowerEClassPCLit	50	0.81	0.081	-0.384	0.888	0.45	0.056	0.461	0.8132	7.22e-13
	CorePowerEClassnoBars	56	0.937	0.097	-1.726	1.084	0.446	0.051	0.458	0.7616	9.38e-12
	PowerE	14	0.924	0.254	-1.681	2.744	0.604	0.167	0.484	0.5016	0.0676
	PowerEClass	36	0.809	0.142	-0.362	1.514	0.475	0.069	0.47	0.5808	0.000204
	PowerEClassPC	42	0.779	0.103	-0.033	1.087	0.474	0.063	0.468	0.6927	3.72e-07
	Pseudo	18	0.087	0.297	6.17	2.96	0.512	0.117	0.466	0.003098	0.99
$M_{BH}-\tau_h$	All	88	1.141	0.109	7.913	0.08	0.666	0.054	0.647	0.7573	1.37e-17
	CoreE	28	1.068	0.325	8.181	0.328	0.468	0.08	0.451	0.5746	0.00138
	CorePowerE	42	1.304	0.192	7.888	0.172	0.515	0.069	0.508	0.672	1.1e-06
	CorePowerEClass	64	1.014	0.133	8.139	0.101	0.546	0.055	0.545	0.702	1.02e-10
	CorePowerEClassPC	70	1.005	0.105	8.136	0.082	0.552	0.053	0.549	0.7479	1.02e-13
	CorePowerEClassPCSINFONI	22	1.092	0.199	8.26	0.171	0.597	0.112	0.514	0.8229	2.57e-06
	CorePowerEClassPCLit	50	0.945	0.123	8.071	0.092	0.54	0.063	0.538	0.7217	3.34e-09
	CorePowerEClassnoBars	56	1.085	0.156	8.074	0.127	0.55	0.061	0.545	0.6875	4.83e-09
	PowerE	14	1.159	0.423	7.809	0.267	0.714	0.19	0.571	0.3099	0.281
	PowerEClass	36	0.73	0.232	8.119	0.116	0.609	0.083	0.583	0.3441	0.0399
	PowerEClassPC	42	0.807	0.167	8.075	0.097	0.605	0.075	0.583	0.4924	0.000924
	Pseudo	18	0.035	0.345	7.044	0.149	0.522	0.121	0.464	0.01962	0.938
$M_{BH}-\rho_h$	All	88	-0.576	0.074	13.39	0.669	0.765	0.063	0.747	-0.6849	1.86e-13
	CoreE	28	-0.528	0.2	13.33	1.563	0.498	0.088	0.481	-0.4936	0.00761
	CorePowerE	42	-0.698	0.132	14.55	1.074	0.584	0.08	0.588	-0.5951	3.22e-05
	CorePowerEClass	64	-0.475	0.084	12.74	0.72	0.629	0.064	0.625	-0.632	2.13e-08
	CorePowerEClassPC	70	-0.495	0.068	12.89	0.603	0.641	0.062	0.635	-0.6888	4.35e-11
	CorePowerEClassPCSINFONI	22	-0.535	0.137	13.42	1.185	0.719	0.133	0.614	-0.7811	1.78e-05
	CorePowerEClassPCLit	50	-0.466	0.079	12.53	0.705	0.62	0.072	0.616	-0.6622	1.63e-07
	CorePowerEClassnoBars	56	-0.5	0.1	12.95	0.841	0.64	0.07	0.63	-0.6109	5.72e-07
	PowerE	14	-0.537	0.279	12.92	2.418	0.819	0.217	0.67	-0.2659	0.358
	PowerEClass	36	-0.223	0.135	10.3	1.238	0.674	0.092	0.647	-0.2036	0.234
	PowerEClassPC	42	-0.319	0.105	11.11	0.995	0.696	0.086	0.665	-0.3821	0.0125
	Pseudo	18	-0.008	0.17	7.111	1.647	0.518	0.117	0.465	-0.09086	0.72
$M_{BH}-M_{Bu}^{0.5}\sigma^2$	All	88	1.195	0.062	-3.626	0.619	0.415	0.038	0.441	0.9119	5.22e-35
	CoreE	28	1.162	0.225	-3.227	2.416	0.376	0.07	0.384	0.6288	0.000339
	CorePowerE	42	1.16	0.112	-3.232	1.173	0.38	0.053	0.395	0.7848	7.66e-10
	CorePowerEClass	64	1.104	0.079	-2.63	0.813	0.345	0.039	0.374	0.8578	1.39e-19
	CorePowerEClassPC	70	1.103	0.065	-2.62	0.663	0.355	0.037	0.378	0.8822	6.3e-24
	CorePowerEClassPCSINFONI	22	1.153	0.129	-3.051	1.328	0.398	0.077	0.359	0.8472	6.55e-07
	CorePowerEClassPCLit	50	1.062	0.078	-2.263	0.787	0.339	0.045	0.373	0.8959	1.56e-18
	CorePowerEClassnoBars	56	1.12	0.086	-2.8	0.891	0.349	0.043	0.38	0.8365	1.01e-15
	PowerE	14	1.074	0.224	-2.411	2.241	0.497	0.135	0.407	0.6264	0.0165
	PowerEClass	36	1.031	0.121	-1.926	1.204	0.358	0.054	0.362	0.7578	8.72e-08
	PowerEClassPC	42	1.046	0.098	-2.083	0.959	0.366	0.05	0.37	0.8148	5.16e-11
	Pseudo	18	0.41	0.379	3.287	3.463	0.489	0.118	0.452	0.2251	0.369
$M_{BH}-M_{Bu}\sigma^2$	All	88	0.747	0.043	-3.183	0.657	0.458	0.04	0.471	0.8941	9.72e-32
	CoreE	28	0.732	0.154	-2.875	2.546	0.396	0.071	0.397	0.6099	0.000569
	CorePowerE	42	0.745	0.074	-3.106	1.196	0.396	0.055	0.409	0.772	2.15e-09
	CorePowerEClass	64	0.698	0.053	-2.336	0.837	0.371	0.041	0.396	0.8377	6.15e-18
	CorePowerEClassPC	70	0.683	0.043	-2.1	0.671	0.38	0.039	0.4	0.8663	3.5e-22
	CorePowerEClassPCSINFONI	22	0.728	0.079	-2.704	1.258	0.403	0.077	0.365	0.876	9.19e-08
	CorePowerEClassPCLit	50	0.651	0.052	-1.664	0.814	0.37	0.047	0.398	0.868	3.36e-16
	CorePowerEClassnoBars	56	0.715	0.061	-2.613	0.968	0.377	0.046	0.401	0.8153	2.02e-14
	PowerE	14	0.697	0.153	-2.421	2.352	0.52	0.14	0.424	0.6044	0.0221
	PowerEClass	36	0.656	0.085	-1.715	1.301	0.389	0.058	0.392	0.7261	5.37e-07
	PowerEClassPC	42	0.643	0.067	-1.515	1.006	0.398	0.053	0.397	0.794	3.51e-10
	Pseudo	18	0.165	0.24	4.714	3.392	0.508	0.118	0.459	0.06402	0.801

Column 1: Fit type; Column 2: Sample type, see Table 8; Column 3: number of data points; Column 4 and 5: slope of the correlation and its error; Column 6 and 7: zero-point of the correlation and its errors; Column 8 and 9: intrinsic scatter and its errors; Column 10: measured scatter; Column 11 and 12: Spearman coefficient and its probability.

TABLE 37

TWO-DIMENSIONAL CORRELATIONS DERIVED WITHOUT THE GALAXIES NGC 2974, NGC 3079, NGC 3414, NGC 4151, NGC 4552, NGC 4621, NGC 5813, NGC 5846.

Fit	Sample	a	da	b	db	Zp	dZp	ϵ	d ϵ	rms	$P(b \neq 0)$	$\Delta cAIC$	RP	τ_S	$P(\tau_S)$
$MBH \cdot \sigma \cdot \rho_h$	All	4.521	0.315	-0.17	0.047	-0.571	1.036	0.376	0.036	0.412	0.999	-10.69	0.005	0.4782	2.46e-06
	CoreE	4.409	0.138	-0.106	0.196	-0.757	3.94	0.356	0.069	0.367	0.7228	2.448	3.74	0.238	0.127
	CorePowerE	3.906	0.246	-0.246	0.109	-1.357	2.03	0.367	0.052	0.369	0.9865	-2.59	0.274	0.4889	0.00002
	CorePowerEClass	3.948	0.365	-0.179	0.054	-0.917	1.165	0.328	0.037	0.35	0.9991	-6.611	0.013	0.4624	0.00012
	CorePowerEClassPC	3.019	0.355	-0.195	0.047	-0.868	1.124	0.343	0.036	0.36	0.9999	-14.76	0.001	0.5261	2.91e-06
	CorePowerEClassPCSNFONI	3.994	0.819	-0.219	0.099	-0.196	2.652	0.453	0.088	0.384	0.9734	-1.02	0.002	0.6077	0.00012
	CorePowerEClassPCSNFONIP	4.014	0.4	-0.19	0.087	-0.815	1.226	0.236	0.044	0.357	0.9894	-12	0.002	0.4256	0.000206
	CorePowerEClassPCSNFONIP	4.014	0.407	-0.152	0.067	-0.753	1.349	0.353	0.042	0.337	0.9894	-28.16	0.002	0.4217	0.000121
	CorePowerEClassPCSNFONIP	3.455	0.963	-0.271	0.185	2.523	1.169	0.431	0.145	0.389	0.9894	1.683	0.589	0.4573	0.0048
	PowerEClass	3.73	0.144	-0.16	0.075	-2.228	1.261	0.341	0.052	0.335	0.9824	-7.027	0.363	0.5344	0.0038
	PowerEClassPC	3.73	0.144	-0.16	0.075	-2.228	1.261	0.341	0.052	0.335	0.9824	-7.027	0.363	0.5344	0.0038
	PowerEClassPC	2.656	1.319	0.016	0.149	1.307	3.214	0.424	0.123	0.336	0.9531	-3.331	0.534	0.4086	0.00303
	Pseudo	1.3	0.15	0.311	0.116	-8.467	2.572	0.534	0.046	0.336	0.9935	4.943	0.084	0.505	0.08566
$MBH \cdot M_{BH} \cdot \rho_h$	All	1.135	0.576	0.212	0.438	-3.664	4.905	0.449	0.081	0.436	0.6864	2.505	3.499	0.2271	5.23e-07
	CoreE	1.16	0.274	0.171	0.239	-3.653	4.919	0.461	0.065	0.455	0.7693	1.94	2.657	0.2388	0.128
	CorePowerE	1.164	0.168	0.232	0.12	-6.198	2.797	0.441	0.048	0.447	0.9724	-1.465	0.481	0.4145	0.000661
	CorePowerEClass	1.128	0.15	0.228	0.11	-5.761	2.541	0.441	0.044	0.445	0.9806	-2.016	0.365	0.4739	3.42e-05
	CorePowerEClassPC	1.301	0.252	0.296	0.185	-8.124	4.276	0.443	0.085	0.382	0.9466	0.464	1.261	0.5257	0.0012
	CorePowerEClassPCSNFONI	1.022	0.182	0.195	0.135	-3.593	3.088	0.453	0.057	0.456	0.9271	0.291	1.157	0.3678	0.0086
	CorePowerEClassPCSNFONIP	1.228	0.183	0.255	0.137	-7.123	3.088	0.453	0.051	0.449	0.9638	-1.172	0.357	0.4162	0.00042
	CorePowerEClassPCSNFONIP	1.084	0.444	0.16	0.373	4.573	7.628	0.632	0.185	0.479	0.9838	3.861	6.893	0.2088	0.474
	PowerEClass	1.08	0.187	0.295	0.132	-5.939	2.956	0.453	0.068	0.436	0.9894	-2.485	0.289	0.5131	0.00131
	PowerEClassPC	1.073	0.159	0.235	0.117	-5.828	2.619	0.457	0.06	0.44	0.9928	-3.688	0.138	0.5736	6.67e-05
	PowerEClassPC	0.065	0.516	0.033	0.315	6.069	7.819	0.537	0.128	0.466	0.9563	3.52	5.543	0.09288	0.971
	Pseudo	4.288	0.371	0.334	0.098	-1.662	0.832	0.381	0.036	0.414	0.9999	3.9437	0.009	0.4902	1.25e-06
	CoreE	4.374	1.305	0.184	0.398	-1.678	2.925	0.358	0.068	0.37	0.6843	2.526	3.535	0.2882	0.168
	CorePowerE	3.583	0.681	0.47	0.219	-0.044	1.508	0.37	0.053	0.374	0.9837	-2.171	0.338	0.4684	0.00076
$MBH \cdot \sigma \cdot \tau_h$	All	3.699	0.42	0.355	0.114	-0.217	0.952	0.331	0.037	0.353	0.9987	-7.459	0.024	0.4636	0.00014
	CorePowerEClass	3.7	0.413	0.397	0.098	-0.262	0.938	0.343	0.036	0.361	0.9999	-14.31	0.001	0.5338	1.14e-06
	CorePowerEClassPC	3.434	0.925	0.508	0.215	0.385	2.125	0.436	0.084	0.372	0.9885	-2.541	0.281	0.6702	0.00042
	CorePowerEClassPCSNFONI	3.744	0.459	0.363	0.104	-0.377	1.039	0.305	0.044	0.346	0.9997	-9.84	0.007	0.4231	0.00022
	CorePowerEClassPCSNFONIP	3.85	0.49	0.305	0.144	-0.341	1.101	0.357	0.042	0.36	0.982	-2.179	0.336	0.4033	0.00205
	CorePowerEClassPCSNFONIP	3.163	1.12	0.524	0.384	0.845	2.474	0.507	0.151	0.38	0.9217	2.184	2.98	0.3011	0.296
	PowerEClass	3.469	0.474	0.314	0.153	0.297	1.075	0.343	0.052	0.337	0.9798	-1.68	0.432	0.2659	0.117
	PowerEClassPC	3.538	0.468	0.388	0.121	0.097	1.061	0.361	0.048	0.355	0.9986	-7.89	0.019	0.4198	0.00564
	PowerEClassPC	2.709	1.357	-0.114	0.3	1.327	2.862	0.422	0.119	0.427	0.6603	3.219	4.999	-0.1063	0.675
	Pseudo	1.609	0.262	-0.926	0.353	-8.74	2.706	0.532	0.047	0.336	0.9935	4.688	0.096	-0.7317	5.59e-16
	CoreE	1.342	1.035	-0.621	1.381	-5.776	7.074	0.449	0.082	0.436	0.6692	2.537	3.555	-0.4439	0.018
	CorePowerE	1.336	0.492	-0.518	0.705	-3.848	5.043	0.46	0.064	0.455	0.7712	1.91	2.598	-0.4098	0.00704
	CorePowerEClass	1.399	0.281	-0.701	0.365	-6.447	2.927	0.442	0.048	0.448	0.9743	-1.402	0.496	-0.6084	9.65e-08
	CorePowerEClassPC	1.351	0.251	-0.681	0.327	-5.921	2.608	0.441	0.045	0.45	0.9816	-2.091	0.352	-0.6483	1.3e-09
$MBH \cdot M_{BH} \cdot \tau_h$	All	1.6	0.42	-0.896	0.548	-8.454	4.381	0.421	0.084	0.382	0.9514	0.344	1.188	-0.7222	0.00048
	CorePowerEClass	1.218	0.308	-0.579	0.404	-4.59	3.189	0.454	0.055	0.455	0.9223	0.319	1.173	-0.6116	2.37e-06
	CorePowerEClassPC	1.483	0.307	-0.771	0.409	-7.344	3.189	0.434	0.052	0.449	0.9717	-1.226	0.542	-0.538	7.9e-06
	CorePowerEClassPCSNFONI	1.204	0.799	-0.461	1.143	-4.528	3.813	0.636	0.183	0.478	0.6698	3.889	6.99	-0.4769	0.0846
	CorePowerEClassPCSNFONIP	1.375	0.295	-0.882	0.393	-6.207	3.073	0.453	0.067	0.435	0.9871	-2.499	0.287	-0.7027	1.77e-06
	CorePowerEClassPCSNFONIP	1.361	0.262	-0.865	0.352	-6.083	2.726	0.445	0.06	0.44	0.9934	-3.003	0.165	-0.7618	4.66e-09
	PowerEClass	1.027	0.82	0.021	0.96	6.78	8.531	0.55	0.131	0.464	0.5035	3.362	5.371	0.09288	0.971
	PowerEClassPC	0.298	0.099	3.933	0.508	-3.949	0.606	0.392	0.038	0.425	0.9985	-6.793	0.033	0.5174	2.44e-07
	PowerEClassPC	0.058	0.366	4.617	1.604	-2.773	2.409	0.361	0.071	0.377	0.9856	2.714	3.885	0.1191	0.546
	Pseudo	0.348	0.209	3.365	0.937	-3.1	1.175	0.382	0.054	0.389	0.9519	-0.323	0.851	0.4401	0.00354
	CorePowerE	0.33	0.123	3.254	0.582	-3.1	0.795	0.339	0.039	0.365	0.9954	-4.909	0.086	0.4953	3.16e-05
	CorePowerEClass	0.381	0.099	3.14	0.537	-2.954	0.69	0.347	0.037	0.371	0.9999	-12.51	0.002	0.6067	2.59e-08
	CorePowerEClassPC	0.589	0.211	2.247	1.154	-3.045	1.397	0.409	0.081	0.359	0.9955	-4.78	0.092	0.7899	1.23e-05
	CorePowerEClassPCSNFONI	0.314	0.111	3.377	0.618	-2.808	0.812	0.319	0.045	0.362	0.9965	-5.709	0.058	0.4788	0.00036
$MBH \cdot M_{BH} \cdot \sigma$	All	0.285	0.149	3.569	0.667	-2.649	0.896	0.334	0.042	0.37	0.9632	2.971	4.416	0.2596	0.37
	CorePowerE	0.391	0.377	2.745	1.573	-2.213	2.233	0.528	0.153	0.402	0.8659	-0.726	0.696	0.3332	0.0346
	CorePowerEClass	0.286	0.158	2.986	0.631	-1.59	1.211	0.348	0.053	0.346	0.9639	-4.076	0.0549	0.5449	0.00019
	CorePowerEClassPC	0.374	0.118	2.848	0.605	-2.241	0.965	0.363	0.05	0.362	0.9984	-7.546	4.01	-0.2673	0.284
	CorePowerEClassPCSNFONI	-0.219	0.287	3.668	1.523	2.769	3.091	0.423	0.122	0.423	0.7966	2.778	4.01	-0.2673	0.284

Table 35: The ratios $(M/L)_{kin}/(M/L)_{best}$ and $(M/L)_{ap}/(M/L)_{best}$ for the SINFONI sample of galaxies, without NGC 3489 (see App. C).

Galaxy	$(M/L)_{kin}/(M/L)_{best}$	$(M/L)_{ap}/(M/L)_{best}$
NGC0307	1.667	1.583
NGC1316	1.015	0.8354
NGC1332	0.9507	1.434
NGC1374	1.336	1.585
NGC1398	1.45	1.84
NGC1407	1.618	1.627
NGC1550	1.328	1.273
NGC3091	1.353	1.337
NGC3368	1.275	2.825
NGC3627	1.35	1.447
NGC3923	1.13	1.456
NGC4371	1.251	1.229
NGC4472	1.592	1.449
NGC4486a	0.9375	0.81
NGC4486b	1.101	1.609
NGC4501	1.358	1.23
NGC4699	1.467	1.451
NGC4751	1.493	1.345
NGC5018	1.04	0.665
NGC5328	1.455	1.706
NGC5419	1.33	1.2
NGC5516	1.386	1.09
NGC6861	1.19	0.8557
NGC7619	1.443	1.37

Column 1: Fit type; Column 2: Sample type, see Table 8; Column 3 and 4: first variable slope of the correlation and its error; Column 5 and 6: second variable slope of the correlation and its error; Column 7 and 8: zero-point of the correlation and its errors; Column 9 and 10: intrinsic scatter and its errors; Column 11: measured scatter; Column 12: probability of the bivariate correlation; Column 13 and 14: $\Delta cAIC$ value and $RP = exp(\Delta cAIC/2)$ (the relative probability of the mono- and bivariate solutions); they are computed matching the bivariate solutions of this table to the monovariate solutions of Table 36 of the respective datasets. The pairings are: $MBH-\sigma-\rho_h$ with $MBH-\sigma$, $MBH-\rho_h$ with $MBH-MB_u$, $MBH-\sigma-\rho_h$ with $MBH-MB_u$, $MBH-MB_u$ with $MBH-\sigma$, $MBH-MB_u$ with $MBH-\sigma$, see Sect. 4, Column 15 and 16; Spearman coefficient and its probability.